Iranian Association of Electrical and Electronics Engineers

Shahid Chamran University of Ahvaz

Journal of Applied Research in Electrical Engineering

Vol. 1, No. 1, Winter and Spring 2022

Publisher: Shahid Chamran University of Ahvaz

E-ISSN: 2783-2864
P-ISSN: 2717-414X

Iranian Association of Electrical and Electronics Engineers

Journal of Applied Research in Electrical Engineering

E-ISSN: 2783-2864
P-ISSN: 2717-414X

Shahid Chamran University of Ahvaz

Journal of Applied Research in Electrical Engineering (JAREE), Volume 1, Number 1, Winter and Spring 2022

Publisher: Shahid Chamran University of Ahvaz, Iran

This magazine is the result of a formal partnership of **Shahid Chamran University of Ahvaz** and **Iranian Association of Electrical and Electronics Engineers**

Website: https://jaree.scu.ac.ir

E-mails: jaree@scu.ac.ir; jaree.scu@gmail.com

Address: **Department of Electrical Engineering, Faculty of Engineering, Shahid Chamran University of Ahvaz, Golestan Street, Ahvaz, Iran**
P.O. Box: **61357-85311**
Tel: **+986133330010-20, Ext. 5632 & 5735**
Fax: **+9861-33336642**

Editorial Board

Editor-in-Chief

Prof. Mahmood Joorabian
Shahid Chamran University of Ahvaz, Ahvaz, Iran
Power System Planning, Renewable Energy and Smart grid, FACTS Devises
mjoorabian@scu.ac.ir

Director-in-Charge

Prof. Seyed Ghodratolah Seifossadat
Shahid Chamran University of Ahvaz, Ahvaz, Iran
Power System Protection, Power Electronics, Power Quality
seifossadatyahood.com

Managing Editor

Dr. Alireza Saffarian (Associate Professor)
Shahid Chamran University of Ahvaz, Ahvaz, Iran
Power System Protection, Power System Stability, Power Quality, Distribution Systems
a.saffarian@scu.ac.ir

Executive Assistant

Dr. Mohammad Nabipour (Assistant Professor)
Shahid Chamran University of Ahvaz, Ahvaz, Iran
Power Electronics and Drive
mo.nabipour@scu.ac.ir

Associate Editor

Dr. Yousef Seifi Kavian (Associate Professor)
Shahid Chamran University of Ahvaz, Ahvaz, Iran
Electronics and Telecommunications
y.s.kavian@scu.ac.ir

Associate Editor

Dr. Mohsen Saniei (Associate Professor)
Shahid Chamran University of Ahvaz, Ahvaz, Iran
Power and Control
m.saniei@scu.ac.ir

Editorial Board

Prof. Saeedallah Mortazavi
Shahid Chamran University of Ahvaz, Ahvaz, Iran
Intelligent Control Systems, Power system Control, Automation, Fuzzy logic, Neural Networks
mortazavi_s@scu.ac.ir

Editorial Board

Prof. Abdolnabi Kosarian
Shahid Chamran University of Ahvaz, Ahvaz, Iran
Solid State Electronic Devices, Solar Cell Fabrication Technology
a.kosarian@scu.ac.ir

Editorial Board

Prof. Ebrahim Farshidi
Shahid Chamran University of Ahvaz, Ahvaz, Iran
Analog and Digital Integrated Circuits, Data Converters, Microelectronics
farshidi@scu.ac.ir

Editorial Board

Prof. Naser Pariz
Ferdowsi University of Mashhad, Mashhad, Iran
Nonlinear Control, Hybrid Systems, Aeronautics, Industrial Control, Applied Mathematics
n-pariz@um.ac.ir

Editorial Board

Prof. Abbas Zarifkar
Shiraz University, Shiraz, Iran
Optical Electronics
zarifkar@shirazu.ac.ir

Editorial Board

Dr. Edris Pouresmaeil (Associate Professor)
Aalto University, Espoo, Finland
Integration of renewable energies into the power grid
edris.pouresmaeil@aalto.fi

Editorial Board

Prof. Reza Ghaderi
Shahid Baheshti University, Tehran, Iran
Control Theory, System Identification, Control Systems, Fuzzy Engineering
r_ghaderisbu.ac.ir

Editorial Board

Prof. Fushuan Wen
Tallinn University of Technology, Tallinn, Estonia
Power systems and power economics
fushuan.wen@taltech.ee

Editorial Board

Prof. Majid Sanaye-pasand
University of Tehran, Tehran, Iran
Power Systems Protection, Digital Protective Relays, Power Systems Automation, Power System Transients
msanaye@ut.ac.ir

Editorial Board

Prof. Zabih (Fary) Ghassemlooy
North Umbria University, Newcastle upon Tyne, United Kingdom
Optical Communications, Visible Light, Communication Systems
z.ghassemlooy@northumbria.ac.uk

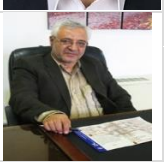

Editorial Board

Prof. Hossein Askarian Abyaneh
Amirkabir University of Technology, Tehran, Iran
Power System Protection
askarianaut.ac.ir

Language Editor

Majid Sadeghzadeh Hemayati
English Language Editing
m_s_hemayatiyahoo.com

Page Designer

Dr. Mahyar Abasi
Shahid Chamran University of Ahvaz, Ahvaz, Iran
mahyarabasi1368@yahoo.com

About Journal

Journal of Applied Research in Electrical Engineering (J. Appl. Res. Electr. Eng.) is a single-blind peer-reviewed, open access and free of charge international journal published by Shahid Chamran University of Ahvaz in cooperation with Iranian Association of Electrical and Electronics Engineers (IAEEE). The JAREE is a medium for global academics to exchange and spread the latest discoveries and advances in their applied research in electrical engineering. The JAREE aims at presenting important results of analytical, computational and experimental works within all specialized fields of electrical engineering (electronics, power, control and telecommunications). It welcomes high quality original research papers from contributors throughout the world. All papers are subject to a peer reviewing procedure. Submission, processing and publication of the papers in JAREE is free of charge.

Types of accepted papers include:

- **Research articles**
- **Review articles**
- **Applied articles**

Research papers are expected to present innovative solutions, novel concepts, or creative ideas that can help to address existing or emerging technical challenges in electrical engineering.

Application papers are expected to share valuable industry experiences on dealing with challenging technical issues, developing/adopting new standards, applying new technologies or solving complex problems. JAREE welcomes application papers that can have a significant impact on industry practices in the coming years.

Review papers are expected to provide insightful and expert reviews, tutorials, or study cases on an important, timely and widely-interested topic in electrical engineering.

All researchers in the fields of electrical science are invited to publish their scientific and research achievements in this journal. Interested authors can submit their manuscripts in the journal's website. More information is available in the website on how to prepare and submit the manuscripts.

Amis and Scope

The *Journal of Applied Research in Electrical Engineering* aims to provide a medium for dissemination of innovative and consequential papers that present analytical, computational and experimental works within all specialized fields of electrical engineering (electronics, power, control and telecommunications). The scope of the journal includes, but is not limited to, the following topic areas:

Electronics:

- **Optical electronics, photonics and solar cells**
- **Integrated analog circuits and mixed signals**
- **Integrated radio frequency circuits**
- **Digital electronics (VLSI)**
- **Semiconductor devices**
- **Sensor technology**

Power:

- **Dynamics and stability of the power systems**
- **Power system protection**
- **Electric power quality**
- **Operation and planning of the power systems**
- **High voltage insulation technology**
- **Flexible AC Transmission Systems (FACTS)**
- **Electric power distribution systems**
- **Smart grids, micro-grids, renewable energies and distributed generation**
- **Reliability of electrical energy systems**
- **Energy management and electricity market**
- **Electric machines and transformers**
- **Power electronic and electric drives**

Control:

- **Linear and non-linear control systems**
- **Adaptive, optimal and stochastic control**
- **Fuzzy systems, neural networks and intelligent control**
- **Robotic and mechatronic**
- **Modeling, Identification and optimization of systems**
- **Guidance and navigation systems**
- **Automation, industrial control and instrumentation**

Telecommunications:

- **Signal and image processing**
- **Wireless and cellular communication systems**
- **Telecommunication networks**
- **Radar and sonar**
- **Information theory and coding**
- **Cognitive radio**
- **Antenna design**
- **Microwave devices**
- **Wave propagation and electromagnetic compatibility**

Indexing Databases and Social Networks

Google Scholar:

https://scholar.google.com/citations?user=F7KQPtYAAAAJ&hl=en&authuser=1

LinkedIn:

https://www.linkedin.com/in/journal-of-applied-research-in-electrical-engineering-jaree-7540871b2/

Academia:

https://shahidchamranahwaz.academia.edu/JournalAppledResearchinElectricalEngineering

Mendeley:

https://www.mendeley.com/profiles/journal-of-applied-res-in-electrical-engineer/

Twitter:

https://twitter.com/jaree_scu

Facebook:

https://www.facebook.com/jaree.scu

Researchgate:

https://www.researchgate.net/profile/Jaree_Engineering

Telegram:

https://t.me/jareescu

Instagram:

https://www.instagram.com/jaree.scu/

Journal homepage:

http://jaree.scu.ac.ir

Journal emails:

jaree@scu.ac.ir, jaree.scu@gmail.com

Guide for Authors

How to submit a manuscript

For the initial submission, the authors have to just send the main manuscript file and the signed Copyright Form of the journal. While preparing manuscripts for initial submission, authors are kindly requested to follow the guidelines, described below:

- **The manuscript should be written in a Microsoft Word file (.doc or .docx).**
- **The file should include text (preferably in 10 points, "Times New Roman" font) and all figures (figures can be placed within the text at the appropriate point or at the end of the text).**
- **The manuscript pages should be prepared either using a double-column single-line spacing layout or a single-column double-line spacing layout. A margin of at least 1.5 cm on each side is required.**
- **All papers should be composed of Title, Author Name, Affiliation, Corresponding author email, Abstract, Keywords, Body, and References.**
- **The manuscript should be written in good English. It should have been carefully checked for clarity, conciseness, the correctness of grammar, and typographical errors.**
- **The corresponding author should sign the journal copyright form on behalf of any and all co-authors and upload it to the Journal's Submission System when submitting the manuscript. The journal copyright form can be downloaded from here.**
- **The corresponding author can use the JAREE Template for Cover Letter as a default text for the cover letter when submitting the manuscript.**
- **It is recommended that the title of the paper does not contain abbreviations or formulae.**
- **The abbreviations used in the abstract should be introduced both in the abstract and again on first use in the body.**
- **References should be numbered in the order they are mentioned in the text.**

Manuscript Submission

Submission to this journal proceeds totally online and you will be guided stepwise through the creation and uploading of your files. All correspondence, including notification of the Editor's decision and requests for revision, takes place by e-mail. To submit your manuscript, click on the Submit Manuscript link on the journal's homepage. Then, click on Register to create an author account. A message is sent to your email address containing your username and password. Then, login to the Journal's Submission System at the User's login page using the username and password to submit your new manuscript. Once you have logged in, you can change your password by clicking on the My Home link at the top menu.

Copyright and Open Access License

An author submitting a paper should ensure that he or she has the right to publish the paper and that it contains nothing defamatory. The JAREE will assume that all co-authors have agreed to the submission of any paper received. The corresponding author should sign the journal copyright form on behalf of any and all co-authors and upload it to the Journal's Submission System when submitting the manuscript.

Contents

Copyrights
© 2022 Licensee Shahid Chamran University of Ahvaz, Ahvaz, Iran. This article is an open-access article distributed under the terms and conditions of the Creative Commons Attribution –Non-Commercial 4.0 International (CC BY-NC 4.0) License (http://creativecommons.org/licenses/by-nc/4.0/).

Shahid Chamran University of Ahvaz

Iranian Association of Electrical and Electronics Engineers

Journal of Applied Research in Electrical Engineering

E-ISSN: 2783-2864
P-ISSN: 2717-414X
Homepage: https://jaree.scu.ac.ir/

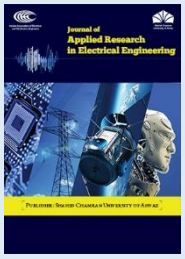

Research Article

Compact All-Optical Encoder Based on Silicon Photonic Crystal Structure

Mohsen Makvandi[1], Mohammad Javad Maleki[2], and Mohammad Soroosh[1,*]

[1] *Department of Electrical Engineering, Faculty of Engineering, Shahid Chamran University of Ahvaz, Ahvaz 61357-85311, Iran*

[2] *Faculty of Engineering, Lorestan University, Khorramabad 68151-44316, Iran*

* *Corresponding Author: m.soroosh@scu.ac.ir*

Abstract: In this paper, a photonic crystal structure composed of silicon rods is proposed for an all-optical 4*2 encoder. Four input ports are connected to two outputs port via the cross-connections. Different radii of rods as defects are placed in the cross-connection region for coupling the optical waves from the input waveguides to the desired outputs. The total size of the device is about 133 μm^2. Plane-wave expansion and finite difference time domain methods are used to calculate the band diagram and simulation of the optical wave propagation inside the structure, respectively. The maximum rise time of the device for all possible states is just about 205 fs, which is less than one in the previous works. No need for a bias port and using the same power at input ports are other advantages of this work. The normalized output power margins for logic 0 and 1 are calculated by 2% and 34%, respectively. The simulation results demonstrate that the presented structure is capable of using in optical integrated circuits.

Keywords: Encoder, optical devices, photonic band gap, photonic crystal.

Article history
Received 18 October 2019; Revised 11 February 2020; Accepted 17 March 2020; Published online 25 March 2020.
© 2020 Published by Shahid Chamran University of Ahvaz & Iranian Association of Electrical and Electronics Engineers (IAEEE)
How to cite this article
M. Makvandi, M. J. Maleki, and M. Soroosh, "Compact all-optical encoder based on silicon photonic crystal structure," *J. Appl. Res. Electr. Eng.*, vol. 1, no. 1, pp. 1-7, 2022. DOI: 10.22055/jaree.2020.31442.1007

Check for updates

1. INTRODUCTION

An ever-increasing demand for fast processing yields to excessive attention to optical communication processors and systems. High data transferring rate with a possibility for integration are the most dominant issues in designing all-optical circuits [1, 2].

Photonic crystals (PhCs), which are periodic arrays of dielectric, are known as an appropriate medium for designing optical devices because of profitable characteristics, including scalability, the capability of integration, and wide wavelength range [3]. Besides, impressive features such as the photonic band gap (PBG), slow light, and super prism can enhance PhCs-based applications. Recently, researchers aim to design all-optical devices based on PhCs, and many attempts have been made. The various optical devices based on PhCs such as filters [4-6], demultiplexers [7-9], adders [10-12], flip-flops [13, 14], analog-to-digital converters [15-17], decoders [18-20], and encoders [21-28] have been proposed.

For optical circuits, multiple sharing among the waveguides occurs; thus, encoders are potentially required for communication and switching operations. Encoders include logic gates which produce output signals depending on their corresponding powers at input ports. Plenty of PhC-based structures have been proposed and designed for encoding operation. Lee et al. [21] have been presented a 4-to-2 encoder based on the silicon rods with triangle arrangement in the air. This structure was constructed of Y-shaped waveguides and point defects. Although the normalized output power levels for logic 0 and 1 were 5 % and 98%, respectively, the large size of the structure was not applicable for integrated circuits. Another 4-to-2 encoder was proposed by Ouahab and Naoum [22] that consisted of both ring and cavity resonators and L-shape waveguides. They used the polystyrene defects among the silicon rods as nonlinear cavities. The normalized power levels for logic 0 and 1 were 5% and 45%, respectively, and the size of the structure was reduced to 18.5×13 μm^2 in comparison to Ref. [22].

Moniem [23] proposed a PhC-based encoder using the silicon rods with a square arrangement. The encoding operation was based on the NOR logic gate and four ring resonators. Unlike previously discussed researches, a time response analysis was reported. The rise time and the steady-state time of the encoder were about 2 ps and 3.5 ps, respectively. Different optical intensities were used for input

and bias waves. Besides, the normalized power levels were not reported. So, the proposed encoder may not be suitable for coupling to other optical devices. Naghizadeh and Khoshsima [24] have presented a 4-to-2 encoder using OR logic gates and ring resonators. They claimed that the encoding operation was correct, but one of the output ports was not active for state 11. The normalized output power levels of logic 0 and 1 were 3% and 45%, respectively. The size of the structure was as large as 723 μm^2, in comparison to other discussed works. Another similar structure was proposed by Mehdizadeh et al. [25], in which the calculated rise time was reduced to less than 1 ps in return for the large size of the structure, which was about 880 μm^2. Moreover, the normalized output power levels of 5% and 27% were reported for logic 0 and 1, respectively.

Gholamnezhad and Zavvari [26] proposed a different structure using GaAs rods with a square arrangement. There were two ring resonators and two bias ports in this structure. The size of the encoder and the rise time were 744 μm^2 and 1 ps, respectively. The normalized output power margins were 1% and 60% for logic 0 and 1, respectively. The radii of rods were reported about 123 nm, which seems to be a challenging issue considering semiconductor fabrication confinements. Another PhC-based encoder has been proposed by Hasangholizadeh-Kashtiban et al. [27] using the elliptical ring resonators and nonlinear rods. The radii of rods and minimum spacing were 106 nm and 100 nm, respectively, which may not be appropriate for semiconductor fabrication technology.

Recently, a 4-to-2 encoder has been proposed by Seif-dargahi [28]. In this structure, four ring resonators were designed, and the size of the device was 792 μm^2. The normalized output power levels for logic 0 and 1 were 5% and 42%, respectively. Although the rise time was almost similar to the previously discussed works, 1.8 ps, the steady-state time obtained for the structure was as long as 6 ps, which reduced the data transfer rate of the encoder. Therefore, the proposed structure may not be applicable for ultra-fast processing systems.

As discussed, some attempts have been made to improve the output characteristics of PhC-based encoders such as rise time, size of the structure, and power margin of output states simultaneously. Besides, considering restrictions imposed by semiconductor fabrication technology, few structures may not be acceptable, even though the operation characteristics were improved. In this study, a new structure is presented using the cross-section waveguides, in which the encoding operation is achieved by altering the radii of defect rods and no optical bias requirement. The size of the structure is decreased to 133 μm^2 in comparison with previous works [21, 22, 24-28]. The rise time is successfully obtained by 205 fs that is less than one in the previous works mentioned earlier [23-26, 28]. Furthermore, the normalized output power margins are 1% and 34% for logic 0 and 1, respectively. By comparing the operating characteristics of all reviewed encoders, it can be stated that the proposed structure can be potentially a proper candidate for being employed as a part of optical integrated circuits.

The paper is organized as follows; in Section 2, the designed encoder is presented, and time and power analysis are investigated in Section 3. Finally, a conclusion of all the above features is presented in Section 4, and the proposed structure is being evaluated.

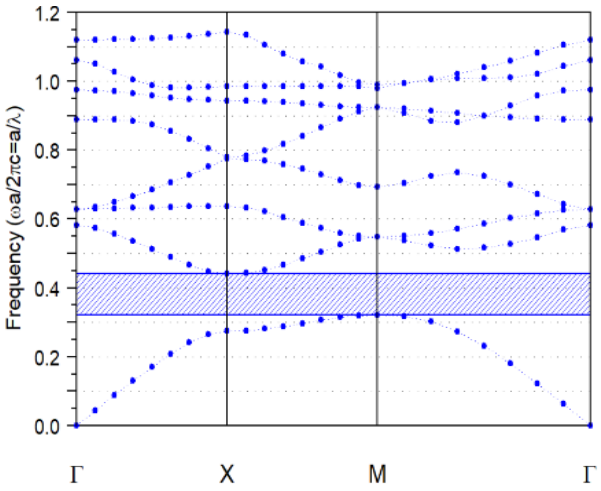

Fig. 1: The band diagram of the fundamental structure.

2. All-Optical 4-to-2 Encoder

The fundamental structure consists of a two-dimensional 22×22 square lattice of silicon rods in the air at X and Z directions. The refractive index and radii of the rods are 3.46 and r=0.2a, where a is the lattice constant. Considering the period of 550 nm for this arrangement, the structure's size will be about 133 μm^2. The plane wave expansion method is used for the calculation of PBG [29]. In this method, Maxwell's equations are defined as follows:

$$\frac{1}{\varepsilon_r}\nabla\times\nabla\times E=\left(\frac{\omega}{c}\right)^2 E \quad (1)$$

$$\nabla\times\frac{1}{\varepsilon_r}\nabla\times H=\left(\frac{\omega}{c}\right)^2 H \quad (2)$$

where ε_r is the relative permittivity, c is the speed of light in vacuum, and ω is the frequency of optical waves. Using Fourier series expansions for the fields, the eigenvalues $(\omega/c)^2$ were obtained for the different wave vectors. As shown in Fig. 1, the structure has one photonic band gap, $0.33 \leq a/\lambda \leq 0.45$, which is equal to the wavelength range of $1222\ \text{nm} \leq \lambda \leq 1667\ \text{nm}$ at TM mode. Because the C and L optical transmission bands are covered by this wide range, it is used for this work. So, the optical waves with the mentioned wavelength will not be propagated inside the structure.

The next step is arranging the rods performing as the encoder. Four input waveguides are constructed by removing specific rows of rods, as depicted in Fig. 2a. These waveguides are labeled as W_0 to W_3. The structure is completed by two couplers, consist of three groups of rods. In Fig. 2b, the magnified view of the cross-section is presented. R_1, R_2, and R_3 show the rods' radii and are equal to 0.8r, 0.5r, and 0.75r, respectively, where r is the radius of the fundamental rods. To guide the wave through output ports O_0 and O_1, two defects are placed at the right corners of W1 and W2 waveguides. Port N is placed to exit the optical waves injected from port I0.

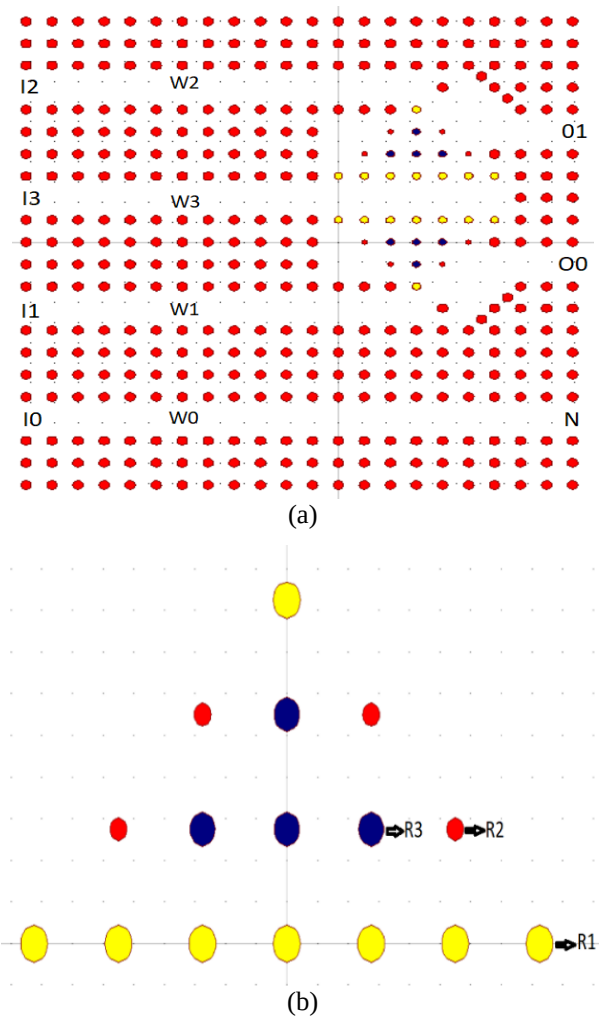

Fig. 2: (a) The proposed structure for optical encoder (b) the magnified view for the cross-section.

According to Bragg's theory, the incident waves with the wavelength of λ and the reflected waves from the periodic bilayers are in phase if the equation $n_a d_a+n_b d_b=\lambda/2$ is satisfied, where n_a and n_b are the refractive indices and d_a and d_b are the thickness of two layers. Considering the square lattice of the dielectric rods in the air gap, one rod and air gap are assumed as two different layers for the mentioned equation. To obtain the dropping operation at the same wavelength for the cavities, the left side of the mentioned equation should be kept in a constant value. So, changing the radii of the nonlinear rods assists to satisfy the equation. As a result, using the different radii in the structure makes the transmission operation toward the desired outputs.

The working states of the structure have been shown in Table 1. At each time, only one of the inputs is active (at logic1), and other inputs are inactive (at logic 0). In corresponding to the input states, O1 in conjunction with O0 generate the different binary codes. For example, O1=1 and O0=0 will be generated if I2 be equal to 1. When the input ports are not activated, no signal is guided toward the output ports O0 and O1 and results in O0=O1=0. Besides, for the working state I0=1, both output ports O0 and O1 will be also equal to 0. To distinguish two mentioned cases, port N has been placed in the structure. So, N=1 shows the proposed device works at I0=1 state.

Table 1: The working states of the presented structure.

Input States				Output Port		Port N
I3	I2	I1	I0	O1	O0	
0	0	0	1	0	0	1
0	0	1	0	0	1	0
0	1	0	0	1	0	0
1	0	0	0	1	1	0

3. RESULTS

In this research, RSoft Photonics CAD 8.2 has been used for simulation of the proposed structure. To simulate the optical wave propagation throughout the structure, the finite difference time domain method is used. In this method, Maxwell's equations are discretised in space and time domains and components of the electric and magnetic fields are calculated. Also, the perfect matched layer (PML) is supposed to the boundary condition.

The length of the cells (Δx and Δz) is equal to 0.25 nm which is less than λ/10 [30]. According to the Courant condition, the time step (Δt) should satisfy the following equation [30]:

$$c\Delta t < \frac{1}{\sqrt{(\frac{1}{\Delta x^2}+\frac{1}{\Delta z^2})}} \quad (3)$$

The time step of 0.029 fs is used for simulation. As shown in Table 1, the optical waves with λ=1550 nm launched at input ports considering the priority of four encoding states and the corresponding field distributions were shown in Fig. 3. Simulation of the structure demonstrates that the incoming optical waves from port I0 guide toward port N, so both O0 and O1 will be at logic 0 (Fig. 3a). As shown in Fig. 3b, the large portion of the launched signal at port I1 was coupled to port O0 and resulted in O0=1. One can see that port O1 will be activated when the optical waves come in port I2 (Fig. 3c). Using the mentioned defect silicon rods in the cross-section region results in the interferences in which the introduced signals from I1 and I2 are guided toward O0 and O1, respectively. Fig. 3d shows that the launched signal from port I3 reach to the cross-section and move toward both ports O0 and O1. In this state, two output ports will be activated.

The correct encoding operation of the proposed structure was shown in Fig. 3, but as discussed previously, the time analysis of the proposed device should be essentially reported. In this work, the time that output power reaches 90% steady-state value is defined as the rise time. The temporal behavior of the proposed encoder is demonstrated in Fig. 4, and the characteristics mentioned above are summarized in Table 2.

For estimating the normalized output power levels of logic states, the worst cases should be considered. So, the minimum power level of all logic states 1 and the maximum power level of all logic states 0 are reported as the encoder's margins. As can be inferred from Table 1, the normalized output power levels for logic 0 and 1 are 2% and 34%,

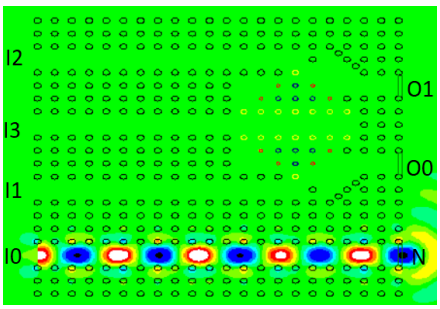

(a)

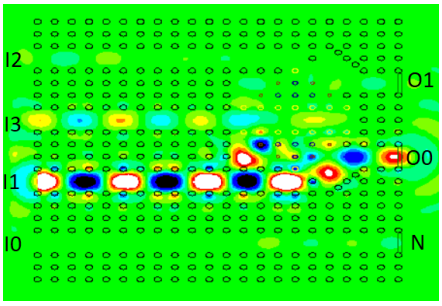

(b)

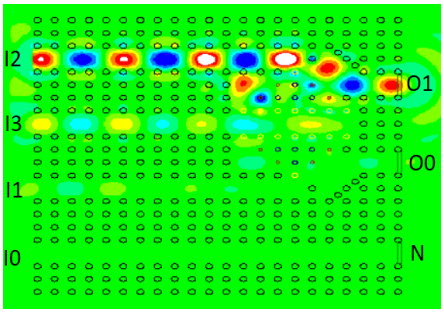

(c)

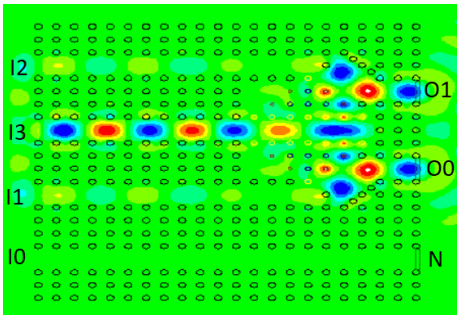

(d)

Fig. 3: The optical wave propagation throughout the structure for different input states in which only ports (a) I0, (b) I1, (c) I2, and (d) I3 are separately active.

Table 2: The results of time analysis for the proposed device.

Input logic states				Output logic states			Normalized output power (%)			Rise time (fs)
I0	I1	I2	I3	N	O1	O0	N	O1	O0	
0	0	0	0	0	0	0	0	0	0	-
1	0	0	0	1	0	0	100	0	0	115
0	1	0	0	0	0	1	10	2	54	205
0	0	1	0	0	1	0	0	52	2	205
0	0	0	1	0	1	1	0	34	35	190

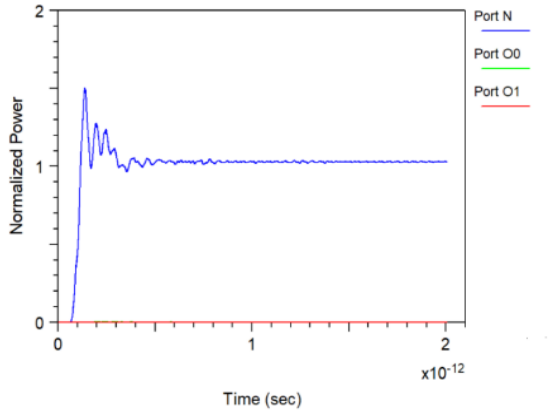

(a)

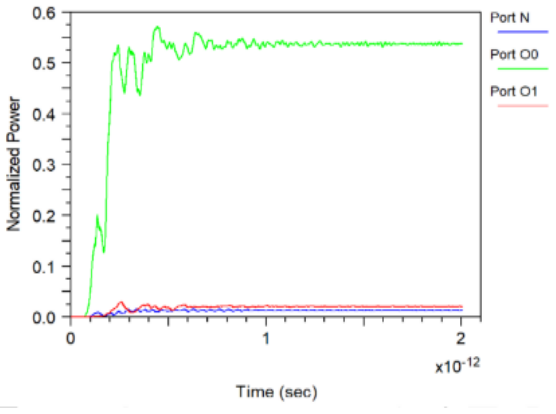

(b)

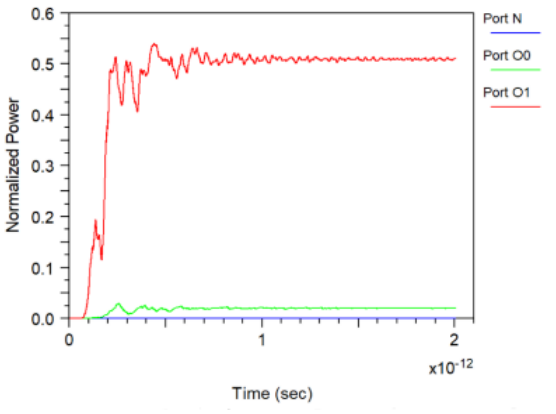

(c)

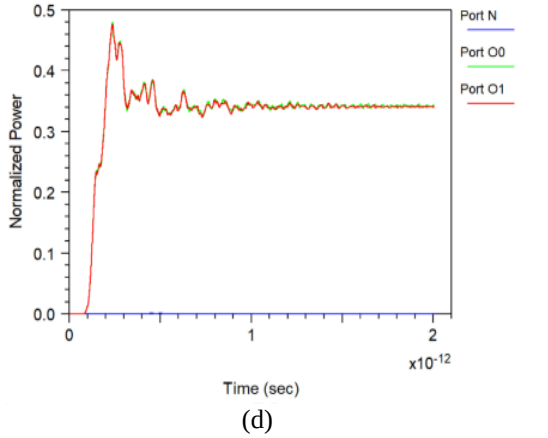

(d)

Fig. 4: The time response of the encoder when only input ports (a) I0, (b) I1, (c) I2, and (d) I3 are separately active.

Table 3: The main characteristics of the proposed structure in comparison with other works.

Work	Output power margin (%)	Size (μm^2)	Rise time (fs)	Regime
[21]	5-98	-	-	Nonlinear
[22]	5-45	757	-	Nonlinear
[23]	-	1225	2000	Linear
[24]	3-45	723	666	Linear
[25]	5-27	880	1000	Linear
[26]	1-60	744	1000	Nonlinear
[27]	5-40	200	-	Nonlinear
[28]	5-42	792	1800	Linear
This work	2-34	133	205	Linear

respectively. Also, the rise time of the presented structure is 205 fs. As the final assessment, challenging features of the proposed encoder are compared with the previously reported ones, and the results are summarized in Table 3.

One can see that the output power margin is successfully increased, and the rise time and the size of the presented encoder are less than all reviewed ones [22-28]. In addition, there were two bias ports in the design proposed in [23], but in the presented encoder, no bias port will be needed. So, inevitable properties imposed by high optical intensities will be disappeared.

Many attempts have been made for the fabrication of photonic crystal-based structures [31-40]. They have used different methods to fabricate these structures such as colloidal self-assembly, electron beam lithography, and direct writing via multiphoton microlithography. Based on these researches, they have been succeeded in decreasing the radius of rods to 75 nm. The smallest radius of rods in the presented structure is equal to 81 nm. So, one can be optimistic to fabricate the proposed device. Besides, the radii of 30 nm [41, 42], 40 nm [12, 19], 44 nm [43], 45 nm [44], 53 nm [45], 60 [46], and 70 nm [47] have been considered in photonic crystal-based structures for other works. According to the obtained results, the proposed structure is capable of using in optical integrated circuits.

4. Conclusion

In this study, a compact photonic crystal-based encoder was presented in which the different radii of rods assisted the optical coupling among the desired waveguides. The total size of the structure was equal to $133 \mu m^2$, which was more compact than other works. The rise time of the presented devices was calculated about 205 fs that was smaller than one in all previous works, so it is proper for optical processing applications. Another advantage of the proposed devices is the encoding operation in the linear regime via using the linear rods. This issue makes the possibility of working in low input powers. Also, the input ports work at the same power, and no bias signal is needed. The margins for logic 0 and 1 were obtained 2% and 34%, respectively. As a result, it seems that the presented encoder can be potentially used in optical integrated circuits.

CRediT Authorship Contribution Statement

Mohsen Makvandi: Formal analysis, Methodology, Resources, Software. **Mohammad Javad Maleki:** Software, Methodology. **Mohammad Soroosh:** Validation, Visualization, Roles/Writing - original draft, Writing - review & editing.

Declaration of Competing Interest

The authors declare that they have no known competing financial interests or personal relationships that could have appeared to influence the work reported in this paper. The ethical issues; including plagiarism, informed consent, misconduct, data fabrication and/or falsification, double publication and/or submission, redundancy has been completely observed by the authors.

References

[1] I. Andonegui, and A. C. Garcia-Adeva. (2013). Designing integrated circuitry in nanoscale photonic crystals. Available: https://spie.org/news/5035-designing-integrated-circuitry-in-nanoscale-photonic-crystals

[2] W. Bogaerts, and L. Chrostowski, "Silicon photonics circuit design: methods, tools and challenges," *Laser & Photonics Reviews*, vol. 12, no. 4, 1700237, 2018.

[3] Q. Gong, and X. Hu, *Photonic crystals: principles and applications*, 1st ed. Jenny Stanford Publishing, 2013.

[4] S. M. Musavizadeh, M. Soroosh, and F. Mehdizadeh, "Optical filter based on photonic crystal," *Indian Journal of Pure & Applied Physics*, vol. 53, no. 11, pp. 736–739, 2015.

[5] A. Tavousi, M. A. Mansouri-Birjandi, M. Ghadrdan, and M. Ranjbar-Torkamani, "Application of photonic crystal ring resonator nonlinear response for full-optical tunable add–drop filtering," *Photonic Network Communications*, vol. 34, no. 1, pp. 131-139, 2017.

[6] D. Qi, X. Wang, Y. Cheng, F. Chen, L. Liu, and R. Gong, "Quasi-periodic photonic crystal Fabry–Perot optical filter based on Si/SiO2 for visible-laser spectral selectivity," *Journal of Physics D: Applied Physics*, vol. 51, no. 22, 225103, 2018.

[7] R. Talebzadeh, M. Soroosh, Y. S. Kavian, and F. Mehdizadeh, "Eight-channel all-optical demultiplexer based on photonic crystal resonant cavities," *Optik*, vol. 140, pp. 331-337, 2017.

[8] V. Fallahi, M. Seifouri, S. Olyaee, and H. Alipour-Banaei, "Four-channel optical demultiplexer based on hexagonal photonic crystal ring resonators," *Optical Review*, vol. 24, no. 4, pp. 605-610, 2017.

[9] F. Mehdizadeh, M. Soroosh, and H. Alipour-Banaei, "An optical demultiplexer based on photonic crystal ring resonators," *Optik*, vol. 127, no. 20, pp. 8706-8709, 2016.

[10] M. Neisy, M. Soroosh, and K. Ansari-Asl, "All optical half adder based on photonic crystal resonant cavities,"

Photonic Network Communications, vol. 35, no. 2, pp. 245-250, 2018.

[11] F. Cheraghi, M. Soroosh, and G. Akbarizadeh, "An ultra-compact all optical full adder based on nonlinear photonic crystal resonant cavities," *Superlattices and Microstructures*, vol. 113, pp. 359-365, 2018.

[12] S. Serajmohammadi, H. Alipour-Banaei, and F. Mehdizadeh, "Proposal for realizing an all-optical half adder based on photonic crystals," *Applied Optics*, vol. 57, no. 7, pp. 1617-1621, 2018.

[13] S. S. Zamanian-Dehkordi, M. Soroosh, and G. Akbarizadeh, "An ultra-fast all-optical RS flip-flop based on nonlinear photonic crystal structures," *Optical Review*, vol. 25, no. 4, pp. 523-531, 2018.

[14] T. A. Moniem, "All-optical S-R flip flop using 2-D photonic crystal," *Optical and Quantum Electronics*, vol. 47, no. 8, pp. 2843-2851, 2015.

[15] F. Mehdizadeh, M. Soroosh, H. Alipour-Banaei, and E. Farshidi, "A novel proposal for All optical analog-to-digital converter based on photonic crystal structures," *IEEE Photonics Journal*, vol. 9, no. 2, pp. 1-11, 2017.

[16] A. Tavousi, and M. A. Mansouri-Birjandi, "Optical-analog-to-digital conversion based on successive-like approximations in octagonal-shape photonic crystal ring resonators," *Superlattices and Microstructures*, vol. 114, pp. 23-31, 2018.

[17] K. Fasihi, "All-optical analog-to-digital converters based on cascaded 3-dB power splitters in 2D photonic crystals," *Optik*, vol. 125, no. 21, pp. 6520-6523, 2014.

[18] T. Daghooghi, M. Soroosh, and K. Ansari-Asl, "Ultra-fast all-optical decoder based on nonlinear photonic crystal ring resonators," *Applied Optics*, vol. 57, no. 9, pp. 2250-2257, 2018.

[19] T. A. Moniem, "All optical active high decoder using integrated 2D square lattice photonic crystals," *Journal of Modern Optics*, vol. 62, no. 19, pp. 1643-1649, 2015.

[20] T. Daghooghi, M. Soroosh, and K. Ansari-Asl, "A low-power all optical decoder based on photonic crystal nonlinear ring resonators," *Optik*, vol. 174, pp. 400-408, 2018.

[21] K. Lee, Y. Yang, Y. Lin, W. Lee, C. Lee, and S. Wong, "The designs of 4×2 encoder based on photonic crystals," in *2009 Asia Communications and Photonics conference and Exhibition*, 2009, pp. 1-2.

[22] I. Ouahab, and R. Naoum, "A novel all optical 4×2 encoder switch based on photonic crystal ring resonators," *Optik - International Journal for Light and Electron Optics*, vol. 127, no. 19, pp. 7835-7841, 2016.

[23] T. A. Moniem, "All-optical digital 4 × 2 encoder based on 2D photonic crystal ring resonators," *Journal of Modern Optics*, vol. 63, no. 8, pp. 735-741, 2016.

[24] S. Naghizade, and H. Khoshsima, "Low input power an all optical 4 × 2 encoder based on triangular lattice shape photonic crystal," *Journal of Optical Communications*, vol. 42, no. 1, pp. 17-24, 2021.

[25] F. Mehdizadeh, M. Soroosh, and H. Alipour-Banaei, "Proposal for 4-to-2 optical encoder based on photonic crystals," *IET Optoelectronics*, vol. 11, no. 1, pp. 29-35, 2017.

[26] S. Gholamnejad, and M. Zavvari, "Design and analysis of all-optical 4–2 binary encoder based on photonic crystal," *Optical and Quantum Electronics*, vol. 49, no. 9, p. 302, 2017.

[27] M. Hassangholizadeh-Kashtiban, R. Sabbaghi-Nadooshan, and H. Alipour-Banaei, "A novel all optical reversible 4×2 encoder based on photonic crystals," *Optik*, vol. 126, no. 20, pp. 2368-2372, 2015.

[28] H. Seif-Dargahi, "Ultra-fast all-optical encoder using photonic crystal-based ring resonators," *Photonic Network Communications*, vol. 36, no. 2, pp. 272-277, 2018.

[29] A. V. Lavrinenko, J. Laegsgaard, N. Gregersen, F. Schmidt, and T. Sondergaard, *Numerical methods in photonics*, 1st ed. ed. CRC Press, 2015.

[30] D. M. Sullivan, *Electromagnetic simulation using the FDTD method*. Wiley-IEEE Press, 2013.

[31] D. Lowell et al., "Holographic fabrication of graded photonic super-quasi-crystals with multiple-level gradients," *Applied Optics*, vol. 57, no. 22, pp. 6598-6604, 2018.

[32] L. Pang, W. Nakagawa, and Y. Fainman, "Fabrication of two-dimensional photonic crystals with controlled defects by use of multiple exposures and direct write," *Applied Optics*, vol. 42, pp. 5450-5456, 2003.

[33] M. Campbell, D. N. Sharp, M. T. Harrison, R. G. Denning, and A. J. Turberfield, "Fabrication of photonic crystals for the visible spectrum by holographic lithography," *Nature*, vol. 404, no. 6773, pp. 53-56, 2000.

[34] D. Lowell, S. Hassan, M. Adewole, U. Philipose, B. Chen, and Y. Lin, "Holographic fabrication of graded photonic super-crystals using an integrated spatial light modulator and reflective optical element laser projection system," *Applied Optics*, vol. 56, no. 36, pp. 9888-9891, 2017.

[35] Y. Liu, S. Liu, and X. Zhang, "Fabrication of three-dimensional photonic crystals with two-beam holographic lithography," *Applied Optics*, vol. 45, pp. 480-483, 2006.

[36] H. M. Ku, C. Y. Huang, and S. Chao, "Fabrication of three-dimensional autocloned photonic crystal on sapphire substrate," *Applied Optics*, vol. 50, no. 9, pp. C1-C4, 2011.

[37] O. J. A. Schueller, G. M. Whitesides, J. A. Rogers, M. Meier, and A. Dodabalapur, "Fabrication of photonic crystal lasers by nanomolding of solgel glasses," *Applied Optics*, vol. 38, no. 27, pp. 5799-5802, 1999.

[38] J.-H. Chen, Y.-T. Huang, Y.-L. Yang, M.-F. Lu, and J.-M. Shieh, "Design, fabrication, and characterization of Si-based ARROW photonic crystal bend waveguides

and power splitters," *Applied Optics*, vol. 51, no. 24, pp. 5876-5884, 2012.

[39] L. Cui, Y. Zhang, J. Wang, Y. Ren, Y. Song, and L. Jiang, "Ultra-Fast Fabrication of Colloidal Photonic Crystals by Spray Coating," *Macromolecular Rapid Communications*, vol. 30, no. 8, pp. 598-603, 2009.

[40] G. von Freymann, V. Kitaev, B. V. Lotsch, and G. A. Ozin, "Bottom-up assembly of photonic crystals," *Chemical Society Reviews*, vol. 42, no. 7, pp. 2528-2554, 2013.

[41] E. h. Shaik, and N. Rangaswamy, "Realization of all-optical NAND and NOR logic functions with photonic crystal based NOT, OR and AND gates using De Morgan's theorem," *Journal of Optics*, vol. 47, no. 1, pp. 8-21, 2018.

[42] C. Harshita, S. K. Rajinder, and P. Balveer, "Photonic crystal waveguide-based biosensor for detection of diseases," *Journal of Nanophotonics*, vol. 10, no. 3, pp. 1-10, 2016.

[43] M. Zaremanesh, and M. Noori, "Large-angle polarization insensitive negative refraction in the diagonal array photonic crystal," *Physica Scripta*, vol. 94, no. 12, 125510, 2019.

[44] J. K. Jayabarathan, G. Subhalakshmi, and S. Robinson, "Design of all-optical 8*3 encoder using hexagonal shaped photonic crystal ring resonator," *Journal of Ovonic Research*, vol. 14, no. 5, pp. 351-358, 2018.

[45] M. R. Geraili, S. E. Hosseini, M. B. Tavakoli, and M. Shokooh-Saremi, "Application of nonlinear photonic crystal ring resonators in realizing all optical OR/NOT/AND gates," *Optical and Quantum Electronics*, vol. 51, no. 7, 228, 2019.

[46] E. H. Shaik, and N. Rangaswamy, "Implementation of 1×2 decoder and XOR-XNOR logic functions on a PhC structure," *Journal of Information and Optimization Sciences*, vol. 38, no. 6, pp. 953-960, 2017.

[47] S. Bakhshi, M. K. Moravvej-Farshi, and M. Ebnali-Heidari, "Proposal for enhancing the transmission efficiency of photonic crystal 60° waveguide bends by means of optofluidic infiltration," *Applied Optics*, vol. 50, no. 21, pp. 4048-4053, 2011.

BIOGRAPHY

Mohsen Makvandi received the B.Sc. and M.Sc. degrees in electronic engineering from Shahid Chamran University of Ahvaz. His fields of interests are all-optical devices based on photonic crystals.

Mohammad Javad Maleki received the B.Sc. and M.Sc. degrees in electronic engineering from Islamic Azad University of Borujerd and Lorestan University, respectively. His fields of interests are all-optical devices based on photonic crystals and plasmonics.

Mohammad Soroosh received the B.Sc. degree from the Isfahan University of Technology at Isfahan in 2000 and the M.Sc. and Ph.D. degrees from Tarbiat Modares University at Tehran in 2003 and 2009, respectively, all in electronics engineering. He joined the Iran Telecommunication Research Center, Tehran in 2003 where he was a researcher at optical communication group. Currently, he is an associate professor of electronics in Shahid Chamran University of Ahvaz, Iran. His research interests are in modeling and simulation of photonic and optoelectronic devices.

Copyrights
© 2020 Licensee Shahid Chamran University of Ahvaz, Ahvaz, Iran. This article is an open-access article distributed under the terms and conditions of the Creative Commons Attribution –Non-Commercial 4.0 International (CC BY-NC 4.0) License (http://creativecommons.org/licenses/by-nc/4.0/).

Shahid Chamran University of Ahvaz

Iranian Association of Electrical and Electronics Engineers

Journal of Applied Research in Electrical Engineering

E-ISSN: 2783-2864
P-ISSN: 2717-414X
Homepage: https://jaree.scu.ac.ir/

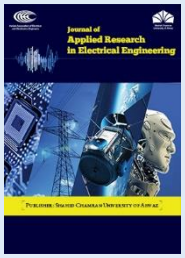

Research Article

A Novel Design for an All-Optical Half Adder Using Linear Defects in Photonic Crystal Microstructure

Saleh Naghizade [1], and Hamed Saghaei [2,*]

[1] *Young Researchers and Elite Club, Tabriz Branch, Islamic Azad University, Tabriz 5157-944533, Iran*

[2] *Department of Electrical Engineering, Shahrekord Branch, Islamic Azad University, Shahrekord 8813-733395, Iran*

** Corresponding Author: h.saghaei@iaushk.ac.ir*

Abstract: This paper reports a new optical half-adder design using linear defects in a photonic crystal (PhC) structure. The half adder's proper design obviates the need to increase the input signal's intensity for the nonlinear optical Kerr effect's appearance, which leads to the diversion of the incoming light toward the desired output. The proposed device is composed of silicon rods consisting of four optical waveguides and a defect in a PhC. Two well-known plane wave expansion and finite difference time domain methods are used to study and analyze photonic band structure and light propagation inside the PhC, respectively. The numerical results demonstrate that the ON-OFF contrast ratios are 16 dB for "Sum" and about 14 dB for "Carry". They also reveal that the proposed half-adder has a maximum time delay of 0.8 ps with a total footprint of 158 μm^2. Due to very low delay time, high contrast ratio, and small footprint, they are more crucial in modern optoelectronic technologies, so this structure can be used in the next generation of all-optical high-speed central processing units.

Keywords: High-speed, all-optical, half-adder, photonic crystals, photonic bandgap.

Article history
Received 26 July 2020; Revised 11 December 2020; Accepted 18 December 2020; Published online 1 January 2021.
© 2021 Published by Shahid Chamran University of Ahvaz & Iranian Association of Electrical and Electronics Engineers (IAEEE)
How to cite this article
S. Naghizade, and H. Saghaei, "A novel design for an all-optical half adder using linear defects in photonic crystal microstructure," *J. Appl. Res. Electr. Eng.*, vol. 1, no. 1, pp. 8-13, 2022. DOI: 10.22055/jaree.2020.34466.1010

Check for updates

1. INTRODUCTION

Photon-based devices have been the focus of researchers in recent decades due to their high processing speed, small area, and low power consumption. The design of optical communication systems based on high-speed devices is one of the aims of research groups so that it has been growing at a high speed in recent years [1–3]. The speed of information processing is critical in telecommunication networks. All-optical logic-based devices are required for realizing a high-speed processor. All-optical half adders are one of the important devices for implementing optical data processing systems because all four basic operations in mathematics, including addition, multiplication, subtraction, and division, can be done using optical half adders [4–8]. Photonic crystals (PhCs) play a vital role in all-optical systems [9,10]. Having photonic band gaps (PBGs) in a certain wavelength range enables them to confine and control the light propagation at the appropriate waveguides [11–13]. Therefore, many optical devices such as optical filters [14–18], PhC fibers [19–28], sensors [20], [29–31], demultiplexers [32–37], switches [13, 38, 39], interferometers [40,41], logic gates such as NOT, AND, OR, NAND, encoders, and decoders [42–45], flip-flops [46], comparators [47– 49], adders [50–52], and analog to digital converters (ADCs) [53–57] have been designed using this property of the PhCs. Recently, all-optical half adders have been designed and studied based on PhCs. Most of the previously proposed logic gates are classified into two main categories. The first structures are working based on nonlinear Kerr-effect, and the second ones are based on linear phase-difference. The structures based on the optical Kerr effect need high intensity of light in order to show the nonlinear optical Kerr effect. However, in this case, the structure is likely to be damaged due to the use of a high-intensity input optical signal. Researchers have already presented different structures for half adders. Jiang et al. [8] proposed an all-optical half adder based on self-collimated beams in a 2D PhC. In the presented structure, two-line defects inside the structure were used to operate as a power splitter. Ghadrdan et al. [58] proposed a half adder in a 2D PhC by a combination of AND and XOR gates. Xavier et al. [59] presented a half adder in a 2D PhC where line defects and self-collimated beams were simultaneously used. The proposed structure consisted of AND and XOR logic gates.

Rahmani and Mehdizadeh [60] reported a new optical half-adder design where three nonlinear ring resonators are used in a 2D PhC. The nonlinear resonators were created by adding some rods, composed of nonlinear material, to the ring resonator structure. The maximum rising time and falling time of the half adder were about 1.5 ps and 1 ps, respectively. Several optical half-adder and full-adder devices have been reported by other authors so far [7,44], [50–52], [61–63].

This paper designs a linear phase-difference-based half-adder structure with a low input optical power intensity of 1 W/μm^2. It has a good capability to separate logics 0 and 1 at the outputs. To confine light in the waveguides and defect region and propagate it as desired, we need wavelengths in the PBG of the PhC. Thus, the proposed structure is simulated at the c-band communication window (*i.e.*, at 1550 nm). This half adder is characterized by a relatively large power difference between the two logical levels. It also has low delay time, low input power, and a small footprint, which reduces the error in high-speed data processing systems.

2. The Proposed Physical Structure

Fig. 1 shows the symbol and truth table of a half adder. As can be observed in the figure, a half adder has two inputs and two outputs. X and Y are the input ports while the output ports are S and C, where S represents the "Sum" and C represents the "Carry". To design an all-optical half adder, we employ a 21×21 array of dielectric rods composed of silicon arranged in a square lattice with an air background. The refractive index of the silicon rods is 3.46 at 1550 nm.

The rods' radius is r=0.2a where *a* is the lattice constant (or pitch size) of the PhC structure, which is 600 nm in this study. We calculated the band diagram of the fundamental structure using the plane wave expansion (PWE) method [64]. Fig. 2 illustrates that there are two PBGs in the TM polarization mode (the blue color areas).

The first PBG in the TM mode that is 0.285<a/λ<0.418 has the appropriate wavelength range for our purposes. By choosing the lattice constant of a = 600 nm, the PBG will be at 1435nm<λ<2105nm, which completely covers the C-band communication window's wavelength range.

For an all-optical half-adder design in a 21×21 array of dielectric rods, four optical waveguides and one resonant cavity are created in the determined regions of the PhC structure shown in Fig. 3. In fact, a combination of W1, W2, W3, and W4 waveguides with resonant cavity builds our optical half adder. The defect region contains ten folds of dielectric rods in which the radius of 9 folds (R_1) is 60 nm. The radius of the last defect rod (R_2) shown by yellow is 30 nm. It is located at the input of W4. X and Y are the half adder's input ports at the beginning of W1 and W2, respectively. The end paths of W3 and W4 are the S and C ports of the proposed half adder.

3. Numerical Results and Discussion

To simulate the proposed structure, we employed the finite difference time domain (FDTD) method [65]. The use of a 3D simulation to study the proposed structure, which is very time-consuming, requires a powerful computer [64]. Due to the time and memory constraints, the effective refractive index method is applied to reduce 3D simulations into 2D simulations with acceptable accuracy in this study [64]. The proposed half adder has two input ports, so we have four different input states. Therefore, we used light waves centered at 1550 nm at the input. All cases of the half adder are shown in Fig. 4 and classified as follows:

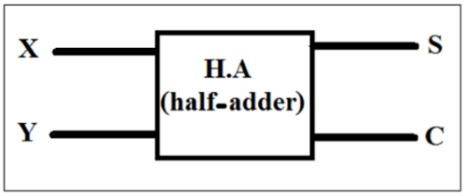

(a)

X	Y	S	C
0	0	0	0
1	0	1	0
0	1	1	0
1	1	0	1

(b)

Fig. 1: An illustration of (a) block diagram and (b) truth table of an all-optical half adder.

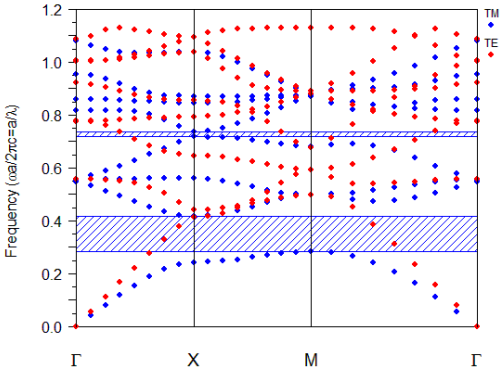

Fig. 2: The photonic band diagram of a fundamental square lattice PhC structure.

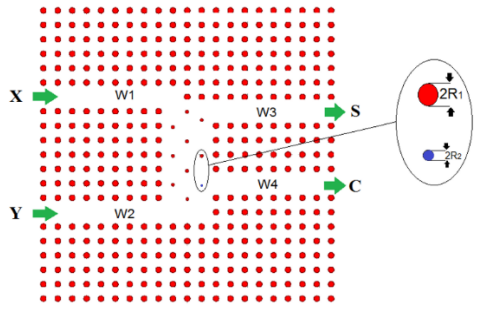

Fig. 3: The proposed all-optical half-adder design in a 21×21 array of dielectric rods consisting of four optical waveguides and one resonant cavity.

Case #1: When both input ports (X and Y) are OFF, there is no optical power inside the structure, so both output ports (S and C) will be OFF (see Fig. 4a).

Case #2 and **#3:** When one of the input ports (either X or Y) is ON, the resonant cavity will couple the optical beams

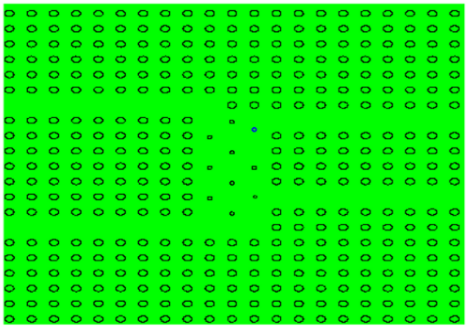

(a)

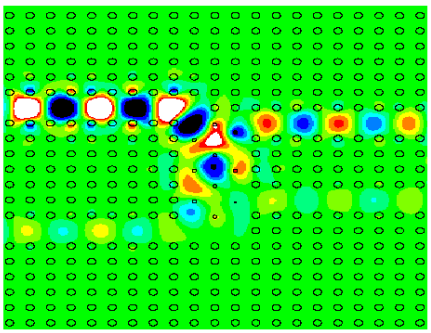

(b)

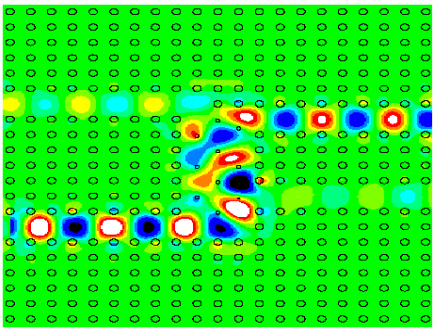

(c)

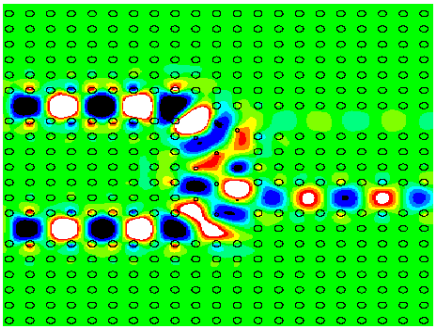

(d)

Fig. 4: Light propagation inside the proposed half adder for (a) Case #1 (b) Case #2, (c) Case #3, and (d) Case #4.

into W3 due to wavelength matching between the resonant mode of the resonant cavity and the input signal. Therefore, in these cases, S will be ON, and C will be OFF (see Fig. 4b, and 4c).

Case #4: When both input ports are ON, the resonant cavity will couple optical beams coming from W1 and W2 into W4. Therefore, in this case, S will be OFF, and C will be ON (see Fig. 4c).

By comparing the results with the truth table shown in Fig. 1b, it is confirmed that the proposed structure can operate as an all-optical half adder. The normalized output of the proposed structure is shown in Fig. 5. As shown in Fig. 5a, when the input port of X is ON, the normalized intensities of the S and C ports are 75% and 5%, respectively. In this case, the time delay (steady-state time) is about 0.8 ps. Fig. 5b demonstrates that when the Y input port is ON, the normalized intensities of the S and C ports are 85% and 2%, respectively. In this case, the time delay is about 0.8ps. Fig. 5c shows when both input ports are ON, the normalized intensities of the S and C ports are 2% and 125%, respectively. In this case, the time delay is about 0.7ps. The results show that our proposed structure has a shorter delay, a lower input intensity (equal to 1 W/μm^2 because nonlinearity is not used), and a smaller footprint compared to previously

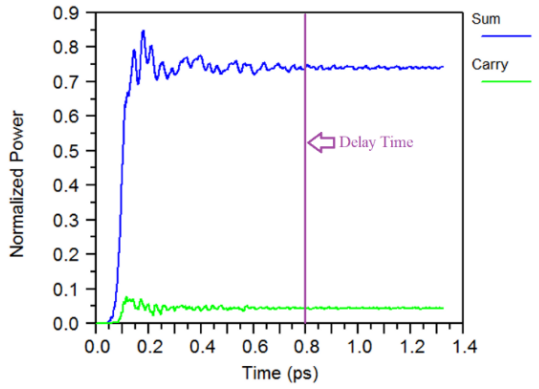

(a)

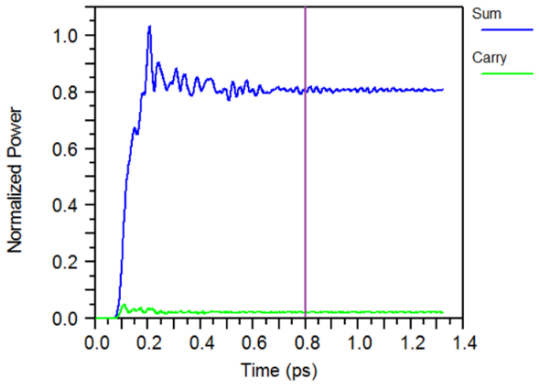

(b)

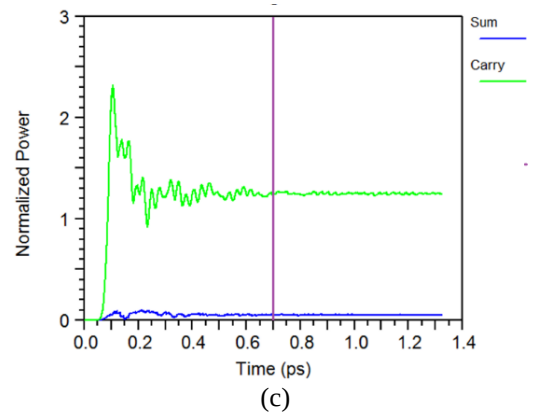

(c)

Fig. 5: Normalized output power versus time of the proposed half adder for (a) Case #1 (b) Case #2 or #3, and (c) Case #4

Table 1: A comparison of the proposed half adder with other published papers.

Works	Method	Min power for logic 1	Max power for logic 0	Time delay	Footprint
Ref. [8]	Self-collimation	50%	7%	-	-
Ref. [58]	Nonlinear	81%	22%	0.85 ps	168 μm^2
Ref. [59]	Self-collimation	73%	24%	-	169 μm^2
Ref. [60]	Nonlinear	100%	0%	1 ps	-
Ref. [7]	Nonlinear	96%	4%	3.6 ps	250 μm^2
Ref. [44]	Linear	71%	22%	-	-
Ref. [61]	Nonlinear	95%	-	0.91 ps	-
Ref. [66]	Linear	95%	19%	4 ps	1056 μm^2
Ref. [67]	Linear	45%	19%	0.48 ps	171 μm^2
This work	Linear	75%	5%	0.8 ps	158 μm^2

reported structures. Considering these results, the ON-OFF contrast ratios ($10\times\log(P_{ON}/P_{OFF})$) for both S and C ports are 16 dB and 14 dB, respectively. Also, according to the presented diagrams, the maximum time delay is about 0.8 ps. We considered the time required for the output port to reach its steady-state as the delay time.

Table 1 compares the proposed device performance with other published papers.

4. Conclusion

In this paper, we designed an ultrafast all-optical half adder based on a photonic crystal microstructure in an area of 158 μm^2. The photonic band diagram was calculated using the plane wave expansion method for TE and TM polarization modes. We also studied the light propagation in the device via the finite-difference time-domain method and calculated the outputs for different input ports' states. One of the most important advantages of our structure compared to similar studies was the non-use of high nonlinear dielectric rods, which eliminated the need to increase the input power to divert the incoming light emission to the desired output. Simulations revealed that the minimum transmission of logic 1 and the maximum transmission of logic 0 are 4% and 75%, respectively. The calculations also demonstrated that the proposed half adder has a steady-state time of 0.8 ps due to its small area.

CRediT Authorship Contribution Statement

Saleh Naghizade: Conceptualization, Data curation, Formal analysis, Funding acquisition, Investigation, Methodology, Software. **Hamed Saghaei:** Project administration, Resources, Software, Supervision, Validation, Visualization, Roles/Writing - original draft, Writing - review & editing.

Declaration of Competing Interest

The authors declare that they have no known competing financial interests or personal relationships that could have appeared to influence the work reported in this paper. The ethical issues; including plagiarism, informed consent, misconduct, data fabrication and/or falsification, double publication and/or submission, redundancy has been completely observed by the authors.

References

[1] H. Saghaei, B. Seyfe, H. Bakhshi, and R. Bayat, "Novel approach to adjust the step size for closed-loop power control in wireless cellular code division multiple access systems under flat fading," *IET Communications*, vol. 5, no. 11, pp. 1469–1483, 2011.

[2] M. Soljačić, and J. D. Joannopoulos, "Enhancement of nonlinear effects using photonic crystals," *Nature materials*, vol. 3, no. 4, pp. 211–219, 2004.

[3] Y. Akahane, T. Asano, B.-S. Song, and S. Noda, "High-Q photonic nanocavity in a two-dimensional photonic crystal," *Nature*, vol. 425, no. 6961, pp. 944–947, 2003.

[4] S. Mukhopadhyay, "An optical conversion system: From binary to decimal and decimal to binary," *Optics Communications*, vol. 76, no. 5–6, pp. 309–312, 1990.

[5] E. Yablonovitch, "Inhibited spontaneous emission in solid-state physics and electronics," *Physical Review Letters*, vol. 58, no. 20, pp. 2059–2062, 1987.

[6] E. Yablonovitch, T. J. Gmitter, and K. M. Leung, "Photonic band structure: The face-centered-cubic case employing nonspherical atoms," *Physical Review Letters*, vol. 67, no. 17, pp. 2295–2298, 1991.

[7] M. H. Sani, A. A. Tabrizi, H. Saghaei, and R. Karimzadeh, "An ultrafast all-optical half adder using nonlinear ring resonators in photonic crystal microstructure," *Optical and Quantum Electronics*, vol. 52, no. 102, pp. 1-10, 2020.

[8] Y. C. Jiang, S. Bin Liu, H. F. Zhang, and X. K. Kong, "Realization of all optical half-adder based on self-collimated beams by two-dimensional photonic crystals," *Optics Communications*, vol. 348, pp. 90–94, 2015.

[9] C. M. Soukoulis, *Photonic crystals and light localization in the 21st century*. Springer Science & Business Media, 2001.

[10] K. Sakoda, *Optical properties of photonic crystals*. Springer Science & Business Media, 2001.

[11] B. F. Diaz-Valencia, and J. M. Calero, "Photonic band gaps of a two-dimensional square lattice composed by superconducting hollow rods," *Physica C: Superconductivity and its Applications*, vol. 505, pp. 74–79, 2014.

[12] H. Alipour-Banaei, M. Hassangholizadeh-Kashtiban, and F. Mehdizadeh, "WDM and DWDM optical filter based on 2D photonic crystal Thue-Morse structure," *Optik*, vol. 124, no. 20, pp. 4416–4420, 2013.

[13] H. Saghaei, A. Zahedi, R. Karimzadeh, and F. Parandin, "Line defects on photonic crystals for the design of all-optical power splitters and digital logic gates," *Superlattices and Microstructures*, vol. 110, pp. 133–138, 2017.

[14] M. R. Rakhshani, and M. A. Mansouri-Birjandi, "Realization of tunable optical filter by photonic crystal ring resonators," *Optik*, vol. 124, no. 22, pp. 5377–5380, 2013.

[15] S. Naghizade, and S. M. Sattari-Esfahlan, "Excellent quality factor ultra-compact optical communication filter on ring-shaped cavity," *Journal of Optical Communications*, vol. 40, no. 1, pp. 21–25, 2019.

[16] S. Naghizade, and S. M. Sattari-Esfahlan, "Loss-less elliptical channel drop filter for WDM applications," *Journal of Optical Communications*, vol. 40, no. 4, pp. 379–384, 2017.

[17] M. Hosseinzadeh Sani, A. Ghanbari, and H. Saghaei, "An ultra-narrowband all-optical filter based on the resonant cavities in rod-based photonic crystal microstructure," *Optical and Quantum Electronics*, vol. 52, no. 6, p. 295, 2020.

[18] S. Naghizade, and H. Saghaei, "Tunable graphene-on-insulator band-stop filter at the mid-infrared region," *Optical and Quantum Electronics*, vol. 52, no. 4, p. 224, 2020.

[19] M. Ebnali-Heidari, H. Saghaei, F. Koohi-Kamali, M. Naser Moghadasi, and M. K. Moravvej-Farshi, "Proposal for supercontinuum generation by optofluidic infiltrated photonic crystal fibers," *IEEE Journal on Selected Topics in Quantum Electronics*, vol. 20, no. 5, 2014.

[20] H. Saghaei, M. K. Moravvej-Farshi, M. Ebnali-Heidari, and M. N. Moghadasi, "Ultra-wide mid-infrared supercontinuum generation in $As_{40}Se_{60}$ chalcogenide fibers: solid core PCF versus SIF," *IEEE Journal of Selected Topics in Quantum Electronics*, vol. 22, no. 2, 2016.

[21] H. Saghaei, M. Ebnali-Heidari, and M. K. Moravvej-Farshi, "Midinfrared supercontinuum generation via As_2Se_3 chalcogenide photonic crystal fibers," *Applied Optics*, vol. 54, no. 8, pp. 2072-2079, 2015.

[22] M. Aliee, M. H. Mozaffari, and H. Saghaei, "Dispersion-flattened photonic quasicrystal optofluidic fiber for telecom C band operation," *Photonics and Nanostructures - Fundamentals and Applications*, vol. 40, 100797, 2020.

[23] A. Ghanbari, A. Kashaninia, A. Sadr, and H. Saghaei, "Supercontinuum generation with femtosecond optical pulse compression in silicon photonic crystal fibers at 2500 nm," *Optical and Quantum Electronics*, vol. 50, 411, 2018.

[24] R. Raei, M. Ebnali-Heidari, and H. Saghaei, "Supercontinuum generation in organic liquid–liquid core-cladding photonic crystal fiber in visible and near-infrared regions," *Journal of the Optical Society of America B*, vol. 35, no. 2, pp. 323-330, 2018.

[25] M. Kalantari, A. Karimkhani, and H. Saghaei, "Ultra-Wide mid-IR supercontinuum generation in As_2S_3 photonic crystal fiber by rods filling technique," *Optik*, vol. 158, pp. 142–151, 2018.

[26] H. Saghaei, and A. Ghanbari, "White light generation using photonic crystal fiber with sub-micron circular lattice," *Journal of Electrical Engineering*, vol. 68, no. 4, pp. 282–289, 2017.

[27] A. Ghanbari, A. Kashaninia, A. Sadr, and H. Saghaei, "Supercontinuum generation for optical coherence tomography using magnesium fluoride photonic crystal fiber," *Optik*, vol. 140, pp. 545–554, 2017.

[28] H. Saghaei, "Supercontinuum source for dense wavelength division multiplexing in square photonic crystal fiber via fluidic infiltration approach," *Radioengineering*, vol. 26, no. 1, pp. 16–22, 2017.

[29] F. Tavakoli, F. B. Zarrabi, and H. Saghaei, "Modeling and analysis of high-sensitivity refractive index sensors based on plasmonic absorbers with Fano response in the near-infrared spectral region," *Applied Optics*, vol. 58, no. 20, pp. 5404–5414, 2019.

[30] H. Saghaei, V. Heidari, M. Ebnali-Heidari, and M. R. Yazdani, "A systematic study of linear and nonlinear properties of photonic crystal fibers," *Optik*, vol. 127, no. 24, pp. 11938–11947, 2016.

[31] M. Diouf, A. Ben Salem, R. Cherif, H. Saghaei, and A. Wague, "Super-flat coherent supercontinuum source in As_388Se_612 chalcogenide photonic crystal fiber with all-normal dispersion engineering at a very low input energy," *Applied Optics*, vol. 56, no. 2, p. 163, 2017.

[32] F. Mehdizadeh, M. Soroosh, and H. Alipour-Banaei, "An optical demultiplexer based on photonic crystal ring resonators," *Optik*, vol. 127, no. 20, pp. 8706–8709, 2016.

[33] S. Naghizade, and S. M. Sattari-Esfahlan, "High-performance ultra-compact communication triplexer on silicon-on-insulator photonic crystal structure," *Photonic Network Communications*, vol. 34, no. 3, pp. 445–450, 2017.

[34] F. Mehdizadeh, and M. Soroosh, "A new proposal for eight-channel optical demultiplexer based on photonic crystal resonant cavities," *Photonic Network Communications*, vol. 31, no. 1, pp. 65–70, 2016.

[35] S. Naghizade, and S. M. Sattari-Esfahlan, "An optical five channel demultiplexer-based simple photonic crystal ring resonator for WDM applications," *Journal of Optical Communications*, vol. 41, no. 1, pp. 37–43, 2018.

[36] M. R. Rakhshani, and M. A. Mansouri-Birjandi, "Design and simulation of four-channel wavelength demultiplexer based on photonic crystal circular ring resonators for optical communications," *Journal of Optical Communications*, vol. 35, no. 1, pp. 9–15, 2014.

[37] S. Asgari, and N. Granpayeh, "Tunable plasmonic dual wavelength multi/demultiplexer based on graphene sheets and cylindrical resonator," *Optics Communications*, vol. 393, pp. 5–10, 2017.

[38] F. Mehdizadeh, M. Soroosh, and H. Alipour-Banaei, "A novel proposal for optical decoder switch based on photonic crystal ring resonators," *Optical and Quantum Electronics*, vol. 48, no. 1, pp. 1–9, 2016.

[39] D. M. Beggs, T. P. White, L. Cairns, L. O'Faolain, and T. F. Krauss, "Demonstration of an integrated optical switch in a silicon photonic crystal directional coupler," *Physica E: Low-Dimensional Systems and Nanostructures*, vol. 41, no. 6, pp. 1111–1114, 2009.

[40] H. Saghaei, P. Elyasi, and R. Karimzadeh, "Design, fabrication, and characterization of Mach–Zehnder interferometers," *Photonics and Nanostructures - Fundamentals and Applications*, vol. 37, 100733, 2019.

[41] A. Kowsari, and H. Saghaei, "Resonantly enhanced all-optical switching in microfibre Mach–Zehnder interferometers," *Electronics Letters*, vol. 54, no. 4, pp. 229–231, 2018.

[42] B. R. Singh, and S. Rawal, "Photonic-crystal-based all-optical NOT logic gate," *Journal of the Optical Society of America A*, vol. 32, no. 12, pp. 2260-2263, 2015.

[43] A. Salmanpour, S. Mohammadnejad, and P. T. Omran, "All-optical photonic crystal NOT and OR logic gates using nonlinear Kerr effect and ring resonators," *Optical and Quantum Electronics*, vol. 47, no. 12, pp. 3689–3703, 2015.

[44] M. M. Karkhanehchi, F. Parandin, and A. Zahedi, "Design of an all optical half-adder based on 2D photonic crystals," *Photonic Network Communications*, vol. 33, no. 2, pp. 159–165, 2017.

[45] S. Naghizade, and H. Saghaei, "A novel design of all-optical 4 to 2 encoder with multiple defects in silica-based photonic crystal fiber," *Optik*, vol. 222, 165419, 2020.

[46] S. S. Zamanian-Dehkordi, M. Soroosh, and G. Akbarizadeh, "An ultra-fast all-optical RS flip-flop based on nonlinear photonic crystal structures," *Optical Review*, vol. 25, no. 4, pp. 523–531, 2018.

[47] Z. Seraj, M. Soroosh, and N. Alaei-Sheini, "Ultra-compact ultra-fast 1-bit comparator based on a two-dimensional nonlinear photonic crystal structure," *Applied Optics*, vol. 59, no. 3, pp. 811–816, 2020.

[48] S. M. H. Jalali, M. Soroosh, and G. Akbarizadeh, "Ultra-fast

1-bit comparator using nonlinear photonic crystalbased ring resonators," *Journal of Optoelectronical Nanostructures*, vol. 4, no. 3, pp. 59–72, 2019.

[49] S. Serajmohammadi, H. Alipour-Banaei, and F. Mehdizadeh, "A novel proposal for all optical 1-bit comparator using nonlinear PhCRRs," *Photonics and Nanostructures-Fundamentals and Applications*, vol. 34, pp. 19–23, 2019.

[50] F. Cheraghi, M. Soroosh, and G. Akbarizadeh, "An ultra-compact all optical full adder based on nonlinear photonic crystal resonant cavities," *Superlattices and Microstructures*, vol. 113, pp. 359–365, 2018.

[51] A. Heydari, and A. Bahrami, "All-optical half adder based on photonic crystals for BPSK signals," *Optical and Quantum Electronics*, vol. 50, no. 5, pp. 1617–1621, 2018.

[52] M. J. Maleki, A. Mir, and M. Soroosh, "Designing an ultra-fast all-optical full-adder based on nonlinear photonic crystal cavities," *Optical and Quantum Electronics*, vol. 52, no. 4, pp. 1–11, 2020.

[53] A. Rostami, and G. Rostami, "Full optical analog to digital (A/D) converter based on Kerr-like nonlinear ring resonator," *Optics Communications*, vol. 228, no. 1–3, pp. 39–48, 2003.

[54] A. Tavousi, M. A. Mansouri-Birjandi, and M. Saffari, "Successive approximation-like 4-bit full-optical analog-to-digital converter based on Kerr-like nonlinear photonic crystal ring resonators," *Physica E: Low-Dimensional Systems and Nanostructures*, vol. 83, pp. 101–106, 2016.

[55] K. Fasihi, "All-optical analog-to-digital converters based on cascaded 3-dB power splitters in 2D photonic crystals," *Optik*, vol. 125, no. 21, pp. 6520–6523, 2014.

[56] F. Mehdizadeh, M. Soroosh, H. Alipour-Banaei, and E. Farshidi, "All optical 2-bit analog to digital converter using photonic crystal-based cavities," *Optical and Quantum Electronics*, vol. 49, 38, 2017.

[57] B. Youssefi, M. K. Moravvej-Farshi, and N. Granpayeh, "Two bit all-optical analog-to-digital converter based on nonlinear Kerr effect in 2D photonic crystals," Optics Communications, vol. 285, no. 13–14, pp. 3228–3233, 2012.

[58] M. Ghadrdan, and M. A. Mansouri-Birjandi, "Concurrent implementation of all-optical half-adder and AND & XOR logic gates based on nonlinear photonic crystal," *Optical and Quantum Electronics*, vol. 45, no. 10, pp. 1027–1036, 2013.

[59] S. C. Xavier, K. Arunachalam, E. Caroline, and W. Johnson, "Design of two-dimensional photonic crystal-based all-optical binary adder," *Optical Engineering*, vol. 52, no. 2, 025201, 2013.

[60] A. Rahmani, and F. Mehdizadeh, "Application of nonlinear PhCRRs in realizing all optical half-adder," *Optical and Quantum Electronics*, vol. 50, 30, 2018.

[61] Q. Liu, and Z. B. Ouyang, C. J. Wu, C. P. Liu, and J. C. Wang, "All-optical half adder based on cross structures in two-dimensional photonic crystals," *Optics Express*, vol. 16, no. 23, pp. 18992–19000, 2008.

[62] M. R. Jalali-Azizpoor, M. Soroosh, and Y. Seifi-Kavian, "Application of self-collimated beams in realizing all-optical photonic crystal-based half-adder," *Photonic Network Communications*, vol. 36, no. 3, pp. 344–349, 2018.

[63] M. Neisy, M. Soroosh, and K. Ansari-Asl, "All optical half adder based on photonic crystal resonant cavities," *Photonic Network Communications*, vol. 35, no. 2, pp. 245–250, 2018.

[64] S. Johnson, and J. Joannopoulos, "Block-iterative frequency-domain methods for Maxwell's equations in a planewave basis," *Optics Express*, vol. 8, no. 3, pp. 173-190, 2001.

[65] S. D. Gedney, *Introduction to the finite-difference time-domain (FDTD) method for electromagnetics*. Morgan & Claypool, 2011.

[66] S. Serajmohammadi, H. Alipour-Banaei, and F. Mehdizadeh, "Proposal for realizing an all-optical half adder based on photonic crystals," *Applied optics*, vol. 57, no. 7, pp. 1617–1621, 2018.

[67] E. H. Shaik, and N. Rangaswamy, "Design of all-optical photonic crystal half adder with T-shaped waveguides using path difference-based interference," in *2017 Progress in Electromagnetics Research Symposium*, Singapore, 2017.

BIOGRAPHY

Saleh Naghizade received the M.Sc. degree in electrical engineering from the University of Tabriz, Iran, in 2021. His research interests are optical communication devices, optical fibers, and photonic integrated circuits.

Hamed Saghaei received the B.Sc., M.Sc., and Ph.D. degrees in electrical engineering in 2004, 2007, and 2015, respectively. He is currently an Assistant Professor at the Islamic Azad University of Shahrekord. His current interest fields are designing all-optical devices based on non-linear phenomena, photonic crystals and nanostructures, and graphene-based devices.

Copyrights
© 2021 Licensee Shahid Chamran University of Ahvaz, Ahvaz, Iran. This article is an open-access article distributed under the terms and conditions of the Creative Commons Attribution –Non-Commercial 4.0 International (CC BY-NC 4.0) License (http://creativecommons.org/licenses/by-nc/4.0/).

Shahid Chamran University of Ahvaz

Iranian Association of Electrical and Electronics Engineers

Journal of Applied Research in Electrical Engineering

E-ISSN: 2783-2864
P-ISSN: 2717-414X
Homepage: https://jaree.scu.ac.ir/

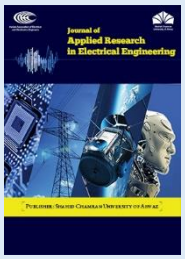

Research Article

Sizing Equations of Axial Flux Permanent Magnet (AFPM) Machine Based on an Analytical Method

Hamid Radmanesh*

Electrical Engineering Department, Shahid Sattari Aeronautical University of Science and Technology, Tehran 15916-34311, Iran

** Corresponding Author: radmanesh@ssau.ac.ir*

Abstract: This paper presents a new algorithm for sizing equations of an Axial Flux Permanent Magnet (AFPM) machine based on an analytical method. To obtain a better performance, the dimensions of the stator and rotor cores are calculated. It is shown that the magnetic flux densities throughout these cores remain closed to the flux density of the B-H curve knee point of the ferromagnetic material characteristics. A new algorithm is proposed to determine the dimensions of the different parts of the machine, and it is used to calculate the height of the permanent magnet precisely. To show the effectiveness of the suggested algorithm, a sample AFPM machine is designed based on sizing equations, and Finite Element Analysis (FEA) is employed to validate these design formulas. A complete simulation study is accomplished, and some of the results are presented to confirm the accuracy of the sizing equations.

Keywords: Axial Flux Permanent Magnet (AFPM), sizing equations, design algorithm, Finite Element Analysis (FEA).

Article history
Received 02 July 2019; Revised 22 June 2020; Accepted 1 July 2020; Published online 10 July 2020.
© 2021 Published by Shahid Chamran University of Ahvaz & Iranian Association of Electrical and Electronics Engineers (IAEEE)
How to cite this article
H. Radmanesh, "Sizing equations of axial flux permanent magnet (AFPM) machine based on an analytical method," *J. Appl. Res. Electr. Eng.*, vol. 1, no. 1, pp. 14-21, 2022. DOI: 10.22055/jaree.2020.30169.1000

Check for updates

1. INTRODUCTION

Recently, the applications of Permanent Magnet (PM) motors in industries have been increased due to their excellent performance, sufficient torque, and low noise capability. On the other hand, reducing the prices of PM materials and power electronic devices directly affects the final prices of the PM motors and increases the use of these types of motors in various applications [1]. PM motors are divided into three categories, including Axial Flux (AF), Radial Flux (RF), and Transverse Flux (TF), depending on the direction of the air gap flux motion. The AFPM motor structure is a disc-shaped motor in which the axial motion of the air gap flux causes outstanding features, such as high torque density and excellent efficiency [2]. Besides, AFPM machine structures are varied in terms of the number of rotor and stator discs and stator structures. There are different structures for the stators of this motor, e.g. slotted stator, slotless stator, and coreless stator. These various structures of AFPM motors have quite different performance characteristics. One of the most important performance differences between these types of motors is torque fluctuations. The most important disadvantage of the slotted AFPM motors is their large cogging torques. There are various methods, e.g., skewing PM [3, 4] and manufacturing slotless [3, 5] or coreless structures, that are used to reduce torque fluctuations and noise of the motor. Since PM skewing has no significant impact on the reduction of torque fluctuations, the slotless stator structure is used to significantly reduce torque fluctuations.

Based on the above explanation, AFPM motors have a large variety in terms of the number of rotors and stators, but double-sided structures are widely applicable [6-9]. Based on the position of the rotor and stator, double-sided structures are classified into two categories, i.e., axial-flux interior-rotor (AFIR) and TORUS structures [10-12]. The AFIR structure has two stators and one rotor placed between the two stators' discs. The TORUS structure has two rotors and one stator placed between the two rotor discs. Because of the simplicity of the manufacturing process and the efficient use of coils and stator core, AFPM motors with TORUS structures have widely been used.

In [13], several ways for skewing PM have been presented to minimize axial flux PM motor cogging torque. This paper has investigated the amount of cogging torque reduction related to the amount of permanent magnet skewing and its geometry. According to the results, the use of skewed PM instead of conventional PM reduces the amount of torque cogging dramatically.

Axial flux PM motors with surface-mounted magnets and without stator core have more efficiency and less axial length than motors with a stator core. The motor presented in [14] has an internal magnet, spoke rotor, and variable air gap that cause sinusoidal waveform of the back EMF. The simulation results reveal that by increasing air gap flux density, the presented motor has higher power density and torque density than conventional motors with surface-mounted magnets.

In [15], an improved magnetic equivalent circuit of a synchronous generator has been used to design a coreless axial flux PM generator with two rotors and one stator and with a direct connection for wind turbines. The rotor saturation is also considered in the introduced equivalent circuit. The multi-objective optimization algorithm PSO has been used to optimize the generator. The design objectives are minimizing the cost of materials used in the generator and maximizing the efficiency of annual energy.

In [16], two methods of PM shift and asymmetric magnet have been used to reduce the amount of motor cogging torque. The results show that the simultaneous use of two methods of magnet skewing and magnet shifting has a significant impact on reducing the amount of cogging torque. These two methods are applicable without adding any complexity to the manufacturing process and changing the structure of the motor. Also, the results show that it is possible to design an axial flux PM motor with small cogging torque and almost sinusoidal back EMF with integer coefficients q.

In [17], an axial flux PM motor with a trapezoidal stator core has been introduced and optimally designed. The optimization objective is maximizing efficiency and minimizing motor volume. Also, the motor with a power of 250-1000 W has been designed and compared. The results show that at the same power and efficiency levels, the motor with a trapezoidal core and a winding angle larger than the PM angle has a smaller volume.

In [18], the equivalent circuit of axial flux PM machine has been introduced. In this equivalent circuit, the magnetic saturation, the leakage flux, the armature reaction, and the rotation of the rotor have been considered. The air gap flux density, the back EMF waveform, and the rotor average torque can be calculated by this equivalent circuit. The magnetic equivalent circuit has a small computational size, which facilitates the use of optimized algorithms.

In [19], an analytical method has been presented to determine the sinusoidal magnet shape in an axial flux PM machine with a speed of 1,000,000 RPM for use in the flywheel. The back EMF waveforms have been investigated for both distributed and centralized windings. The results show that the use of a sinusoidal magnet causes sinusoidal back EMF and thus a reduction of the output torque fluctuations. Also, the concentrated winding back EMF has a bigger main component and THD than distributed winding.

This paper uses a particle swarm optimization (PMO)-based method to optimally design a TORUS axial flux motor. In this design, process design variables of the electric motor (the number of pole pairs, input voltage, air gap flux density, air gap length, the ratio of internal to external diameter of the motor, ratio of pole arc to pole pitch, and electrical loading) are employed to reduce the consumed magnet volume and Total Harmonic Distortion (THD) of back Electro Magnetic Field (EMF). The results of the presented sizing equations and PSO algorithm are validated by using FEM simulation results.

PM motors are always proposed as a substitute for conventional induction motors, but their higher prices compared to induction motors are the main reason that makes this type of motor be used to a lesser extent. Since the price difference between these two types of motors is often due to the use of PM, this paper considers the minimization of the PM amount a design optimization objective function.

This paper is organized as follows. Section 2 presents the sizing equations of a slotless AFPM machine. Section 3 discusses the proposed design algorithm. Then, FEM software is applied in Section 4 to investigate the operational behavior of the suggested model, and the related simulation results are analyzed. Finally, comparative cost analysis and conclusion are given.

2. SIZING EQUATIONS OF A SLOTLESS AFPM MACHINE

The flux path in non-slotted AFPM machines is shown in Fig. 1. By studying the flux path, the sizing equations of this machine can be derived.

By neglecting leakage inductance and winding resistance, the output power of the machine is obtained as follows [7, 8]:

$$P_{out} = \eta \frac{m}{T} \int_{.}^{T} e(t) i(t) dt = m K_p \eta E_{pk} I_{pk} \quad (1)$$

where η, m, $e(t)$, $i(t)$, K_p, E_{pk}, and I_{pk} are efficiency, number of phases, the instantaneous value of the induction voltage, the instantaneous value of the phase current, electrical power waveform factor, the maximum value of the back EMF and the maximum value of the phase current, respectively. K_p can be calculated from the following equation:

$$K_p = \frac{1}{T} \int_{.}^{T} \frac{e_{(t)} i_{(t)}}{E_{pk} I_{pk}} dt \quad (2)$$

If a conductor is placed inside a time-varying magnetic field, the voltage will be induced in the conductor. The induced voltage in the conductor is calculated by

$$E_p = V \times l B_{gp} K_w \quad (3)$$

where V is the speed of conductor motion or the rate of the flux density variation, l is the length of the conductor, B_{gp} is the maximum flux density, and K_w is the winding coefficient. By using Eq. (3), the voltage induced in the TORUS axial flux permanent magnet motor can be obtained. In this type of

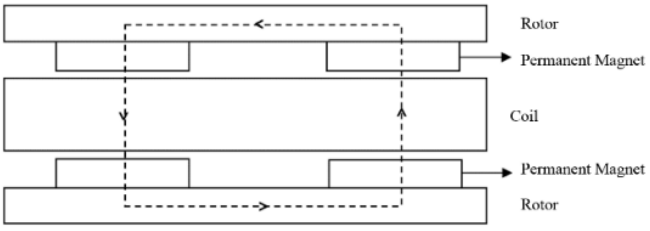

Fig. 1: Flux path in AFPM coreless

machine, the values of l and V can be calculated as follows:

$$V = \frac{D_o(1+\lambda)\pi}{4p} f \tag{4}$$

$$l = 4N_{ph} \frac{D_o(1-\lambda)}{2} \tag{5}$$

By substituting Eq. (4) and (5) in (3), we have:

$$E_p = K_e N_{ph} B_{gp} \frac{f}{p}(1-\lambda^2) D_o^2 \tag{6}$$

where K_e is the EMF coefficient, p is the number of pole pairs, D_o is the outer diameter of the stator, B_{gp} is the maximum flux density in the air gap, and λ is the ratio of inner diameter to the outer diameter of the machine. The rms value of the phase current of the stator winding is obtained by using the following equation:

$$I_{rms} = \frac{A\pi D_{ave}}{2mN_{ph}} \tag{7}$$

where A and D_{ave} are electrical loading and average diameter of the stator, respectively. D_{ave} can be calculated by

$$D_{ave} = D_o \frac{1+\lambda}{2} \tag{8}$$

By substituting Eq. (8) in Eq. (7), the peak value of the current is obtained as follows:

$$I_{pk} = \frac{A\pi}{2mN_{ph}} D_o \frac{1+\lambda}{2} K_i \tag{9}$$

where K_i is the current waveform factor, which is calculated by using the following equation:

$$K_i = \frac{I_{pk}}{I_{rms}} = \frac{1}{\sqrt{\frac{1}{T}\int_0^T (\frac{i_{(t)}}{I_{pk}})^2 dt)}} \tag{10}$$

By substituting Eq. (6) and (9) in (1) and simplifying the final equation, the outer diameter of the stator is obtained as follows:

$$D_o = \sqrt{(\frac{P_{out}}{\frac{\pi}{2}\eta m K_e K_i K_p B_{gp} A \frac{f}{p}(1-\lambda^2)\frac{1+\lambda}{2}\cos(\varphi)})} \tag{11}$$

The saturation phenomenon increases the core losses of the machine. Therefore, the axial length of the stator and rotor cores should be calculated so that the fever local saturation occurs in the cores. On the other hand, to reduce machine weight and cost, the core should be as small as possible. Therefore, the axial length of the core must be determined so that the flux density of the core becomes close to the flux density of the B-H curve knee point of the core ferromagnetic material.

By formulating the flux passing through the air gap and flux inside the core and simplifying it, the axial length of the stator core is obtained as follows:

$$L_{cs} = \frac{B_{gp} K_a \pi D_o (1+\lambda)}{4pB_{cs}} \tag{12}$$

where L_{cs} is the axial length of the stator core, B_{cs} is the maximum flux density in the stator core, and K_a is the ratio of the average flux density to the maximum flux density in the air gap.

In addition, by formulating the flux passing through the rotor core and the magnet flux, the axial length of the rotor core is calculated as follows:

$$L_{cr} = \frac{B_u \pi D_o (1+\lambda)}{8pB_{cr}} \tag{13}$$

where L_{cr} is the axial length of the rotor core and B_u is the ratio of air gap flux density to the leakage factor. The thickness of the stator winding increases the effective air gap length and consequently increases the axial length of the machine. In slotless AFPM machines, the inner diameter of the machine limits the number of wires placed next to each other and in some cases, the wires are wrapped on one another due to space constraint. For this reason, the thickness of the winding layer is dependent on the inner diameter of the machine. The thickness of the winding layer in slotless AFPM machines can be calculated by using the following equation:

$$W_{cu} = \frac{D_o\lambda - \sqrt{(D_o\lambda) - \frac{12}{\pi K_{cu}} N_{ph} A_{cu}}}{2} \tag{14}$$

where A_{cu} is the cross-section of the wire, N_{ph} is the number of turns per phase, and K_{cu} is the coil fill factor.

To produce flux in the air gap, a PM is used because its thickness is dependent on the desired flux density in the air gap, the air gap length, and the thickness of stator winding. Various methods are used to calculate the length of the magnet, but in most research projects, Eq. (15) is used to calculate the thickness of the magnet. In this equation, the important influence of the magnet width on the thickness of the magnet is neglected, which reduces design accuracy [2].

$$L_{pm} = \frac{\mu_r B_g}{B_r - \frac{B_{gp}}{K_d}} K_c (g + W_{cu}) \tag{15}$$

where W_{cu}, g, and L_{pm} are the thickness of the stator winding, the air gap length, and the thickness of the magnets, respectively.

The following equation can be used recursively to exactly calculate the magnet thickness [10,11]:

$$B_{pm} = -\sum_{n=1,3,5,\ldots}^{\infty} \frac{B_1}{B_2} \cos(\frac{n\pi x}{t_p}) \tag{16}$$

where

$$B_1 = \frac{8B_r}{n\pi}\sin(\frac{\alpha n\pi}{2})e^{-\frac{n\pi(g+w_{cu})}{t_p}} \quad (17)$$

$$B_2 = (e^{-\frac{2n\pi(g+w_{cu})}{t_p}}+1) + \frac{\mu_r(-e^{-\frac{2n\pi(g+w_{cu})}{t_p}}+1)}{e^{\frac{2n\pi L_{pm}}{t_p}}-1} \times(e^{\frac{2n\pi L_{pm}}{t_p}}+1) \quad (18)$$

where t_p, B_r, and α are pole pitch, the residual flux density of the magnet, and the ratio of the pole arc to the pole pitch, respectively. Also, the power density of the machine, i.e., the ratio of the output power to the machine volume can be calculated using the following equation:

$$P_{den} = \frac{P_{out}}{\frac{\pi}{4}D_o^2 L_{tot}} \quad (19)$$

where L_{tot} is the axial length of the machine obtained by

$$L_{tot} = L_{cs} + 2L_{cr} + 2W_{cu} + 2g + 2L_{pm} \quad (20)$$

By using the extracted sizing equations and the PSO algorithm, the desired electric motor can be designed.

3. Proposed Design Algorithm

By using the above equations, a design algorithm is proposed for slotless AFPM machines. The flowchart of the proposed algorithm is shown in Fig. 2. According to this flowchart, the overall machine design limitations, such as axial length, outer diameter, and efficiency of the machine, are first determined. In the machine design, some design parameters are optionally determined and the values of the other parameters (unknown problems) are calculated from these optional parameters. In the second step, the values of these optional parameters are determined independently of the other parameters.

Then, the dimensions and computational parameters are obtained based on the equations presented in Section 2. The most important point in the proposed design flowchart is the calculation of the air gap flux density by using Eq. (16).

The flux density, which is obtained from this equation, is compared with the reference value. In the case of inequality of these two values, the thickness of the PM is increased or decreased until these two values become equal. In this case, the exact thickness of the magnet is obtained to generate the desired flux density in the air gap. The objective function of the optimization algorithm is then calculated. This design process is repeated until the objective function is met, and the design algorithm converges. The results of the design algorithm are presented in the following sections.

4. Simulation Results

To validate the equations presented in the previous section, these equations are used to design a sample slotless AFPM machine. The list of the materials used in different parts of the machine is listed in Table 1. Due to the lack of slots in the stator core, it is possible to distribute the arm of each coil in the stator periphery. This has a direct effect on the THD amount of the induced voltage in the windings. To illustrate this issue, motors with different stator winding distribution are designed. By using the equations presented in this paper, the dimensions of these machines are determined. Table 2 presents the basic dimensions and the parameters of the designed machines. According to the parameters in this table, the designed motor with 60° electrical distributed coil has better performance characteristics compared to the other three motors.

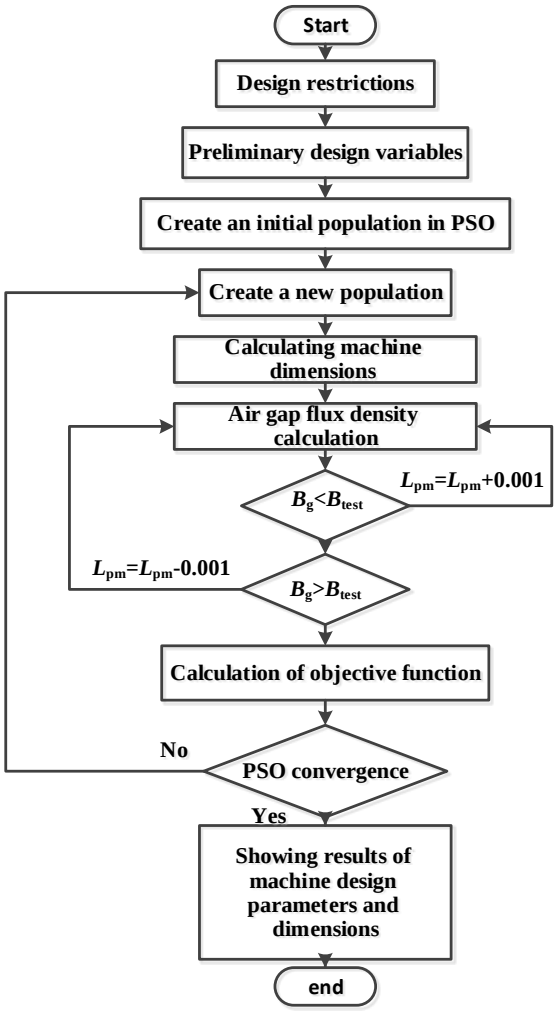

Fig. 2: The flowchart of the machine design process

Table 1: The materials used in different parts of the machine

Permanent magnet	N45
Stator core type	50A470
Rotor core type	50JN400
Coil type	Copper

Table 2: The basic dimensions and parameters of the designed machines with different stator winding distributions

Coil distribution (Electrical degrees)	PM_{den} (cm^3)	D_o (mm)	V_L (V)	THD Back EMF	A
60	21.048	161.692	107.314	6.4031	25571
54	23.345	155.371	161.784	6.5018	28897
42	27.145	175.843	115.271	8.5723	19963
30	35.846	179.091	146.289	9.8065	19047
L_{pm} (mm)	L_{cs} (mm)	L_{cr} (mm)	B_g (T)	α	λ
2.872	10.078	5.8875	0.35	0.699	0.7
3.463	12.101	7.0662	0.35	0.697	0.7
3.137	10.957	6.3974	0.35	0.698	0.7
3.988	13.913	8.1064	0.349	0.699	0.7

Further analyses are done on this type of motor. The optimization objective function of the electrical machine is one of the most important parts of the design process. So, by changing the optimization objective function, the dimensions and performance characteristics of the machine can be changed significantly. The optimization objective function is determined based on the application type of the machine, consumer demands, and mechanical and magnetic constraints. Considering the AFPM motors with better performance characteristics in comparison with the conventional induction motors, it is possible to introduce this type of PM machines as a substitute alternative for conventional induction motors.

But, due to the use of PM in AFPM motors and the high price of this type of material, AFPM motors are more expensive compared to conventional induction motors. Therefore, this paper considers minimizing the volume of used permanent magnet as an optimization objective function. In this case, the price difference between AFPM motor and conventional induction motor can be reduced as much as possible. Therefore, the usage of AFPM motors instead of conventional induction motors is economically justified.

By using the PSO algorithm, the dimensions and basic parameters of the slotless axial flux permanent magnet machine with 60° electrical distributed winding are calculated to achieve an almost sinusoidal back EMF. In addition, this algorithm is used to minimize the needed magnet. This optimum design process is done by using MATLAB software. The characteristics of the motor for minimization of magnet weight are given in Table 3.

Now, by using parameters values given in Table 3 and finite element analysis, the designed motor is evaluated.

The machine is constructed by putting identical pole pairs around the axis of the machine. Only one pole pair is considered in the processes of design. Based on this structure, the machine performance is evaluated to reduce the analysis time of the machine. Flux density distributions in the stator and rotor cores for open-circuit conditions are shown in Fig. 3 and Fig. 4, respectively.

Table 3: The basic dimensions and parameters of the designed machine

Parameter	Value	Unit
λ	0.7	-
α	0.6992	-
$B_g(T)$	0.3501	Tesla
$g(mm)$	1	mm
P	5	-
$V_L(V)$	60.44	Volt
$L_{pm}(mm)$	2.8583	mm
A	25598	A/m
D_o	161.53	mm
L_{cs}	10.068	mm
L_{cr}	5.2959	mm
P_{den}	1.3551	W/Cm^2

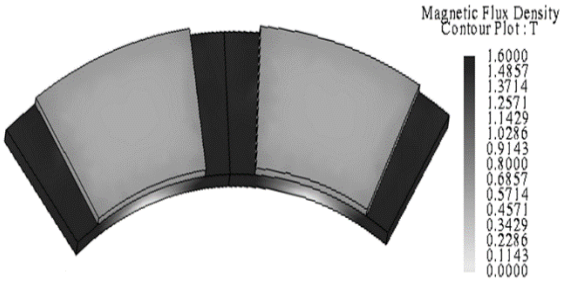

Fig. 3: The flux density distribution of the rotor core

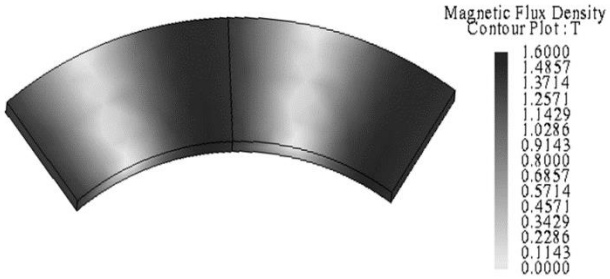

Fig. 4: The flux density distribution of the stator core

The maximum flux densities in the stator and rotor cores are equal to 1.5021 Tesla and 1.4910 Tesla, respectively, which are equal to the values considered at the beginning of the design process. As shown in these figures, no local saturation occurs in the stator and rotor cores.

The air gap flux density of the motor in no-load conditions is shown in Fig. 5. According to the equations presented in the previous section, the magnet thickness and coefficient α have significant impacts on the amplitude and shape of the air gap flux density. In this paper, the magnet thickness is designed to achieve the maximum air gap flux density of 0.5 Tesla and the average air gap flux density of 0.35 Tesla. Furthermore, the FEA results show the maximum air gap flux density of 0.494 Tesla and the average air gap flux density of 0.3409 Tesla, so the equation presented for calculating magnet thickness has high accuracy and the results show that the presented method is effective.

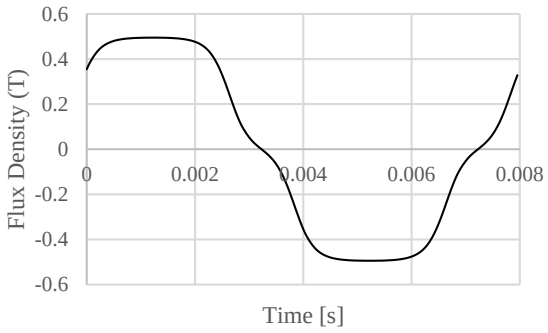

Fig. 5: Air gap flux density

Waveform and the value of the back EMF have a significant influence on almost all performance characteristics of the machine, including power capability, power factor, and torque ripples. The back EMF waveform of the designed machine is shown in Fig. 6. Also, the values of the harmonic component of the back EMF waveforms are presented in Fig. 7. It is clear that the back EMF waveform is almost a pure sinusoidal waveform that results in the reduction of the motor torque fluctuations. Fig. 8 shows the rated torque of the motor. As shown in this figure, the motor torque is almost constant.

The THD reduction of the back EMF waveform reduces the THD of the input current and motor torque fluctuations. For this reason, another optimization objective function is used to reduce the back EMF waveform THD. This is possible by making the air gap flux density sinusoidal and avoiding the saturation of the rotor and stator cores. As shown in Fig. 7, the THD of the back EMF waveform is about 6.4031 percent, reflecting that it is almost sinusoidal and one of the design objectives is accomplished.

According to the results presented in this section, the values obtained from the introduced equations are largely close to FEA results, showing high accuracy of these equations. To better investigate these equations, a comparison has been made in Table 4 between these equation results and FEA results, which confirms the accuracy of the presented scheme.

5. CONCLUSION

This paper presented a new optimization algorithm for the calculation of the basic dimensions of a slotless AFPM machine. The presented equations can be applied to design a machine in such a way that the magnetic flux density throughout the stator and rotor cores remains just below the saturated values. This value is specified by the ferromagnetic material characteristics, which results in using active materials most effectively. To verify the design procedure of the present paper, a sample machine is designed. FEA is carried out for performance evaluations of the machine. The simulation results present the uniform distribution of the flux density inside the cores, which leads to the design of a machine with a lower total iron loss. It is shown that the amplitude of the back EMF is in accordance with the value considered at the beginning of the design algorithm. Also, it is obvious that the back EMF is almost sinusoidal. Some other results have been presented, according to all of which the validity of the proposed design algorithm is confirmed.

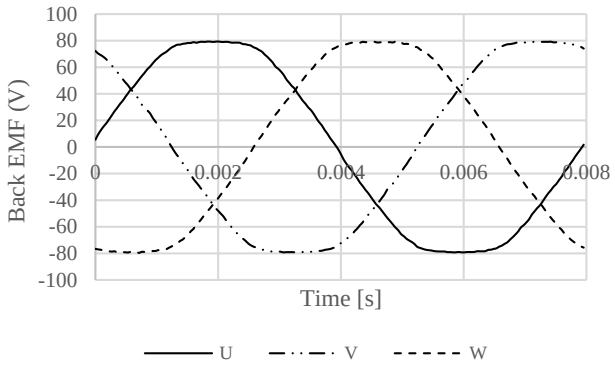

Fig. 6: The induction voltage of the motor

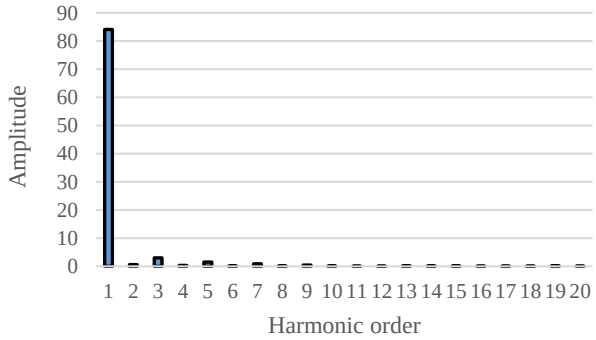

Fig. 7: The harmonics of the induction voltage

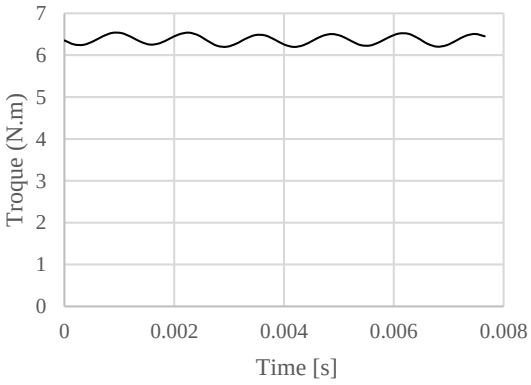

Fig. 8: The rated torque of the motor

Table 4: A comparison of the results obtained from sizing equations and finite element method.

Parameter	FEM	Sizing Equations	Unit
B_g	0.3409	0.35	Tesla
B_{gp}	0.494	0.50	Tesla
B_{cs}	0.9585	0.9549	Tesla
B_{csp}	1.5021	1.5	Tesla
B_{cr}	0.9515	0.9549	Tesla
B_{crp}	1.4910	1.5	Tesla
B_u	0.6044	0.5857	Tesla
I_{ph}	6.016	5.965	A
E_{ph}	119.78	123.18	Volt
K_i	1.3360	1.3485	

DECLARATION OF COMPETING INTEREST

The author declares that he has no known competing financial interests or personal relationships that could have appeared to influence the work reported in this paper. The ethical issues, including plagiarism, informed consent, misconduct, data fabrication and/or falsification, double publication and/or submission, redundancy, have been completely observed by the author.

REFERENCES

[1] A. Mahmoudi, S. Kahourzade, N. Abd Rahim, and W. P. Hew, "Design, analysis, and prototyping of an axial-flux permanent magnet motor based on genetic algorithm and finite-element analysis," *IEEE Transactions on Magnetics*, vol. 49, no. 4, pp. 1479-1492, 2012.

[2] A. Mahmoudi, S. Kahourzade, N. A. Rahim, and H. W. Ping, "Improvement to performance of solid-rotor-ringed line-start axial-flux permanent-magnet motor," *Progress In Electromagnetics Research*, vol. 124, pp. 383-404, 2012.

[3] M. Aydin, and M. Gulec, "Reduction of cogging torque in double-rotor axial-flux permanent-magnet disk motors: A review of cost-effective magnet-skewing techniques with experimental verification," *IEEE Transactions on Industrial Electronics*, vol. 61, no. 9, pp. 5025-5034, 2013.

[4] M. Aydin, and M. Gulec, "A new coreless axial flux interior permanent magnet synchronous motor with sinusoidal rotor segments," *IEEE Transactions on Magnetics*, vol. 52, no. 7, pp. 1-4, 2016.

[5] Daghigh, H. Javadi, and H. Torkaman, "Design optimization of direct-coupled ironless axial flux permanent magnet synchronous wind generator with low cost and high annual energy yield," *IEEE Transactions on Magnetics*, vol. 52, no. 9, pp. 1-11, 2016.

[6] W. Tong, S. Wang, S. Dai, S. Wu, and R. Tang, "A quasi-three-dimensional magnetic equivalent circuit model of a double-sided axial flux permanent magnet machine considering local saturation," *IEEE Transactions on Energy Conversion*, vol. 33, no. 4, pp. 2163-2173, 2018.

[7] G. Yang, M. Lin, N. Li, and L. Hao, "Magnetization state regulation characteristic study of series hybrid permanent magnet axial field flux-switching memory machine," *IEEE Transactions on Applied Superconductivity*, vol. 29, no. 2, pp. 1-6, 2019.

[8] E. Yıldırız, M. Güleç, and M. Aydın, "An innovative dual-rotor axial-gap flux-switching permanent-magnet machine topology with hybrid excitation," *IEEE Transactions on Magnetics*, vol. 54, no. 11, pp. 1-5, 2018.

[9] M. F. Khatab, Z. Zhu, H. Li, and Y. Liu, "Comparative study of novel axial flux magnetically geared and conventional axial flux permanent magnet machines," *CES Transactions on Electrical Machines and Systems*, vol. 2, no. 4, pp. 392-398, 2018.

[10] W. Zhang, X. Liang, and F. Yu, "Fault-tolerant control of hybrid excitation axial field flux-switching permanent magnet machines," *IEEE Transactions on Magnetics*, vol. 54, no. 11, pp. 1-5, 2018.

[11] M. C. Gardner, M. Johnson, and H. A. Toliyat, "Comparison of surface permanent magnet axial and radial flux coaxial magnetic gears," *IEEE Transactions on Energy Conversion*, vol. 33, no. 4, pp. 2250-2259, 2018.

[12] G. Messina, E. T. De Bella, and L. Morici, "HTS axial flux permanent magnets electrical machine prototype: Design and test results," *IEEE Transactions on Applied Superconductivity*, vol. 29, no. 5, pp. 1-5, 2019.

[13] M. Gulec, and M. Aydin, "Magnet asymmetry in reduction of cogging torque for integer slot axial flux permanent magnet motors," *IET Electric Power Applications*, vol. 8, no. 5, pp. 189-198, 2014.

[14] P. Hekmati, R. Yazdanpanah, and M. Mirsalim, "Design and analysis of double-sided slotless axial-flux permanent magnet machines with conventional and new stator core," *IET Electric Power Applications*, vol. 9, no. 3, pp. 193-202, 2015.

[15] Y. Liang, L. Wu, X. Bian, and H. Yu, "The influence of transposition angle on 3-D global domain magnetic field of stator bar in water-cooled turbo-generator," *IEEE Transactions on Magnetics*, vol. 51, no. 11, pp. 1-4, 2015.

[16] S. Kumar, W. Zhao, Z. S. Du, T. A. Lipo, and B.-I. Kwon, "Design of ultrahigh speed axial-flux permanent magnet machine with sinusoidal back EMF for energy storage application," *IEEE Transactions on Magnetics*, vol. 51, no. 11, pp. 1-4, 2015.

[17] S. Huang, J. Luo, F. Leonardi, and T. A. Lipo, "A general approach to sizing and power density equations for comparison of electrical machines," *IEEE Transactions on Industry Applications*, vol. 34, no. 1, pp. 92-97, 1998.

[18] M. Aydin, S. Huang, and T. A. Lipo, "Design and 3D electromagnetic field analysis of non-slotted and slotted TORUS type axial flux surface mounted permanent magnet disc machines," in *2001 IEEE International Electric Machines and Drives Conference*, Cambridge, MA, USA, 2001, pp. 645-651.

[19] D. Wang, C. Peng, D. Xue, D. Zhang, and X. Wang, "Performance assessment and comparative study of a permanent magnet machine with axial flux regulator," *IEEE Transactions on Energy Conversion*, vol. 34, no. 3, pp. 1522-1531, 2019.

BIOGRAPHY

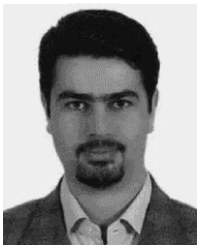

Hamid Radmanesh (Member, IEEE) was born in 1981. He received the B.Sc. degree in electrical engineering from the Malek-Ashtar University of Technology, Tehran, Iran in 2006, the M.Sc. degree in electrical engineering from Shahed University, Tehran, Iran in 2009, and the Ph.D. degree in electrical engineering

from the Amirkabir University of Technology, Tehran, Iran in 2015. He has authored more than 100 published technical papers. His research interests include transient in power systems and renewable energy.

Copyrights © 2021 Licensee Shahid Chamran University of Ahvaz, Ahvaz, Iran. This article is an open-access article distributed under the terms and conditions of the Creative Commons Attribution –Non-Commercial 4.0 International (CC BY-NC 4.0) License (http://creativecommons.org/licenses/by-nc/4.0/).

Shahid Chamran University of Ahvaz

Iranian Association of Electrical and Electronics Engineers

Journal of Applied Research in Electrical Engineering

E-ISSN: 2783-2864
P-ISSN: 2717-414X
Homepage: https://jaree.scu.ac.ir/

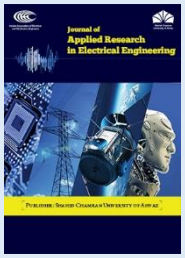

Research Article

Broken Conductor Fault Location in Power Transmission Lines Using GMDH Function and Single-Terminal Data Independent of Line Parameters

Mahyar Abasi [1,*], Nima Heydarzadeh [2], and Arash Rohani [3]

[1] *Department of Electrical Engineering, Faculty of Engineering, Shahid Chamran University of Ahvaz, Ahvaz 61357-85311, Iran*

[2] *Department of Electrical Engineering, Central Tehran Branch, Islamic Azad University, Tehran 13117-773591, Iran*

[3] *Khuzestan Regional Electric Company (KZREC), Ahvaz 61365-1373, Iran*

* *Corresponding Author: mahyarabasi1368@yahoo.com*

Abstract: The phenomenon of broken conductor faults (BCFs) in power transmission lines and, consequently, the suspension of the hot-line with no connection to ground, tower, or other conductive/non-conductive bodies is amongst special faults in terms of fault detection and location in the protection industry. Once such a failure occurs, the current of the faulty phase does not increase, which leads to the inability of standard fault detection functions in detecting the event. On the other hand, the variable nature of transmission line parameters due to weather conditions leads to misoperation and malfunction of fault detection and protection schemes of industrial relays in some cases. This paper, for the first time, presents a BCF location scheme without requiring line parameters data and only using magnitudes of current and voltage phasors of a single terminal based on Group Method of Data Handling (GMDH). In this method, a function is interpolated, the inputs of which are the current and voltage of the faulty phase, and its output are the accurate location of the fault. The function can be developed for all topologies of transmission lines. The proposed method is implemented in the MATLAB software and the obtained results verify the solidity and perfect performance of the method for different fault conditions.

Keywords: Broken conductor fault location, series conductor, GMDH, current and voltage phasors, single-terminal method, transmission line parameters.

Article history
Received 18 October 2020; Revised 19 February 2021; Accepted 16 March 2021; Published online 31 March 2021.
© 2021 Published by Shahid Chamran University of Ahvaz & Iranian Association of Electrical and Electronics Engineers (IAEEE)
How to cite this article
M. Abasi, N. Heydarzadeh, and A. Rohani, "Broken conductor fault location in power transmission lines using GMDH function and single-terminal data independent of line parameters," *J. Appl. Res. Electr. Eng.*, vol. 1, no. 1, pp. 22-32, 2022.
DOI: 10.22055/jaree.2021.35473.1012

Check for updates

1. INTRODUCTION

1.1. Motivation

In general, normal shunt and series faults always threaten the power system. Normal shunt faults include phase-to-ground and phase-to-phase faults which occur due to factors such as lightning, flashes or arcs, bird collision, the connection of a conductive object between phases, or between a phase and the tower, to name but a few [1]. Series faults include the interruption of one or more phases in which the phase or phases have no connection to ground or other conducting objects. Such faults typically happen due to broken conductors, misoperation of single-phase switchgear, or single-phase fuses [2]. In electrical transmission lines, the phase current is not increased when the phenomenon of broken phase occurs between the conductors connected to the towers, which results in the misoperation of standard protection algorithms embedded in the relays. Thus, manufacturers of protection relays attempt to find suitable protection functions and algorithms to detect, classify, and locate BCFs in transmission lines.

Another issue that always causes errors in protection algorithms is the implementation of line parameters in algorithms. Because electrical transmission lines are always exposed to changing weather conditions, their parameters change over a long time when compared to the initial values provided in their catalogs, hence leading to malfunctions [3]. Therefore, designing a protection algorithm requiring none of the transmission line parameters is a very useful advantage for protection schemes. According to the issues raised above, this study aims to design an algorithm for BCF location in

transmission lines using current and voltage values of a single terminal without requiring line parameters.

1.2. Literature Review

In general, series fault location methods in transmission lines are divided into four basic categories including the impedance or phasor theory-based methods, the traveling waves-based methods, the digital signals analysis and processing-based methods, the methods based on teaching and learning, and those which focus on pattern designs such as artificial neural networks (ANNs), fuzzy logic (FL), and optimization [4].

Ref. [5] presents three methods for locating BCFs. These three methods include fault location based on capacitive charging current ratio, according to the line hyperbolic equation analysis, in which the third method is based on the analysis of positive-sequence components of the faulty network. Capacitive charging current ratio is the simplest approach to calculate the distance between the relay terminal and the broken conductor. The first method can be employed only for lines with significant capacitive charging current; otherwise, the relay cannot locate the fault. In the distance calculation method using full line equations, it is assumed that the lines are completely transposed and zero-sequence parameters are employed, which may not be accurate due to changes in weather conditions and the return paths of zero-sequence to ground. This method is computationally inefficient and the calculation of distance is erroneous due to the non-transposable nature of the lines and its dependence on zero-sequence parameters. Calculating the fault location using positive-sequence components utilizes only positive-sequence parameters, which are probably more accurate than zero-sequence parameters. This method is more computationally efficient as it does not use iterative methods to solve the equations. However, this method assumes that transmission lines are completely transposed and can therefore have computational errors due to the nature of the non-transposed lines.

In [6], BCF detection and location are presented using communication-based techniques. The authors in this paper have used an open conductor detection (OCD) system, where BCF sensors are used in towers and inter-conductor bases. OCD sends this data to the control center through some communication devices using GSM technology. The main purpose of this system is to transmit and interpret the abnormal conditions of the network concerning BCF conditions, and transfer the information of this power outage to the control center. The network operator searches for the last active OCD and the first inactive OCD, locates the fault, and then takes actions to prevent accidents and minimize the failure.

Two different methods based on other communication-based techniques, namely the F-PLCCG and the Hybrid AD Method, are also presented in [7]. The F-PLCCG method is designed to detect broken conductors between two substations, which requires very expensive hardware and highly advanced communication systems that are not cost-effective. Nonetheless, the Hybrid AD method is less expensive and provides the exact location. In this method, the power line guardian (PLG) plays a key role and can locate the BCF that does not touch the ground using the second-harmonic traveling waves. PLG uses a current transformer and measures the high-frequency range (traveling wave frequency). However, it should be noted that the implementation of communication-based techniques leads to additional hardware and software complexity and is not economical.

The two main BCF detection and location methods based on digital signal processing and analysis (harmonic components) are described in [8-11]. In the first method, the status of the BCF is provided based on monitoring harmonic components 1, 3, 5, and other harmonics in the neutral current of the transformer and using dominant component changes. Nevertheless, the technical justification behind this approach is not available. Determining the threshold value in this method is difficult because the measured harmonics can be affected by other factors such as resonance. As a result, applying this approach to different cases can be challenging [8-9]. The second method utilizes a voltage source in the neutral of the transformer and measures its corresponding excitation current. If the current is low, the BCF condition is detected [10].

The BCF detection scheme based on the third harmonic is described in [11]. This design is used for lines connected to a no-load transformer with a grounded star, and its principles are based on reducing (near zero) zero-sequence voltage and current on the primary side of the ground transformer. To detect BCFs in this method, it is necessary to determine the threshold values and measure the zero-sequence impedance of the transformer's downstream network. To obtain threshold values in this paper, day-ahead measurements of zero-sequence current and voltage values were used. This method may also be affected by noise and abnormal harmonics (inter-harmonics) and may fail to correctly detect the BCF event.

In [12], the ANN is employed as a BCF detector. The only problem with this design is its complexity in terms of hardware implementation. Moreover, only the BCF detection problem was taken into account with no idea on how to solve the BCF location problem.

Additionally, ABB-REL 521 and SIPROTEC 4 (7SA612) as industrial relays employ BCF detection methods based on the calculation of the asymmetry between phase currents. These methods are realized by measuring the ratio between maximum and minimum phase currents, i.e., they compare the minimum and maximum current values, and the relay issues a trip command if the minimum current is less than 80% of the maximum current for a certain time interval. After about five seconds, a "Broken Conductor" alarm or a three-phase interruption signal is issued by the relay [13-14]. Moreover, the BCF algorithm in the Areva MICOM P443 [15] relay is based on the negative-sequence phase current level or the ratio between negative- and positive-sequence currents. However, if the above-mentioned methods are used in a low-load line, the negative-sequence current caused by a series fault may be very close to or less than the full-load steady-state imbalance value which is caused by current transformer faults, load imbalance, etc. As a result, the negative-sequence module of the relay cannot work well in low-load conditions [16].

1.3. The Challenge

According to the literature review in the previous section, the BCF location problem without requiring the data of transmission line parameters has so far remained unsolved. The problems caused by this phenomenon threaten the stability of the power system because of the shortcomings of the proposed methods in this field. Many reports are submitted every year from the protection units of electrical energy companies complaining about the failures. On the other hand, a suspended line without connection to any point endangers lives due to direct contact of humans or their vehicles with the phases suspended in the air and creates irreparable damages. Therefore, designing a suitable fault location algorithm without the need for transmission line parameters in this field is necessary. The independent performance of such an algorithm is considered as a very desirable advantage for a BCF location scheme.

1.4. Contributions

The main contribution of this paper is proposing a BCF location algorithm in electric power transmission lines based on the GMDH function fitting method using current and voltage measurement data of a terminal requiring no information regarding transmission line parameters. The scheme hypothesis presented in this paper is that the interrupted phase is identified by a BCF detection algorithm. Then the current and voltage data of the interrupted phase, which were calculated during the conductor breakage period using the full-cycle Fourier algorithm with a sampling frequency of 2.4 kHz, are used as inputs for the BCF location function calculated by the GMDH function fitting method to estimate the fault location. The GMDH function fitting method is performed by teaching and learning the GMDH network, and finally, a function was extracted as the BCF location estimation function based on the current and voltage phasors of the interrupted phase. The successful output results of the algorithm test given in the simulation results section confirm the correct performance of the algorithm proposed in this paper.

1.5. Organization of the Study

The paper is organized into eight sections. Section 1 presents the introduction to the topic. In Section 2, the GMDH structure analysis theory is fully described. Section 3 explains the theory of the proposed method in detail. Section 4 provides test results of software simulation. In Section 5 of the paper, the types of sensitivity analyses affecting the algorithm results are given. In Section 6, the discussion and comparison between the results of the proposed algorithm and its counterparts are presented. Section 7 presents research suggestions for future work, and finally, in Section 8, the conclusion is presented.

2. STRUCTURE OF GMDH

The GMDH function fitting method was first introduced in 1968 by Ivakhnenko [17]. The bases of this structure are the repetition of a series of simple mathematical operations to find the relationship between inputs and outputs and the establishment of layers in which low-impact parameters are removed and more effective parameters are transferred to the next layers. In general, it can be said that the process of output estimation is such that by combining small and simple components, it will be able to describe and analyze large and complex systems. In the GMDH structure, an attempt is made to determine the relationship between correlated inputs x and outputs y. This relationship can be expressed clearly using (1) [18-19]:

$$Y(x_1,\ldots,x_n)=a_0+\sum_{i=1}^{m}a_i f_i \tag{1}$$

where, a_0 is the bias coefficient, a_i is the i-th weighting coefficients, and f_i is the i-th base function. In (1), the function $\hat{f}$ is supposed to be a good approximation of f so that for the inputs $X=(x_1,x_2,x_3,\ldots,x_n)$ we will have the outputs $\hat{y}$, which is a good approximation of y. The value of $\hat{y}$ will an approximation of the value of y, and it can be replaced with an acceptable amount of error. A set of partial models are fitted by the least-squares method, and we will achieve the optimal model using the initial models based on the considered indices. By cascading the previous models and applying them to the next models, the final model will be created. This process will continue until we reach the final optimal model. The principle behind the technique is defined by expressing a few sentences of Volterra, known as Kolmogorov-Gabor [17]:

$$\begin{aligned}Y(x_1,\ldots,x_n)=a_0+\sum_{i=1}^{n}a_i x_i+\sum_{i=1}^{n}\sum_{j=i}^{n}a_{ij}x_i x_j\\+\sum_{i=1}^{n}\sum_{j=i}^{n}\sum_{k=j}^{n}a_{ijk}x_i x_j x_k+\ldots\end{aligned} \tag{2}$$

As can be seen, (2) will increase exponentially as the number of inputs increases and the system practically begins to become too complex to solve this problem by dividing the model into smaller problems and solving them separately. According to Ivakhnenko's theory, a relation can be calculated for both inputs from *n* inputs. For *n* inputs, we have $\binom{n}{2}=\frac{n(n-1)}{2}$ primary nodes, each of which is calculated based on (3):

$$\hat{y}_l=G_l(x_i,x_j)=c_0+c_1x_i+c_2x_j+c_3x_i^2+c_4x_j^2+c_5x_ix_j \tag{3}$$

where, index *l* denotes the number of the layer that creates the nodes, and coefficients *c* are the weights that establish the relationship between the two inputs and outputs. These nodes are the primary nodes created by the GMDH equations. In the next step, and to minimize the error, the algorithm uses (4) to properly fit $\hat{y}_m$.

$$E=\frac{\sum_{i=1}^{M}(y_i-G_i)}{M}\rightarrow\min \tag{4}$$

Based on (4), which is considered as the fitting condition, it is possible to reach the final optimal model from the initial models. Using this method, a set of outputs are fitted in each step and sent to the next step and a set of them will be deleted. Then, in the next step, according to (3) by employing the input values from the previous step, the relationship between the winning inputs will be compiled in pairs and the fitting will be done. These steps continue until a certain level of error or

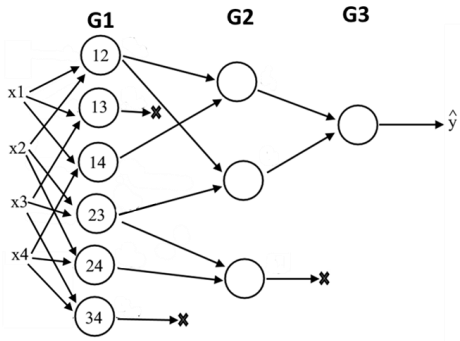

Fig. 1: Hypothetical structure of the considered GMDH network.

a certain number of layers is obtained. This problem can be represented graphically as in Fig. 1 [17-19].

To calculate coefficients *C* in (3), the problem can be analysed in matrix form. To this end, (3) can be rewritten as (5). Also, to simplify the calculations, (5) can be written in closed-form as given by (6):

$$\hat{y}_l = G_l = \begin{bmatrix} c_0 & c_1 & c_2 & c_3 & c_4 & c_5 \end{bmatrix} \begin{bmatrix} 1 \\ x_i \\ x_j \\ x_i^2 \\ x_j^2 \\ x_i x_j \end{bmatrix} \quad (5)$$

$$\hat{y}_l = G_l = C^T x \quad (6)$$

This equation should be rewritten for all inputs and outputs assuming the corresponding *m*:

$$Y_l = C^T X \quad (7)$$

In (7), Y as the outputs corresponding to X and C are the weighting coefficients of the function. To solve this equation, according to (8), both sides of the equation must first be multiplied by X^T and then by $(XX^T)^{-1}$.

$$YX^T = C^T XX^T \Rightarrow YX^T (XX^T)^{-1} = C^T XX^T (XX^T)^{-1} \quad (8)$$

In (8), as it is known, the right side of the equation, i.e., $XX^T (XX^T)^{-1}$, is equal to the unity matrix. Besides, if we show the final result of the matrix $X^T (XX^T)^{-1}$ as a matrix $X^\dagger$, then the constant coefficients of the final function can be calculated using (9):

$$YX^\dagger = C^T \quad (9)$$

Utilizing this solution, the values of the coefficients c_i in C^T are calculated and finally sent to (4) for fitting, and of the nodes in the next step will be formed step by step. The main point about the difference between GMDH and conventional neural networks concerns the topology form. Usually, in neural networks, the network topology is predetermined and the weights are calculated. However, in GMDH, as mentioned earlier, the network structure is organized by itself. Based on the fitting conditions, it will obtain the complexity required for describing the model. At the end of this section, as a complete summary of all the steps presented in this section, Fig. 2 illustrates the complete plan of the steps of the GMDH method. According to the proposed flowchart, the constant coefficients of (9) will eventually be calculated as the outputs of the GMDH algorithm.

3. Proposed Method

The main objective of this paper is to derive a function to determine the location of BCFs based on current and voltage phasors of the faulty phase. In general, protection of a transmission line consists of three basic stages. The fault detection stage is the phase of determining the faulty phase and the final stage is locating the fault point in the transmission line. In this paper, it is assumed that the time of fault incidence and the faulty phase are known and only the fault location problem is analyzed. Fig. 3 shows the electrical energy transmission line in the case of a broken conductor.

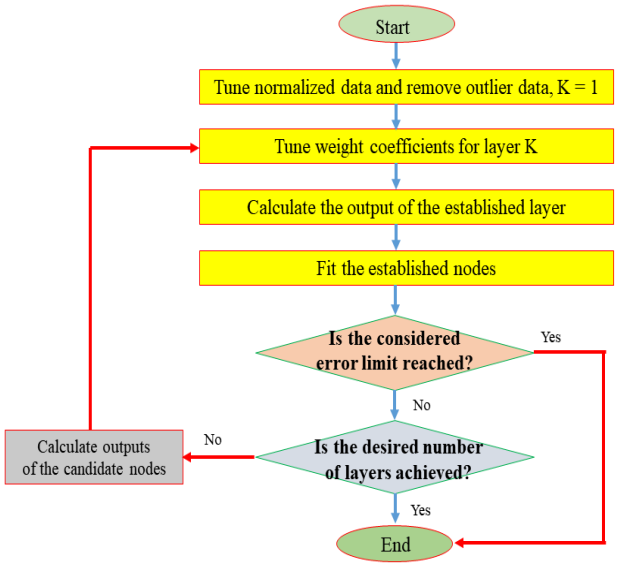

Fig. 2: Flowchart of GMDH network training and how constant coefficients of (3) are calculated.

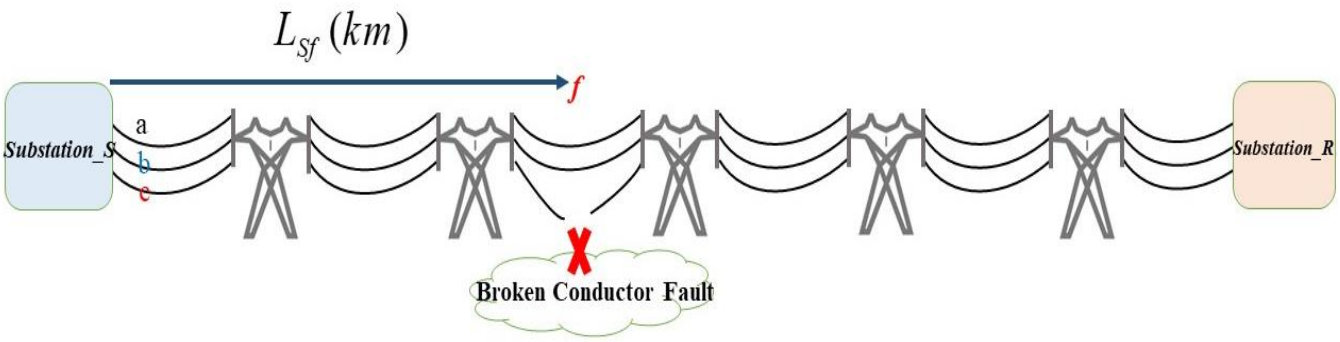

Fig. 3: Diagram of the electrical energy transmission line in case of a broken conductor.

According to Fig. 3, the ultimate goal in this scheme is to calculate L_{Sf} only by the current and voltage phasors of the local terminal S. The GMDH theory has been used to obtain the BCF location function. To achieve this, a sample transmission line has been used as a case study. The full data of the simulation system is given in the Appendix of the paper. To obtain the BCF location function in each phase based on the values of the current and voltage phasors of that phase, it is necessary to collect the current and voltage phasors of the faulty phase for specific spans of the transmission line. In this paper, it is assumed that the BCF phenomenon occurs for each phase with spans of 0.25 km, that the measurements of current and voltage phasors are the inputs to the problem, and that the fault location is used as the output for training the GMDH.

The magnitude of the current and voltage phasors considered in this paper have been calculated using the full-cycle Fourier algorithm with a sampling frequency of 2.4 kHz so that these 40 samples, in a complete cycle, are obtained after detecting the time of fault incidence from current and voltage waveforms. After storing the input and output data for each span of 0.25 km for each phase separately, BCF location can be used to train the GMDH network. Finally, the constant coefficients of the BCF location equation for each phase are extracted as follows:

$$L_{Sf\,(i=a,b,c)} = c_0 + c_1 V_i + c_2 I_i + c_3 V_i^2 + c_4 I_i^2 + c_5 V_i I_i \qquad (10)$$

According to (2) and (5), a suitable approximation for calculating Y is provided in (10), where $L_{Sf\,(i=a,b,c)}$ is the length of the fault location in km, V_i denotes the voltage phasor magnitude of the faulty phase in volts, and I_i shows the current phasor magnitude of the faulty phase in amperes. In the end, according to the training and testing results of the GMDH network for the data collected for its training, constant coefficients of (10) are provided in the form of numbers in Table 1 for each phase when BCF occurs.

Fig. 4 shows the output diagram for the training data of the GMDH network for phase *a*. Fig. 4a illustrates the actual output value and the output value of the trained GMDH. As shown in this figure, the generated GMDHs perfectly follow the behaviour of the output data. Fig. 4b shows the difference between each sample and its true value as an error. Fig. 4c shows the histogram of the mean error and the standard deviation error of that data. Figs. 5 and 6 are the same as described in Fig. 4 but have been created and extracted for the data test and all the data. Also, the values of the regression coefficient for the training data, the test data, and all the data are calculated and displayed in Figs. 7a, 7b, and 7c, respectively.

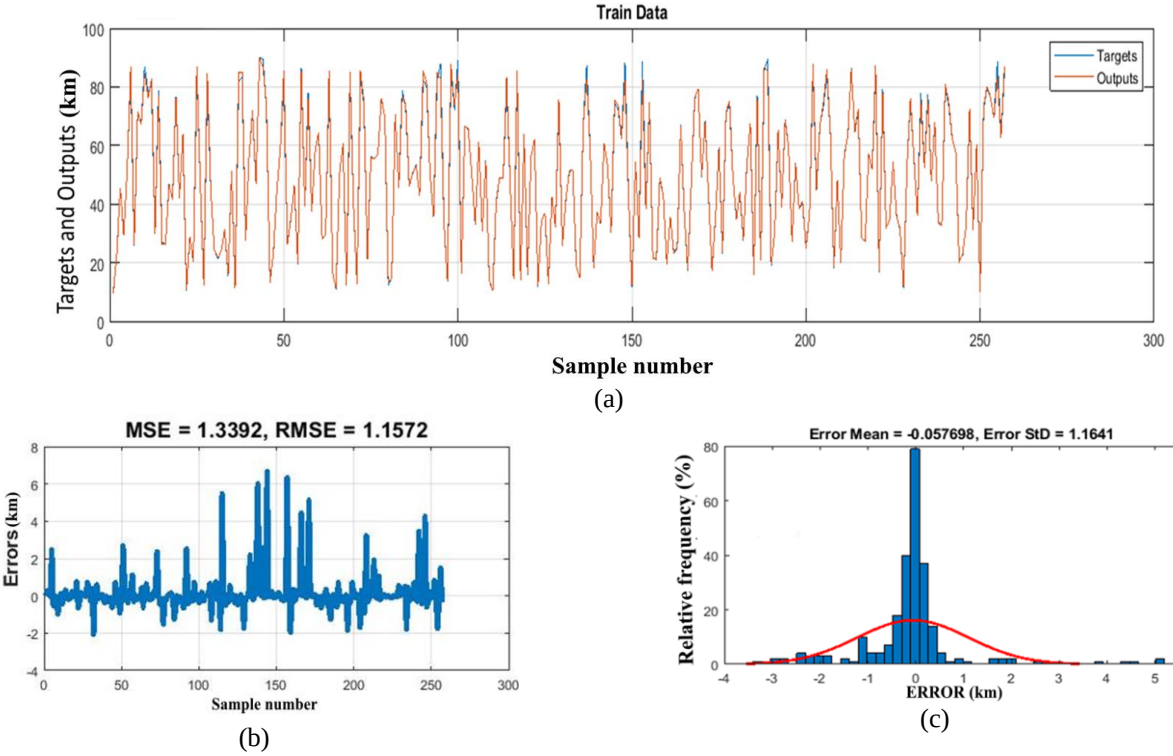

Fig. 4: (a) Random sample number training data and actual value, (b) error among output and actual value, and (c) the standard deviation error value histogram of phase *a*.

Table 1: Constant coefficients of the BCF location equation for each phase.

Coefficients	Faulty phase		
	Phase a	Phase b	Phase c
c_0	-0.001807483476824	-0.000347153512442	0.000435823636190
c_1	0.001883852022470	-0.000729128826911	0.000060757724125
c_2	29.600376454232446	4.828049106209392	-5.292283067420200
c_3	-0.000000010043424	0.000000003885341	-0.000000000340196
c_4	0.000329108037455	0.000072001088415	-0.000849774628931
c_5	-0.000151549141822	-0.000019915640640	0.000034247064010

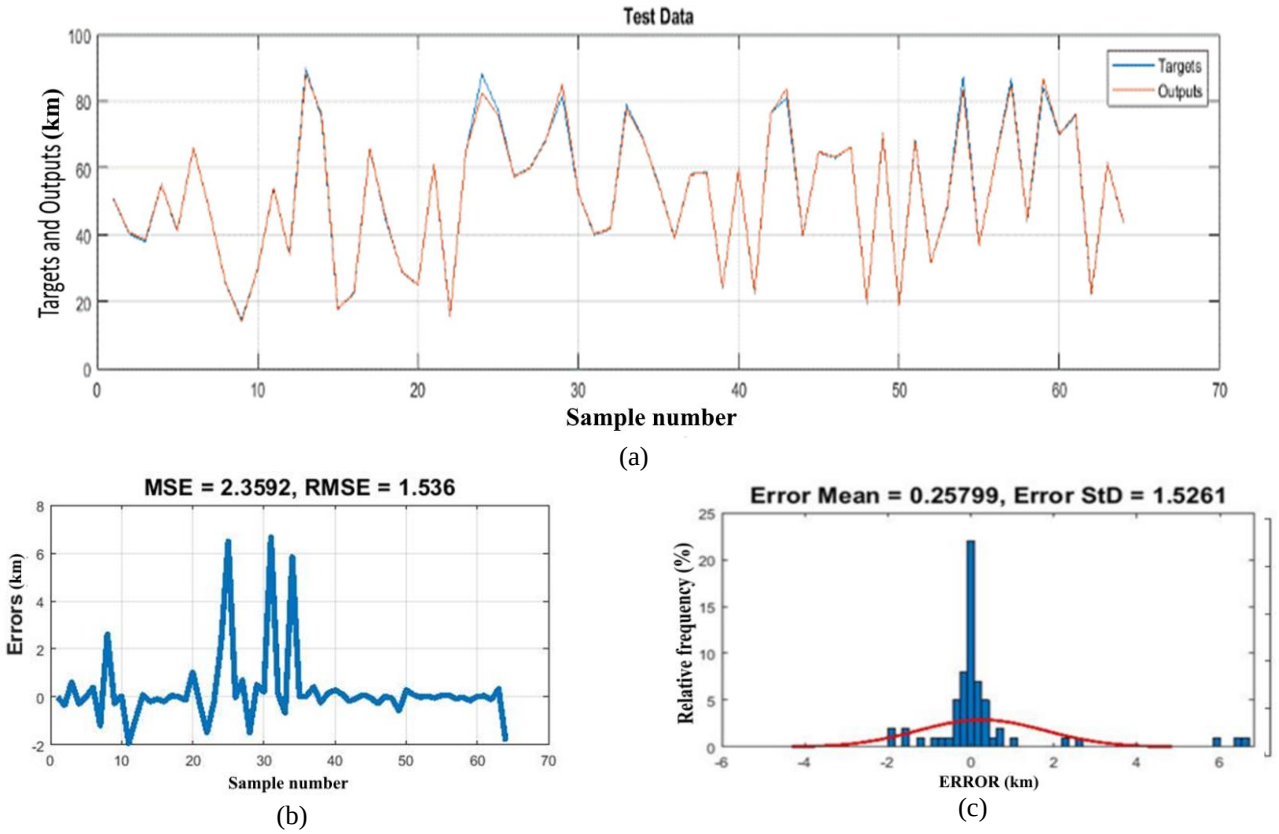

Fig. 5: Neuron analysis results of the test data of phase *a*. (a) Random sample number training data and actual value, (b) error among output and actual value, and (c) the standard deviation error value histogram

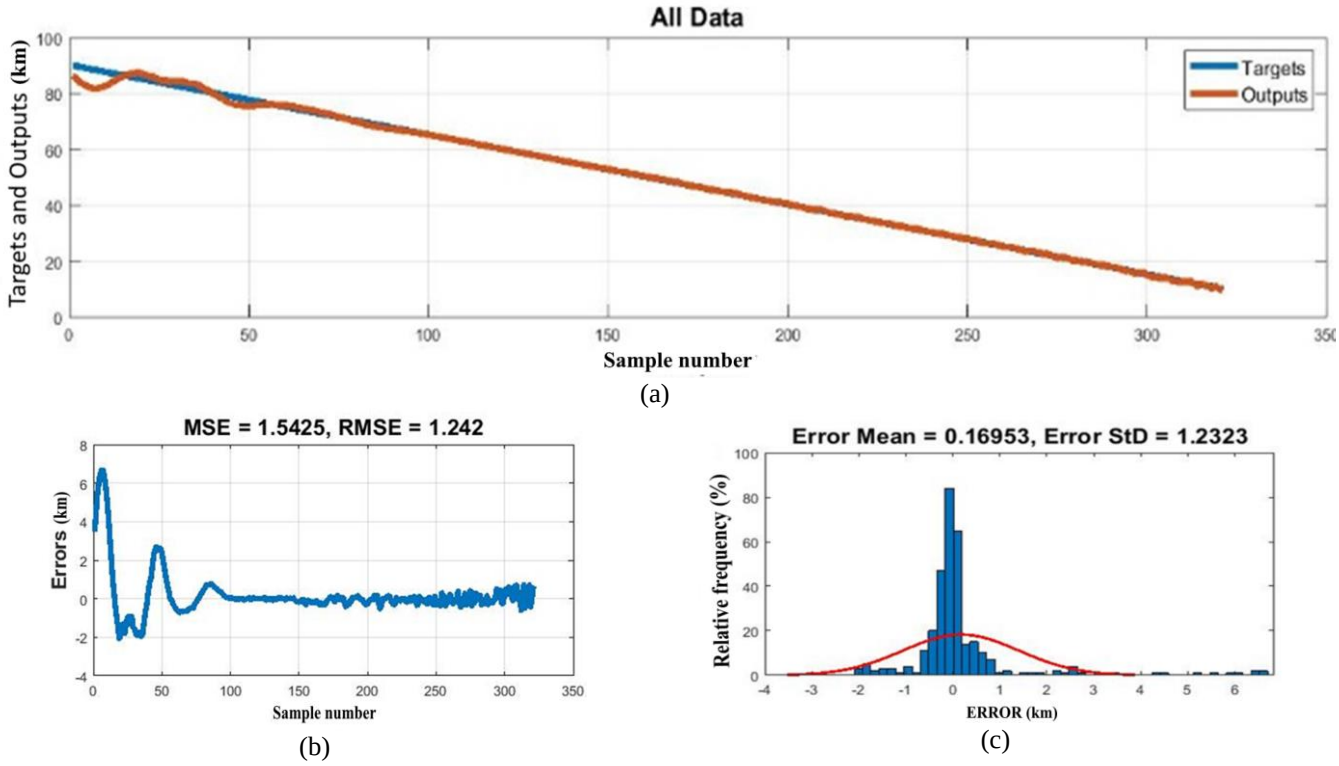

Fig. 6: Neuron analysis results of all the data of phase *a*, (a) Training data, actual value, (b) error among output and actual value, and (c) the standard deviation error value histogram.

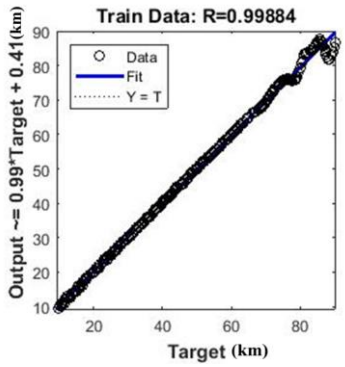

(a)

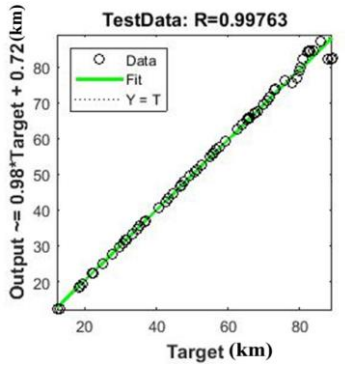

(b)

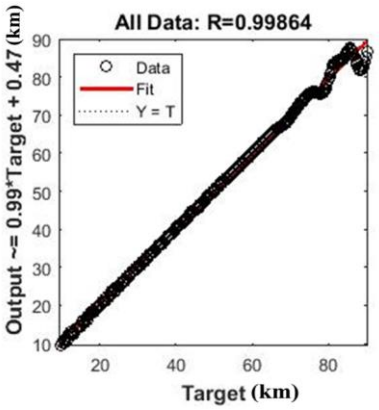

(c)

Fig. 7: Regression coefficient governing the (a) training data, (b) the test data, and (c) all the data of phase *a*.

The results presented in Figs. 4-7 correspond to the analysis of a BCF for phase *a*. The output results can be displayed in the same way for the other two phases, which are neglected due to similarity. Finally, using the BCF location function for each phase, the fault location can be calculated in proportion to the magnitudes of current and voltage phasors of the faulty phase. As it turns out, the presented function is completely independent of line parameters, and this is an advantage for the proposed scheme in this paper. Fig. 8 shows the final flowchart of the proposed BCF location scheme.

4. Simulation Results

This section presents the test results of the designed algorithm in MATLAB/Simulink environment. To test the algorithm, a bidirectionally-fed transmission line (see Fig. 9) has been used. The purpose is to implement several faults in different phases for different locations and to calculate the magnitudes of current and voltage phasors of the faulty phase in terminal S. These values can be used as input values for the function given in (10) to calculate the BCF location. According to the results tabulated in Table 2, the maximum fault location estimation error according to the proposed algorithm is +0.814%. The BCF location estimation error given in Table 2 is calculated using the equations given in [20-21]. the tolerance level of the system to the error can be considered by the calculated standard deviation value. To put it simply, if the input value differs from the specified value by the actual value, the generated GMDH structure will delete it and display the actual output value.

5. Sensitivity Analysis

This section investigates the sensitivity of the algorithm to some critical conditions in the power system. The selected scenarios are the most probable conditions that can have negative and destructive effects on fault location algorithms. This section also examines five critical scenarios to evaluate the robustness of the suggested algorithm.

5.1. Sensitivity Analysis with Respect to the Noise

The presence of noise in the power system and the measuring devices is undeniable. To investigate the effect of

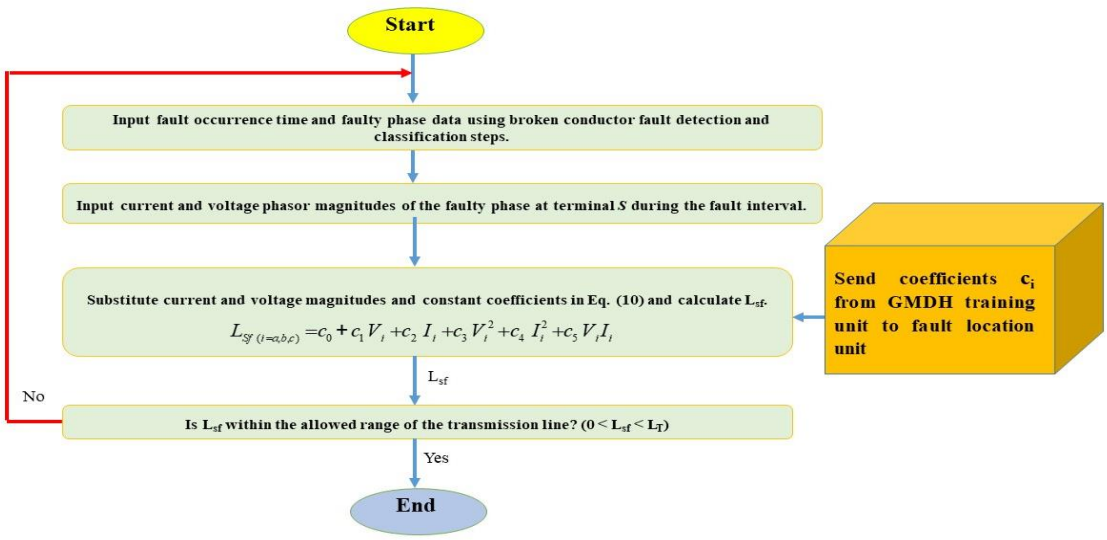

Fig. 8: Flowchart of a complete layout of BCF location in electrical power transmission lines.

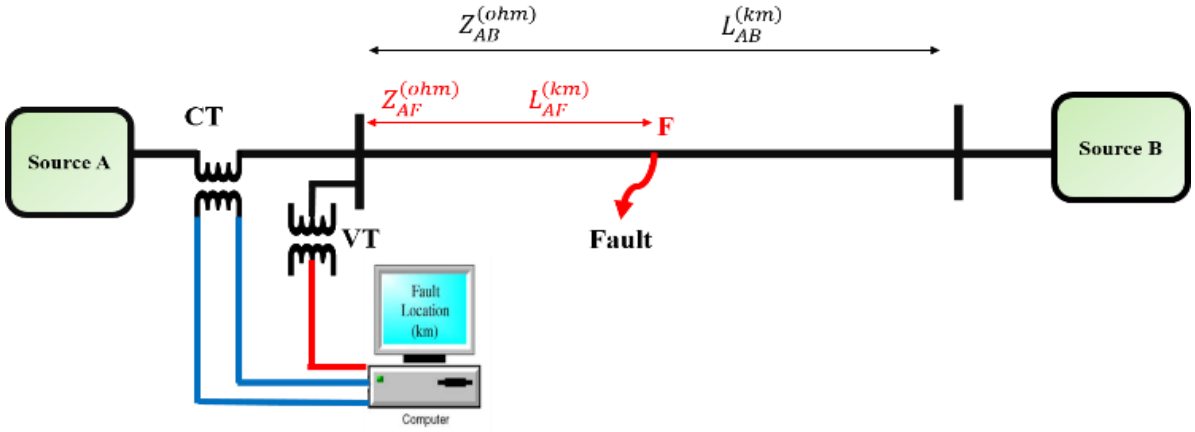

Fig. 9. Single-line diagram of the network under study.

Table 2: Test results of the proposed algorithm.

Faulty phase	V (V)	I (A)	Real value (km)	Algorithm test results (km)	Error (%)
a	187846.3	8.67981	10	9.3323	+0.667
	187937.4	23.3095	25.5	25.559	-0.059
	187996.5	31.7863	34.75	34.798	-0.048
	188111.3	54.9415	60	59.981	+0.018
	188249.6	80.1913	85	86.061	-1.061
b	187897.1	13.4925	15	14.837	+0.162
	187926.4	21.9055	24.25	24.003	+0.246
	188048.9	45.7785	50	50.008	-0.008
	188143.8	57.6458	62.75	62.909	-0.159
	188683.5	82.5139	95	94.005	+0.995
c	187862.2	9.52651	4	5.2051	-1.205
	187930.5	19.8844	21.75	21.811	-0.061
	188004.1	43.0578	47	47.180	-0.180
	188162.1	59.4319	64.75	64.835	-0.085
	188193.7	77.7361	83.5	83.864	-0.364

noise, the efficiency of the proposed method has been investigated for different signal-to-noise (SNR) ratios. This quantity represents the ratio of signal power to noise power that contaminates the signal in dB. White noise is used here to simulate the noise effects. To investigate this scenario, white Gaussian noise with different SNR ratios was added to the received current and voltage samples. The intended noise level is 30 dB. On the other hand, as can be seen in Fig. 6.c, In this case, it is assumed that a BCF occurs at a distance of 10 km from terminal S at t = 0.5 s in phase *c*. In this case, the calculated distance of fault from terminal S by the proposed algorithm is 9.09 km, where the estimation error is 0.91%.

5.2. Sensitivity Analysis with Respect to the Transformer Saturation

In this section, the sensitivity of the algorithm to the CT saturation installed in terminal S is investigated. The damping constant of the DC component for this CT is set 50 ms. This value is considered as the maximum critical value for this algorithm. The algorithm performs well for damping constants lower than 50 ms but it fails and shows poor performance for values higher than 50 ms. The detailed data of the CT can be found in [4]. In this case, it is assumed that a BCF occurs at a distance of 50 km from terminal S at t = 1.5 s in phase *a*. The damping constant of the DC component is assumed to be 48 ms. The calculated value for the fault distance from terminal S by the proposed algorithm is 49.17 km, where the estimation error is 0.83%.

5.3. Sensitivity Analysis with Respect to the Power Swing

Power swing is one of the most controversial issues in the protection of power systems due to the occurrence of some dynamic disturbances such as abrupt changes in electrical loads, irregular operation of reclosers, uncontrolled switching operations, phase-to-phase and phase-to-ground short circuits, etc. The occurrence of this phenomenon may lead to malfunctioning of distance relays and improper interruption of transmission lines, which endangers the stability of the power system. As a result, the malfunction of the remote relay should be prevented during power swing. To simulate the effect of power swing on the performance of the proposed method, we assume that the voltage phase angle starts fluctuating by 40° with 1° steps and with a frequency of 1 Hz in the generator located in terminal S. In this case, it is assumed that a BCF occurs at a distance of 70 km from terminal S at t = 2.8 s in phase *b*. The calculated value of the fault distance from terminal S using the proposed algorithm is 69.55 km, where the estimation error is 0.45%. In this case, it is assumed that a BCF occurs at a distance of 40 km from terminal S at = 3 s in phase *a*. The calculated value of the fault distance from terminal S in this case is 41.39 km, where the estimation error is 1.39%.

5.4. Sensitivity Analysis with Respect to a Harmonic-Polluted Voltage Source

The presence of harmonic power sources is one of the main challenges that affect all parts of the power system. The proposed scheme in this paper employs current and voltage phasors with the fundamental frequency of the system, i.e., 60 Hz, to solve the problem. These quantities are calculated by the phase measurement units (PMUs), installed at the measurement points, which are then given to the algorithm. Algorithms designed in PMUs use the discrete full-cycle Fourier theory along with the DC offset removal algorithm or a frequency filtering to calculate the fundamental frequency phasor. This section presents a scenario for analyzing the sensitivity of the algorithm to harmonic pollution. To investigate the effect of the harmonic current and voltage of terminal S, a harmonic voltage source with harmonic orders of 3, 5, 7, 9, 11, and 13 are connected to terminal S. In this case, it is assumed that a BFC occurs at a distance of 80 km from point S in phase *c*. The calculated value of the fault

distance from terminal S by the proposed algorithm is 79.50 km, where the estimation error is 0.5%.

5.5. Sensitivity Analysis with Respect to the Changes in Transmission Line Parameters

The algorithm proposed in this paper is completely independent of the system parameters and the transmission line parameters. Referring to (10), the only inputs to the fault location function are the magnitudes of current and voltage phasors at terminal S during the BCF period. Therefore, changes in system parameters for any reason in any situation will not affect the performance of the proposed algorithm. In this scenario, it is assumed that after calculating the coefficients of the BCF location function by GMDH, positive- and zero-sequence parameters of the line are increased by 20%. To investigate the sensitivity of the algorithm to line impedance changes, it is assumed that a BCF occurs in phase *b* at 50 km from terminal S in t = 2 s. The calculated value of the fault distance from terminal S by the proposed algorithm is 49.63 km, where the estimation error is 0.47%.

5.6. Sensitivity Analysis of the Algorithm Performance in Low-Load Mode

In this section, the purpose is to investigate the performance of the algorithm in low -load mode. According to the network topology designed in this paper, both sides of the protected transmission line are modelled as Thevenin-equivalent circuits. To create low -load conditions in this topology, the magnitude and angle of the source voltages on both sides of the line must be controlled. Thereby, the active and reactive power flow will be controlled and thus the electric current flowing in the transmission line can be controlled. To implement this mode, the voltage magnitude and angle of the sources on both sides must be equalized. According to the information provided in the appendix of the paper, the voltage of the two sources is equal and it is only necessary to make the angle of the two sources equal, so the angle is set 9.2°. In this case, the amplitude of transmission line current is reduced from 2000 A (in the initial state of the simulation) to 100 A (in the case of low -loaded conditions).

To examine the results of the algorithm, in this case, three scenarios are considered, which are presented below.

Scenario 1. In this scenario, a phase interruption fault occurs in phase *a* at a distance of 50 km from station S. The values of faulty voltage and current phasors during the fault are 188061.853V and 45.227 A, respectively. According to (10) and constant coefficients presented in the first column of Table 1, the estimated distance for the fault location is 49.49 km from station S. The fault location estimation error in this case is 0.52%.

Scenario 2. In this scenario, a phase interruption fault occurs in phase *b* at a distance of 75 km from station S. The values of faulty voltage and current phasors during the fault are 188076.181V and 68.027 A, respectively. According to (10) and constant coefficients presented in the second column of Table 1, the estimated distance for the fault location is 74.25 km from station S. The fault location estimation error in this case is 0.75%.

Scenario 3. In this scenario, a phase interruption fault occurs in phase *c* at a distance of 90 km from station S. The values of faulty voltage and current phasors during the fault are 188103.753V and 81.775A, respectively. According to (10) and constant coefficients presented in the third column of Table 1, the estimated distance for the fault location is 88.72 km from station S. The fault location estimation error in this case is 1.28%.

Regarding the performed sensitivity analysis, one can observe that the proposed algorithm in this paper is robust against critical conditions and shows good performance.

6. Discussion and Comparison

This section aims to analyse and compare different BCF location algorithms in electrical power transmission lines with the results presented in the literature. Six basic indices are used to make this comparison, as introduced below.

Index 1: This index specifies the scope of problem analysis. As explained in the Introduction section, there are generally five areas of analysis to solve fault location problems, including phasor analysis (Ph), equation analysis in the time domain (TW), signal processing (SP) analysis, Teaching-Learning (TL) and Pattern extraction analysis, and communication-based (CM) analysis.

Index 2: This index determines the number of terminals from which current and voltage data is received. If the number of terminals is more than one, the number is determined using this index whether the data is synchronized or not.

Index 3: This index determines the sampling frequency rate in kHz.

Index 4: This index determines the dependence of the algorithm on system parameters.

Index 5: This index determines the coverage of the algorithm for all the three stages of line protection. In other words, the designed algorithm covers several stages of protection. The first stage is related to fault detection (FD), the second stage concerns fault classification (FC), and the third stage is fault location (FL).

Index 6: This index determines the average error value of the algorithm for all simulation output results.

Index 7: This index determines the level of implementation of the algorithm in terms of hardware.

Table 3: The analysis results of the proposed method and different literature.

Ref.	Index1	Index2	Index3	Index4	Index5	Index6	Index7
[5]	Ph	1	1000	✓	FD&FL	3.3	-
[6]	CM	many	NA	-	FD&FL	NA	✓
[7]	CM	many	NA	-	FD&FL	NA	✓
[8]	SP	1	NA	-	FD	NA	-
[9]	SP	1	NA	-	FD	NA	-
[10]	SP	1	256	✓	FD	NA	✓
[11]	SP	1	256	✓	FD	NA	✓
[12]	TL	1	1000	✓	FD&FC	NA	-
Proposed method	TL	1	2.4	-	FL	0.8	✓

According to the results listed in Table 3, the scheme presented in this paper can completely analyze the BCF location problem without requiring the transmission line parameters. It can also be implemented in industrial relays in terms of sampling frequency. Furthermore, the average error presented in this method is significantly low and appropriate as compared to the other methods.

7. Future Works

As stated in this paper, the problem of protecting transmission lines against the broken conductor phenomenon is one of the major challenges in protection systems. Due to the special conditions of this type of fault, the design of the relay function to protect the line against this type of fault is different from normal shunt faults. According to the literature review conducted in the Introduction section, detecting these types of faults and discriminating them from low-load conditions constitute a major problem. On the other hand, locating these types of faults along the transmission line with specific topologies is a vital issue in the protection industry. The following are the suggestions of the authors for future research in this field:

A) Designing and presenting normal and series shunt fault detection algorithms relative to each other in transmission lines.

B) Designing a faulty phase detection algorithm when BCF occurs.

C) Designing detection, classification, and location algorithms for BCFs in transmission lines compensated with FACTS devices, series capacitor compensators, and single- or dual-terminal data.

8. Conclusion

This paper presents a complete scheme for broken conductor fault location in electric power transmission lines based on the GMDH function fitting method using single-terminal data without the need for transmission line parameter data. The scheme presented in this paper utilizes currents and voltage phasors of the faulty phase during the fault as the input to the fault location function. The collected data from each of the 0.25 km spans of the transmission line for each phase, once the fault occurred, is used to train the GMDH network. Eventually, a model is suggested for estimating the fault location based on the magnitudes of current and voltage phasors of one terminal during the fault without the need for transmission line parameters. BCF location equations for each phase are tested and analyzed for important factors under different scenarios in normal and fault conditions as well as critical conditions. The results in the Simulation and Sensitivity Analysis sections confirm the suitable performance of the proposed scheme. Additionally, based on the simulation results, the average error of location estimation is −1.205% and in the Sensitivity Analysis section, its value is 1.39%.

CRediT Authorship Contribution Statement

Mahyar Abasi: Conceptualization, Data curation, Formal analysis, Methodology, Software, Supervision, Validation, Roles/Writing - original draft, Writing - review & editing. **Nima Heydarzadeh:** Data curation, Investigation, Software, Visualization. **Arash Rohani:** Investigation, Project administration, Visualization.

Declaration of Competing Interest

The authors declare that they have no known competing financial interests or personal relationships that could have appeared to influence the work reported in this paper. The ethical issues; including plagiarism, informed consent, misconduct, data fabrication and/or falsification, double publication and/or submission, redundancy has been completely observed by the authors.

Appendix

Table 4 provides Simulink system data. The system under test is implemented in MATLAB ver.2018, and the line protection program is coded in an m file.

Table 4: Data of substations and transmission lines implemented in MATLAB software.

Substation Information					
Substation	V (kV)	F (Hz)	S (MVA)	X/R	Config.
S	230	60	9000	10	Yg
R	230	60	9000	10	Yg
Line Information					
$[R_1 , R_0]$ (Ohm/km)			[0.01273*2 , 0.3864]		
$[L_1 , L_0]$ (H/km)			[0.9337e-3 , 4.126e-3]		
$[C_1 , C_0]$ (F/km)			[12.74e-9 , 7.75e-9]		
Length (km)			100		
Frequency (Hz)			60		

References

[1] A. Ghaderi, H. L. Ginn, and H. A. Mohammad pour, "High impedance fault detection: A review." *Electric Power Systems Research*, vol. 143, pp. 376-388, 2017.

[2] B. Patel, and P. Bera, "Fast fault detection during power swing on a hybrid transmission line using WPT", *IET Generation, Transmission & Distribution*, vol. 13, no. 10, pp. 1811-1820, 2019.

[3] M. Abasi, S. G. Seifossadat, M. Razaz, and S. S. Moosapour, "Presenting a new Formulation to analyze and determine unbalance voltage produced at the place of load resulting from network and loads unbalance and asymmetry of transmission", *Majlesi Journal of Energy Management*, vol. 4, no. 3, pp.1-7, 2015.

[4] A. Saffarian, and M. Abasi, "Fault location in series capacitor compensated three-terminal transmission lines based on the analysis of voltage and current phasor equations and asynchronous data transfer", *Electric Power Systems Research*, vol. 187, 106457, 2020.

[5] K. Dase, S. Harmukh, and A. Chatterjee, "Detecting and locating broken conductor faults on high-voltage lines to prevent autoreclosing onto permanent faults", in *46th Annual Western Protective Relay Conference Spokane*, Washington 2019.

[6] S. H. Al-Ghannam, Y. Khan, U. Ahmad, N. H. Malik, A. A. Al-Arainy, and B. S. Al-Shahrani, "Development of open (broken) conductor detection system for high resistivity areas", in *2017 Saudi Arabia Smart Grid*, Jeddah, Saudi Arabia, IEEE, pp. 1-8, 2017.

[7] B. Nuthalapati, and U.K. Sinha, "Fault Detection and Location of Broken Power Line Not Touching the Ground", *International Journal of Emerging Electric Power Systems*, vol. 20, no. 3, pp.1-10, 2019.

[8] W. Johnson, "Nuclear maintenance application center: Development and analysis of an open-phase detection scheme for various configurations of auxiliary transformers," *EPRI, Palo Alto, CA, USA*, Rep. 3002000764, 2013.

[9] W. Johnson, "Interim report: EPRI open-phase detection method," *EPRI, Palo Alto, CA, USA*, Rep. 3002004432, 2014.

[10] X. Wang, T. Ding, and W. Xu, "An Open Conductor Condition Monitoring Scheme Using Natural Voltage and Current Disturbances", *IEEE Transactions on Power Delivery*, vol. 34, no. 3, pp. 1193-1202, 2019.

[11] X. Wang, and W. Xu, "A 3rd harmonic power based open conductor detection scheme", *IEEE Transactions on Power Delivery*, vol. 36, no. 2, pp. 1041-1050, 2021.

[12] A. M. Abdel-Aziz, B. M. Hasaneen, and A. A. Dawood. "Detection and classification of one conductor open faults in parallel transmission line using artificial neural network", *International Journal of Scientific Research & Engineering Trends*, vol. 2, no. 6, pp. 139-146, 2016.

[13] ABB, REL 521 Line distance protection terminal, ABB Technical brochure, 2003. [Online]. Available: https://library.e.abb.com/public/433f46304583cd01c12578570041e44b/1MRK506069-UEN_en_Technical_reference_manual_REL_521_2.3.pdf (accessed March 24, 2021).

[14] SIEMENS, AG. "SIPROTEC 4–Distance Protection 7SA6-Catalog", 2003. [Online]. Available: https://www.downloads.siemens.com/download-center/Download.aspx?pos=download&fct=getasset&mandator=ic_sg&id1=DLA06_4794 (accessed March 24, 2021).

[15] AREVA, "MiCOM P443 fast multifunction distance protection." [Online]. Available: https://download.schneider-electric.com/files?p_enDocType=User+guide&p_File_Name=P44y_EN_M_Kc3__K1__M.pdf&p_Doc_Ref=P44y_EN_M_Kc3_K1_M (accessed March 24, 2021).

[16] X. Song, F. Gao, Z. Chen, and W. Liu. "A negative selection algorithm-based identification framework for distribution network faults with high resistance", *IEEE Access*, vol. 7, pp. 109363-109374, 2019.

[17] A. G. Ivakhnenko, "Polynomial theory of complex systems." *IEEE Transactions on Systems, Man, and Cybernetics*, vol: SMC-1, no. 4, pp. 364-378, 1971.

[18] S.J. Farlow, *Self-organizing methods in modeling: GMDH type algorithms*. 1st ed., CRC Press, 1984.

[19] N. Narimanzadeh, A. Darvizeh, M. Darvizeh, and H. Gharababaei, "Modeling of explosive cutting process of plates using GMDH-type neural network and singular value decomposition", *Journal of Materials Processing Technology*, vol. 128, no. 1-3, pp. 80-87, 2002.

[20] A. Rohani, M. Joorabian, M. Abasi, and M. Zand, "Three-phase amplitude adaptive notch filter control design of DSTATCOM under unbalanced/distorted utility voltage conditions", *Journal of Intelligent & Fuzzy Systems*, vol. 37, no. 1, pp. 847-865, 2019.

[21] M. Abasi, A. Saffarian, M. Joorabian, and S. G. Seifossadat, "Fault location in double-circuit transmission lines compensated by generalized unified power flow controller (GUPFC) based on synchronous current and voltage phasors", *IEEE Systems Journal*, 2020 , to be published.

BIOGRAPHY

Mahyar Abasi was born in 1989 in Iran. He received the Ph.D. degree in Electrical Power Engineering in 2021 from the Shahid Chamran University of Ahvaz, Ahvaz, Iran. He is currently a research assistant in scientific and industrial research in the field of power electrical engineering at Shahid Chamran University of Ahvaz. His research interests are fault location, power system protection, FACTS devices, and power quality assessment.

Nima Heydarzadeh was born in 1990 in Iran. He received his B.Sc. degree in electronics engineering at Islamic Azad University of Arak Branch, Arak, Iran in 2012 and his M.Sc. degree in electronics engineering majoring in digital at Islamic Azad University of Central Tehran Branch, Tehran, Iran in 2020. He is currently working as a design engineer in the field of intelligent systems, automation, and instrumentation in engineering companies in Tehran, Iran. His scientific and professional interests are in the fields of artificial neural networks, deep learning, optimization algorithms, reverse engineering, and Industrial Motion Controller.

Arash Rohani received the B.Sc. and M.Sc. degrees in electrical engineering from the Shahid Chamran University of Ahvaz, Iran, in 2009 and 2013, respectively. Currently, he works for the Khuzestan Regional Electric Company. His research interests are Power Electronics, Power System Protection, and AC/DC microgrid.

Copyrights
© 2021 Licensee Shahid Chamran University of Ahvaz, Ahvaz, Iran. This article is an open-access article distributed under the terms and conditions of the Creative Commons Attribution –Non-commercial 4.0 International (CC BY-NC 4.0) License (http://creativecommons.org/licenses/by-nc/4.0/).

Shahid Chamran University of Ahvaz

Iranian Association of Electrical and Electronics Engineers

Journal of Applied Research in Electrical Engineering

E-ISSN: 2783-2864
P-ISSN: 2717-414X
Homepage: https://jaree.scu.ac.ir/

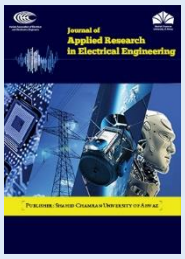

Research Article

A New Peer-to-Peer Energy Trading Model in an Isolated Multi-agent Microgrid

Mahyar Tofighi-Milani [1,*], Sajjad Fattaheian-Dehkordi [1,2], and Mahmud Fotuhi-Firuzabad[1,2]

[1] *Department of Electrical Engineering, Sharif University of Technology, Tehran 14588-89694, Iran*

[2] *Department of Electrical Engineering and Automation, Aalto University, Espoo 11000, Finland*

* *Corresponding Author: mahyar.tofighimilani@gmail.com*

Abstract: Microgrids, which have newly been included in power systems, have facilitated the management of distributed generations. In this context, the privatization of power systems, as well as flexible sources like electrical vehicles and storage systems, has been enhanced significantly by the advent of microgrids. In a microgrid structure, the microgrid's operator coordinates the agents and ensures the reliability of the network, while the agents manage their local resources independently. Nonetheless, new management methods should be implemented into the multi-agent-structured microgrids to meet their distributed nature. This paper proposes a new peer-to-peer energy market to optimize the operation of a multi-agent microgrid run in the isolated mode. The designed framework facilitates power trading between the system agents and addresses the privacy issues of the network consumers or producers. The proposed scheme is finally simulated on a 15-bus multi-agent-structured microgrid to study its effect on microgrid management in the isolated mode.

Keywords: Multi-agent system, microgrid, distributed energy resources, peet-to-peer transaction, flexibility.

Article history
Received 17 December 2020; Revised 08 March 2021; Accepted 12 March 2021; Published online 27 April 2021.
© 2021 Published by Shahid Chamran University of Ahvaz & Iranian Association of Electrical and Electronics Engineers (IAEEE).
How to cite this article
M. Tofighi-Milani, S. Fattaheian-Dehkordi, and M. Fotuhi-Firuzabad, "A new peer-to-peer energy trading model in an isolated multi-agent microgrid," *J. Appl. Res. Electr. Eng.*, vol. 1, no. 1, pp. 33-41, 2022.
DOI:10.22055/jaree.2021.36078.1014

Check for updates

1. INTRODUCTION

Integration of distributed energy resources, as well as the benefits of reducing dependency on the upstream network, has contributed to prospering microgrids at a notable pace. Microgrids are small-scale systems that could operate several distributed generation units, flexible resources, and load demands. The development of microgrids has many positive effects on power systems, such as decreasing power transmission losses, increasing system reliability, and facilitating the high-rate integration of renewables to the grid [1]. Furthermore, the distributed energy resources installed in a microgrid can be operated by independent agents. In this regard, a new energy management framework is required to ensure the supply-demand balance during the real-time operation of a system.

Energy management in microgrids can be complicated by the large number of distributed resources and information required for the operational scheduling of the resources. So, researchers have employed various methods to handle this complexity, which can be divided into two general categories of centralized and decentralized management. In the centralized management, the microgrid control unit (MCU) will do the overall optimization of the local generations considering society welfare while, in the decentralized management, every consumer/producer will optimize its own objective function. Although the centralized way gives the exact optimum answers, the decentralized way is preferable mainly because it conserves the privacy of the consumer/producer in novel microgrids with multi-agent structures [2, 3].

Recently, several decentralized concepts have been introduced to address the operational scheduling of multi-agent systems (MASs) [4]. In an MAS, the energy system is assumed to consist of several independent entities (i.e. agents) that manage their own local generations independently and can produce/consume energy and participate in various power markets [5]. The capability of buying/selling any amount of power from/to a favorite agent in an MAS is an expedient capability that a peer-to-peer (P2P) market framework enables in distributed systems. This is the reason why the P2P concept has recently been taken into account in operating distributed energy systems.

Reference [6] aims to cluster different loads of buildings and extract their related utility functions. Moreover, this paper focuses on designing two-stage management for facilitating energy sharing in the system. In the first stage, it minimizes the whole energy cost of society to extract the optimum power exchanges for all agents. In the second stage, a non-cooperative game is conducted among the agents, in which the agents' profits are considered to be maximized. This reference, however, has not considered various distributed generations for agents. A new model for P2P trading between agents is proposed in [7] based on the game theory. According to this reference, sellers compete in the price within a non-cooperative game, while buyers compete to select the sellers to purchase energy within an evolutionary game. Finally, the sellers and buyers play a Stackelberg game to interact with each other and determine the optimum power exchange between system agents although they do not predict the prices of next time intervals for the sake of better decision makings in this paper.

Authors in [8] run a market between microgrids in which sellers independently select their respective selling energy with respect to the revenue of selling and the utility of storing the energy. Buyers, on the other side, bid prices to the sellers independently. In this regard, energy is allocated to the buyers based on their announced prices. An auction-based P2P market framework is proposed in [9] to enable the distributed energy resources to trade energy in a distributed system. This paper employs the knapsack approximation algorithm to develop the P2P process, but it considers neither the electrical vehicles (EVs) of the system nor the utility function of agents, which takes the flexibility of loads into account.

Two methods for designing the P2P market are discussed in [10], i.e., auction-based P2P mechanism and bilateral contract-based P2P mechanism. Their capability in the management of electricity markets is then investigated in a distribution system. In [11], authors propose a double auction-based decentralized P2P market, in which agents determine their supply and demand data using the distributed model of management, maximize their benefits, and finally attend in the abovementioned double auction market. A hierarchical P2P framework is designed in [12] for future distribution systems. In this work, the P2P trading market is considered in three levels; i.e., P2P between nano-grids in a microgrid, P2P between microgrids in a multi-microgrid, and P2P between the multi-microgrids.

In [13], authors define a willingness function for every buyer and seller in the P2P energy market. This function consists of various functions, such as historical records, the time pressure owing to market closure, and the supply and demand amounts. In the proposed market of this paper, the first bids of the sellers are equal to the maximum limit of the price, and those of the buyers are equal to its minimum limit. In the next steps of the market's algorithm, the sellers decrease their price bids and buyers increase their price bids. A pair of a buyer and a seller are matched for trading when the price bid of the seller is less than the buyer's bid. In the market proposed in [14], the sellers/buyers first announce their desired sell/buy amount of energy, and the energy price is declared based on the bids. Then, a probability distribution is considered for distributed generations and a Bayesian game is implemented in the market model, in which the players' strategies are the buy/sell amount of energy.

In [15], a non-cooperative game is devised between sellers, in which energy demand and price are known, but the sell amounts of sellers are unknown. After the determination of the seller's supplies in the mentioned game, a double auction is run in which the sellers announce their desired amounts for sale and their minimum prices on one hand, and the buyers announce their desired amounts to buy and the maximum price that they can accept on the other hand. In this auction, the energy price is supposed to be determined having the sell amounts of sellers and the buyers' demand. In this paper, the result of the non-cooperative game is used in the auction, and the result of the auction is used in the game iteratively. It is noteworthy to mention that in [10-15], the model predictive control (MPC) method, which enables the agents to make better decisions about their local resources, is entirely dismissed.

This paper's contribution is designing a new P2P market scheme for energy management in an isolated microgrid with a multi-agent structure, in which the MPC method could be implemented. In the proposed framework, a vast variety of distributed generations are also considered for the agents' resources, which can be demonstrated as $D=\{PV, WT, FC, MT, CHP, DG\}$ representing photo-voltaic, wind turbine, fuel cell, microturbine, combined heat and power, and diesel generator, respectively. In this model, every agent could have any favorite subset generations of *D*, in addition to the energy storage system (ESS) and EV.

The proposed framework facilitates the P2P energy management among the system's agents that can use the MPC method to consider the next time intervals' predicted data in their decisions. Note that, besides the market perspectives, considering different kinds of flexible resources (i.e., distributed generation units, ESSs, and EVs) will improve the flexibility of the agents, which finally results in improving microgrid flexibility [16-18].

In this paper, the multi-agent structure of islanded microgrids is discussed in Section 2.1, Sections 2.2 and 2.3 study how to model the cost function of distributed generation units and the overall cost of each agent. The proposed P2P market framework is discussed in Section 2.4. Finally, Section 3 reports the results of implementing the proposed framework on an islanded microgrid composed of various agents, followed by the concluding points in Section 4.

2. METHODOLOGY

2.1. System Modeling

The system considered in this work is an MAS structured microgrid that is operated in the islanded mode. A simplified structure of the islanded microgrid with a multi-agent structure is shown in Fig. 1. In such a system, the agents will tend to participate in markets, which enable them to sell their extra energy or buy their energy shortage at a lower price. Therefore, this paper aims to address a new and efficient decentralized P2P market framework for the islanded microgrid. In this framework, there is an MCU to monitor the operation of the P2P market among the agents. In this context, for the sake of simplicity, the sets $N=\{1,2,\ldots,n\}$ and $T=\{1,2,\ldots,t\}$ are defined for agents and time intervals, respectively. The notation *n* represents the number of the

agent, and *t* shows the number of the time interval throughout the paper.

2.2. Modeling Cost Functions of Distributed Generations

2.2.1. Cost functions of PV and WT units

Since PVs and WTs have only the maintenance and operation costs, their cost functions will be obtained as follows.

$$C_n^{pv}(P_{n,t}^{pv}) = \alpha_n^{pv} \cdot P_{n,t}^{pv} \quad (1)$$

$$C_n^{wt}(P_{n,t}^{wt}) = \alpha_n^{wt} \cdot P_{n,t}^{wt} \quad (2)$$

$$P_{n,t}^{pv} \le P_n^{pv,\max}, P_{n,t}^{wt} \le P_n^{wt,\max} \quad (3)$$

where C_n^{pv}, $P_{n,t}^{pv}$, α_n^{pv}, and $P_n^{wt,\max}$ are the total cost of utilizing PV, the PV's generated power amount, the maintenance and operation cost per unit of $P_{n,t}^{pv}$, and the maximum generation limit of the PV, respectively. Note that C_n^{wt}, $P_{n,t}^{wt}$, α_n^{wt}, and $P_n^{wt,\max}$ are similarly total cost, power generation, operating cost per unit, and maximum power generation associated with wind power units at node *n*.

2.2.2. The cost function of FC

Since FCs utilize fuel for the generation of electricity, their cost functions are mainly dependent on the fuel price, which is obtained as follows.

$$C_n^{fc}(P_{n,t}^{fc}) = (\frac{\pi^{fc}}{L^{fc}\eta_n^{fc}} + \alpha_n^{fc})P_{n,t}^{fc} \quad (4)$$

$$P_n^{fc,\min} \le P_{n,t}^{fc} \le P_n^{fc,\max} \quad (5)$$

where C_n^{fc}, $P_{n,t}^{fc}$, π^{fc}, L^{fc}, η_n^{fc}, and α_n^{fc} present the cost of the FC, the amount of power generation of the FC unit, the FC's fuel cost per m^3, the FC's generation amount per m^3 of fuel, efficiency, and maintenance and operation cost per unit of $P_{n,t}^{fc}$, respectively. Note that $P_n^{fc,\min}$ and $P_n^{fc,\max}$ demonstrate the minimum and maximum generation capability of the FC unit, respectively [19].

2.2.3. The cost function of MT

Similar to the FCs, MTs' cost functions are highly dependent on their fuel prices. Therefore, their cost could be calculated as follows:

$$C_n^{mt}(P_{n,t}^{mt}) = (\frac{\pi^{mt}}{L^{mt}\eta_n^{mt}} + \alpha_n^{mt})P_{n,t}^{mt} \quad (6)$$

$$P_n^{mt,\min} \le P_{n,t}^{mt} \le P_n^{mt,\max} \quad (7)$$

where C_n^{mt}, $P_{n,t}^{mt}$, π^{mt}, L^{mt}, η_n^{mt}, α_n^{mt}, $P_n^{mt,\min}$, and $P_n^{mt,\max}$ are the cost of the MT, power generation amount of the MT unit, the MT's fuel cost per m^3, generation amount of the MT per m^3 of fuel, MT efficiency, maintenance and operation cost per unit of $P_{n,t}^{mt}$, the minimum generation capability of the MT unit, and its maximum capability, respectively [19].

2.2.4. The cost function of CHP

As both the generated heat and the electric power are used in CHP units, the cost function of a CHP unit is like the MT units, but with higher efficiency. In this respect, the related cost function could be extracted as below:

$$C_n^{chp}(P_{n,t}^{chp}) = \left[\frac{\pi^{mt}}{L^{mt}\eta_n^{mt}}\left(1 - \frac{\xi_n^{rec}(\eta_n^{chp} - \eta_n^{e})}{\eta_n^{b}}\right) + \alpha_n^{chp}\right]P_{n,t}^{chp} \quad (8)$$

$$P_n^{chp,\min} \le P_{n,t}^{chp} \le P_n^{chp,\max} \quad (9)$$

where C_n^{chp}, $P_{n,t}^{chp}$, α_n^{chp}, $P_n^{chp,\min}$, and $P_n^{chp,\max}$ represent the cost of the CHP, the amount of power generation of the CHP unit, the maintenance and operation cost per unit of $P_{n,t}^{chp}$, the minimum generation capability of the CHP unit, and its maximum capability, respectively. Furthermore, π^{mt}, L^{mt}, and η_n^{mt} show the MT's parameters that are utilized inside the CHP system, ξ_n^{rec} is the factor of heat recovery, and η_n^{chp}, η_n^{e}, and η_n^{b} denote the efficiencies of the CHP, MT, and boiler, respectively [19].

2.2.5. The cost function of DG

DGs consume diesel fuel to produce energy, and their costs are modeled by a quadratic function as follows [20].

$$C_n^{dg}(P_{n,t}^{dg}) = a_n(P_{n,t}^{dg})^2 + (b_n + \alpha_n^{dg})P_{n,t}^{dg} + c_n \quad (10)$$

$$P_n^{dg,\min} \le P_{n,t}^{dg} \le P_n^{dg,\max} \quad (11)$$

where C_n^{dg}, $P_{n,t}^{dg}$, α_n^{dg}, $P_n^{dg,\min}$, and $P_n^{dg,\max}$ are the cost of the DG, the power generation amount of the DG unit, the maintenance and operation cost per unit of $P_{n,t}^{dg}$, the minimum generation capability of the DG unit, and its maximum capability, respectively. Moreover, a_n, b_n, and c_n are the fixed constants modeling the cost function of the DG unit. It is noteworthy that in the case of existing multiple DGs, they can be mathematically modeled as an equivalent DG according to [21].

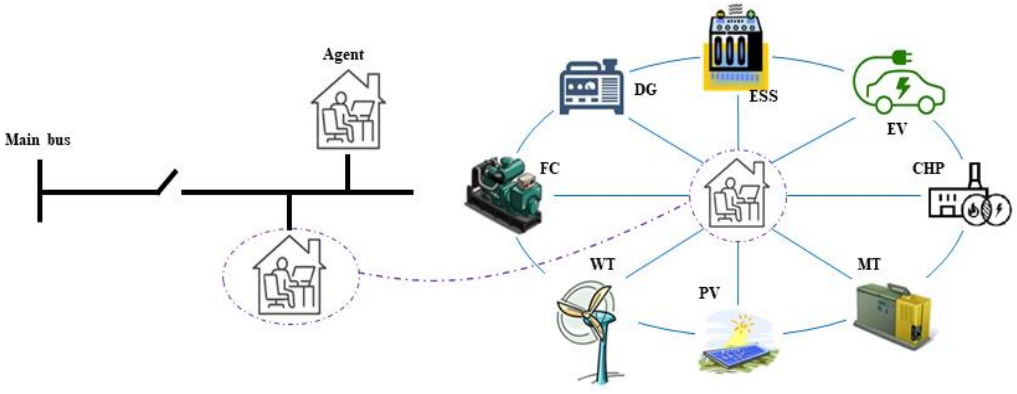

Fig. 1: A simplified model of a multi-agent structured microgrid.

2.3. Modeling Overall Cost Function of Agents

In the proposed P2P model, agents should make some decisions about the amount of power they want to buy/sell. Therefore, they need to extract their overall cost function to utilize it in their respective optimization problem. In this regard, this section develops the overall cost function associated with each agent based upon their different kinds of resources.

2.3.1. The cost function of distributed generations

As was already explained, the agents can have six types of generation units. In this regard, the total cost of the generation units in each agent is modeled as follows:

$$C_{n,t}^{gen} = \sum_{d \in D} G_{nd} \cdot C_n^d (P_{n,t}^d) \tag{12}$$

where $C_{n,t}^{gen}$ is the overall generation cost and G_{nd} is a binary parameter that determines whether or not agent *n* has the generation type *d*.

2.3.2. The cost function of ESS

Agents can also enjoy the ESS to increase their flexibility against the price spikes. In this context, the ESS's cost can be modeled as follows:

$$C_{n,t}^{ess} = \mu_n^{ess,c} P_{n,t}^{ess,c} \Delta t + \mu_n^{ess,d} P_{n,t}^{ess,d} \Delta t \tag{13}$$

$$0 \le P_{n,t}^{ess,c} \le P_{n,\max}^{ess,c}, 0 \le P_{n,t}^{ess,d} \le P_{n,\max}^{ess,d} \tag{14}$$

$$E_{n,t}^{ess} = E_{n,t-1}^{ess} + \eta_n^{ess,c} P_{n,t}^{ess,c} \Delta t - \eta_n^{ess,d} P_{n,t}^{ess,d} \Delta t \tag{15}$$

$$EL_{n,\min}^{ess} E_{n,cap}^{ess} \le E_{n,t}^{ess} \le EL_{n,\max}^{ess} E_{n,cap}^{ess} \tag{16}$$

where $C_{n,t}^{ess}$, $P_{n,t}^{ess,c}$, $P_{n,t}^{ess,d}$, $\mu_n^{ess,c}$, and $\mu_n^{ess,d}$ are the ESS's total cost, charging/discharging power, and the amortized costs of charging/discharging, respectively. Moreover, $P_{n,\max}^{ess,c}$, $P_{n,\max}^{ess,d}$, $E_{n,t}^{ess}$, $\eta_n^{ess,c}$, and $\eta_n^{ess,d}$ demonstrate the maximum limit of charging/discharging, the energy level of the ESS, and the charging/discharging efficiency, respectively. Finally, $EL_{n,\min}^{ess}$, $EL_{n,\max}^{ess}$, and $E_{n,cap}^{ess}$ indicate the ESS's minimum and maximum percent of energy level that ensures ESS's lifetime and models the capacity of ESS [6]. It should be noted that in (15), $\eta_n^{ess,c} \le 1$ while $\eta_n^{ess,d} \ge 1$.

2.3.3. The cost function of EV

Similar to ESSs, the cost function of EVs can be modeled as follows:

$$C_{n,t}^{ev} = \mu_n^{ev,c} P_{n,t}^{ev,c} \Delta t + \mu_n^{ev,d} P_{n,t}^{ev,d} \Delta t \tag{17}$$

$$0 \le P_{n,t}^{ev,c} \le P_{n,\max}^{ev,c}, 0 \le P_{n,t}^{ev,d} \le P_{n,\max}^{ev,d} \tag{18}$$

$$E_{n,t}^{ev} = E_{n,t-1}^{ev} + \eta_n^{ev,c} P_{n,t}^{ev,c} \Delta t - \eta_n^{ev,d} P_{n,t}^{ev,d} \Delta t \tag{19}$$

$$EL_{n,\min}^{ev} E_{n,cap}^{ev} \le E_{n,t}^{ev} \le EL_{n,\max}^{ev} E_{n,cap}^{ev} \tag{20}$$

where $C_{n,t}^{ev}$, $P_{n,t}^{ev,c}$, $P_{n,t}^{ev,d}$, $\mu_n^{ev,c}$, and $\mu_n^{ev,d}$ are the EV's total cost, charging/discharging power, and the amortized costs of charging/discharging, respectively. Additionally, $P_{n,\max}^{ev,c}$, $P_{n,\max}^{ev,d}$, $E_{n,t}^{ev}$, $\eta_n^{ev,c} \le 1$, and $\eta_n^{ev,d} \ge 1$ represent the maximum limit of charging/discharging, the energy level of the EV, and the charging/discharging efficiency, respectively. Finally, $EL_{n,\min}^{ev}$, $EL_{n,\max}^{ev}$, and $E_{n,cap}^{ev}$ indicate the EV's minimum and maximum percent of energy level that ensures the EV's lifetime and the capacity of EV. It is worth noting that $P_{n,t}^{ev,c}$ and $P_{n,t}^{ev,d}$ are the charging/discharging amount of EV only when it is available, while the availability of an EV is defined as the connectivity of the EV to the grid. An EV unit can be operated as vehicle-to-grid (V2G), grid-to-vehicle (G2V) while connecting to the grid. Without loss of generality, it is assumed that the EV unit can merely be connected to the grid when it is at home. In this regard, when an EV arrives at home at t_{arrive}, its energy level is considered to be $EL_{n,arrive}^{ev}$. Moreover, when the unit wants to exit from the home at the time interval t_{exit}, its energy level is assumed to be shown by $EL_{n,exit}^{ev}$. These constraints are mathematically modeled as:

$$E_{n,t_{arrive}}^{ev} = EL_{n,arrive}^{ev} \tag{21}$$

$$E_{n,t_{exit}}^{ev} \ge EL_{n,exit}^{ev} \tag{22}$$

2.3.4. Utility function of agents

In this scheme, the cost of the loads in each agent is modeled using a utility function defined as follows:

$$U_{n,t} = \begin{cases} \beta_{n,t} P_{n,t}^{load} - \frac{\gamma_n}{2} (P_{n,t}^{load})^2 & 0 \le P_{n,t}^{load} \le \frac{\beta_{n,t}}{\gamma_n} \\ \frac{1}{2} \frac{(\beta_{n,t})^2}{\gamma_n} & \frac{\beta_{n,t}}{\gamma_n} \le P_{n,t}^{load} \end{cases} \tag{23}$$

$$P_n^{load,\min} \le P_{n,t}^{load} \le P_n^{load,\max} \tag{24}$$

where $U_{n,t}$ is the utility earned by agent *n* and $\beta_{n,t} > 0$ and $\gamma_n > 0$ are the parameters of consumption. Moreover, $P_{n,t}^{load}$ is the amount of power consumption, which should be greater than the minimum need of the agent (i.e. $P_n^{load,\min}$) and less than the maximum consumption of agent (i.e. $P_n^{load,\max}$) [7, 22].

2.3.5. Trading cost function

In the proposed P2P framework, every agent can trade a favorite amount of power with other agents. Therefore, each agent will earn profits if it sells energy, while the agent will pay the cost of the energy if it buys energy. In this respect, the cost function of each agent can be formulated as follows.

$$C_{n,t}^{trad} = \left(\sum_{i \in N} \pi_{i,t} P_{in,t}^{buy} \right) - \pi_{n,t} P_{n,t}^{\sup} \tag{25}$$

where $C_{n,t}^{trad}$, $\pi_{n,t}$, $P_{in,t}^{buy}$, and $P_{n,t}^{\sup}$ are the trading costs, price of power, power amount that agent *n* wants to buy from agent *i*, and the power amount that agent *n* wants to sell. There are also some constraints for this cost function as follows:

$$P_{in,t}^{buy} \ge 0, P_{n,t}^{\sup} \ge 0 \tag{26}$$

$$P_{nn,t}^{buy} = 0 \tag{27}$$

$$P_{n,t}^{buy} \cdot P_{n,t}^{\sup} = 0 \tag{28}$$

These constraints demonstrate that all amount of power purchased or sold should be positive (26), nobody trades with itself (26), and an agent cannot be a buyer and a seller simultaneously (28). It is noteworthy that the constraint (28) can also be written as (29) which causes the running time of

the optimization stage in the simulation to be decreased significantly.

$$P_{n,t}^{buy} + P_{n,t}^{\sup} = \left| P_{n,t}^{buy} - P_{n,t}^{\sup} \right| \quad (29)$$

2.3.6. Total cost function in the current time interval

To derive an overall cost function for the agent *n* in the current time interval (i.e., *t*), all of the previously discussed cost functions are simply added up as follows. It is noteworthy that here it is hypothesized that *t* is the current time interval that the P2P market is conducted for real-time operation of the microgrid.

$$C_{n,t}^{now} = C_{n,t}^{gen} + C_{n,t}^{ess} + C_{n,t}^{ev} - U_{n,t} + C_{n,t}^{trad} \quad (30)$$

2.3.7. MPC method

In the designed P2P market, agents need to decide about the operation of their ESSs and EVs, as well as their generation units. In this regard, to determine the optimum charging/discharging of ESSs/EVs, the operational information of the current time interval is not sufficient. So, the agent estimates its PV/WT power generation, power consumption, purchasing/selling power, and power prices of next upcoming time intervals to realize the optimum charging/discharging amounts at the considered time intervals [23]. The concept that employs operational scheduling of the agent in future time intervals while participating in the P2P market at the current time interval is called the MPC method. In this work, it is assumed that all the agents anticipate the next H time intervals. In this context, it is necessary to consider a cost function for future time intervals [24] as follows:

$$C_{n,h}^{fut} = C_{n,h}^{gen} + C_{n,h}^{ess} + C_{n,h}^{ev} - U_{n,h} + \pi_h^{fut} P_{n,h}^{fut,buy} \quad (31)$$

where $C_{n,h}^{fut}$, π_h^{fut}, and $P_{n,h}^{fut,buy}$ are the total cost, the predicted average power price, and the amount of power that the agent wants to buy at the future time interval *h*. Note that, in this model, $P_{n,h}^{f,buy}$ is considered to be either negative or positive; negative amounts imply the selling power, and positives imply the purchasing power.

2.4. P2P Market Structure

The corresponding flowchart of the proposed P2P market is shown in Fig. 2. According to this flowchart, the first step is the initialization of prices, which means that all the agents should announce their initial price. Agents can select their respective initial prices based on their prediction of the agents' behavior. Note that as the scheme proceeds, the agents may reconsider their positions as sellers, which means that they will not benefit from power selling. In other words, as the framework proceeds, the buyers will automatically be separated from the sellers. On the other hand, in the model, an agent cannot be both seller and buyer simultaneously.

After the price initializations, the agents run an optimization problem to decide about their power exchanges with the other agents in the market. In the next step, the agents update the prices, and then a termination criterion is checked. If the criterion is satisfied, the market will be cleared and the exchanges will be fixed; otherwise, the same process will be conducted until the criterion is satisfied. These steps are explained in the next subsections as follows.

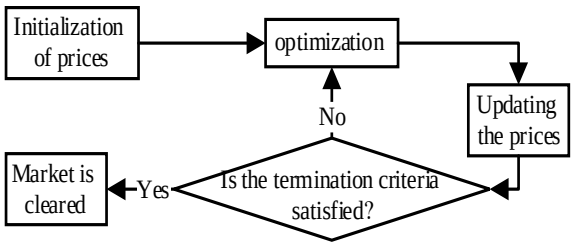

Fig. 2: The flowchart of the proposed P2P market in an islanded multi-agent microgrid.

2.4.1. Optimization problem of Agents

The optimization problem of agent *n* aimed to minimize its prices is described as follows.

$$Min\left\{ C_{n,t}^{now} + \sum_{h=t+1}^{t+H} C_{n,h}^{fut} \right\} \quad (34)$$

which is subject to the predefined constraints of (3), (5), (7), (9), (11), (14), (16), (18), (20) to (22), (24), (26), (27), and (29). Moreover, the power balance constraint for the current time interval and the future time intervals can be modeled as follows:

$$\sum_{d\in D} G_{nd} P_{n,t}^{d} = P_{n,t}^{load} - P_{n,t}^{buy} + P_{n,t}^{\sup} + P_{n,t}^{ess,c} - P_{n,t}^{ess,d} + P_{n,t}^{ev,c} - P_{n,t}^{ev,d} \quad (35)$$

$$\sum_{d\in D} G_{nd} P_{n,t}^{d} = P_{n,t}^{load} - P_{n,t}^{fut,buy} + P_{n,t}^{ess,c} - P_{n,t}^{ess,d} + P_{n,t}^{ev,c} - P_{n,t}^{ev,d} \quad (36)$$

2.4.2. Updating the prices

After conducting agents' optimizations, the power demand of agent *n*, or the requested amount from him/her (i.e., $P_{n,t}^{dem}$), as well as the total power amount that he/she wants to sell (i.e., $P_{n,t}^{\sup}$), will be determined. Having the demand and supply amounts, the agents update their prices according to the following equation:

$$\pi_{n,t}(j+1) = \pi_{n,t}(j) + \varphi\left[P_{n,t}^{dem}(j) - P_{n,t}^{\sup}(j) \right] \quad (37)$$

where *j* is the iteration index, $\pi_{n,t}$ is the price of agent *n*, and φ is the factor of progression pace.

It is noteworthy to mention that the power demand of agent *n* would be calculated easily by summing up all the buy amounts requested from agent *n* in each iteration as the following equation shows.

$$P_{n,t}^{dem}(j) = \sum_{m\in N} P_{nm,t}^{buy}(j) \quad (38)$$

2.4.3. The termination criterion

To ensure the convergence of the proposed iterative P2P market framework, a suitable criterion should be defined. In this regard, if the prices of the agents do not change in every iteration, it means that nobody wants to alter his/her buy/sell amount, and all of the agents are satisfied by the power exchanges. This optimum point will also address the criteria associated with the Nash equilibrium concept. Consequently, the termination criterion is defined as follows:

$$\left| \pi_{n,t}(j+1) - \pi_{n,t}(j) \right| < \varepsilon \quad (39)$$

where ε is a small number that the price variation under this value is negligible.

3. Case Study

The proposed structure has been simulated on a small 15-bus microgrid (MG) demonstrated in Fig. 3. It is assumed that the MG is operated in an islanded mode and each node of the system is considered to be managed by one agent. Moreover, the time intervals in the operational management of the system are considered to be equal to one hour. Fig. 3 also indicates the resources operated by each agent in the P2P market framework. The simulation has been conducted for 24 hours a day considering $H=8$, which means that the agents take into account the next 8 hours in their optimization for the current time interval.

The optimal purchased/sold power by agents 4, 5, 10, and 12, as a sample of agents, over 24 hours are shown in Fig. 4 in which there are both buyers and sellers in every hour of the day. In this figure, agent 4 is a seller, and agent 10 is a buyer all over the 24 hours, but agents 5 and 12 are buyers in some hours and sellers in others. In Fig. 5, the total power exchange amounts between agents over 24 hours are depicted as a Chord diagram. It should be mentioned that for the sake of simplicity, only the total exchanges that are greater than 20 kW are shown in this figure.

In the 24-hour simulation, agent 5 has been selected as an example to investigate its scheduling results over the 24 hours. In this regard, Fig. 6 shows the power generation amounts for each type of distributed generation unit that agent 5 possesses in 24 hours. Moreover, Fig. 7 demonstrates the load consumption amounts of agent 5, and Fig. 8 depicts the average price of seller agents in 24 hours of the day. Note that the MG is operated in the islanded mode, so the energy prices are significantly high in some hours due to generation shortage according to Fig. 8.

Figs. 9 and 10 show the power charging/discharging amounts of agent 5's ESS and EV at each hour of the day, respectively. It is noteworthy that in Fig. 9, the charging/discharging amounts of the EV are shown only when it is available or connected to the grid. Therefore, as the availability hours of this EV are assumed to be in the range of [1,6] and [22,24] in this simulation, the discharge amounts in the other hours are not shown in the figure.

In order to justify the behavior of agent 5 about the charging/discharging amounts of his ESS/EV, it is important to represent Fig. 11, which shows the predicted prices by the agent in 36 hours (one and a half days), noting that he/she always anticipates the prices of next 8 hours. As an example, when the current hour is the 12th hour, he/she uses real-time determined prices from the market as this hour's prices and predicts the average prices of the next 8 hours (i.e., from 13th hour to 20th), which are presented in Fig. 11, as the future hours' prices. Thus, according to this figure, the behavior of agent 5 in Fig. 9 and 10 can be grasped. For instance, when the current time interval is equal to one, he/she does not charge his/her ESS because the current prices' average is nearly 25 and he/she predicts that in hours 4 to 6, the prices will be less than 25. Note that he/she does not discharge his/her ESS because it is assumed that the ESS's initial charge amount and also $E^{ess}_{5,\min}$ are equal to 20%. The ESS in the 2nd hour has a similar scenario, but in the 3rd hour, since the current prices' average is much less than his/her next-8-hour prediction amounts, he/she charges his/her ESS with the maximum charge rate which is postulated to be 6 kW per hour. The ESS charge/discharge behavior of the agent in the

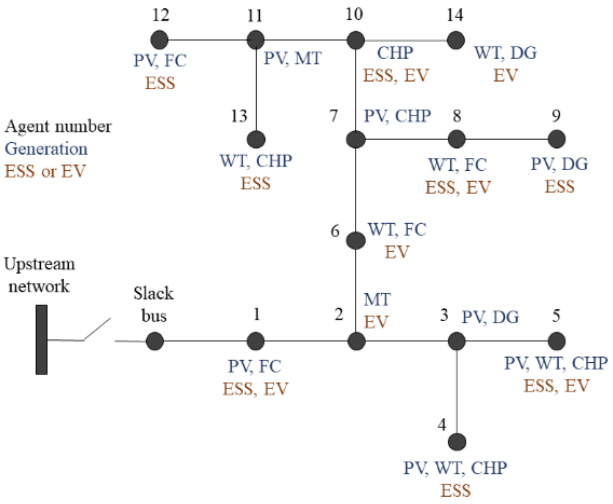

Fig. 3: The islanded microgrid with multi-agent structure considered as a test system.

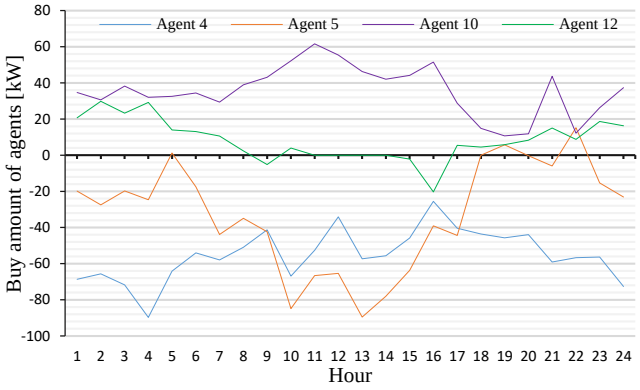

Fig. 4: Purchased/sold power by a sample of agents in 24 hours.

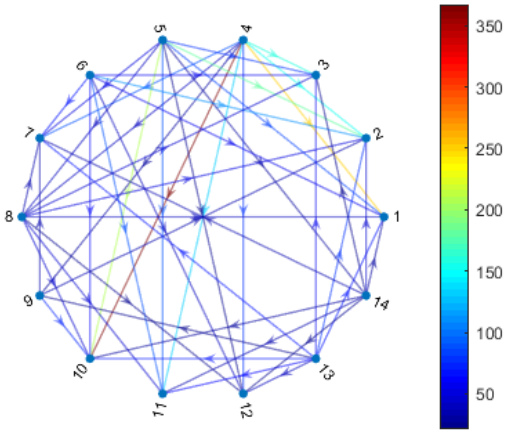

Fig. 5: Chord diagram of the total power exchanges between the agents in kW.

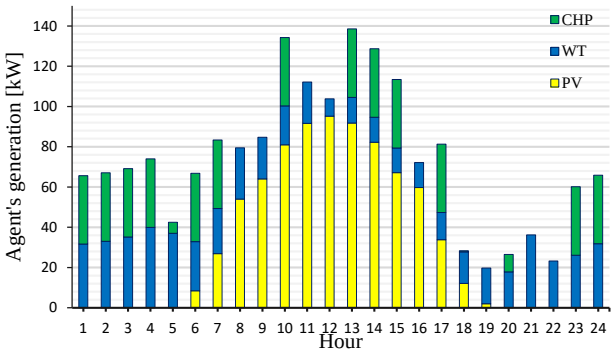

Fig. 6: Power generation amounts of agent 5 in 24 hours.

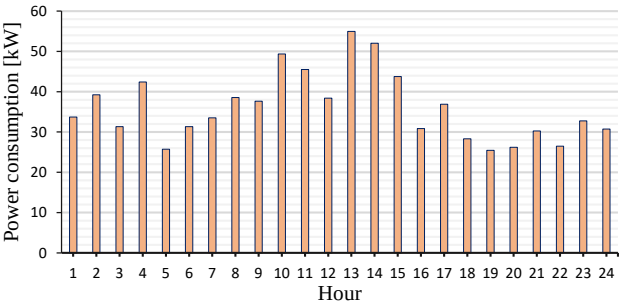

Fig. 7: Consumption power amounts of agent 5 in 24 hours.

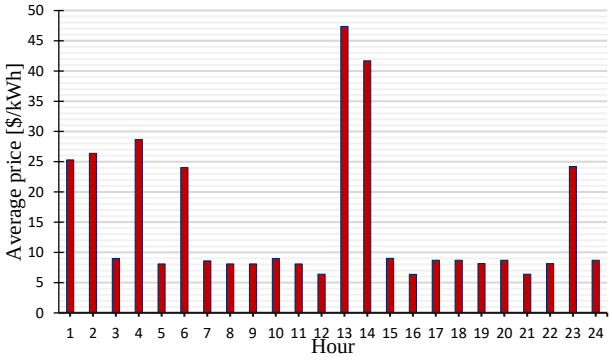

Fig. 8: The seller agents' average energy prices in 24 hours

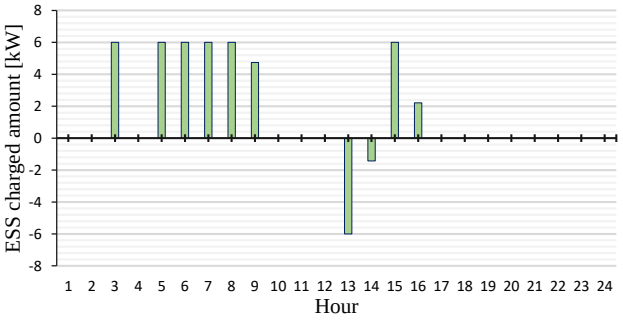

Fig. 9: Charging/discharging amounts of agent 5's ESS.

other hours can be justified similarly.

About the EV of agent 5, it is assumed that the initial EV charge is 10%, $EL^{ev}_{5,exit} = 0.85$, $E^{ev}_{5,cap} = 70kWh$, $\eta^{ev,d}_{5} = 1.05$, and he/she exits home after the 6th hour.

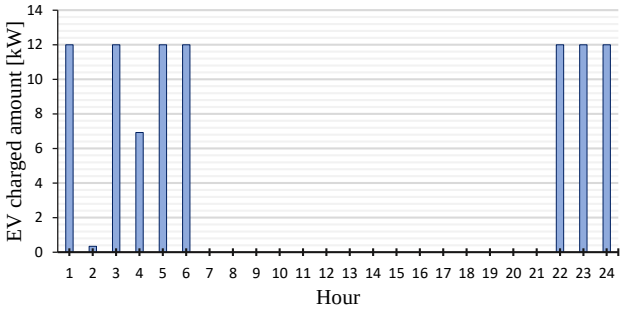

Fig. 10: Charging/discharging amounts of agent 5's EV.

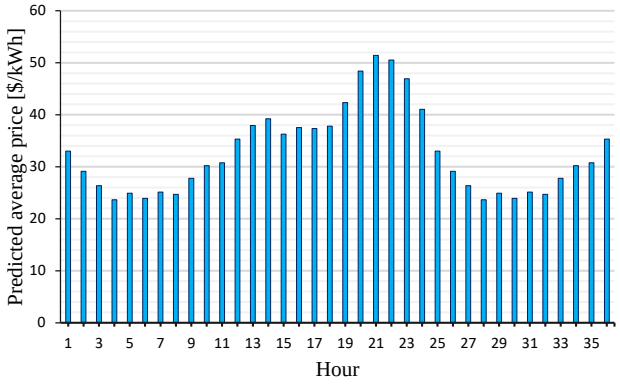

Fig. 11: Average power prices of future hours predicted by agent 5.

Therefore, his/her total charge amount of EV from the 1st to 6th hours should be equal to $(0.85-0.1)\times 70\times 1.05 = 55.125kWh$ which coincides with the amounts shown in Fig. 10. For the justification of EV charge/discharge amounts in Fig. 10, an argument similar to the ESS's charge/discharge amounts can be done. It is noteworthy to mention that although the discharge ability is enabled for agent 5, he/she did not discharge any amount of power in any hours of the day, according to Fig. 10. This is because, in the period of $[1,6]$ hours, he/she does not have any opportunities to discharge his EV due to the high amount of charge that he/she should do in total till the end of the 6th hour (i.e., $55.125kWh$). Moreover, in the period of [22,24], according to the prices shown in Figs. 8 and 11, it is beneficial for agent 5 to charge his/her EV at its maximum rate (which is assumed to be 12 kW per hour) because the energy prices in the current hours are less than the future hours in his/her opinion.

For the sake of investigating the convergence status of the prices in the proposed model, the prices of the agents 5, 6, 9, and 12 at the 15th hour are represented in Fig. 12 in all iterations. These agents have been selected as a sample of sellers at the 15th hour. According to this figure, the mentioned agents' prices have been converged appropriately through 756 iterations into $9\$/kWh$ approximately.

It should be noted that, as Fig. 12 shows, the converged prices of the mentioned agents are almost equal to each other. To find out the reason behind this, two cases are remarkable. First, if a seller agent rises his price into a value more than the others' prices, the buyer agents will decrease their purchase amounts from him/her, thus he/she has to decrease his/her

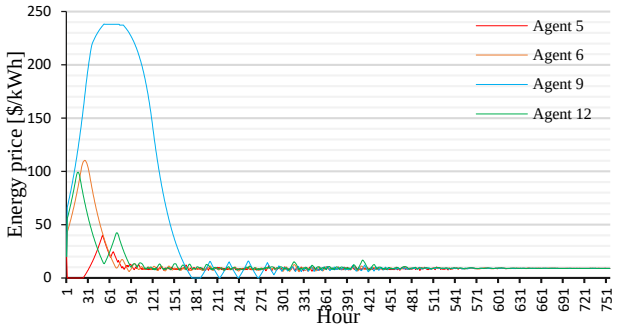

Fig. 12: The prices of a sample of sellers at the 15th hour in all iterations.

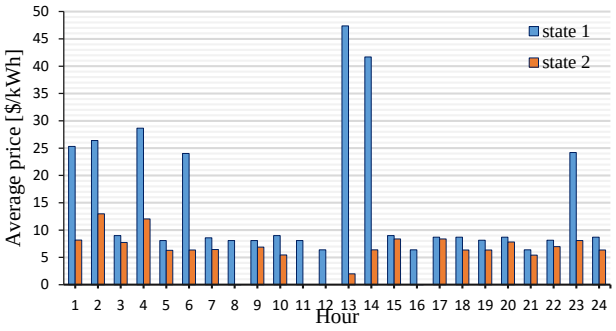

Fig. 13: Sellers average prices in 24 hours in states 1 and 2.

price again. Second, if the seller decreases his/her price to a value less than the others' prices, although the buyers will be motivated to buy more power amounts from him/her, this price will not be the optimum value for him/her because he/she will earn fewer benefits compared to the case that his/her price is just a little lower than the others. Therefore, the sellers will compete with each other and their final prices will be similar.

In addition to the aforementioned 24-hour simulation, named state 1 in this section, another similar simulation has been run for 24 hours, in which the values of $\beta_{n,t}$ for all agents in all hours have been decreased by 30% to analyze the sensitivity of prices to the values of $\beta_{n,t}$. In this context, the new simulation is named state 2. The averages of the sellers' prices for both state 1 and state 2 in 24 hours are shown in Fig. 13. As can be seen in the figure, the amounts of state 2 are lower than those of state 1 because when the amounts of $\beta_{n,t}$ decrease, the demand of seller agents diminishes. Thus, the prices come down due to the dominance of supply amounts over the demand amounts. In some hours such as the 8th and 11th, the energy prices are zero, which shows that the overall supply is much greater than the demand.

4. Conclusion

This paper provided a P2P framework to facilitate energy management in a multi-agent microgrid operating in the islanded mode. The proposed framework enables the power exchange among independent agents while addressing the privacy concern of private customers. Furthermore, it is considered that each agent can operate load demands, different kinds of distributed generation units, ESSs, and EVs, which will improve the flexibility of the agents participating in the P2P scheme. Finally, the proposed scheme is applied to a microgrid composed of nine agents operating different resources to investigate its effectiveness in islanded operating mode with a distributed structure.

CRediT Authorship Contribution Statement

Mahyar Tofighi-Milani: Data curation, Formal analysis, Investigation, Methodology, Resource, Software, Validation, Roles/Writing - original draft. **Sajjad Fattaheian-Dehkordi:** Conceptualization, Data curation, Methodology, Project administration, Validation. **Mahmud Fotuhi-Firuzabad:** Supervision, Writing - review & editing.

Declaration of Competing Interest

The authors declare that they have no known competing financial interests or personal relationships that could have appeared to influence the work reported in this paper. The ethical issues; including plagiarism, informed consent, misconduct, data fabrication and/or falsification, double publication and/or submission, redundancy has been completely observed by the authors.

References

[1] H. Wang, and J. Huang, "Incentivizing energy trading for interconnected microgrids," *IEEE Trans. Smart Grid*, vol. 9, no. 4, pp. 2647–2657, 2016.

[2] M. W. Khan, and J. Wang, "The research on multi-agent system for microgrid control and optimization," *Renew. Sustain. Energy Rev.*, vol. 80, pp. 1399–1411, 2017.

[3] F. Khavari, A. Badri, A. Zangeneh, and M. Shafiekhani, "A comparison of centralized and decentralized energy-management models of multi-microgrid systems," in *2017 Smart Grid Conference*, Dec. 2017, pp. 1–6.

[4] S. Fattaheian-Dehkordi, M. Tavakkoli, A. Abbaspour, M. Fotuhi-Firuzabad, and M. Lehtonen, "An incentive-based mechanism to alleviate active power congestion in a multi-agent distribution system," *IEEE Trans. Smart Grid*, 2020, to be published.

[5] A. Anvari-Moghaddam, A. Rahimi-Kian, M. S. Mirian, and J. M. Guerrero, "A multi-agent based energy management solution for integrated buildings and microgrid system," *Appl. Energy*, vol. 203, pp. 41–56, 2017.

[6] S. Cui, Y. Wang, and J. Xiao, "Peer-to-Peer energy sharing among smart energy buildings by distributed transaction," *IEEE Trans. Smart Grid*, vol. 10, no. 6, pp. 6491–6501, 2019.

[7] Paudel, K. Chaudhari, C. Long, and H. B. Gooi, "Peer-to-Peer energy trading in a prosumer-based community microgrid: A game-theoretic model," *IEEE Trans. Ind. Electron.*, vol. 66, no. 8, pp. 6087–6097, 2019.

[8] J. Lee, J. Guo, J. K. Choi, and M. Zukerman, "Distributed energy trading in microgrids: a game-theoretic model and its equilibrium analysis," *IEEE Trans. Ind. Electron.*, vol. 62, no. 6, pp. 3524–3533, 2015.

[9] M. Khorasany, Y. Mishra, and G. Ledwich, "Peer-to-peer market clearing framework for DERs using knapsack approximation algorithm," in *2017 IEEE PES Innovative Smart Grid Technologies Conference Europe*, pp. 1–6.

[10] Y. Liu, L. Wu, and J. Li, "Peer-to-peer (P2P) electricity trading in distribution systems of the future," *The Electricity Journal*, vol. 32, no. 4, pp. 2–6, 2019.

[11] Z. Wang, X. Yu, Y. Mu, and H. Jia, "A distributed Peer-to-Peer energy transaction method for diversified prosumers in urban community microgrid system," *Appl. Energy*, vol. 260, 114327, 2020.

[12] A. Paudel and G. H. Beng, "A hierarchical Peer-to-Peer energy trading in community microgrid distribution systems," in *2018 IEEE Power & Energy Society General Meeting*, Aug. 2018, pp. 1–5.

[13] N. Wang, W. Xu, Z. Xu, and W. Shao, "Peer-to-peer energy trading among microgrids with multidimensional willingness," *Energies*, vol. 11, no. 12, 3312, 2018.

[14] J. Hu, Q. Sun, and F. Teng, "A game-theoretic pricing model for energy internet in day-ahead trading market considering distributed generations uncertainty," in *2016 IEEE Symposium Series on Computational Intelligence*, 2016, pp. 1–7.

[15] Y. Wang, W. Saad, Z. Han, H. V. Poor, and T. Başar, "A game-theoretic approach to energy trading in the smart grid," *IEEE Trans. Smart Grid*, vol. 5, no. 3, pp. 1439–1450, 2014.

[16] S. Fattaheian-Dehkordi, M. Tavakkoli, A. Abbaspour, M. Fotuhi-Firuzabad, and M. Lehtonen, "Distribution Grid Flexibility-ramp Minimization using Local Resources" in *2019 IEEE PES Innovative Smart Grid Technologies Europe*, Oct. 2019, pp. 1–5.

[17] S. Fattaheian-Dehkordi, M. Tavakkoli, A. Abbaspour, M. Fotuhi-Firuzabad, and M. Lehtonen, "incentive-based ramp-up minimization in multi-microgrid distribution systems," in *2020 IEEE PES Innovative Smart Grid Technologies Europe*, 2020, pp. 839–843.

[18] F. Kamrani, S. Fattaheian-Dehkordi, A. Abbaspour, M. Fotuhi-Firuzabad, and M. Lehtonen, "Investigating the impacts of microgrids and gas grid interconnection on power grid flexibility," in *2019 Smart Grid Conference*, Dec. 2019, pp. 1–6.

[19] N. Nikmehr, and S. Najafi Ravadanegh, "Optimal power dispatch of multi-microgrids at future smart distribution grids," *IEEE Trans. Smart Grid*, vol. 6, no. 4, pp. 1648–1657, 2015.

[20] F. Mohamed, and H. Koivo, "System modelling and online optimal management of microgrid with battery storage," in *6th Int. Conf. Renew. Energ. Power Qual.*, vol. 1, Mar. 2007.

[21] J. J. Grainger, W. D. Stevenson, and W. D. Stevenson, *Power system analysis*. Mc Graw Hill Education, 2003.

[22] P. Samadi, A. Mohsenian-Rad, R. Schober, V. W. S. Wong, and J. Jatskevich, "Optimal real-time pricing algorithm based on utility maximization for smart grid," in *2010 First IEEE International Conference on Smart Grid Communications*, Oct. 2010, pp. 415–420.

[23] S. Fattaheian-Dehkordi, A. Fereidunian, H. Gholami-Dehkordi, and H. Lesani, "Hour-ahead demand forecasting in smart grid using support vector regression (SVR)," *Int. Trans. Electr. Energy Syst.*, vol. 24, no. 12, pp. 1650-1663, 2014.

[24] F. Arasteh, and G. H. Riahy, "MPC-based approach for online demand side and storage system management in market based wind integrated power systems," *Int. J. Electr. Power Energy Syst.*, vol. 106, pp. 124–137, 2019.

BIOGRAPHY

Mahyar Tofighi-Milani received his B.Sc. degree in electrical engineering from the Iran University of Science and Technology (IUST), Tehran, Iran in 2018. He is currently an M.Sc. student in electrical engineering, power systems, at the Sharif University of Technology, Tehran. His research interests are smart grids, electricity markets, renewable and distributed energy resources, and microgrids.

Sajjad Fattaheian-Dehkordi received his M.Sc. degree in electrical engineering, power systems, from the Sharif University of Technology, Tehran, Iran in 2014. Currently, he is completing his Ph.D. in electrical engineering, power systems, at the Sharif University of Technology and Aalto University, Espoo, Finland. His research interests include power systems planning, operations, and economics, with a focus on issues relating to the integration of renewable energy resources in the system.

Mahmud Fotuhi-Firuzabad (F'14) received the B.Sc. degree in electrical engineering from the Sharif University of Technology, Tehran, Iran, in 1986, the M.Sc. degree in electrical engineering from Tehran University, Tehran, Iran in 1989, and the M.Sc. and Ph.D. degrees in electrical engineering from the University of Saskatchewan, Saskatoon, SK, Canada, in 1993 and 1997, respectively. Currently, he is a professor and the president of the Sharif University of Technology. Dr. Fotuhi-Firuzabad is a member of the Center of Excellence in Power System Management and Control. He serves as an editor in the IEEE Transactions on Smart Grid.

Copyrights
© 2021 Licensee Shahid Chamran University of Ahvaz, Ahvaz, Iran. This article is an open-access article distributed under the terms and conditions of the Creative Commons Attribution –NonCommercial 4.0 International (CC BY-NC 4.0) License (http://creativecommons.org/licenses/by-nc/4.0/).

Shahid Chamran University of Ahvaz

Iranian Association of Electrical and Electronics Engineers

Journal of Applied Research in Electrical Engineering

E-ISSN: 2783-2864
P-ISSN: 2717-414X
Homepage: https://jaree.scu.ac.ir/

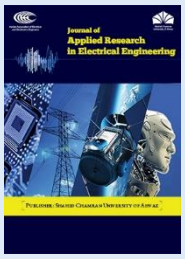

Research Article

Design and Parameter Estimation of Series Resonant Induction Heating Systems Using Self-Oscillating Tuning Loop

Behzad Jaafari, and Alireza Namadmalan *

Department of Electrical and Computer Engineering, Jundi-Shapur University of Technology, Dezful 64615-334, Iran

** Corresponding Author: namadmalan@jsu.ac.ir*

Abstract: This paper presents a design procedure and a new control method for power regulation of series resonant Induction Heating (IH) systems using a self-oscillating tuning loop. The proposed power regulator can accurately estimate the instantaneous phase angle and the main parameters of the resonant load. Moreover, the power control algorithm is devised based on a combination of Phase Shift (PS) and Pulse Density Modulation (PDM) methods. For simplicity, the tuning loop utilizes the PS control method for power regulation. Moreover, the Pulse Density Modulation (PDM) and frequency-sweep methods can be used in the proposed tuning loop. The new method is verified by a laboratory prototype with an output power of about 220 W and an operating frequency of about 60 kHz.

Keywords: Self-Oscillating tuning loops, induction heating systems, phase-shift control, series resonant inverters.

Article history
Received 13 March 2021; Revised 10 April 2021; Accepted 18 April 2021; Published online 30 June 2021.
© 2021 Published by Shahid Chamran University of Ahvaz & Iranian Association of Electrical and Electronics Engineers (IAEEE)

How to cite this article
B. Jaafari, and A. Namadmalan, "Design and parameter estimation of series resonant induction heating systems using self-oscillating tuning loop," *J. Appl. Res. Electr. Eng.*, vol. 1, no. 1, pp. 42-49, 2022.
DOI: 10.22055/jaree.2021.36904.1025

Check for updates

1. INTRODUCTION

Induction Heating (IH) systems play a fundamental role in modern heating systems such as annealing, hardening, and melting furnaces and cooking systems [1-7]. IH systems commonly require a medium- or high-frequency current or voltage source of power supply with fixed or variable frequencies. The resonant inverters are widely used to supply IH systems because of their near sinusoidal waveforms, less Electromagnetic Interference (EMI), and switching losses [3-5,7-9].

Two common types of resonant inverters are voltage source and current source inverters among which voltage source resonant inverters are commonly used due to their reliability and various controlling methods [2,4,10-12]. Resonant inverters are named after their resonant tank configuration, such as Series Resonant Inverters (SRIs), Parallel Resonant Inverters (PRI), and Series-Parallel Resonant Inverter (SPRI) [2,12,13]. Among the voltage source resonant inverters, SRIs are more common for IH systems as they have various control methods, more stability in frequency tuning, and simplicity in load estimation and regulation [15-19].

For SRIs, there are four common methods for power and frequency regulations, i.e., Frequency-Sweep (FS) [20], Phase-Shift (PS) control [2,21], Pulse Width Modulation (PWM) [12,22,23], and Pulse Density Modulation (PDM) [1,11,24-26]. FS methods require complex algorithms for uncertainties and load variations. Moreover, FS methods have a slow response time for power and frequency tuning. In PS, PWM, and PDM methods, the frequency tuning loop is based on Phase-Locked Loop (PLL) [7,11,27] or Self-Oscillating Switching (SOS) methods [5,10,28]. PLL circuits are sensitive to uncertainties and have stability problems, while SOS circuits have a fast response and are more reliable and uncertainty-tolerant [5].

Recently, SOS techniques have been proposed for power and frequency tuning loops of resonant converters due to their simple circuit and reliability in uncertainties. SOS methods have a quick response in frequency tuning and power regulation. Moreover, by developing SOS tuning loops, PDM, PS, and FS methods can be utilized in one of the switching frequency harmonics [5].

Besides the benefits of SOS methods, previous works have no straightforward design procedure for the tuning loop parameters. The aim of this paper is to present a design

procedure for the desired load variations and operating frequencies.

Moreover, this paper presents a new power regulation method based on the SOS tuning loops, which has a simple structure and estimates the load and its phase angle for an SRI instantly. The proposed control method is based on a combination of a first-order phase-shifter and PDM, which can properly regulate the output power [5].

One of the main problems associated with a well-designed power and frequency tuning loop is its robustness under uncertainties of the resonant tank. Typically, parameters of IH systems have tolerances of about 20%-50%, especially in their working coils. The presented solution can simply estimate the main parameters of the SRI at start-up duration for effective prediction and regulation of the power.

The presented analysis shows that the proposed method properly regulates power for practical deviations and errors in parameters' estimation. The new method estimates the instantaneous phase displacement of the load without phase detector circuits and reduces the time response and robustness of the tuning loop.

The paper is organized as follows. Section 2 presents the modeling of SRIs, the new tuning loop, and the design procedure. Section 3 discusses a power regulation method and parameters' estimation. Sections 4 and 5 present the experimental results and main conclusions of the paper.

2. System Modelling and Design Consideration

A schematic of a half-bridge SRI based on the SOS tuning loop is shown in Fig. 1, while the tuning loop can be applied for a full-bridge SRI. The main units of the tuning loop are a Current Transformer (CT), a lead phase-shifter, a Zero-Detector, a Micro Controller Unit (MCU), and logic gates.

For simplicity, the PS unit is considered a first-order leading phase shifter circuit that can properly make phase displacement, φ, up to $+45^0$. Phase displacement is controlled by changing a tuning resistor, R_T, implemented by a digital potentiometer connected to the MCU. The Zero-Detector unit is constructed by an ultra-fast comparator, LT1016, which improves the performance of the tuning loop at start-up cycles. As seen from Fig. 1, the gate driver of the SRI is based on the bootstrap technique, IR2104S, so the low side switch, S1, must be kept turn on before start-up to ensure the charging of the bootstrap capacitor.

At start-up, the high side switch, S2, is turned on and S1 is turned off, so a step voltage is applied to the series resonant load, and the resonant current, I_o, flows into the load. The start-up begins by enabling the MCU's starting signal, *Sig*, as connected to the AND gate. As is seen from Fig. 1, the phase of the measured current is made lead using the PS block shifts. The zero crossing of the PS unit changes the state of the power switches. At the first zero crossing, the state of the switches is changed and continuously repeats for the next cycles [5].

As described, the output voltage of the SRI, V_o, will be lead with respect to I_o with a phase displacement of φ at steady-state conditions. Hence, the PS block controls the output power by shifting the phase of the SRI. The following sections present the main equations of the SRI and the design procedure of the tuning loop.

2.1. SRI and Formulation

As shown in Fig. 1 and described in the SOS principle of operation, SRI generates square wave output voltage, V_o, with a duty cycle of about 50%. Equations of V_o, output current, I_o,

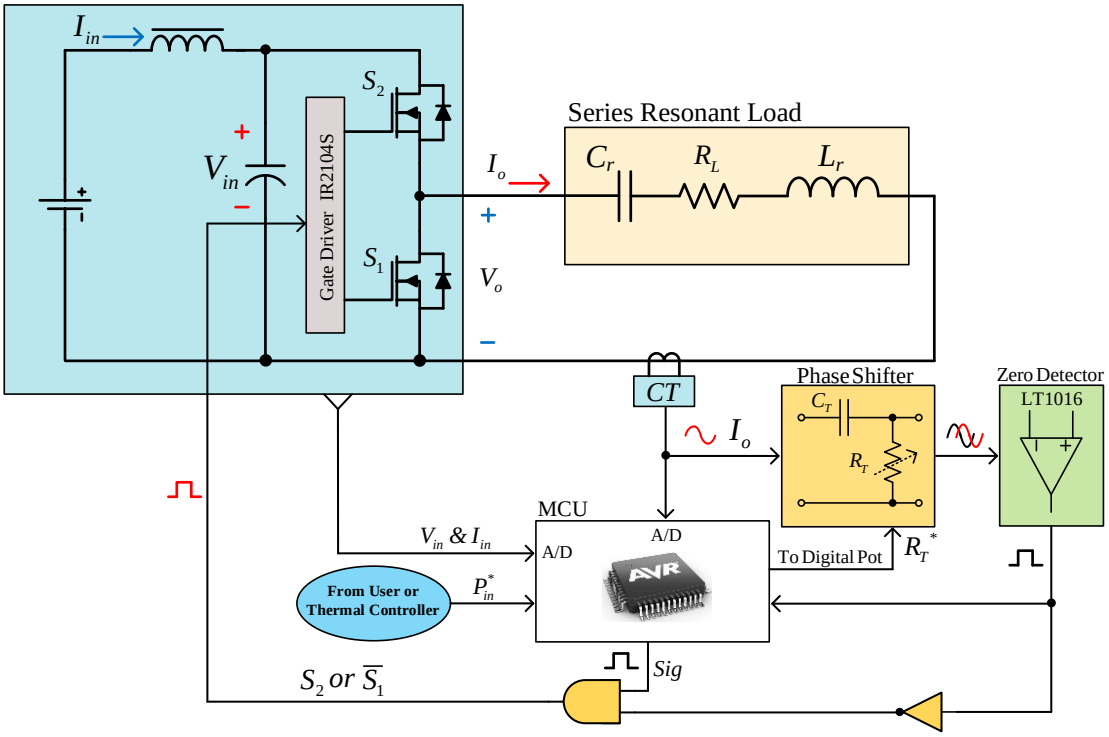

Fig. 1: A schematic of the half-bridge SRI based on the proposed SOS power and frequency tuning loop.

and series resonant impedance, $Z(j\omega_s)$, are given by (1), (2), and (3) as follows considering fundamental harmonic approximation:

$$V_o(t)=\sum_{n=1}^{\infty}\frac{2V_{in}}{n\pi}\sin(n\omega_s t), \quad for\ n=1,3,5,... \tag{1}$$

$$I_o(t)\approx\frac{2V_{in}}{\pi\,|\,Z(j\omega_s)\,|}\sin(\omega_s t-\varphi). \tag{2}$$

$$Z(j\omega_s)=\left(j\omega_s L_r-\frac{j}{\omega_s C_r}+R_L\right). \tag{3}$$

where V_{in} is the dc-link voltage of SRI, $Z(j\omega_s)$ is the load impedance of SRI, ω_s is the angular switching frequency, φ is the phase angle between the output voltage and current, L_r is the equivalent resonant inductance, R_L is the summation of the intrinsic resistance of working coil and reflected load resistance, and C_r is the value of the resonant capacitor. The quality factor, Q, damping factor, ζ, natural frequency, f_n, and the characteristic impedance, Z_0, are derived as follows:

$$Q=\frac{1}{2\zeta}=\frac{Z_0}{R_L}. \tag{4}$$

$$Z_0=\sqrt{\frac{L_r}{C_r}},\ f_n=\frac{1}{2\pi\sqrt{L_r C_r}}. \tag{5}$$

The relation between natural-frequency, f_n, and resonant-frequency, f_r, where Zero Voltage and Zero Current Switching (ZVZCS) occurs, is derived by (6):

$$f_r=\frac{1}{2\pi}\sqrt{\frac{1-\zeta^2}{L_r C_r}}=f_n\sqrt{1-\zeta^2}. \tag{6}$$

Regarding Fig. 1, the lead phase-shifter makes phase displacement equal to φ, which is derived by (7) with respect to its tuning resistor, R_T, and capacitor, C_T:

$$\varphi=\tan^{-1}\left(\frac{1}{\omega_s\tau_T}\right),\quad \tau_T=R_T C_T. \tag{7}$$

The tuning resistor, R_T, can be an adjustable digital potentiometer controlled by an MCU. On the other hand, the phase displacement of the series resonant load can be derived using fundamental harmonic approximation as follows:

$$\angle Z(j\omega_s)=tan^{-1}\left(\frac{\omega_s^2\omega_n^{-2}-1}{\omega_s R_L C_r}\right). \tag{8}$$

Phase displacement of the PS unit is approximately equal to the phase of $Z(j\omega_s)$, so the switching frequency of the SRI can be derived by solving (7) and (8), as derived by (9).

$$\omega_s=\omega_n\sqrt{1+\frac{R_L C_r}{R_T C_T}}. \tag{9}$$

Regarding (9), (7) can be rewritten by (10) as a function of the PS unit parameters:

$$\varphi=\tan^{-1}\left(\frac{1}{\alpha\sqrt{1+\frac{1}{\alpha Q}}}\right),\quad \alpha=\tau_T\omega_n\approx\tau_T\omega_r. \tag{10}$$

where τ_T is the time constant and α is the normalized time constant of the phase-shifter with respect to ω_n. Regarding φ, the output power, P_o, of the SRI can be approximated by (11) as a function of α. To show the accuracy of the above equations, simulations are done based on the PSIM simulator with V_{in} = 70 V, Q = 10, C_r = 250 nF, and L_r = 50 µH. C_T is 2 nF, and R_T is considered variable.

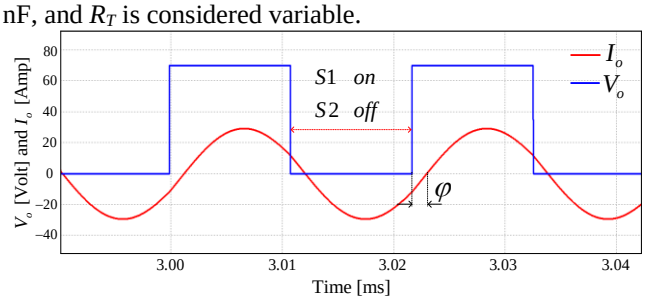

Fig. 2: The output voltage, V_o, and current, I_o, of the SRI at steady-state conditions with $\varphi\approx 21^0$, V_{in} = 70 V, Q = 10, C_r = 250 nF, L_r = 50 µH and an operating frequency of about 45.95 kHz.

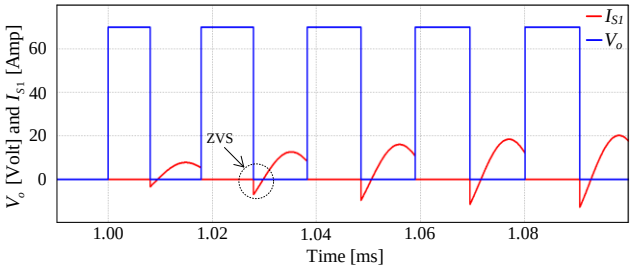

Fig. 3: The output voltage of SRI, V_o, and current of S1, I_{S1}, at start-up conditions using the SOS method with Q = 10, R_T = 2 kΩ, and V_{in}=70 V.

Regarding the mentioned parameters, natural frequency and resonant frequency are about 45.016 kHz and 44.960 kHz, respectively. Fig. 2 shows I_o and V_o at steady-state conditions with $\alpha\approx 2.262$, i.e., R_T = 4 kΩ. Regarding Fig. 2, f_s and φ are about 45.95 kHz and 21^0 while considering (9), f_s is derived to be 45.93 kHz. Fig. 3 shows the current of S1, I_{S1}, and V_o at start-up while Zero Voltage Switching (ZVS) is achieved at the beginning cycles.

$$P_o\approx\frac{1}{2}\left(\frac{2V_{in}}{\pi\,|\,Z(j\omega_s)\,|}\right)^2 R_L=\frac{2(V_{in}\cos\varphi)^2}{\pi^2 R_L},$$

$$P_o(\alpha)=\frac{2V_{in}^{\ 2}}{\pi^2 R_L}\cos^2\left(\tan^{-1}\left(\frac{1}{\alpha\sqrt{1+\frac{1}{\alpha Q}}}\right)\right). \tag{11}$$

One of the most important advantages of the SOS methods is their ability to predict parameters of SRI load. Regarding Fig. 3, the natural frequency of the SRI can be predicted at the beginning cycles of the start-up by counting intervals between zero crossings of the ZD unit directly connected to the MCU, as is seen in Fig. 1. To accurately detect f_r, it is proposed to start and stop SRI for a few cycles in minimum phase displacement, φ_{min}. For an SRI utilized for IH systems, quality factors are larger than 5, so $f_n\approx f_r$ and L_r can be derived by detecting f_r for a known resonant capacitor and using (5).

2.2. Design Procedure

The main parameters for the design of an SRI based on the SOS tuning loop are calculating V_{in}, the variation range of RT, and tuning capacitor according to the resonant load parameters. Considering the maximum output power, P_o^{max}, which occurs at the minimum phase angle, $\varphi_{min} \approx 10^0$, the required dc-link voltage is designed by (13) for the maximum value of the equivalent load resistance, R_L^{max}. The minimum phase displacement is considered to ZVS operation SRI.

$$V_{in} = \sqrt{\frac{\pi^2 P_o^{\max} R_L^{\max}}{2\cos^2 \varphi_{\min}}}. \tag{13}$$

The range of the tuning resistor, R_T, must be determined for the PS unit. Regarding (10) and considering φ_{min} and Q_{min}, as well as the minimum value of the normalized time constant of the PS, α_{min} can be calculated by solving (14), which has two answers, but the acceptable one is positive and is derived by (15). Hence, assuming C_T and the possible minimum natural angular frequency, ω_n^{min}, the upper limit of R_T can be obtained by (16):

$$\alpha_{\max}^2 + Q_{\min}^{-1}\alpha_{\max} - \left(\tan\varphi_{\min}\right)^{-2} = 0. \tag{14}$$

$$\rightarrow \alpha_{\max} = \frac{\sqrt{1+\left[2Q_{\min}\left(\tan\varphi_{\min}\right)^{-1}\right]^2}-1}{2Q_{\min}}. \tag{15}$$

$$\rightarrow R_{T,\max} = \frac{\alpha_{\max}}{\omega_n^{\min} C_T}. \tag{16}$$

To obtain the lower limit of the tuning resistor, R_T, it is necessary to determine φ_{max}, according to P_o^{min}. The maximum amount of the possible phase displacement in the first-order phase-shifter is 45^0, which reduces the output power to about 50%. Hence, by using (11) and determining P_o^{min}, the maximum phase of the PS is calculated from (17). Thus, by having φ_{max}, the minimum normalized time constant of the phase-shifter can be obtained using (18), i.e., similar to (15). Regarding (18), the minimum normalized time constant is derived at the possible maximum natural angular frequency, ω_n^{max}, of the system.

$$\alpha_{\min} = \frac{\sqrt{1+\left[2Q_{\max}\left(\tan\varphi_{\max}\right)^{-1}\right]^2}-1}{2Q_{\max}}. \tag{17}$$

$$\rightarrow R_T^{\min} = \frac{\alpha_{\min}}{\omega_n^{\max} C_T}. \tag{18}$$

3. Power Control and Parameters' Estimation

For simplicity in analyses, the first-order PS is analyzed in the above formulations, which can properly regulate the output power up to 50%. For wider power regulation, power, the PS technique, and PDM are used simultaneously.

As shown in Fig. 1, in this paper, the input current and voltage are measured to calculate instant input power, P_{in}. Since the losses of the half-bridge inverter and dc-link filter are typically less than 5%, so the input power is measured and regulated instead of the output power of the inverter for simplicity. Using (7) and the measured switching frequency, MCU calculates the instantaneous phase displacement, φ. Regarding Fig. 1, P_{in}^* is considered the reference input power, which can be applied from the user or output of a thermal controller. In the proposed control method, the reference phase displacement, φ^*, can be calculated using (11) with respect to φ and the ratio P_{in}^* and P_{in}, as derived by (19).

$$\varphi^* = \cos^{-1}\left(\cos\varphi \times \sqrt{\frac{P_{in}^*}{P_{in}}}\right). \tag{19}$$

For IH systems, the quality factor is typically larger than 5 or $\zeta < 0.1$. Therefore, the resonant frequency is equal to the natural frequency with good approximation, i.e., $f_n \approx f_r$. Moreover, the quality factor is not changed much for designing a specific load.

In practice, due to the uncertainties of the resonant tank like the aging effect in the resonant capacitor or variations in the resonant tank parameters during the heating treatments, the estimations are prone to errors and deviations.

One of the main problems associated with a well-designed power and frequency tuning loop is its robustness under uncertainties of the load variations.

Practically, the input power and Po can be considered approximately equal to calculate equivalent series resistance, R_L. Moreover, at steady-state conditions, the phase displacement can be calculated by (7) using τ_T and detecting the instant switching frequency, f_s. As a result, R_L can be estimated using the following equation:

$$P_o \approx P_{in} = V_{in} I_{in}, \quad \rightarrow R_L \approx \frac{2(\cos\varphi)^2 V_{in}}{\pi^2 I_{in}}. \tag{20}$$

Regarding trigonometric rules and (7), R_L can be rewritten as follows:

$$\cos^2\varphi = \frac{\left(\omega_s \tau_T\right)^2}{1+\left(\omega_s \tau_T\right)^2}. \tag{21}$$

$$R_L \approx \frac{2V_{in}}{\pi^2 I_{in}}\left(\frac{\left(\omega_s \tau_T\right)^2}{1+\left(\omega_s \tau_T\right)^2}\right). \tag{22}$$

Moreover, the PDM is used simultaneously when the reference phase displacement is greater than 45° from (19). Hence, the R_L should be estimated using (23) for wider power regulation.

$$R_L \approx \frac{2V_{in}D}{\pi^2 I_{in}}\left(\frac{\left(\omega_s \tau_T\right)^2}{1+\left(\omega_s \tau_T\right)^2}\right), \quad D = \frac{T_{on}}{T_{on}+T_{off}}. \tag{23}$$

where D is the duty cycle of the MCU's squared signal, Sig, and T_{on} and T_{off} are the time duration in which the Sig turns on and off, respectively. Furthermore, at steady-state conditions, the summation of T_{on} and T_{off} should be much larger than the time period of the output current.

To apply the PDM technique, it is necessary to calculate the reference duty-cycle, D^*. Therefore, the reference duty-cycle can be obtained from (24):

$$D^* = \frac{2\pi^2 R_L P_{in}^*}{V_{in}^2 Cos^2 \varphi^*} = \frac{\pi^2 R_L P_{in}^*}{V_{in}^2}. \quad (24)$$

where φ^* is set to 45°.

Like (15) and (17), the reference tuning resistor, R_T^*, can be calculated using (25) as follows:

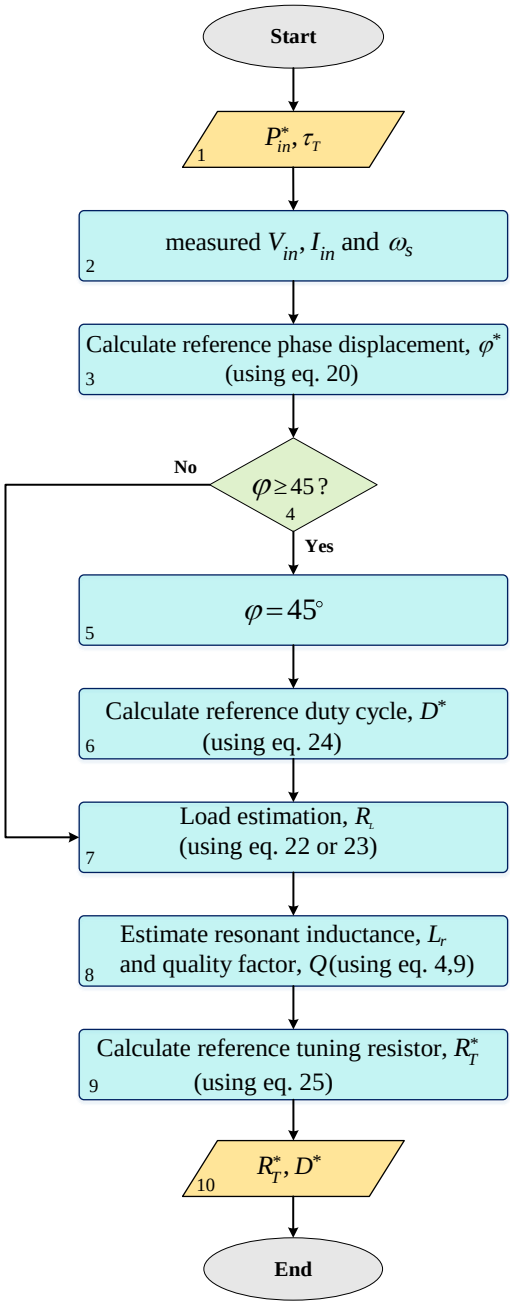

Fig. 4: The flowchart of the power regulation

$$\alpha^* = \frac{\sqrt{1+\left[2Q\left(\tan\varphi^*\right)^{-1}\right]^2}-1}{2Q}, \quad (25)$$

$$\rightarrow R_T^* = \frac{\alpha^*}{\omega_n C_T}.$$

Fig. 4 illustrates the flowchart of the proposed power regulation procedure and the parameters' estimation of tuning loops. In the proposed method, the MCU receives P_{in}^*, C_r, and τ_T as inputs. In practice, C_r and C_T are fixed values and could be estimated using their step responses. To estimate output power, the input voltage and current are measured. The switching-frequency can estimate instantly. Moreover, the MCU can estimate natural-frequency in initial cycles when the phase displacement is considered minimum. Using (22), R_L can estimate when the PS technique is used alone. When the PS technique and PDM are used simultaneously, RL should be estimated using (23).

Moreover, the value of L_r can be estimated by (4), (9), τ_T, and C_r. Therefore, regarding (10) and C_T, the value of the reference tuning resistor, R_T^*, is determined. Then, R_T^* is applied to the PS unit. Hence, the input power can instantly track the reference input power with fewer transients, which reduces the possible voltage and current stresses of the SRI.

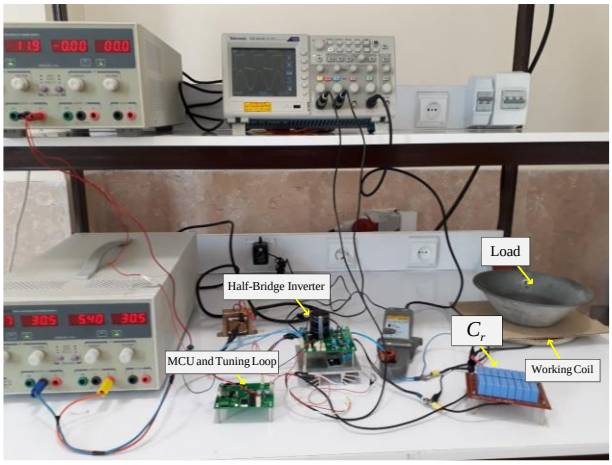

Fig. 5: The experimental setup of the IH system based on the SOS method.

Hence, for an instant quality factor, the measured P_{in} and the estimated L_r and ω_s, instant φ, and the reference parameters can be calculated with negligible errors according to the reference input power, i.e., (24) and (25).

As was already described, the presented control method can simply estimate the main parameters of the SRI at start-up duration for effective prediction and regulation of the power. Basically, the behavior of the proposed power regulating loop directly depends on the estimation of φ.

4. Experimental Results

A laboratory prototype was developed based on the designing method proposed in Section 2. Fig. 5 shows an experimental setup of the IH system based on the SOS power and frequency tuning loop. The parameters of the half-bridge inverter and the tuning system are given in Table 1. The half-bridge inverter is constructed by two IRFP250 power MOSFETs, S1 and S2, and IR2104 gate driver. SRI is designed for a maximum input voltage of 100 V. The tuning loops are constructed by logic elements, ATMEGA8 MCU, and LT1016 comparator for zero detector units.

The value of the load, R_L, is about 1.92 Ω, which is estimated at the steady-state operation using (22). According to (4), the characteristic impedance, Z_r, is estimated at 12.14 Ω while the natural-frequency, f_r, and the value of C_r are 52.44 kHz and 250 nF, respectively. Hence, the quality factor is about 6.3 using (4). For the working coil, a spiral coil with an inner diameter of 5 cm and outer diameters of 20 cm is used. The spiral coil is wound with a Litz wire that is built

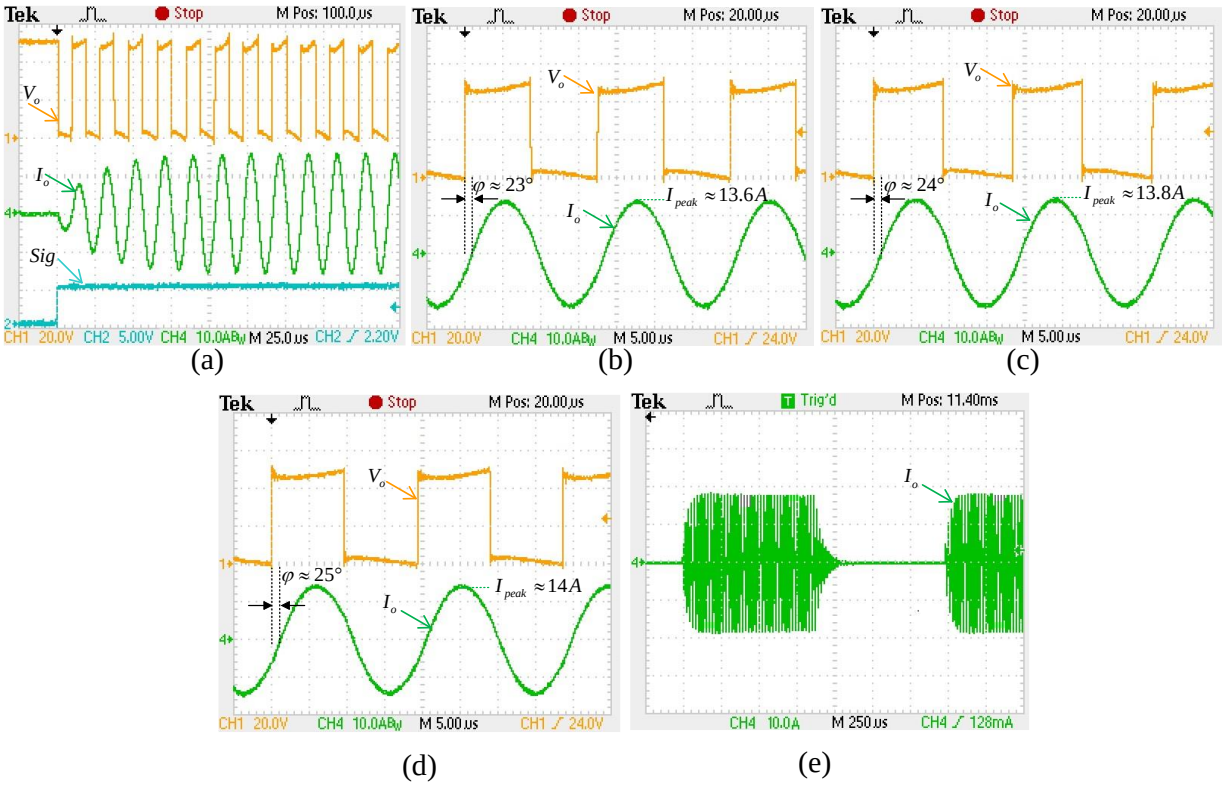

Fig. 6: (a) *Sig*, V_o and I_o at start-up conditions with $Q \approx 6.3$, $C_r \approx 250$ nF, $V_{in} \approx 50$ V. (b) V_o and I_o at 10% decrease in the capacitor and steady-state conditions with $f_s \approx 56$ kHz, $\alpha \approx 2$, $C_r \approx 225$ nF, $V_{in} \approx 50$ V. (c) V_o and I_o without deviation in C_r while $f_s \approx 54$ kHz, $\alpha \approx 2$, $C_r \approx 250$ nF, $V_{in} \approx 50$ V. (d) V_o and I_o for 10% increase in C_r while $f_s \approx 56$ kHz, $\alpha \approx 2$, $C_r \approx 275$ nF, $V_{in} \approx 50$ V. (e) I_o in the PDM technique for the SOS method with $D \approx 50\%$ while frequency of *Sig* is about 580 Hz.

with 19 insulated strands Lacquered wire. For 19 turns and loading effect from the pot, L_r is about 36.84 µH, and the material of the pot is iron. The air gap between the pot and coil is considered 5 mm. Fig. 6(a) shows the input signal, Sig, the output voltage, the current, V_o, and I_o, of the IH system at the start-up conditions. Regarding Fig. 6(a), the IH system based on SOS has a proper dynamic in transient conditions.

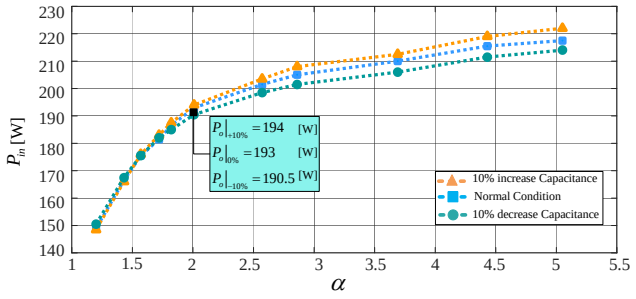

Fig. 7: Input power curve, P_{in}, in different normalized time constants in which the sweeping phase shifts approximately from 10° to 42°.

In order to analyze the sensitivity of the proposed method, three practical steps are performed. The first step is to reduce the capacitor by 10% ($C_r \approx 225$ nF) and record the input power and the tuning resistance, R_T, or record the normalized time constant of the phase shifter, α.

At steady-state, for input power, Pin, of about 190.5 W, the normalized time constant and phase displacement are about 23°, which are shown in Fig. 6(b). The second step is to test under normal conditions, i.e., $C_r \approx 250$ nF, while P_{in} is about 193 W for $\alpha \approx 2$ and $\varphi \approx 24^{\circ}$ as shown in Fig. 6(c). Regarding simulations and formulations, the output power is calculated to be about 189 W. In the last step, the capacitor increases by 10%, i.e., $C_r \approx 275$ nF. Fig. 6(d) shows the output voltage and current in these conditions while Pin is measured to be 194 W for $\alpha \approx 2$ and $\varphi \approx 25°$. Fig. 6(e) displays the output current of the IH system when the PDM technique is used for the SOS method with $D \approx 50\%$ and signal-frequency of about 580 Hz.

Table 1: The design information of the IH system and tuning loop for the laboratory prototype

Parameter	Quantity
Input voltage, V_{dc}	50 [V]
Maximum input power, P_{in}	220 [W]
Minimum phase delay	10 [degrees]
R_T	10 kΩ potentiometer
C_T	2 [nF]
Q	~6.3
C_r	250 [nF]
L_r (with pot)	38.6 µH
Comparator for ZD unit	LT1016
Power MOSFETs	IRFP250
Gate driver	IR2104
Logic element	74HC04, 74HC08
Opto-couplers	6N137

Finally, the input power of the SRI is measured for different values of α and the variations in the resonant capacitor as shown in Fig. 7. Regarding Fig. 7, there are larger power deviations for the higher values of α in comparison with the lower values of α. This phenomenon relates to the SRI and dc-link filter losses and variations in equivalent

resistance caused by the deviation of the resonant frequency. However, the deviations can be neglected.

In general, there are two kinds of changes in the load, either due to the type of work-piece material, such as steel, aluminum, etc. or due to the frequency variations. In this IH system, the load changes only by changing the frequency.

According to Fig. 7, in $\alpha \approx 5$ or $\varphi \approx 10°$ and for 10% increase, the maximum power difference is about 2%. This difference is very low and results from changing the load caused by a change in the resonant frequency. Hence, this is an advantage in large phases, i.e., $\alpha < 2$, while these deviations almost neutralize each other and make the total power deviation to be less than 0.5%, as seen from Fig. 7. Therefore, the practical estimation deviations and errors are very low, and the tuning loops can adjust the power more accurately.

5. Conclusions

This paper presents a design procedure and a new power regulation algorithm for series resonant IH systems based on a tunable self-oscillating tuning loop. The proposed method accurately estimates instant phase displacement, resonant frequency, equivalent load resistance, and inductance of the SRI. Based on the estimations, the instant power reference can be tuned with low transients, which is important for high-power IH systems. To show the accuracy of the proposed method, experimental tests have been done for possible estimation deviations. Experimental results show that using the proposed power tuning loop, negligible power deviations occur, about 2%, under large tolerances in the resonant tank circuit.

CRediT Authorship Contribution Statement

Behzad Jaafari: Data curation, Formal analysis, Investigation, Software. **Alireza Namadmalan:** Conceptualization, Investigation, Project administration, Supervision, Validation, Roles/Writing - original draft, Writing - review & editing.

Declaration of Competing Interest

The authors declare that they have no known competing financial interests or personal relationships that could have appeared to influence the work reported in this paper. The ethical issues; including plagiarism, informed consent, misconduct, data fabrication and/or falsification, double publication and/or submission, redundancy has been completely observed by the authors.

References

[1] VB. Devara, V. Neti, T. Maity, et al., "Capacitor-sharing two-output series-resonant inverter for induction cooking application", *IET Power Electronics*, Vol. 9, no. 11, pp. 2240-2248, 2016.

[2] V. Esteve, J. Jordán, E. Sanchis-Kilders, et al., "Improving the reliability of series resonant inverters for induction heating applications", *IEEE transactions on industrial electronics*, Vol. 61, no. 5, pp. 2564-2572, 2014.

[3] O. Lucia, J. Acero, C. Carretero, et al., "Induction heating appliances: Toward *more* flexible cooking surfaces", *IEEE Industrial Electronics Magazine*, Vol. 7, no. 3, pp. 35-47, 2013.

[4] O. Lucia, P. Maussion, E.J. Dede, et al., "Induction heating technology and its applications: past developments, current technology, and future challenges", *IEEE Transactions on Industrial Electronics*, Vol. 61 no. 5, pp. 2509-2520, 2014.

[5] A. Namadmalan, "Universal tuning system for series-resonant induction heating applications", *IEEE Transactions on Industrial Electronics*, Vol. 64, no. 4, pp. 2801-2808, 2017.

[6] H. Sarnago, O. Lucia, A. Mediano, et al., "Modulation scheme for improved operation of an RB-IGBT-based resonant inverter applied to domestic induction heating", *IEEE Transactions on Industrial Electronics*, Vol. 60, no. 5, pp. 2066-2073, 2013.

[7] J. Zerad, S. Riachy, P. Toussaint, et al., "Novel Phasor Transformation for Feedback Control Design of Induction Heating Systems With Experimental Results", *IEEE Transactions on Industrial Electronics*, 2015, 62, (10), pp. 6478-6485.

[8] A.R. Namadmalan, S.H. Fathi, J.S. Moghani, et al., "Power quality improvement for three phase current source induction heating systems", in *2011 6th IEEE Conference on Industrial Electronics and Applications* pp. 2580-2584, 2011.

[9] H. Sarnago, O. Lucia, A. Mediano, et al., "Analytical model of the half-bridge series resonant inverter for improved power conversion efficiency and performance", *IEEE Transactions on Power Electronics*, Vol. 30, no. 8, pp. 4128-4143, 2015.

[10] A. Namadmalan, J.S. Moghani, " Single-phase current source induction heater with improved efficiency and package size", *Journal of Power Electronics*, Vol. 13, no. 2, pp. 322-328, 2013.

[11] B. Nagarajan, R.R. Sathi, "Phase locked loop based pulse density modulation scheme for the power control of induction heating applications", *Journal of Power Electronics*, Vol. 15, no. 1, pp. 65-77, 2015.

[12] T. Mishima, S. Sakamoto, C. Ide, "ZVS phase-shift PWM-controlled single-stage boost full-bridge AC–AC converter for high-frequency induction heating applications", *IEEE Transactions on Industrial Electronics*, Vol. 64, no. 3, pp. 2054-2061, 2017.

[13] M. Uno, A. Kukita, "Double-switch equalizer using parallel-or series-parallel-resonant inverter and voltage multiplier for series-connected supercapacitors", *IEEE Transactions on Power Electronics*, Vol. 29, no. 2, pp 812-828, 2014.

[14] A. Namadmalan, "Bidirectional current-fed resonant inverter for contactless energy transfer systems", *IEEE Transactions on Industrial Electronics*, Vol. 62, no. 1, pp. 238-245, 2015.

[15] H.P. Park, J.H. Jung, "Load Adaptive Modulation of Series Resonant Inverter for All-Metal Induction

Heating Applications", *IEEE Transactions on Industrial Electronics*, Vol. 65, no. 9, pp. 6983-6993, 2018.

[16] O. Lucia, J.M. Burdio, I. Millan, et al., "Load-adaptive control algorithm of half-bridge series resonant inverter for domestic induction heating", *IEEE transactions on industrial electronics*, Vol. 56, no. 8, pp. 3106-3116, 2009.

[17] I. Millan, J.M. Burdío, J. Acero, et al., "Series resonant inverter with selective harmonic operation applied to all-metal domestic induction heating", *IET power electronics*, Vol. 4, no. 5, pp. 587-592, 2011.

[18] B.A. Nguyen, Q.D. Phan, D.M. Nguyen, et al., "Parameter Identification Method for a Three-Phase Induction Heating System", *IEEE Transactions on Industry Applications*, Vol. 51, no. 6, pp. 4853-4860, 2015.

[19] N. Domingo, L.A. Barragán, J.M.M. Montiel, et al., "Fast power–frequency function estimation for induction heating appliances", *Electronics Letters*, Vol. 53, no. 7, pp. 498-500, 2017.

[20] L.A. Barragán, D. Navarro, J. Acero, et al., "FPGA implementation of a switching frequency modulation circuit for EMI reduction in resonant inverters for induction heating appliances", *IEEE Transactions on ndustrial Electronics*, Vol. 55, no. 1, pp. 11-20, 2008.

[21] S. Komeda, H. Fujita, "A Phase-Shift-Controlled Direct AC-to-AC Converter for Induction Heaters", *IEEE Transactions on Power Electronics*, Vol. 33, no. 5, pp. 4115-4124, 2018.

[22] T. Mishima, Y. Nakagawa, M. Nakaoka, "A bridgeless BHB ZVS-PWM AC–AC converter for high-frequency induction heating applications", *IEEE Transactions on Industry Applications*, Vol. 51, no. 4, pp. 3304-3315, 2015.

[23] B. Saha, R.Y. Kim, "High power density series resonant inverter using an auxiliary switched capacitor cell for induction heating applications", *IEEE Transactions on Power Electronics*, Vol. 29, no. 4, pp. 1909-1918, 2014.

[24] N.A. Ahmed, "High-frequency soft-switching ac conversion circuit with dual-mode PWM/PDM control strategy for high-power IH applications", *IEEE transactions on industrial electronics*, Vol. 58, no. 4, pp. 1440-1448, 2011.

[25] V.Esteve, J. Jordán, E. Sanchis-Kilders, et al., "Enhanced pulse-density-modulated power control for high-frequency induction heating inverters", *IEEE Transactions on Industrial Electronics*, Vol. 62, no. 11, pp. 6905-6914, 2015.

[26] O. Lucia, H. Sarnago, J. M. Burdio, "Pulse density modulated control for the series resonant multi-inverter for induction heating applications", in *IECON 2016-42nd Annual Conference of the IEEE Industrial Electronics Society*, pp. 5995-6000, 2016.

[27] Gati, E., Kampitsis, G. and Manias, S., "Variable frequency controller for inductive power transfer in dynamic conditions", *IEEE Transactions on Power Electronics*, Vol. 32, no. 2, pp. 1684-1696, 2017.

[28] A. Namadmalan, "Self-oscillating tuning loops for series resonant inductive power transfer systems", *IEEE Transactions on Power Electronics*, Vol. 31, no. 10, pp. 7320-7327, 2016.

BIOGRAPHY

Behzad Jaafari was born in Andimeshk City, Khuzestan, Iran in 1993. He received his B.Sc. degree from the Jundi-Shapur University of Technology (JSU), Dezful, Iran in 2016 and his M.Sc. degree (with hons.) in electrical engineering from the same university in 2018. His current research interests include power electronics, electric vehicles, induction systems, and inductive power transfer.

Alireza Namadmalan received his B.Sc. degree from the Isfahan University of Technology, Isfahan, Iran in 2009 and his M.Sc. and Ph.D. degrees (with hons.) in electrical engineering from the Amirkabir University of Technology, Tehran, Iran in 2011 and 2014, respectively. From 2012 to 2014, he had research activities with the R&D Centre of Damavand Induction Furnace Company, Damavand, Iran where he was working on industrial induction heating systems. He is currently an assistant professor at the Department of Electrical and Computer Engineering, the Jundi-Shapur University of Technology, Dezful, Iran. His current research interests include power electronics, electromagnetic design using finite element methods, inductive power transfer, and renewable energy conversion.

Copyrights
© 2021 Licensee Shahid Chamran University of Ahvaz, Ahvaz, Iran. This article is an open-access article distributed under the terms and conditions of the Creative Commons Attribution –NonCommercial 4.0 International (CC BY-NC 4.0) License (http://creativecommons.org/licenses/by-nc/4.0/).

ShahidChamran University of Ahvaz

Iranian Association of Electrical and Electronics Engineers

Journal of Applied Research in Electrical Engineering

E-ISSN: 2783-2864
P-ISSN: 2717-414X
Homepage: https://jaree.scu.ac.ir/

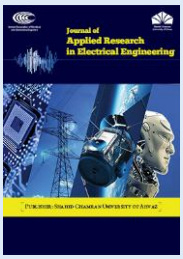

Applied Article

Improved Laser Beams-Based Security Fence to Protect Borders

Rahim Ildarabadi *, and Zohreh Keramat

Faculty of Electrical and Computer Engineering, Hakim Sabzevai University, Sabzevar 9617976487, Iran

** Corresponding Author: r.ildar@hsu.ac.ir*

Abstract: In this paper, the procedure for the protection of borders-based security fences improved using laser beams. Laser beams can be used to protect the border of large departments, large agencies, large universities, and large companies that have a large yard with several-kilometre erecting walls based on laser optic. But it has problems. To implement this system, it uses invention protocol transmission data. The cost of implementing this system is very low. The older methods of this system have been implemented in Hakim Sabzevery University.

Keywords: Infrared beam, security fence, data transmission, optic communication.

Article history
Received 08 August 2020; Revised 22 April 2021; Accepted 02 May 2021; Published online 28 June 2021.
© 2021 Published by Shahid Chamran University of Ahvaz & Iranian Association of Electrical and Electronics Engineers (IAEEE)
How to cite this article
R. Ildarabadi, and Z. Keramat, "Improved laser beams-based security fence to protect borders," *J. Appl. Res. Electr. Eng.*, vol. 1, no. 1, pp. 50-58, 2022. DOI: 10.22055/jaree.2021.34586.1011

Check for updates

1. INTRODUCTION

The protection of very vast lands, such as large universities, military facilities, department agencies, and companies with several borders is a difficult task. These facilities are traditionally protected by inspection by operators, the use of barbed wire interval along its length, and so on. However, these methods have certain assumptions and problems. Inspection by operators can only be performed to a limited extent. When using the barbed wire method, robbers or saboteurs can cut the barbed wire. In addition, this method is costly. Putting closed-circuit television (CCTV) to supervise borders is much more costly and, at the same time, undesirable and irrational. This paper presents an approach for protecting the borders of very vast lands based on infrared beams, which is much less costly and easy to implement.

Laser radiation can pass through various channels, such as fibre optics and atmosphere or open space communications. [1].

Optical communications were used in various forms for messaging or warning thousands of years ago. For example, ancient people used to establish these communications by polishing their shields. Today, optical communications are also done by encoding and decoding optical signals with the help of semaphores and wireless solar telegraphs called heliographs [2].

Many simple and inexpensive consumer remote controls use low-speed communications using infrared (IR) light, which is known as consumer IR technologies.

Atmospheric conditions can cause disturbance in optical connection with open space channels. Like any other communication channel, open space can change both the amplitude and the phase of news signals. Therefore, in a news transmission route, if necessary, relays and amplifiers should be used to minimize the probability of news loss [3]. Although optical relays reduce the speed of data exchange, open space optical communication is still used to exchange data between spacecraft. One of the very simple technologies in outdoor optical communications is Infrared Communication Technology (IrDA) [4]. Due to atmospheric conditions, such as dust particles, fog, and the effects of heat, rain, and snow, the maximum range of optical light communications is usually considered to be less than 3 km above the ground. Due to this fact and even obstacles that sometimes interrupt light transmission completely, this method is not suitable for data transmission at the ground level and on very long distances. However, in 2007, amateur radio operators also reported outdoor light transmission (atmosphere) up to about 278 km with the help of high-power LEDs. According to the conditions of open space channels (atmosphere), one cannot expect too much speed for news transmission, and the cut-off frequency cannot be more than about 4 kHz [5].

Outside the atmosphere, it is practically possible to communicate light in the open air for several thousand kilometres owing to the much lower density of particles in space. In January 2013, NASA used optical telescopes to expand its beams, sending infrared optical communications to transmit space images up to a distance of about 400,000 kilometres using atmospheric interference data correction code algorithms. This algorithm is similar to the algorithm used to correct the data error of compact discs [6].

Secure open-space optical communications can be suggested using the N-infrared interferometer where the infrared signal is in the form of an interference pattern. It can be shown that this method is practically effective and works at the desired emission intervals and can basically be used at long distances in outer space [7].

In Ilderabadi's patent, he used this method to protect the environment from laser beams [8]. The visible laser beam cannot be used during the day. It is also difficult to regulate the transmission and reception of data and maintain it between the transmitter and the receiver through the communication of the laser beam. In this paper, free-space optical communications were used to defend the fence of large agencies based on IR beam communication. The next section describes how the proposed method works.

It should be noted that this work was presented as a research project for the protection of the university environment and was implemented to some extent. But, it was not implemented completely due to the need for about 80 nodes and their installation and adjustment, which was costly and required skilled people who were not available. The project report was also presented at the Twelfth International Conference ICTPE 2016 [9]. In addition, a part of it was published under the title of protection of the walls of cement factories in the scientific, technical, and economic monthly of Cement No. 250 in 2019 [10].

2. Border Security Based on Infrared Beam

This section presents a new approach to protecting the borders of large facilities against unwanted intrusion of people.

This method is simple. An infrared beam is created at one point of the border and an infrared beam receiver is placed at another point of the border as is shown in Fig. 1. In this design, the laser beam is used to detect night traffic on the wall. Thus, if the laser beam sent by the transmitter is received by the receiver according to Fig. 1, it means that there is no traffic between the receiver and the transmitter (normal state), otherwise if according to Fig. 1b, the transmission is cut off, the lack of laser beam will indicate traffic between the receiver and the transmitter. The distance between the transmitter and receiver can be variable from around 5 to 15 meters. If anyone passes on the border (fence), it will interrupt the infrared beam and the transmitted data will not be received by the receiver, implying that somebody has entered or exited.

In this design, the transmitter and receiver are placed at a distance of about 30 to 80 meters on the sides of the wall according to Fig. 2. As such, traffic on both sides of the wall is practically recognizable. Fig. 3 shows how each node is placed on the fence.

After a node detects an unauthorized bus, the location of the unauthorized password is transferred by that node to the adjacent node in two directions. The sending of the mentioned code continues in the same way and in two directions, until the mentioned code reaches the initial and final nodes and after decoding, the location of the error is determined. Fig. 4 shows how data is exchanged between different nodes. Each node can have four terminals, which are represented by the letter B in which B_{n1} and B_{n2} are the input terminals and B_3 and B_4 are the output terminals.

The possible states for each node are expressed below.

1) Initial display node (first terminal):

Mode A): daytime; if the laser receiver receives continuous light for more than about 10 seconds, it indicates that the air is bright (day) and daytime is shown on the display (Fig. 5).

Mode B): The received code is normal and in this case, the normal state is shown in the display (Fig. 6).

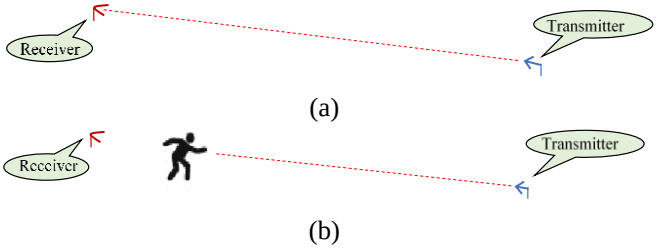

Fig. 1: (a) Data receipt from the wall in normal mode, (b) Data receipt interruption due to traffic through the fence.

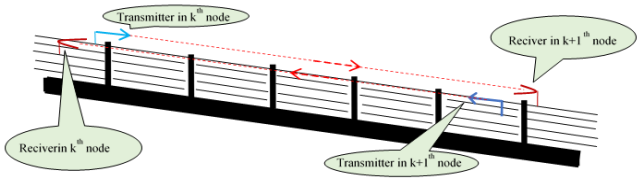

Fig. 2: Schematic of the position of infrared transmitter and receiver.

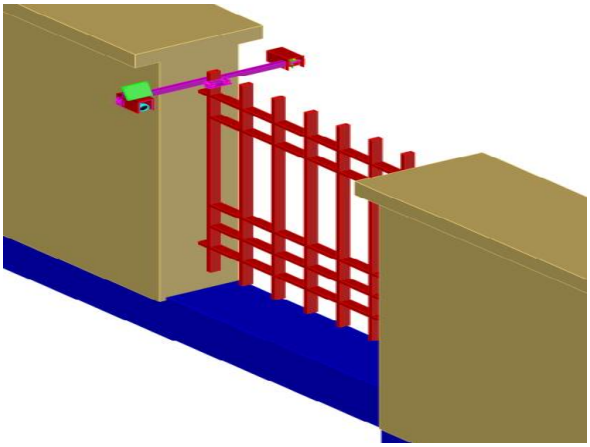

Fig. 3: How to place each node on the fence.

Fig. 4: How to exchange data between nodes.

Fig. 5: Format of received data in mode 'a'.

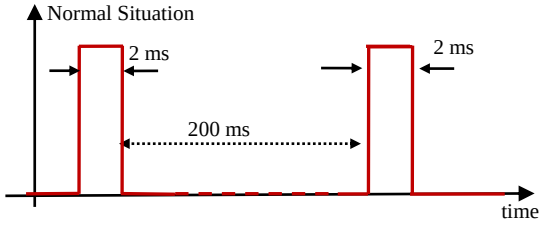

Fig. 6: Format of received data in normal mode.

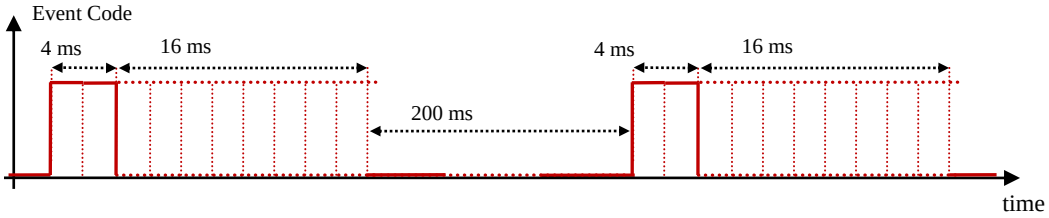

Fig. 7: Format of received data for unauthorized crossing case.

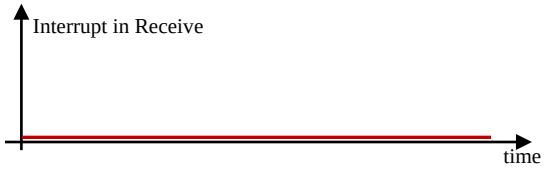

Fig. 8: Format of received data when an interruption occurs.

Mode C) The received code is the error code of one node, so this code should be displayed in the output (Fig. 7).

Mode D) No data is received. It is considered an error between this node and the first node, so the breakdown code in data receiving is shown in the output (Fig. 8).

2) First node:

Mode A) being up to date. If the laser receiver receives continuous light for more than about 10 seconds, do not send light from this node. But always check the status of the receiver (Fig. 9).

Mode B) The received code is normal and in this case, the normal state is sent on both sides (Fig. 10).

C) The received code is the error code sent from other nodes; In this case, this error code will be sent to the primary display node. On the other hand, normal code is still sent to the adjacent node (Fig. 11).

D) Not receiving the signal. It is the occurrence of an error between the first group and its adjacent (second) node. In this case, the corresponding error code is sent to both the display group and the second node (on the other side) (Fig. 12).

3) Middle nodes:

A) If the middle node receives data from both parties, send the received data of each party to the same party. This condition is considered the absence of traffic on both sides of this node. Fig. 13 shows the conditions that can occur in this case.

B) If data is not received from one side, the related error code in this node is sent to the nodes of the parties, and if data is not received from both sides, the error code is sent consecutively (one in between) on both sides. To be. (As shown in Fig. 14).

C) Being up to date. If the receivers of this node receive light continuously for more than about 10 seconds, the data transmission to the parties is interrupted. But, recipients should always check the status (as shown in Fig. 15).

3) End node:

It is like the primary node. The performance algorithm of each node is presented in Fig. 16.

For the end node, B3 is received and checked instead of B4. Also, the normal code is still sent by B1 when receiving the error code via B3, and the received error code is sent by B2 (B4 moves with B3 and B2 with B1).

System implementation in Proteus software is shown in Fig. 19. In this figure, the first node، the middle node, and the end node are implemented by the Atiny13 Atmel microcontroller. The displayer node is implemented by the Atemga 32 microcontroller and shows the result on an LCD. Three state switches are used to create the normal situation, day state, and error accruing state.

(a) (b)

Fig. 9: The format of (a) incoming, and (b) outgoing data during the day

(a) (b)

Fig. 10: The format of (a) incoming, and (b) outgoing data in normal mode

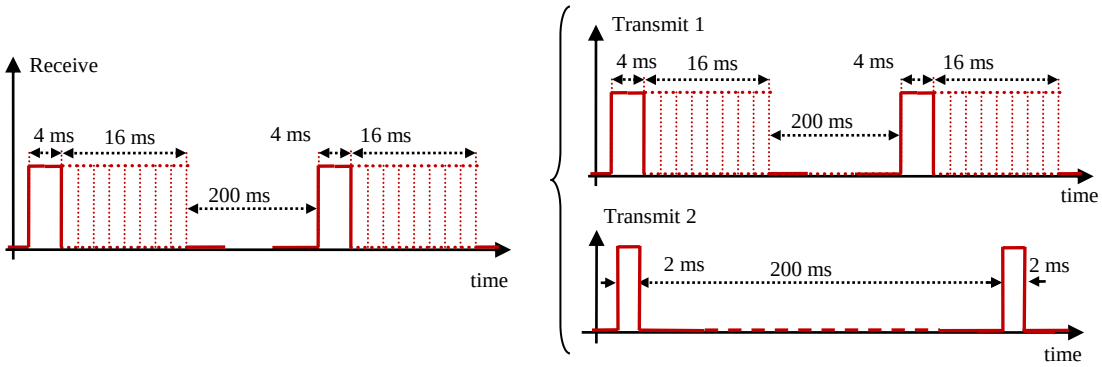

Fig. 11: The format of the received and transmitted data in the error code and the sent normal code to other side

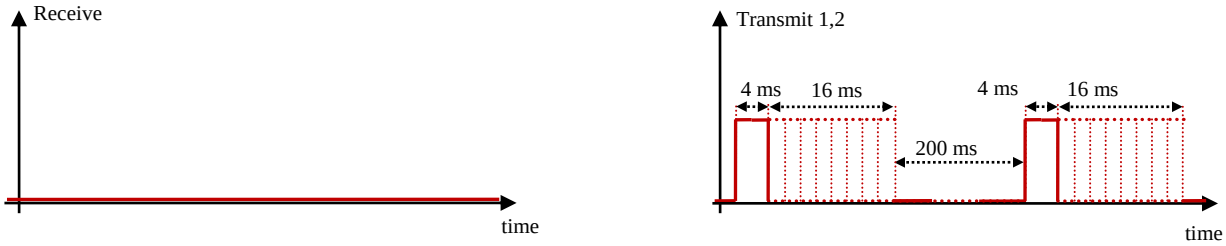

(a) (b)

Fig. 12: Format of (a) received, and (b) sent data in the absence of data.

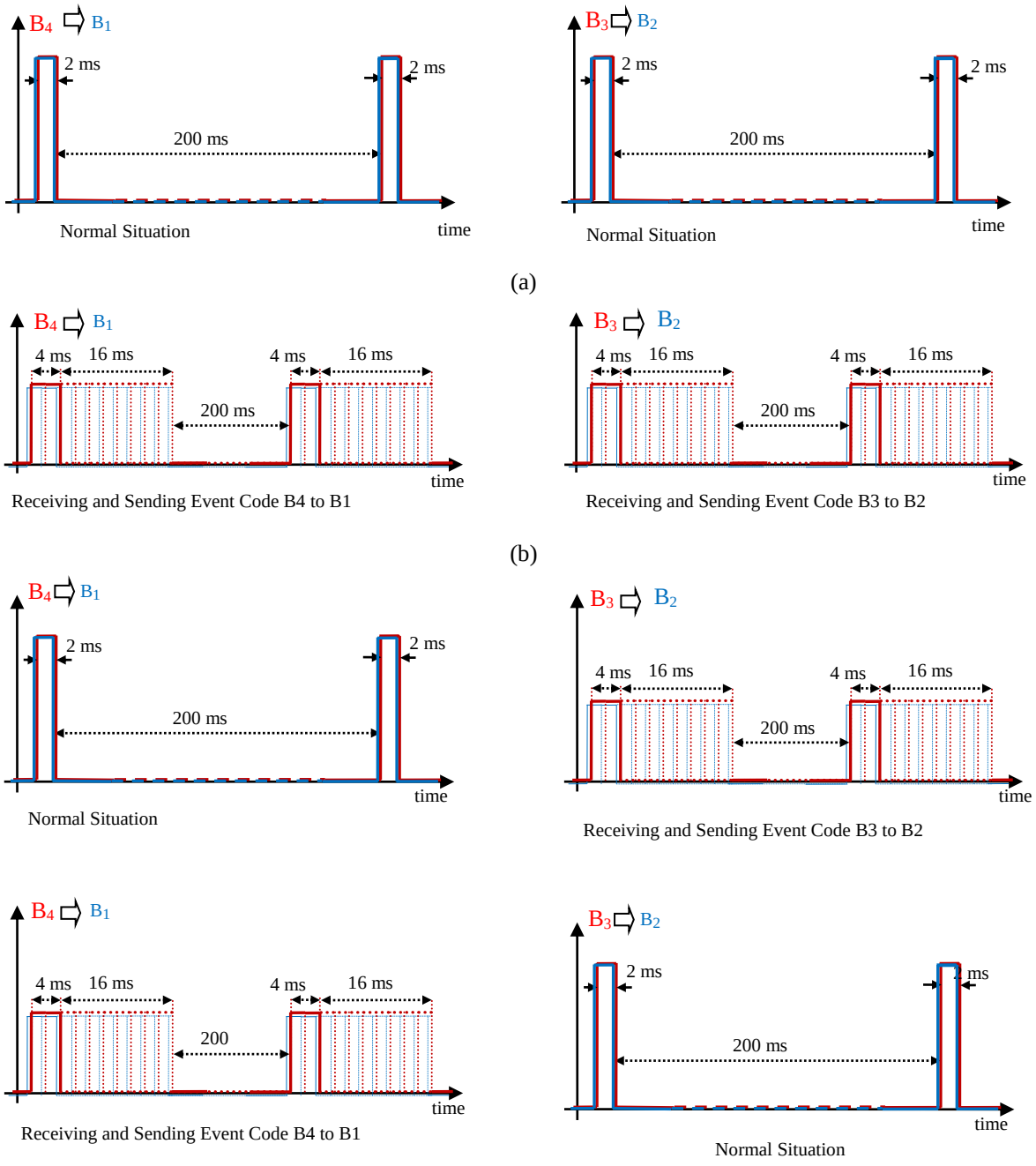

Fig. 13: (a) The format of incoming and outgoing data in the case of the middle's nodes receiving data from both sides. B_1 and B_2 are input terminals and B_3 and B_4 are output terminals (Normal Situation), (b) Receiving and sending event code between two middle nodes, and (c) From one side Receiving and sending error code, and from another side Receiving and sending Normal code.

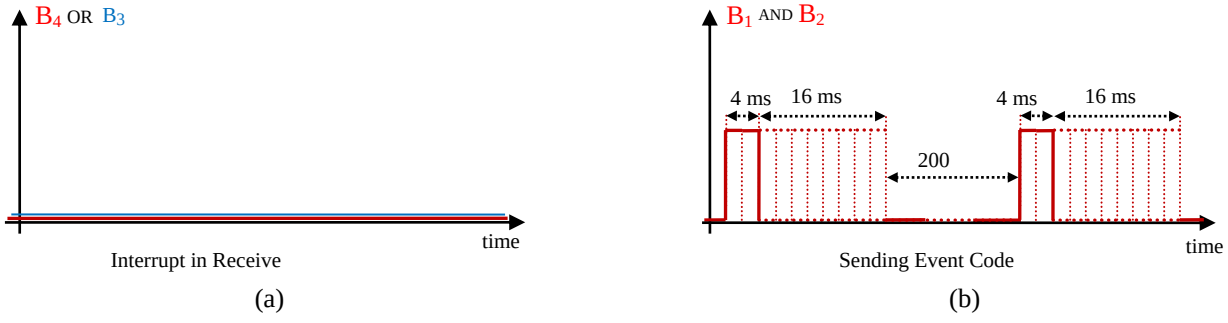

Fig. 14: The format of (a) incoming and outgoing data in the case of the middle group does not receive data on one side.

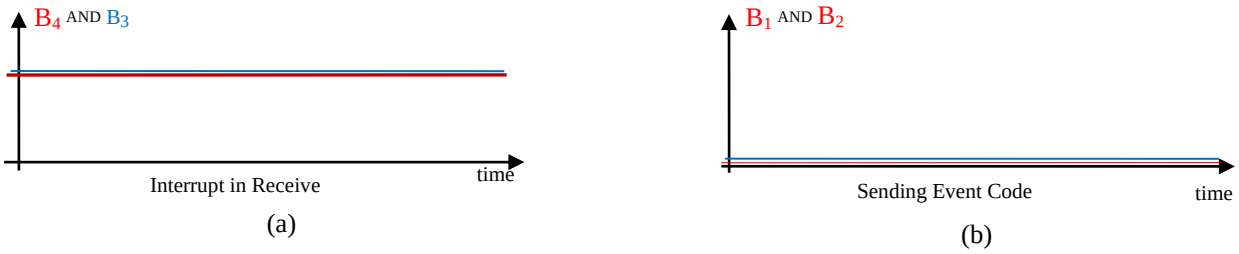

Fig. 15: The format of (a) incoming and (b) outgoing data in the current state.

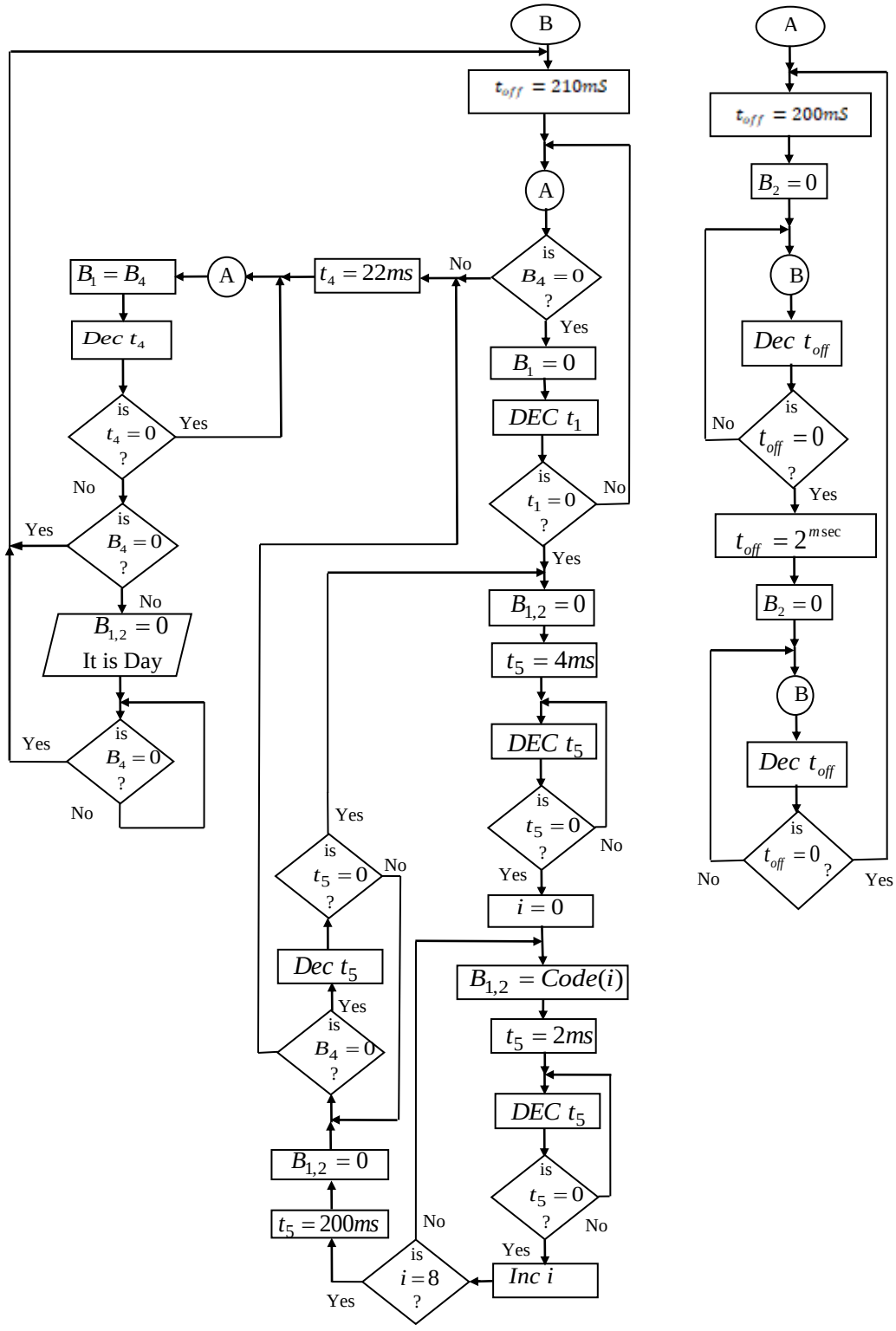

Fig. 16: System performance algorithm for the first node.

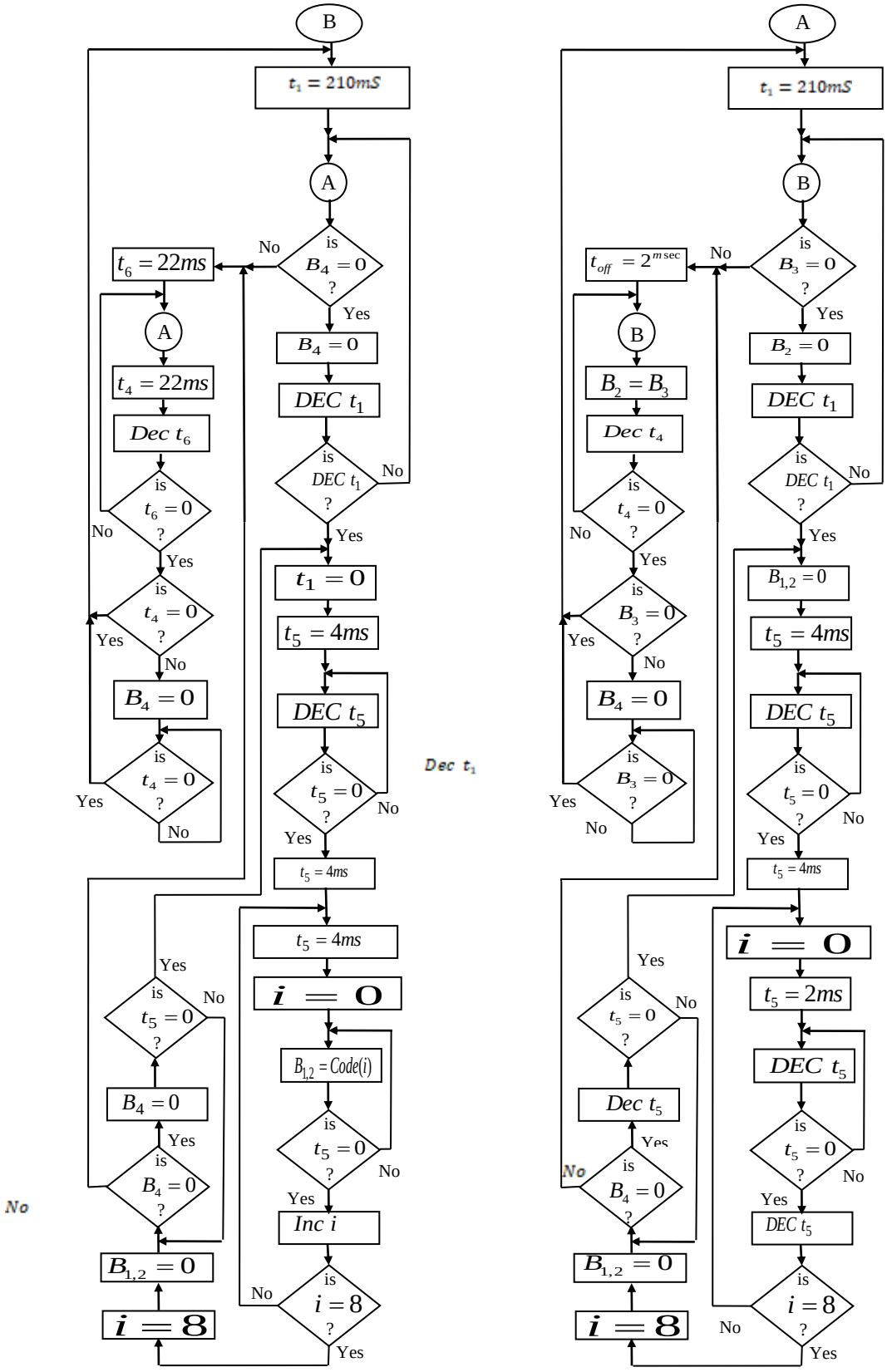

Fig. 17: System performance algorithm for the first intermediate nodes.

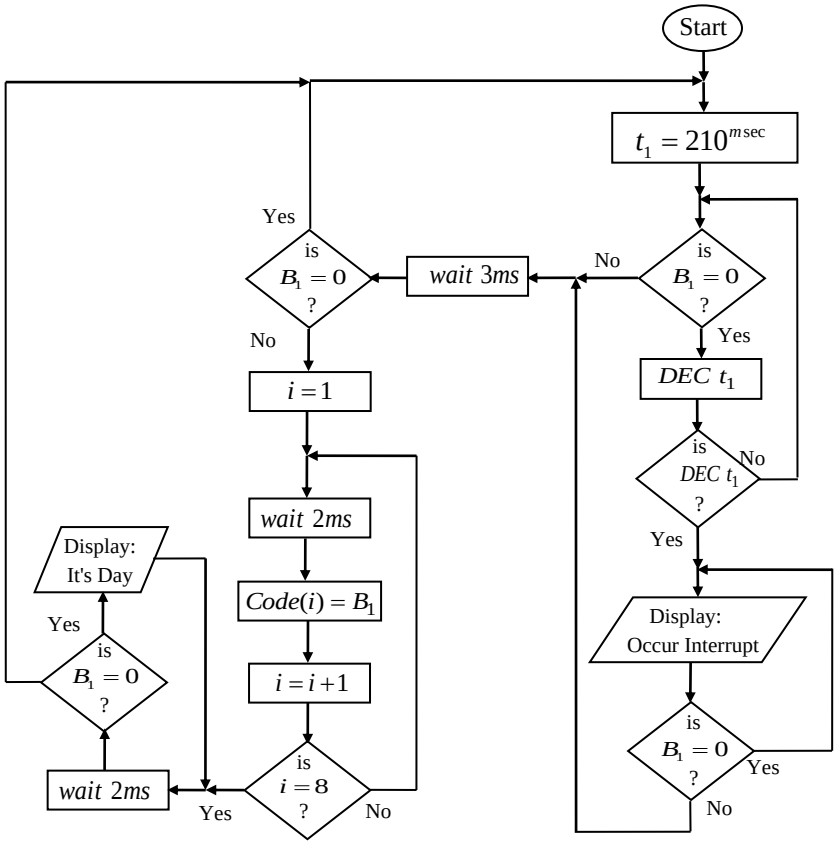

Fig. 18: System performance algorithm for display node.

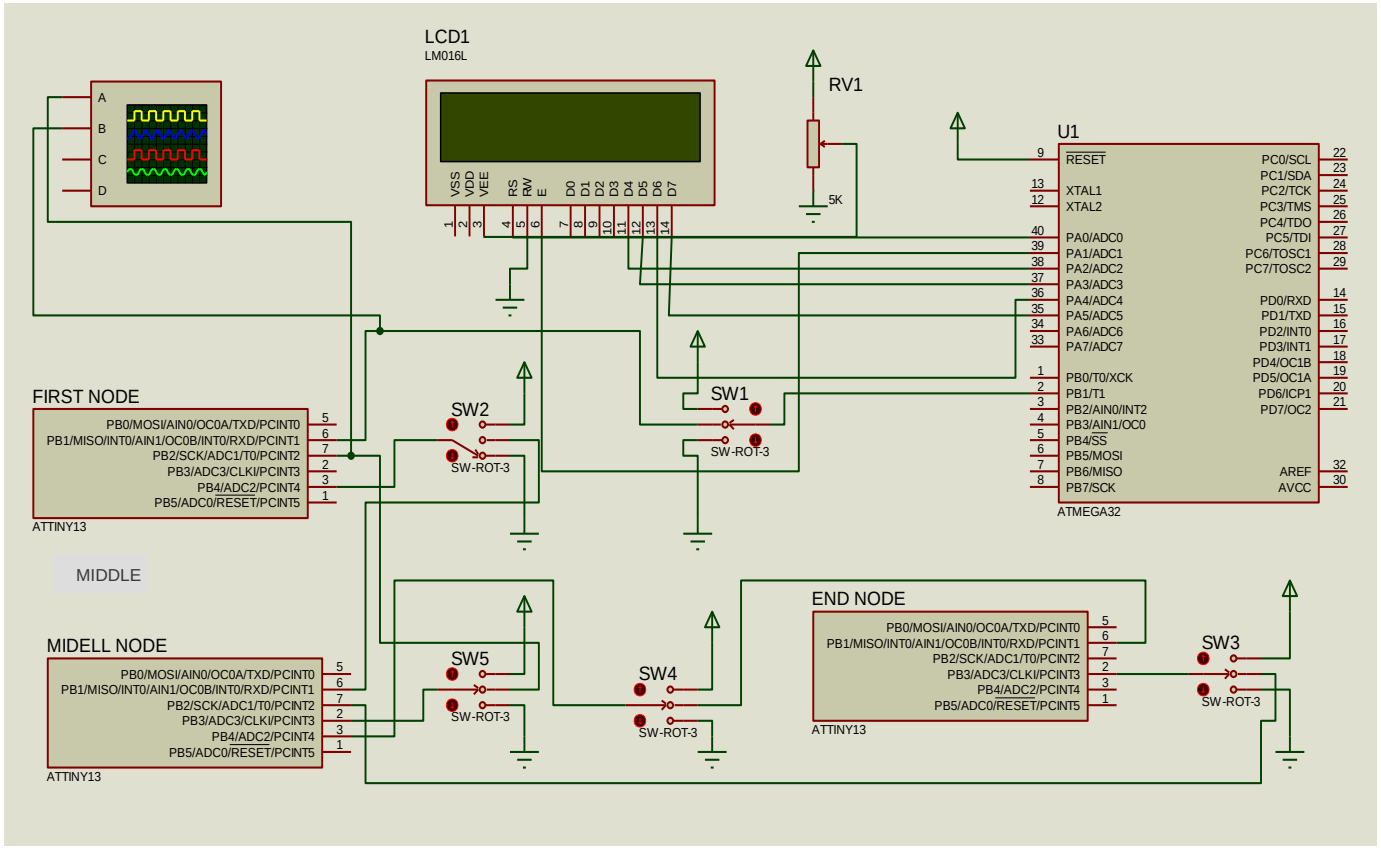

Fig. 19: System implementation in Proteus software.

3. Conclusion

This paper presented a new approach to protecting vast locations, such as large universities, military organizations, and corporations. Operator inspection, the use of barbed wire on walls and borders, and the like are used as traditional methods to protect these types of places. But they have their own problems. In this paper, a method based on optical communication based on laser light beam was presented. This system can reduce the cost of protection in the establishment and operation. This version is a new version of the enhanced protection system previously provided by the first patent author.

CRediT Authorship Contribution Statement

Rahim Ildarabadi: Conceptualization, Data curation, Formal analysis, Software, Supervision, Visualization. **Zohreh Keramat:** Formal analysis, Roles/Writing - original draft.

Declaration of Competing Interest

The authors declare that they have no known competing financial interests or personal relationships that could have appeared to influence the work reported in this paper. The ethical issues; including plagiarism, informed consent, misconduct, data fabrication and/or falsification, double publication and/or submission, redundancy has been completely observed by the authors.

References

[1] C. Lim, A. Nirmalaths, and D. Novak, "Techniques for multichannel data transmission using a multisection infrared in millimetre-wave fibre-radio systems", *IEEE Transactions on Microwave Theory and Techniques*, vol. 47, no. 7, pp. 1351-1357, 1997

[2] H.D. Wacker, J. Borcsok, and H. Hillmer, "Redundant optical data transmission using semiconductor infrareds", in *IEEE/ACS International Conference on Computer Systems and Applications*, pp. 1040-1045, 2008.

[3] M. A. Khalighi, and M. Ugsal, "Survey on Free Space Optical Communication: A Communication Theory Perspective", *IEEE Communications Surveys & Tutorials*, vol. 16, no. 8, pp. 2281-2258, Nov. 2014.

[4] Xiaoming Zhu, and J. M. Kahn, "Free-space optical communication through atmospheric turbulence channels", *IEEE Transactions on Communications*, vol. 50, no. 8, pp. 1293 – 1300, 2002.

[5] Clint Turner. (June 28, 2011). *A 173-mile 2-way all-electronic optical contact*. Available: http://www.modulatedlight.org/optical_comms/optical_qso_173mile.html

[6] I. E. Lee, M. L. Sim, and F. W. L. Kung, "Performance enhancement of outdoor visible-light communication system using selective combining receiver", *IET Optoelectron*, vol. 3, no. 1, pp. 30-39, 2009.

[7] F. J. Lopez-Martinez, G. Gomez; and J. MaríaGarrido-Balsells, "Physical-Layer Security in Free-Space Optical Communications", *IEEE Photonics Journal*, vol. 7, no. 2, pp. 1-14, 2015.

[8] R. Ildarabadi, "Environmental protection system based on optical data communication for universities, military barracks and boundaries", I.R. Iran Patent 1396/7/3-93679, International Classification: "G06F/00; G08B 13/00; G06f 19/00"

[9] R. Ildarabadi, and Z. Keramat, "Laser based security fence to protect military and administrative organs", in *12th International Conference on Technical and Physical Problems of Electrical Engineering*, 2016, p.p. 1-6.

[10] R. Ildarabadi, and Z. Keramat, "Infrared Beam based Security Fence to Protect the Border of Cement Factory", *in 5th conference and exhibition of cement industry*, 2019.

Biography

Rahim Ildarabadi was born in Sabzevar, Iran in 1975. He received his Ph.D. degree from the Ferdowsi University of Mashhad in 2010. His main areas of interest are automation systems, electrical machine drives, renewable energy, instruments, and measurement. He is currently an Assistant Professor of electrical engineering at Hakim Sabzevari University.

Zohreh Keramat was born in Sabzevar, Iran in 1983. She received her M.Sc. degree in mechatronics at Hakim Sabzevari University, Sabzevar, Iran in 2015. Her research areas include automation systems, electrical machines, variable frequency drive, and modeling and control of systems.

Copyright
© 2021 Licensee Shahid Chamran University of Ahvaz, Ahvaz, Iran.This article is an open-access article distributed under the terms and conditions of the Creative Commons Attribution –NonCommercial4.0 International (CC BY-NC 4.0) License (http://creativecommons.org/licenses/by-nc/4.0/).

Shahid Chamran University of Ahvaz

Iranian Association of Electrical and Electronics Engineers

Journal of Applied Research in Electrical Engineering

E-ISSN: 2783-2864
P-ISSN: 2717-414X
Homepage: https://jaree.scu.ac.ir/

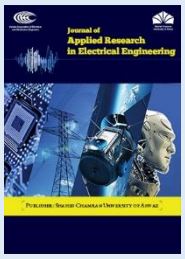

Research Article

A High-Performance MEMRISTOR-Based Smith-Waterman DNA Sequence Alignment Using FPNI Structure

Mahdi Taheri [1], Hamed Zandevakili [2], and Ali Mahani [2,*]

[1] *Department of Information and Communication Technology, Tallinn University of Technology, Tallinn 19086, Estonia*

[2] *Reliable and Smart Systems Lab (RSS), Shahid Bahonar University of Kerman, Kerman 7616913439, Iran*

* *Corresponding Author: amahani@uk.ac.ir*

Abstract: It is crucial to detect potential overlaps between any pair of the input reads and a reference genome in genome sequencing, but it takes an excessive amount of time, especially for ultra-long reads. Even though lots of acceleration designs are proposed for different sequencing methods, several crucial drawbacks impact these methods. One of these difficulties stems from the difference in read lengths that may take place as input data. In this work, we propose a new Race-logic implementation of the seed extension kernel of the BWA-MEM alignment algorithm. The first proposed method does not need reconfiguration to execute the seed extension kernel for different read lengths. We use MEMRISTORs instead of the conventional, complementary metal-oxide-semiconductor (CMOS), which leads to lower area overhead and power consumption. Also, we benefit from Field-Programmable Nanowire Interconnect Architecture as our matrix output resulting in a flexible output that bypasses the reconfiguration procedure of the system for reads with different lengths. Considering the power, area, and delay efficiency, we gain better results than other state-of-the-art implementations. Consequently, we gain up to 22x speedup compared to the state-of-the-art systolic arrays, 600x speed up considering different seed lengths of the previous state-of-the-art proposed methods, at least 10x improvements in area overhead, and 105x improvements in power.

Keywords: Bioinformatics, BWA-MEM, memristor, race logic.

Article history
Received 31 December 2020; Revised 27 April 2021; Accepted 27 May 2021; Published online 28 June 2021.
© 2021 Published by Shahid Chamran University of Ahvaz & Iranian Association of Electrical and Electronics Engineers (IAEEE)
How to cite this article
M. Taheri, H. Zandevakili, and A. Mahani, "A high-performance MEMRISTOR-based smith-waterman DNA sequence alignment using FPNI structure," *J. Appl. Res. Electr. Eng.*, vol. 1, no. 1, pp. 59-68, 2022.
DOI: 10.22055/jaree.2021.36117.1016

Check for updates

1. INTRODUCTION

DNA sequencing is a laboratory technique used to determine the exact sequence of bases (A, C, G, and T) in a DNA molecule. The DNA base sequence carries the information a cell needs to assemble protein and RNA molecules. DNA sequence information is essential to scientists investigating the functions of genes [1]. Based on the recent research on genomic sequence alignment, various algorithms and specific designs improve the sequencing aligners' performance and energy consumption. We can put genomics in the category of big data science, and by growing technology, it is getting much bigger. The volume of produced data by genomics can be compared with three main big data generators [2]:

I. astronomy: Over these decades, Astronomy is placed in the group of Big Data challenges.

II. YouTube: There is a huge number of sharing stuff and videos that are created and shared on YouTube

III. Twitter: Makes a lot of opportunities for new insights by mining more than 400 million messages that are sent every day.

Table 1 [3] compares these four groups of data generators, showing how genomics is increasingly overcoming in the case of demanding data acquisition, storage, distribution, and analysis.

The first step for most genomics applications is sequence alignment. Many reads of DNA strands have to be aligned against the reference genome, and the best alignment for each read is produced as output. There are a variety of sequence alignment tools such as:

1. Bowtie [4]

Table 1: Comparison of four groups of Big Data in 2025 are shown in this Table [3].

Data Phase	Astronomy	Twitter	YouTube	Genomics
Acquisition	25 zetta-bytes/year	0.5-15 billion tweets/year	500-900 million hours/year	1 zetta-bases/year
Storage	1 EB/year	1-17 PB/year	1-2 EB/year	2-40 EB/year
Analysis	In situ data reduction	Topic and sentiment mining	Limited requirement	Heterogeneous data and analysis
	Real-time processing	Metadata analysis		Variant calling, ~2 trillion central processing unit (CPU) hours
	Massive volumes			All-pairs genome alignments, ~10,000 trillion CPU hours
Distribution	Dedicated lines from antennae to server (600 TB/s)	Small units of distribution	Major component of modern user's bandwidth (10 MB/s)	Many small (10 MB/s) and fewer massive (10 TB/s) data movement

2. BWA [5]
3. MAQ [6]
4. SOAP [7]
5. BWA-MEM [8]

Consider the state that we want to find all local alignment using a dynamic programming approach as an example of the alignment algorithms. If we choose the Smith and Waterman algorithm [9], which uses O (nm) time for aligning a read of length n against a reference of length m, it can be concluded that the approach is too slow.

For example, as the fastest sequencing, NGS takes about hours with a lot of memory usage to sequence an entire human DNA. Based on the [10] experimental results, aligning 1000 characters as a read against the human genome will take more than 15 hours.

In the case of actual application, we work with genes or chromosomes that are about a few thousand to a few hundred million lengths. If we align the whole human genome with the SW method, it will last for about some days to weeks.

There are other algorithms like BLAST [11], which are heuristic methods. They are used to find local alignments very efficiently. Using BLAST takes 10-20 seconds to align a read of 1000 bp against the human genome [11].

Obviously, with these time-consuming calculations, general-purpose processors are not a good solution for executing these bioinformatics workloads. Thus, we need more parallel and specific hardware such as GPU or FPGA dedicated to massively accelerating the intensive computations and leading to large speedups.

In this work, we accelerate the Smith-waterman-like algorithm with a race logic strategy based on memristor elements to speed up the execution time. The rest of this paper is organized as follows: We provide related works in section 2. Our design contributions and details of our MEMRISTOR-based design are discussed in Section 3. Section 4 evaluates the results, and finally, Section 5 concludes this article.

2. Related Works

We are experiencing exponential growth of experimental data and information in biology called data explosion [12]. One of the most valuable operations in Bioinformatics is DNA sequencing. Four nucleotides (A, C, G, T) make the foundation of the DNA sequences. Swapping these nucleotides causes alternate biochemical functions and products within the DNA. One of the most Severe computational parts of Bioinformatics is finding similarities between two DNA sequences called pairwise alignment. Different methods accomplish this for Biologists, which leads to different time consumption. The Smith-Waterman (SW) is one of the most accurate algorithms with high sensitivity degree but high computational time and high hardware resource usage. Consider that the complexity of SW is of quadratic order. The BLAST [13] and FASTA [14] are derivative methods of SW which do not lead to optimal solutions because of sensitivity loss but are significantly faster. Another dynamic programming method for comparing two macromolecules is the Needleman-Wunsch algorithm (NW) [15], which calculates the alignment score between two sequences based on the Levenshtein distance. There are different other efforts to reduce the computational time of different parts of the pairwise alignment algorithms. A custom ASIC implementation of a BioSCAN is introduced in [16], in which heuristic and very high-density implementation caused the high performance. A new method of information representation was proposed in [17] that performs computation by setting up logical race conditions in a circuit on ASIC platform and they achieved about 3x higher throughput at 5x lower power density. The authors in [18] evaluate SWIFOLD: A SW parallel implementation for long DNA sequences implemented on Intel core with OpenCL. They claim that their method increases better performance with higher resource consumption. In another work, in [19], a ReRAM-based process-in-memory architecture is designed to improve short read alignment throughput per Watt by 13×. Several techniques have been proposed to accelerate the SW inexact alignment algorithm. However, the seed extension

step of this algorithm makes it inherently a slow design. The authors provided a new 2-D technique regarding SW inexact alignment algorithm in which they have used fixed numbers for Match, Mismatch, and gap penalty [20]. The authors in [21] propose a new hardware accelerator in which the most incorrect candidate locations fill out with 130-fold speedup than software. There is a faster implementation of SW in [22] which achieves 2to8× performance improvement compared to other SIMD-based SW implementations. Also, intrinsic delay of the circuits edit-distance computation elements as in [23] was utilized to propose the ASAP accelerator based on the RACE-logic hardware acceleration presented in [17] for accelerating SW and NW algorithms on an ASIC platform. Their work leads to 200× speedup than an equivalent SW-C implementation. Some other works accelerated BWA-MEM genomic mapping algorithm on different platforms such as GPU and FPGA. BWA-MEM is a widely used algorithm to map genomic sequences onto a reference genome. This algorithm is composed of three main computational kernels [8]:

I. SMEM Generation: This kernel is used to find seeds (sub-strings of the reads) that are likely mapping the read against the reference genome. There is a chance of generating several seeds with the variable length for each read [5]. This step is an exact-match-finding phase that uses the Burrows-Wheeler transform. For this work, seeds are at least nineteen characters and a maximum of 131.

II. Seed Extension: This step is an inexact-matching step that executes chaining and extending seeds in two directions using an SW-like algorithm [9]. This part of the BWA-MEM algorithm finds the optimal local alignment by using a scoring system.

III. Output Generation: In this step, the best alignment (i.e., with the highest score) is finalized and provided as the output in SAM format, if necessary.

Note that the seed extension kernel used in BWA-MEM is different from the SW algorithm in two substantial ways (Table 2) [24]: (1) Non-zero initial values: The initial values in the first column and the first row depending on the alignment score of the seed found by the SMEM Generation kernel. (2) Additional output generation: Other than the local and global alignment scores, the exact location inside the similarity matrix and a maximum offset (indicating the distance from the diagonal at which a maximum score has been found) are also generated.

The first accelerated implementation of BWA-MEM is presented in [24] with evaluating several FPGA-based systolic array architectures. Their implementation is 3× faster than the software-only execution. Another hardware acceleration of the BWA-MEM genomics short read mapping for longer read length is stated in [25]. The authors discussed accelerating the seed extension kernel of the BWA-MEM algorithm on a GPU accelerator and achieved up to 1.6× improvement compared to application-level execution time [26]. Power efficiency analysis of accelerated BWA-MEM implementations on heterogeneous computing platform against the software-only baseline system is studied in [27] by offloading the seed extension phase on an accelerator.

Table 2: Profiling the BWA-MEM algorithm [24].

Kernel	Execution time (%)	Bound
SMEM generation	56	Memory
Seed extension	32	Computational
Output generation	9	Memory
Other	3	I/O

A high-performance FPGA-based Seed Extension IP core is designed [28] for BWA-MEM DNA alignment that achieves 350× speedup than an Intel Core i5 general-purpose processor. Authors gain up to 14.5× speedup than the SW algorithm by :(a) Applying heuristics; (b) Processing MEMs, and (c) Extracting MEMs by using a bit-level parallel method [29]. It is considered that after all these works, the problem of memory accessory, area overhead, time, and power consumption of the alignment algorithms methods and implementations are still extremely problematic. Thus, we aimed these problems in our work, and by our suggested methods, improved all of the problems mentioned above.

3. PROPOSED DESIGN

This section describes the proposed method for filling the similarity matrix of the SW-based algorithm and shows how it can speed up time and reduce power consumption compared to state-of-the-art architectures. Besides, our method uses an unfixed length strategy that can leads to higher speedup due to it does not need to be reconfigured for different reads lengths.

There is a new data representation that is used for a broad class of optimization problems which is called "race logic." This method can be used for the kind of problems that use dynamic programming algorithms to be solved. There are different implementations of race logic, such as synchronous and asynchronous, which we focus on synchronous type for our design. Race logic idea is based on the race conditions in a circuit to optimize computation in case of time.

We designed an SW similarity matrix with the idea of the race logic design. Also, we use MEMRISTOR instead of conventional, complementary metal-oxide-semiconductor (CMOS), which leads to better performance. In addition, we considered Field-Programmable Nanowire Interconnect [30] Architecture as our matrix output. Significantly, we achieve lower power consumption and area overhead due to using a MEMRISTOR structure compared to the previous CMOS, ASIC, and FPGA structures mentioned in the results. Moreover, we gain lower delay as a result of

I. Using MEMRISTOR structure that is using race logic strategy which leads to lower circuit delay.

II. Utilization of FPNI as a flexible output that bypasses the system's reconfiguration procedure for reads with different lengths.

3.1. Algorithm Description

First, we describe the main idea of our design and show how it can lead to a proper answer to the SW-like matrix with performance improvement. As we know, the SW algorithm is a dynamic programming algorithm that can compute the alignment score (Levenshtein distance) of two reads and

partial-reference genome string with the Q, R length, respectively. For calculating the scoring alignment of these two strings, the algorithm constructs a matrix S that is a lattice of size IQ × IR (IQ, IR are the length of two strings). With the recursive equation, it can calculate the minimum edit distance between two strings. Notice that in the BWA-MEM algorithm, which is in our consideration for implementing our proposed design, the length of two strings is as same as each other, and we have a Square matrix in each solution. But its dimension may be different based on the length of the reads. We solve this problem by using FPNI as a flexible output of the circuit which helps us earn all the outputs of different matrix dimensions without any problem to change the circuit of any reconfigurations.

$$DP_{(i,i)} = MIN \begin{Bmatrix} DP_{(i-1,i-1)} + T_{(Match,Miss-match)} \\ DP_{(i-1,i)} + T_{(Gap)} \\ DP_{(i,i-1)} + T_{(Gap)} \end{Bmatrix} \quad (1)$$

where DP denotes the similarity matrix, $T_{(Match,Miss-match)}$ is the assigned score for when a match or a mismatch occurs (usually 0 for a match and a 2 for a mismatch [23]), and $T_{(Gap)}$ is the gap penalty with the usual one value [23]. It is worth mentioning that Match is for a situation where two corresponding nucleotides are the same as each other, and Miss-match states that they are not the same. Notice that we can choose these parameters to optimize the accuracy of the alignment based on the structure of the sequences compared [31-33]. Besides, we use fixed penalties for the gap between nucleotides with the more commonly used value [33]. The above equation, which is representative of the SW similarity matrix local alignment, leads to finding the largest sub-string of R, which is mapped with string Q with the lowest Levenshtein distance (LD) (See [34,35] for more information). However, this method is accurate and yields optimal alignment with high computational complexity. To overcome this problem, we can replace the LD values in (1) with their equivalent propagation delays and use the delay-based approach for addition and minimization. Accordingly, these two operations (addition and minimization) are necessary for recursive (1).

We give some examples of how the addition and minimization operations can be modeled by the race logic strategy for more clearance (Fig. 1).

Suppose that we have two signals (M and N) set to logic value '1' (inject a high signal) at different times. This time delay is representing the different values of these two signals. For example, consider that the signal M is set to '1' with a specific time delay (time delay = D1) that means the value of M is "D1" and the second signal is set after D2 second-time delay (time delay = D2) that mean N value is "D2".

I. If we want to add these two values with each other, we can combine the circuit elements of M and N in series. That means the total propagation delay of the output results from adding "D1" with "D2".

II. If we connect these two circuit elements to an OR gate, the signal that arrives first to OR gate emerges out of that. This structure is a Viewer of the minimization operator. Because both signals have the '1' value and the signal which have less amount of delay, will arrive first to OR gate and make the output of this gate '1' earlier.

III. For calculating the output value, we can place a counter at the end of our race logic design that serves as a decoder [23].

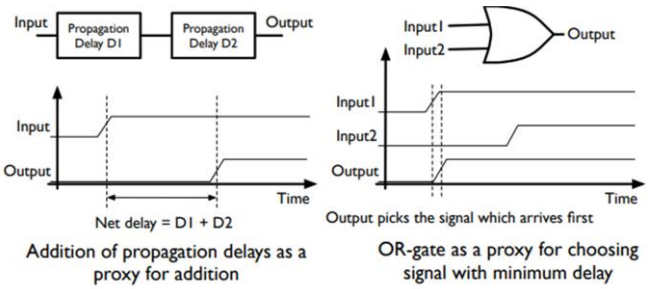

Fig. 1: Computing with propagation delays: Delay-based proxy for the addition operator is a series connection, and the proxy for the min operator is the OR gate [23].

We can apply these delay-based computations to SW similarity matrix of LD calculation. So, the delay between the rising edge of the input signal in the lattice and its emergence at any element on the last row is the minimum score of the local alignment.

3.2. Proposed Architecture

Fig. 2 demonstrates our accelerated architecture. It includes some basic cells to easily implement the desired functionality and a routing network to access some predefined basic cells' output. More details about the different parts of our proposed architecture will be presented in the following:

3.2.1. MEMRISTOR-element

Memristors [36] are new two-terminal logical and scientific basis and fourth classical circuit elements like resistors, inductors, and capacitors.

Memristors are changeable resistors that can be used for memory. In this case, the resistance will be stored as data. We can also use Memristive devices [37] in other applications such as logic and analogue circuits.

We can refer to some points of using memristors instead of CMOS circuits in our race logic:

I. With these devices, we can read and write data faster than CMOS circuits [38].

II. They are typically small devices. Hence, the CMOS circuits are usually bigger than the memristive-based circuits.

III. Nonvolatility is the main feature of memristors and their compatibility with standard CMOS technology [39]. They are either ideal for FPGA-like applications.

From above, we can conclude that memristive devices provide nonvolatile, dense, fast, and power efficiency to solving many major problems of the semiconductor devices.

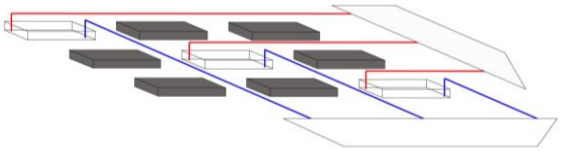

Fig. 2: Accelerated architecture.

Consider that we make a programmable design in which the user can set the corresponding delay of "match", "mismatch", and "gap" penalties. For example, when we know that the most nucleotide comparisons are Match, we can encode in how "match" delay has' 0' time delay, which ensures that large portions of our SW matrix are taken zero time to be explored. Different values for penalties help us to optimize the search time.

3.2.2. *Basic cells*

The schematic of our proposed cell is shown in Fig. 3. Accordingly, it includes three delay elements (DM, DI, DD) responsible for the mathematical operations of (1), respectively; a comparator/selector unit to compare the value of two nucleotides that are the inputs of each matrix cell and decides if Match or mismatch occurs, one local OR gate to implement the Min operation in (1), and one global OR gate to give us the flexibility of choosing output from different stages of the SW matrix.

3.2.3. *The comparator/selector unit*

This section includes several CMOS XNOR gates, and a memristor-based NAND gate to compare the "Ref" and Read" data. Also, the multiplexer controlled by the comparator stage's output defines the corresponding Match or mismatch penalty as its output. When the output value of the comparator becomes "0", this means the "Ref" data is equal to the "Read" data, and the proportional delay value for Match (which can be defined by the user in our design) goes out as output of the selector unit. The structure of our proposed comparator/selector unit is shown in Fig. 4.

3.2.4. *The delay element (DE)*

Delay elements are composed of:

I. Three input wavefront, which is the representation of the input signals and are the results of the preceding DEs in grid

II. Two corresponding nucleotides as input signals which have to be compared by the element

III. Three input signals representing the (Match, Mismatch, Gap penalty) values

IV. One output signal (global OR gate) which represent the output of the (1) ($DP_{(i,j)}$)

V. One output signal (local OR gate) which is designed to perform our desired flexible matrix output and used for local alignment.

The propagated output wavefront of each DE is a delay signal considering the corresponding match, mismatch, and gap delay penalties. When the other DE's outputs or signal

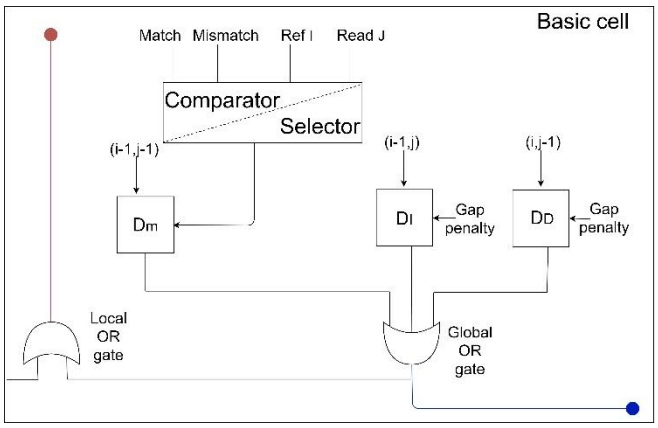

Fig. 3: Basic cell of our proposed design.

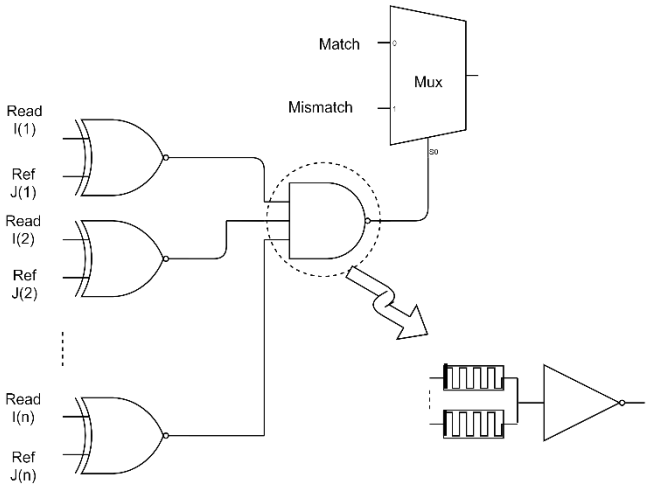

Fig. 4: Comparator/selector unit.

wavefront reaches an element, a delay is created based on the gap penalty specified for match/mismatch and gap penalty by propagating the signals through the memristors. The other advantage of our design is that it allows the user to program (i.e., dynamically set at runtime) the value of the Match, mismatch, and gap penalty based on the different applications and give the flexibility to use our approach in cases that merely require re-parameterization of the gap-penalties. The structure of our proposed delay element is shown in Fig. 5. It includes some delay elements to build different delays and a multiplexer to select the desired delay. As shown in Fig. 5, we have used memristors to implement the delay elements to reduce the area overhead.

3.2.5. *Local OR gate*

The local OR gate is used to make it possible to avoid unnecessary latency that is due to the variable input length. OR gate is a proxy for minimization operator, which emerges out the signal that arrives first at the gate. As shown in Fig. 6, to reduce the area overhead, we have used a memristor-based OR gate for this sake.

3.2.6. *Global OR gate*

The global OR gate is used to implement the minimization operation in (1). The structure of our proposed global OR gate is shown in Fig. 6. We have used a memristor-based OR gate for this sake to reduce the area overhead.

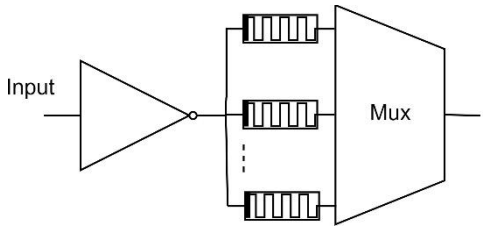

Fig. 5: Delay element unit that includes some delay elements to build different delays and a multiplexer to select the desired delay.

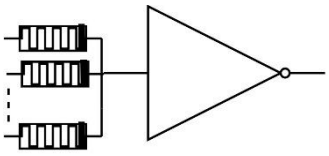

Fig. 6: Structure of memristor base OR gate in our design.

3.2.7. The routing network

Needleman and Wunsch [15] and Smith and Waterman [9] algorithms are well-known dynamic programming algorithms that lead to optimum global and local alignment of a read against the reference genome. A similarity matrix is filled in these approaches that have to find the local and global alignment score of reads against the corresponding reference sub-string [8]. Consider the practical scenario that read data has at most 150 base pairs (bp) for our comparison. Then we construct our similarity matrix with 131×131 dimension based on the BWA-MEM approach. We desire that the processing time of filling the similarity matrix kernel be independent of the read length but because of the fixed similarity matrix dimension, for shorter reads, we incur unnecessary latency.

To avoid this unnecessary latency, we have to contemplate a method that can be flexible with different read lengths and get output ready from the desired dimensions of the similarity matrix. Therefore, we can omit the unnecessary latency, which is the reason for not traveling through the entire elements irrespective of their length.

The original race logic design was demonstrated in simulation as an ASIC [14]. Even though this method has advantages in power consumption and substantial improvement in throughput in comparison of the state-of-the-art systolic implementations, but it suffers from the following problems:

I. The original race logic design uses conventional, complementary metal-oxide-semiconductor (CMOS) with size, power consumption, read and write time problems, and our approach.

II. Traveling through the entire elements irrespective of their length with the fixed similarity matrix dimension design that incurs unnecessary latency for shorter read size.

Our proposed accelerator is runtime-programmable for changing the input data size, which defines the size of the accelerator lattice. For this sake, we have used a nanowire-based routing network which is inspired by the FPNI technique [30]. Field-programmable nanowire interconnect (FPNI) is a new hybrid structure with advantages that are mentioned below:

I. high flexibility

II. low fabrication cost

By this technique, we can change the size of the accelerator lattice during the runtime according to the input data size. As shown in Fig.4, our proposed routing network includes some nanowires to access the output of some predefined basic cells and a selection unit controlled by the input data size to select the desired output. Each nanowire is connected through a "via" to the output of the local OR gate in the desired basic cell.

4. RESULTS

In this section, the simulation results of the proposed method will be compared with some well-known approaches. Performance of the mentioned methods is evaluated using several criteria such as area, delay, and power consumption. In Fig. 7, the numerical results of the proposed structure for delay parameter are compared with state-of-the-art systolic arrays and race logic design. In general, these are two of the best implementations of dynamic programming methods that achieve accuracy and speedup. Therefore, we compare our design to show the consummate performance of our work.

More details about each of the evaluation criteria will be presented in the following.

4.1. Area

To compute the occupied area of the mentioned methods, we have used the transistor counting technique in 65nm technology. According to the presented results in Table 3, the

Table 3: Occupied area of three methods in nm based on the transistor counting technique in 65nm technology

Read Length	Proposed	Systolic	Race logic
1	8.51E+02	7.34E+04	9.18E+03
2	3.40E+03	1.18E+05	2.09E+04
4	1.36E+04	2.34E+05	7.31E+04

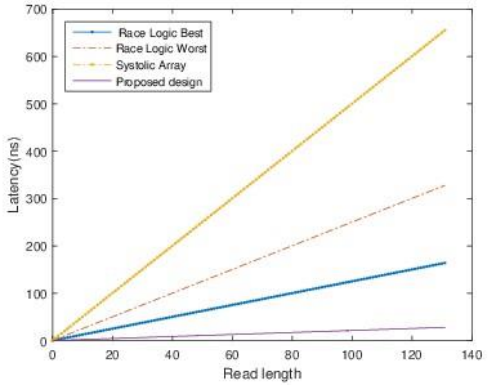

Fig. 7: Latency of the proposed method compared to the state-of-the-art systolic array and race logic designs.

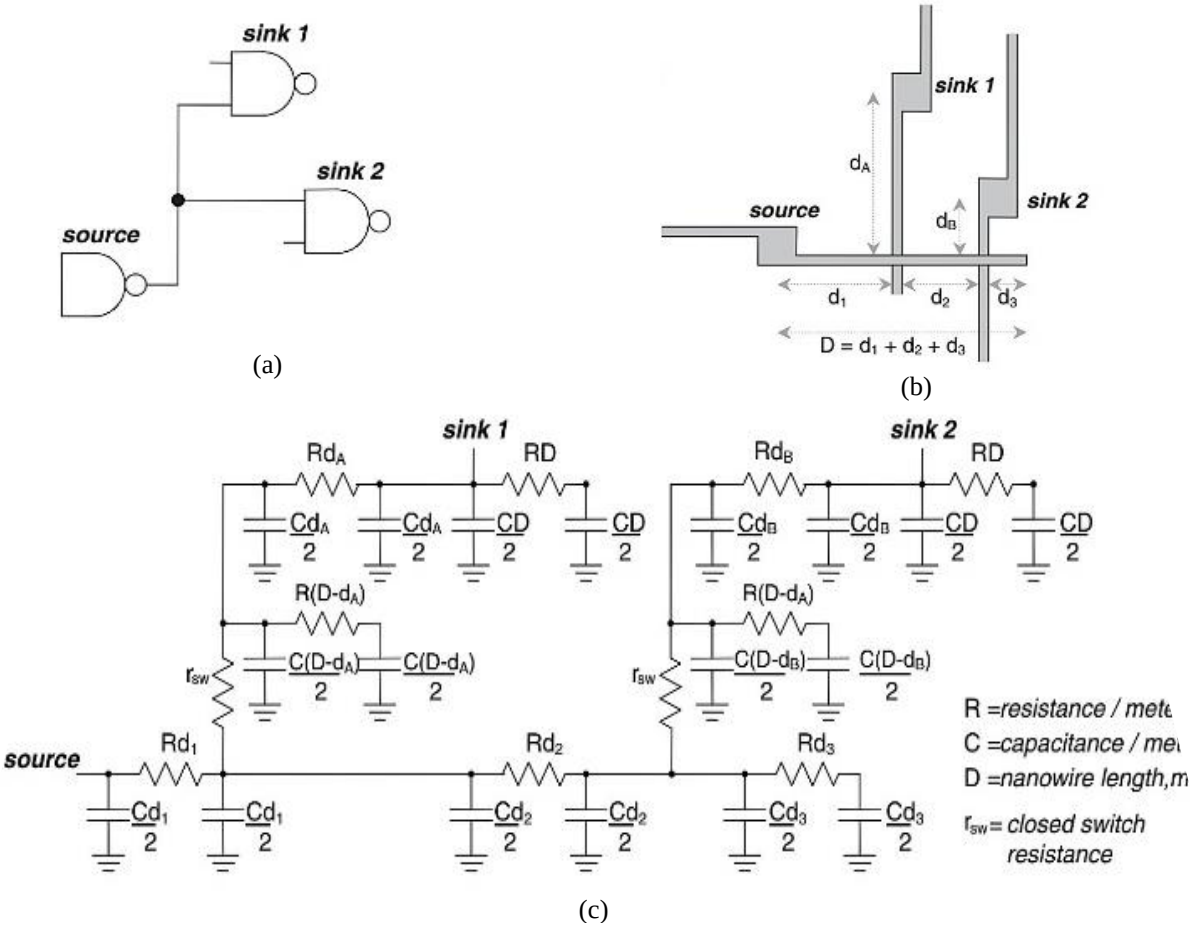

Fig. 8: (a) A signal with a fan-out of 2 (b) the implemented form by the nanowires (c) the electrical model [40].

4.2. Power Consumption

occupied area of the proposed method is compared with two other methods, and the results show that we achieve up to 10fold area improvement.

4.3. Delay

We need an electrical model of the nanowires, junctions, and CMOS components to calculate the delay of the proposed structure. For this sake, we have used the electrical model proposed in [40] for the FPNI structure. The electrical model for a simple circuit is shown in Fig. 8. Some of the model parameters such as closed junction resistance, the capacitance and resistance per unit length and geometry of the wires are also listed in Table 4 [40]. In this paper, we have used the HSpice tool to calculate the delay of the proposed structure. The presented results in Fig. 9 show how our design flaunts himself in case of fixed length matrix dimension implementation.

Power consumption of the proposed structure is evaluated using the formula presented in [40]:

$$Dynamic - power = \frac{1}{2} ANCV_{dd}^{2} f \qquad (2)$$

where A is the average 'activity' of a signal, N is the number of allocated nanowires, C is the capacitance of a single nanowire, V_{dd} is the supply voltage used by the CMOS, and f is the maximum clock frequency determined by timing analysis. To calculate the power consumption of the proposed

Table 4: Experimental parameters for FPNI architecture [40]

Parameter	Description	FPNI 30 nm
Pnano	Nanowire pitch	30 nm
Wnano	Nanowire width	15 nm
Wpin	Pin diameter	90 nm
Wpinvar	Pin size variation	20 nm
Walign	Alignment error	40 nm
Wsep	Pin/wire separation	15 nm
Rclosed	Closed junction resistance	24 K
p	On/off resistance ratio	>200
	Nanowire resistivity	8u cm
	Nanowire length	7115 nm
	Nanowire resistance	2.53 K

structure, we have used the HSpice tool. According to the presented results in Fig. 10, we compare our design with systolic arrays and the race logic approach. Results show those designs are power-hungry compared to our memristor-base design.

5. Conclusion

We present a new memristor-based SW matrix implementation that achieves more than six times speedup compared to the state-of-the-art race logic approach and 22

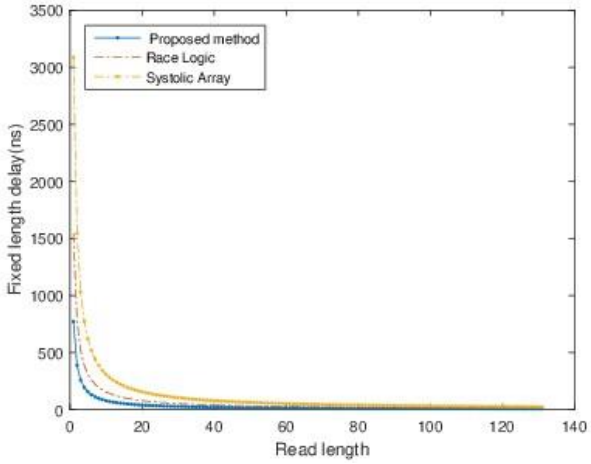

Fig. 9: Delay ratio of the proposed method, Systolic array, and race logic considering the fixed 131×131 SW matrix dimension in different read lengths.

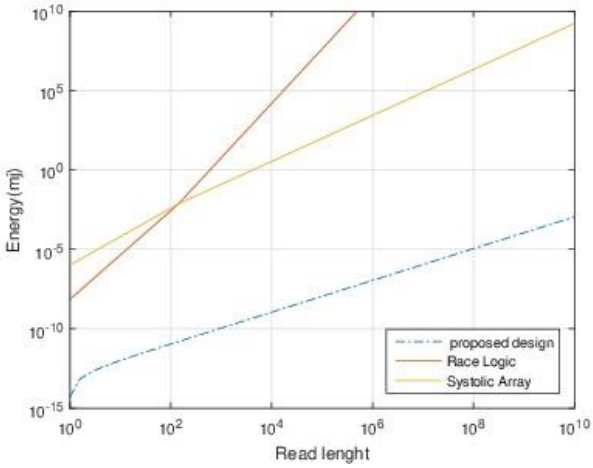

Fig. 10: Power consumption of our proposed design in comparison of Systolic arrays and race logic design.

times speedup than the systolic arrays implementation. We show how our design gives this flexibility to get the matrix output depending on the different input dimensions without unnecessary latency. Our implementation achieves up to 600x speedup with considering the fixed 131×131 SW matrix dimension by testing different read lengths. We also achieved at least 10x improvements in area overhead and also 10^5x improvements in power. Furthermore, our approach can be more practical and optimum in presenting programmable penalty matches, which gives the initiative to change them based on the biological application.

CRediT Authorship Contribution Statement

Mahdi Taheri: Conceptualization, Formal analysis, Methodology, Resources, Roles/Writing - original draft, Writing - review & editing. **Hamed Zandevakili:** Formal analysis, Software, Writing - review & editing. **Ali Mahani:** Project administration, Supervision, Writing - review & editing.

Declaration of Competing Interest

The authors declare that they have no known competing financial interests or personal relationships that could have appeared to influence the work reported in this paper. The ethical issues, including plagiarism, informed consent, misconduct, data fabrication and/or falsification, double publication and/or submission, redundancy, have been completely observed by the authors.

References

[1] M. Taheri, and A. Mahani, "Development and hardware acceleration of a novel 2-D BWA-MEM DNA sequencing alignment algorithm", in *The First Conference on Applied Research in Electrical Engineering*, Iran, 2021.

[2] J. Giles, "Computational social science: Making the links", *Nature*, vol. 488, no. 7412, pp. 448-450, 2012.

[3] Z. D. Stephens, S. Y. Lee, F. Faghri, R. H. Campbell, C. Zhai, M. J Efron, R. Iyer, M. C. Schatz, S. Sinha, and G. E. Robinson, "Big data: astronomical or genomical?", *PLoS Biology*, vol. 13, no. 7, 2015.

[4] B. Langmead, C. Trapnell, M. Pop, and S. L. Salzberg. "Ultrafast and memory-efficient alignment of short dna sequences to the human genome", *Genome Biology*, vol. 10, no. 3, pp. 1-10, 2009.

[5] H. Li, and R. Durbin, "Fast and accurate short read alignment with burrows– wheeler transform", *Bioinformatics*, vol. 25, no. 14, pp. 1754–1760, 2009.

[6] H. Li, J. Ruan, and R. Durbin, "Mapping short dna sequencing reads and calling variants using mapping quality scores", *Genome Research*, vol. 18, no. 11, pp. 1851– 1858, 2008.

[7] R. Li, C. Yu, Y. Li, T. Lam, S. Yiu, K. Kristiansen, and J. Wang. "Soap2: an improved ultrafast tool for short read alignment", *Bioinformatics*, vol. 25, no. 15, pp. 1966–1967, 2009.

[8] H. Li, "Aligning sequence reads, clone sequences and assembly contigs with bwa-mem", arXiv preprint arXiv:1303.3997, 2013.

[9] T. .F Smith, M. S. Waterman, "Identification of common molecular subsequences", *Journal of Molecular Biology*, vol. 147, no. 1, pp. 195–197, 1981.

[10] T. W Lam, W. Sung, S. Tam, C. Wong, and S. Yiu, "Compressed indexing and local alignment of dna", *Bioinformatics*, vol. 24, no. 6, pp. 791– 797, 2008.

[11] W. J. Kent, "Blat—the blast-like alignment tool", *Genome Research*, vol. 12, no. 4, pp. 656– 664, 2002.

[12] V. Marx, "Biology: The big challenges of big data", vol. 498, no. 7453, pp. 255-260, 2013.

[13] S. F. Altschul, T. L. Madden, A. A. Schäffer, J. Zhang, Z. Zhang, W. Miller, and D. J. Lipman, "Gapped blast and psi-blast: a new generation of protein database search programs", *Nucleic Acids research*, vol. 25, no. 17, pp. 3389–3402, 1997.

[14] W. R. Pearson, and D. J. Lipman, "Improved tools for biological sequence comparison", *Proceedings of the National Academy of Sciences*, vol. 85, no. 8, pp. 2444–2448, 1988.

[15] W. Wilbur, and D. J. Lipman, "The context dependent comparison of biological sequences", *SIAM Journal on Applied Mathematics*, vol. 44, no. 3, pp. 557–567, 1984.

[16] R. K. Singh, DL Hoffman, S. G. Tell, and C. Thomas White, "Bioscan: a network sharable computational resource for searching biosequence databases", Bioinformatics, vol. 12, no. 3, pp.191–196, 1996.

[17] A. Madhavan, T. Sherwood, and D. Strukov, "Race logic: A hardware acceleration for dynamic programming algorithms", in *2014 ACM/IEEE 41st International Symposium on Computer Architecture*, 2014, pp. 517–528.

[18] E. Rucci, C. Garcia, G. Botella, A. De Giusti, M. Naiouf, and M. Prieto-Matias, "Swifold: Smith-waterman implementation on fpga with opencl for long dna sequences", BMC systems biology, vol. 12, no. 5, pp. 96, 2018.

[19] F. Zokaee, H. R Zarandi, and L. Jiang, "Aligner: A process-in-memory architecture for short read alignment in rerams," *IEEE Computer Architecture Letters*, vol. 17, no. 2, pp. 237–240, 2018.

[20] M. Taheri, M. S. Ansari, S. Magierowski, and A. Mahani, "Hardware acceleration of the novel two dimensional burrows-wheeler aligner algorithm with maximal exact matches seed extension kernel", *IET Circuits, Devices and Systems*, vol. 15, no. 2, pp. 94-103, 2021.

[21] M. Alser, H. Hassan, H. Xin, O. Ergin, O. Mutlu, and C. Alkan, "Gatekeeper: a new hardware architecture for accelerating pre-alignment in dna short read mapping", *Bioinformatics*, vol. 33, no. 21, pp. 3355–3363, 2017.

[22] M. Farrar, "Striped smith–waterman speeds database searches six times over other simd implementations," *Bioinformatics*, vol. 23, no. 2, pp. 156–161, 2006.

[23] S. S. Banerjee, M. El-Hadedy, J. Bin Lim, Z. T. Kalbarczyk, D. Chen, S. S Lumetta, and R K Iyer, "Asap: accelerated short-read alignment on programmable hardware", *IEEE Transactions on Computers*, vol. 68, no. 3, pp. 331–346, 2018.

[24] E. J. Houtgast, V. Sima, K. Bertels, and Z. Al-Ars, "An fpga-based systolic array to accelerate the bwa-mem genomic mapping algorithm", in *2015 International Conference on Embedded Computer Systems: Architectures, Modeling, and Simulation (SAMOS)*, 2015, pp. 221–227.

[25] E. J. Houtgast, V. Sima, K. Bertels, and Z. Al-Ars, "Hardware acceleration of bwa-mem genomic short read mapping for longer read lengths", *Computational biology and chemistry*, vol. 75, pp. 54–64, 2018.

[26] E. J. Houtgast, V. Sima, K. Bertels, and Z. Al-Ars, "Gpu accelerated bwa-mem genomic mapping algorithm using adaptive load balancing", in *International Conference on Architecture of Computing Systems*, 2016, pp. 130– 142.

[27] E. J. Houtgast, V. Sima, G. Marchiori, K. Bertels, and Z. Al-Ars, "Power-efficiency analysis of accelerated bwa-mem implementations on heterogeneous computing platforms", in *2016 International Conference on ReConFigurable Computing and FPGAs (ReConFig)*, 2016, pp. 1–8.

[28] C. Pham-Quoc, B. Kieu-Do, and T. Ngoc Thinh, "A high-performance fpga-based bwa-mem dna sequence alignment", *Concurrency and Computation: Practice and Experience*, vol. 33, no. 2, e5328.

[29] A. Bayat, B. Gaëta, A. Ignjatovic, and S. Parameswaran, "Pairwise alignment of nucleotide sequences using maximal exact matches", *BMC bioinformatics*, vol. 20, no. 1, pp. 1-15, 2019.

[30] H. Zandevakili and A. Mahani, "A new asic structure with self-repair capability using field-programmable nanowire interconnect architecture", *IEEE Transactions on Very Large Scale Integration (VLSI) Systems*, vol. 26, no. 11, pp. 2268–2278, 2018.

[31] C. Wang, R. Yan, Xi. Wang, Jing-Na Si, and Ziding Zhang, "Comparison of linear gap penalties and profile-based variable gap penalties in profile–profile alignments", *Computational biology and chemistry*, vol. 35, no. 5, pp. 308–318, 2011.

[32] S. Henikoff and J. G Henikoff, "Amino acid substitution matrices from protein blocks", *Proceedings of the National Academy of Sciences*, vol. 89, no. 22, pp. 10915– 10919, 1992.

[33] W. Sung, "*Algorithms in bioinformatics: A practical introduction*," CRC Press, 2009.

[34] G. Navarro, "A guided tour to approximate string matching", *ACM computing surveys (CSUR)*, vol. 33, no. 1, pp. 31–88, 2001.

[35] V. I Levenshtein, "Binary codes capable of correcting deletions, insertions, and reversals", in *Soviet physics doklady*, vol. 10, no.8, pp. 707–710, 1966.

[36] L. Chua, "Memristor-the missing circuit element", *IEEE Transactions on circuit theory*, vol. 18, no. 5, pp. 507–519, 1971.

[37] L. O. Chua, and S. Mo Kang, "Memristive devices and systems", *Proceedings of the IEEE*, vol. 64, no. 2, pp. 209–223, 1976.

[38] A. C Torrezan, J. Paul Strachan, G. Medeiros-Ribeiro, and R S. Williams, "Sub-nanosecond switching of a tantalum oxide memristor", *Nanotechnology*, vol. 22, no. 48, pp. 1-7, 2011.

[39] J. Borghetti, Z. Li, J. Straznicky, X. Li, D. AA Ohlberg, W. Wu, D. R. Stewart, and R. S. Williams, "A hybrid nanomemristor/transistor logic circuit capable of self-programming", *Proceedings of the National Academy of Sciences*, vol. 106, no. 6, pp. 1699–1703, 2009.

[40] G. S. Snider, and R. S. Williams, "Nano/cmos architectures using a fieldprogrammable nanowire

interconnect", *Nanotechnology*, vol. 18, no. 3, 035204, 2007.

BIOGRAPHY

Mahdi Taheri received the B. Sc. degree in electronic engineering from Khaje Nasir University of Technology (KNTU), Tehran, Iran, in 2017 and The M.Sc. degree in Electronic Engineering from Shahid Bahonar University of Kerman, Kerman, Iran, in 2020. Since then, he has been with the RSS Lab at shahid bahonar university of Kerman for one year, and now, he is studying his Ph.D. at Tallinn University of Technology (TalTech). His research interests focus on Hardware assessment and reliability of neural networks, Fault-tolerant design, and FPGA-based accelerators.

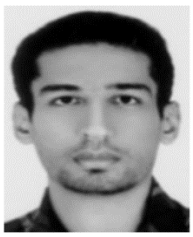

Hamed Zandevakili received an M.S. degree in electronic engineering from Shahid Bahonar University, Kerman, Iran, in 2013. Since September 2014, he has been a Ph.D. student in the Department of Electrical Engineering at Shahid Bahonar University of Kerman, Iran. His research interests include reliable computing, VLSI testing, and reconfigurable computing.

Ali Mahani received the B. Sc. degree in electronic engineering from Shahid Bahonar University of Kerman, Iran, in 2001, The M.Sc. and Ph.D. degrees both in Electronic engineering from Iran University of Science and Technology (IUST), Tehran, Iran, in 2003 and 2009 respectively. Since then he has been with the electrical engineering department of shahid bahonar university of kerman, where he is currently an associate professor. His research interests focus on Fault tolerant design, FPGA-based accelrators, approximate digital circuits, stochastic computing and Networked Systems.

Copyrights
© 2021 Licensee Shahid Chamran University of Ahvaz, Ahvaz, Iran. This article is an open-access article distributed under the terms and conditions of the Creative Commons Attribution –NonCommercial 4.0 International (CC BY-NC 4.0) License (http://creativecommons.org/licenses/by-nc/4.0/).

Shahid Chamran University of Ahvaz

Iranian Association of Electrical and Electronics Engineers

Journal of Applied Research in Electrical Engineering

E-ISSN: 2783-2864
P-ISSN: 2717-414X
Homepage: https://jaree.scu.ac.ir/

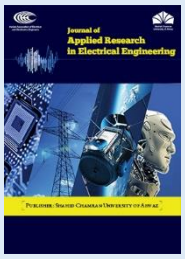

Research Article

A Novel Energy-Efficient Weighted Multi-Level Clustering Protocol

Ebrahim Farahmand, and Ali Mahani *

Department of Electrical Engineering Shahid Bahonar University of Kerman, Kerman 76169133, Iran

** Corresponding Author: amahani@uk.ac.ir*

Abstract: Wireless sensor networks (WSNs) consist of a large number of sensor nodes that allow users to accurately monitor a remote environment by aggregating the data from the individual nodes. These networks require robust and energy-efficient protocols that are improved reliability and lifetime of WSNs. Clustering of sensor nodes is an emerging paradigm for the energy-efficient approach to improve lifetime and the reliability of WSN by reducing energy consumption. In this paper, a new Energy-efficient weighted multi-level Clustering Protocol (EWCP) is proposed. Cluster heads (CHs) are selected based on the allotted weight to each sensor nodes. The weight includes the parameters of sensors such as density, residual energy, and distance to prolong the network's lifetime and increase its efficiency. Also, the cluster members are selected based on their distance to the selected CHs. The lifetime of EWCP is improved significantly to compare with the other protocols. This improvement is attributed to the fact that EWCP is energy-efficient in clustering protocol.

Keywords: Wireless sensor networks (WSNs), clustering of WSNs, weight-based clustering.

Article history
Received 24 December 2020; Revised 21 April 2021 Accepted 02 June 2021; Published online 29 June 2021.
© 2021 Published by Shahid Chamran University of Ahvaz & Iranian Association of Electrical and Electronics Engineers (IAEEE)

How to cite this article
E. Farahmand, and A. Mahani, "A novel energy-efficient weighted multi-level clustering protocol," *J. Appl. Res. Electr. Eng.*, vol. 1, no. 1, pp. 69-78, 2022. DOI: 10.22055/jaree.2021.36169.1019

Check for updates

1. INTRODUCTION

In recent decades, remote sensing systems have taken into consideration in the academic and industrial community. The sensor is equipment to study the surrounding environment. They can sense the possible changes in the environment, detect events, and provide an appropriate output. Sensor nodes are the fundamental elements in Wireless Sensor Networks (WSNs) which constructed from transceiver, microcontroller and power sources [1]. The sensor nodes gather data from the environment and, the practical information can be taken from the sensors by extra process on data. Sensor network [2] include a massive number of sensors that are deployed and communicated wireless with each other. These networks consist of a huge number of nodes to aggregate and send data from an unaccessible environment to Base Station (BS) – which is called also sink.

In most application of WSNs, especially when sensor nodes are deployed in inaccessible areas, sensor nodes have a non-rechargeable and non-replaceable battery. Hence, WSNs are constrained with a limited sensor nodes' energy capacity. In order to extend the lifetime, WSNs and efficient deployment of power sources, all aspects of the network should be designed accurately. In this regards, routing protocols are crucial in WSNs [3]. Usually, routing protocols based on network structure are divided into two main groups: flat and hierarchical routing [4]. Here, the hierarchical routing protocols, also known as cluster-based routing. This technique is proved to be a smart solution to optimise energy consumption in WSNs, which can help these networks improve the lifetime and scalability of these networks.

Generally, in clustering algorithms, the nodes split into various groups called clusters. These networks consist of three pillar components: 1. Clusters, 2. Cluster Heads (CHs) and 3. Base station (BS) [5].

The clustering algorithms provide an efficient and reliable routing between sensor nodes and BS [6]. The routing of clustering technique is as follows: first, all cluster members aggregate data from the environment and send them to their assigned cluster heads based on a given routing table. Then, CHs sent the data to the other CHs or BS using the shortest route. Hence, this routing strategy provides low bandwidth usage. The communication between cluster members and assigned CH called internal communication which can be a hybrid of single- or multi-hop communication protocol [1,7]. Also, the communication between CHs and BS called external communication. These communications, same as

internal communication, can be single- or multi-hop communication protocol.

In the single-hop communication protocol, all nodes can send data directly to BS. This communication protocol causes some drawbacks, such as a large transmitting domain and high energy consumption during the transmitting. Therefore, due to the limited source of nodes' energy, the multi-hop communication can be considered a suitable alternative to address the single-hop communication drawbacks. In the multi-hop communication protocol, the transmitting domain of CHs is limited by sending data in several hops to reach BS.

All these two communication protocols have an inevitable challenge of imbalanced energy consumption, resulting in problems such as the increased concentration of data transmission in part of the network and poor performance of the network lifetime. Clustering algorithms consider several criteria to control energy consumption WSNs. These criteria include energy, lifetime calculations, number of hops, distance from CHs, and control form, i.e., centralised or distributed control schemes [8]. Hence, the clustering algorithm is designed to solve problems such as minimising cluster size, CHs selection or re-selection, and operation and maintenance of clusters.

In WSNs, CHs consume the highest energy consumption than other nodes due to their communication with the base station. The major drawback in existing clustering protocols is inefficient distributed CHs. The inefficient distributed CHs cause CHs are located near to each other or close to the edge of a network, or CHs are located in a spars area. When CHs are near each other, data transmission concentration in the area and the energy consumption is increased. In this situation, data traffic of CHs are heavy, and the risk of draining of their energy is increased [9].

If CHs are located close to the edge of a network, the time of data transmitting is increased. Also, if CHs are located in a spars area, the data transmitting range of those CHs are increased. Thus, high data transmitting time and range lead to depleting the energy of nodes.

To address these drawbacks, an optimal clustering protocol is proposed in this paper. The main focus of the proposed EWCP is to select optimal cluster heads by considering minimise the energy consumption and routing method together to enhance the lifetime of WSNs. In the proposed EWCP, the optimal CHs are selected based on the distance from BS, nodes' energy level, and network density. After that, the members for each cluster are chosen based on the distance between nodes and CHs. Moreover, the routing method based on hierarchical clustering protocol has more capability for scalability and communication. This method is adopted to design the proposed protocol.

The remainder of this paper is organised as follows: An overview of related work on clustering protocol provides in section 2. The proposed protocol describes in section 3, which includes the energy dissipation model and network model applied in this paper. Section 4 discusses applying the proposed clustering protocol to the sample network and comparing the protocol with some other clustering protocols. Eventually, Section 5 explain concluding remarks.

2. RELATED WORK

In this section, we review some literature that proposed some clustering protocols to enhance the lifetime of WSNs by reducing energy consumption.

The primary clustering protocol for WSNs is Low Energy Adaptive Clustering Hierarchy (LEACH) protocol proposed by Heinzelman and et al. in [10]. LEACH protocol selects and rotating CHs with the random number. This protocol is a distributed scheme design. Since decisions on, it is still plausible that sensor nodes with low residual energy are selected as CHs. LEACH protocol impossible to ensure that cluster heads are distributed optimally over the network. A various number of the enhanced model of LEACH have been proposed, e.g., HEED [11], TEEN [12] and PEGASIS [13], to overcome mentioned issues. The aim of the proposed Distributed Weight-based Energy-efficient Hierarchical Clustering (DWEHC) protocol in [14] is to develop Hybrid Energy Efficient (HEED) protocol by constructing clusters with balanced size and optimising the topology of clusters. The weight is a locally calculated parameter used as a criterion in CH election and is defined using (1).

$$W_{weight(s)} = \frac{E_{residual(s)}}{E_{initial(s)}} \times \sum_{u} \frac{R-d}{6R} \quad (1)$$

where, $E_{residual}(s)$ and $E_{initial}(s)$ are residual and initial energy levels in sensor node *s*, respectively. *R* is the cluster range, and *d* is the distance from node *s* to neighbouring node *u*. Therefore, this protocol is not appropriate for a network with a large area because of its enormous energy consumption. A decentralised energy-efficient hierarchical cluster-based routing protocol that enhances the network's lifetime by protocol comprising a multi-criterion clustering algorithm is proposed in [15]. The protocol contains an Energy-Aware Distributed Clustering EADC algorithm is presented in [16], which can be applied in WSNs with non-uniform node distribution. The protocol includes an energy-aware clustering algorithm and a cluster-based routing algorithm. The whole process is divided into three phases: information collection phase, cluster head competition phase, and cluster formation phase. The protocol initially selects fixed CHs using two weights, including energy and distance to the other nodes. Tang, Chengpei, *et al.* [17] proposed a collaborative weighted clustering algorithm (CWCA) weighted clustering protocol. It used in monitoring the oil pipeline. In this method, the weight of the nodes is assigned by four factors, i.e., degree, Euclidean distance, mobility, and a lifetime of nodes. The weights of nodes are expressed by (2):

$$weight(i) = \alpha_1 \times D_i + \alpha_2 \times P_i + \alpha_3 \times M_i + \alpha_4 \times T_i \quad (2)$$

Consequently, in this equation, the sum of coefficients is one (i.e., $\alpha_1 + \alpha_2 + \alpha_3 + \alpha_4 = 1$) and in the static network without mobility, M_i is assumed zero.

In clustering iterations, this protocol requires a large amount of control overhead compared to the other protocols. The main challenge in clustering algorithms is selecting the optimal CHs. Thus, the computation of selecting the CHs in the large-scale networks is heavy by classical analyses, and it grows exponentially. For example, we need to assess 2^N-1 states to choose optimal CHs for *N* nodes. We can conclude that this mentioned problem is a Nondeterministic

Polynomial NP-hard [18]. Furthermore, to reach the optimal CHs the optimisation methods should search over a vast space. Due to vast space this problem becomes infeasible. Thus, the efficient solutions in dealing with selecting clusters and cluster members is heuristic optimisation algorithms.

Genetic Algorithm-based Optimized Clustering protocol (GAOC) is proposed in [19-20]. The selection of CHs is made by the genetic algorithm (GA), which the fitness function formulates by integrating residual energy, distance to the BS, and node density. Shuffled frog leaping algorithm (SFLA) proposed in [21] to select CH, which reduced energy consumption. Ant Colony Optimizer (ACO) used in ACO Optimized Self-Organized Tree-Based Energy Balance (AOSTEB) to discovers an efficient route during intra-cluster communication [22]. Evolutionary game is used to formulate the clustering machine-type devices [23]. This model decreases the number of redundant bits transmitted to the BS in order to decrease the transmission power. AOSTEB operates in three phases: cluster-formation, multi-path creation, and data transmission. The desired number of sensor nodes is a candidate as cluster heads (CHs) during cluster-formation, and the remaining sensor nodes join the nearest CHs to create a cluster. The optimised route is selected by using the ACO to consider the shortest distance and less energy consumption to initiate the data exchange process within the cluster. In the literature [24], to reduce the energy consumption of the sensor nodes, used ARSH-FATI algorithm, a metaheuristic algorithm to select CHs (ARSH-FATI-CHS). Particle Swarm Optimization (PSO) algorithm implemented at the BS as a centralised method [25]. In this algorithm, both distance and energy consider as multi-objective function. The objective is to minimise the average Euclidean distance between the cluster members and their assigned CHs and the proportion of the total energy consumption of the entire nodes to the total energy sum of the CH candidates. P. C. Srinivasa Rao *et al.* [26] proposed the cluster heads election by PSO algorithms, which is named PSO-ECHS. In this method, the parameters like intra-cluster distance, distance from the sink and residual energy of sensor nodes are considered, so by these parameters, the particles of algorithms are coded. After CHs selection, the clusters are formed, and the members of every cluster should be elected. In CH formation, (3) express the weight assigned to every node, and the nodes with the highest weight are jointed to the CH.

$$CH_{weight(s_i,CH_j)} = \frac{E_{residual}(CH_j)}{dis(s_i,CH_j) \times dis(CH_j,BS) \times node\_degree(CH_j)} \quad (3)$$

In this section, a review of popular clustering protocols in WSNs is presented, and the advantages and disadvantages of each protocol are studied. This paper focuses on using these advantages and addressing some of the aforementioned disadvantages of these protocols. Consequently, the prominent objective of the proposed protocol, i.e., EWCP, is to minimise the network's energy consumption and prolong the network lifetime simultaneously.

3. PROPOSED METHOD

In this section, we explain our clustering method for WSN. The main drawbacks of clustering the WSN are selecting CHs and maximising the network coverage. Before we dive into the details of EWCP, we briefly present the energy model in sub-section 3.1 and the network model, which is adjusted for this protocol in sub-section 3.2.

3.1. Model of Dissipated Energy in One Sensor Node

In this paper, the one node's energy consumption model including dissipated energy in transmitter and receiver of data and control packets. The energy dissipation applied for EWCP is model in [27]. Equations (4) and (5) present energy dissipation in the transmitter and receiver, respectively.

$$E_{Tx}(l,d) = lE_{elec} + l\, e_{amp} d^n \quad (4)$$

$$E_{Rx}(l,d) = lE_{elec} \quad (5)$$

where,

E_{elect} Present the consumption of energy to run the electronic circuit of transmitter /receiver one bit of data.

e_{amp} Present the consumption of energy to run the radio amplifier of the transmitting node to transmit one bit of data.

l Present data package length

d Present distance between the transmitter and receiver

n n sets to 2 and 4 for free space and multi-path fading channel models, respectively.

The selection of energy model between free space model and multi-path fading is made according to the distance threshold value, i.e., d_0. In this paper, we assume the threshold to be 87.7 throughout simulations. Therefore, considering the threshold energy consumption model for both free space and multi-path fading channel models is presented by (6).

$$\begin{cases} E_t = lE_{elec} + l\varepsilon_{emp} d^4 + lE_{DA} & if\ d > d_0 \\ E_t = lE_{elec} + l\varepsilon_{fs} d^2 + lE_{DA} & if\ d \le d_0 \end{cases} \quad (6)$$

where, E_{DA} is the energy consumption to aggregate data. The above energy model use for one sensor node.

3.2. Network Model

The network model with an area of $m \times m$ considered in this protocol includes N sensors distributed randomly in the area and know its location. These sensor nodes include a source of energy that is not rechargeable, and the range of the monitoring and communicating is similar and identical. BS is aware of the positions, energy levels and IDs of all nodes in the network.

The network is split into several layers with a fixed radius, and BS is located at a fixed point. Nodes are uniformly dispersed across the layered network. The network considers as a homogenous network which is shown in Fig. 1. All nodes have similar initial energy and sensing range as same as processing properties.

Fig. 1 is a sample of a *50×50* square network's model with 100 nodes dispersed randomly. The BS node is located at the coordinate of (50,25), and the network is divided into six layers. The nodes shown by × are located in the first layer, and similarly, the nodes are shown by +, □, ◊ and * are located in the second, third, fourth, fifth and sixth layers, respectively.

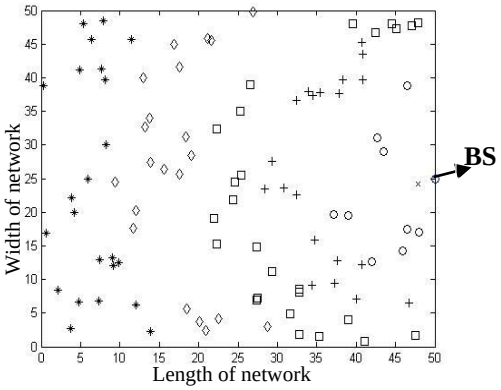

Fig. 1: Network's model with layer and random node distributed.

Once the nodes are distributed over the network, every node finds its neighbouring (the nodes located in its communication radius) by sending a controlling massage. Next, each node creates an information table of its neighbouring nodes, including their residual energy information, associated weight and ID numbers, and saves the table in its memory.

In EWCP, a weight is assigned in every node, which is explained by (7).

$$node.weight = \alpha \times E + \beta \times distance + \delta \times D \tag{7}$$

In (7), E and distance represent the residual energy of node and normalised Euclidean, which is calculated by (8), respectively. D present the density of a node which is calculated using (9). Moreover, α, β, and δ are dynamic coefficients, which dynamically change by the number of rounds in EWCP and can be calculated using (10) to (12).

$$distance = \frac{(max\_distance\_to\_BS) - (distance\_CH\_to\_BS)}{(max\_distance\_to\_BS) - (max\_distance\_to\_BS)} \tag{8}$$

$$D = \frac{the\ number\ of\ neighboring\ CH}{the\ number\ of\ all\ alive\ nodes} \tag{9}$$

$$\alpha = 0.3333 \times \left(\left(\frac{r}{rmax} \right) + 1 \right) \tag{10}$$

$$\beta = \frac{0.3333}{\frac{r}{rmax} + 1} \tag{11}$$

$$\delta = 1 - \alpha - \beta \tag{12}$$

The EWCP operation is split into various iterations, and r represents the current iteration. The maximum possible iteration for the protocol is represented by *rmax* parameter. The parameter α is an energy coefficient. It grows by the increasing number of rounds, hence in the later rounds, the nodes with high residual energy level have larger weight. The parameter β is the distance coefficient, and it declines with the increasing number of rounds, hence in the later rounds, the impact of this parameter drops. The parameter δ is a density coefficient, and its values stay approximately constant in each round. This coefficient is directly proportional to the sum of coefficients α and β. Since these coefficients are varying in opposite directions, their total sum stays approximately constant in each round.

Three parameters of *residual energy*, *distance* and *density* are combined to assign a weight to each sensor node. We note that CHs consume more energy compared with cluster members. Hence, a node with a higher residual energy level is appropriate to become a CH. The residual energy level of the nodes is high at the beginning rounds, whereas it becomes marginal in the later rounds. Hence, it is important to increase the effect of residual energy in later rounds compared to the beginning rounds. This trend is reflected in the dynamic values of coefficient α. Another effective parameter in improving the lifetime of WSNs is the distance to BS. The less distance to BS, the less energy consumption is required to transmit data to BS. Thus, in the energy dissipation model, i.e., (6), if the distance is less than the threshold distance, the free space model (d^2 power loss) is used. The impact of this parameter on the node's weights in EWCP is assumed in the opposite direction of residual energy. At the beginning rounds, the distance coefficient is deemed to be more important than energy residual in the beginning rounds in order to optimise energy consumption. However, when we approach the final rounds, the energy level of nodes becomes marginal, and the impact of this parameter is reduced; hence, energy residual becomes more important. The last parameter included in the calculation of weight factors is density. Generally, to balance the data transmission and reduce the collision, more CHs should be allocated in the specific area in which nodes are concentrated. This allocation leads to reduce consumed energy and improves WSN lifetime. The impact of the density factor is assumed to be constant in the protocol. Fig. 2 present a schematic overview of the EWCP set-up.

In the first step, the nodes whose energy is less than the given threshold, called dead nodes, are removed from the network. The given threshold in this paper is assumed zero. The weight of all the live nodes is calculated using (7). The remain nodes exchange control message which contains their weight information. Then, based on candidates using a distributed cluster head selection, the node selects a number of CH. This selection is made using a multi-layer set-up according to the distance between nodes and BS. The nodes can decide to select their own CH autonomously. The conditions of this selection are listed below:

- The distance of CH candidates to BS must be larger than a given threshold distance calculated by the communication radius of nodes. Hence, this condition distributes CHs and improve network coverage.
- The CH weight, i.e., (7), must be larger than its neighbouring nodes' average weights. This condition balances the total energy consumption of the network.

Next step is to inform the nodes in each layer of the number of CH candidates. In this way, the CH candidates broadcast a control massage (CH-msg) to their neighbours. To have full coverage in each layer, we select one-third of the some nodes are selected as CH candidates from remain nodes existing in the layer to achieve a third of the nodes. In this

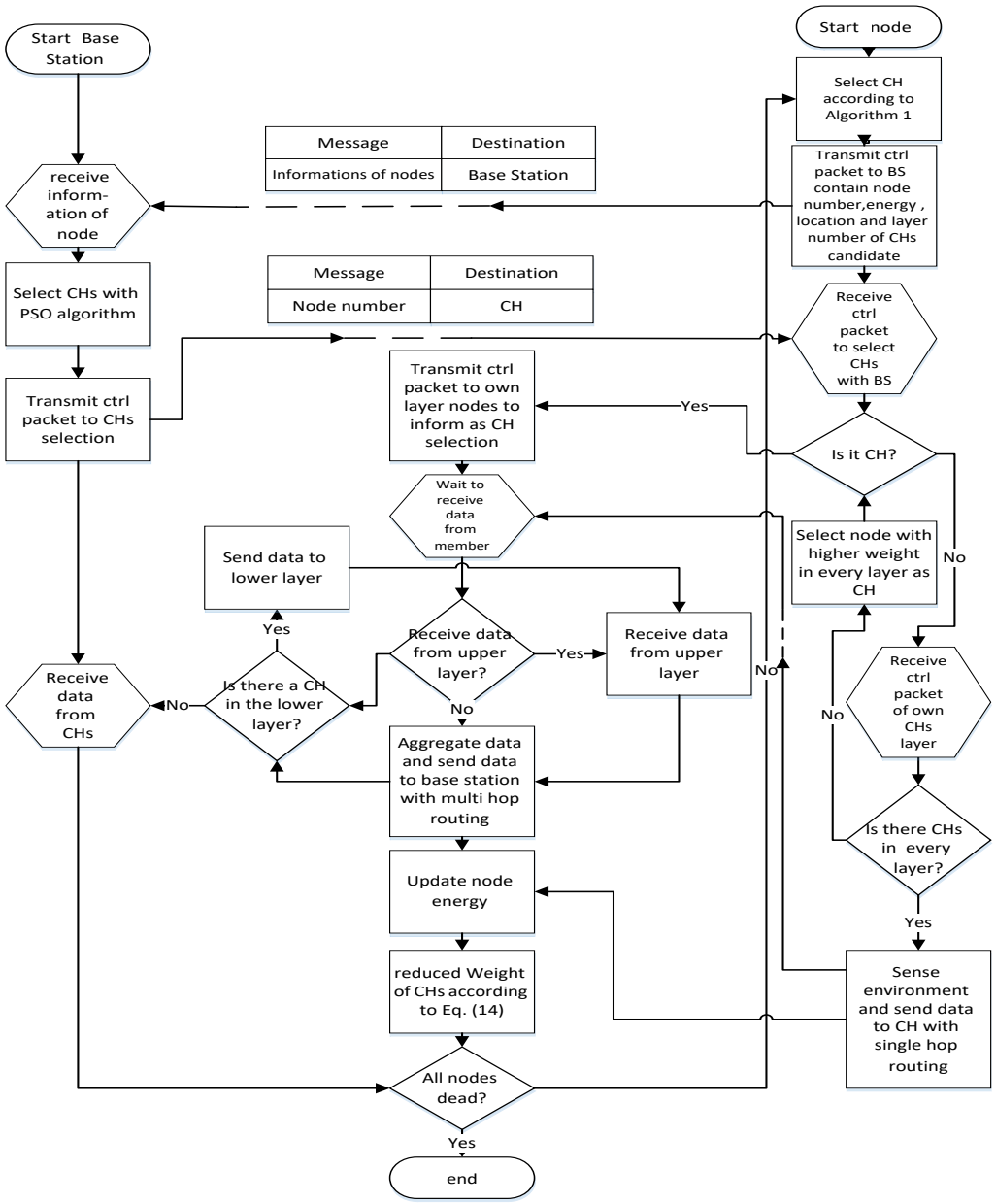

Fig. 2: An overview of EWCP.

situation, the non-candidate nodes with the top highest weight among the nodes are selected as CH candidates. After the candidates are selected, these nodes send a second control message to BS to report their new status, and BS saves the ID number and location information of each node. The algorithm of selecting CH candidates in EWCP is illustrated in Algorithm 1.

In the next step, BS selects appropriate CHs by Particle Swarm Optimisation (PSO) algorithm. In this regards, the selected CH candidates as an initial swarm and their location, transfer communication radius and assigned ID numbers to the PSO algorithm. The fitness value of every particle is calculated using (13).

$$\text{fitness function} = \min\left(\left(1-\text{network coverage}\right)^{2} \times \frac{\text{the number of selected CH}}{\text{the number of candidate CH}}\right) \quad (13)$$

The fitness function in (13) is a minimisation problem, and the objective is to maximise the network coverage with a minimal number of nodes as CHs. In this formula, the square value used for network coverage indicates the importance of this parameter compared with the number of nodes. We have applied the "grid base" method [28] in order to calculate the network coverage. Once the fitness value of each particle is calculated, PSO updates the position and velocity of particles, and this process continues until a termination criterion is achieved. Once the optimum set of CHs is identified, BS sends a control message (Cluster-head-elect) to the selected CH and inform them of their new role. Next, the selected CHs exchange control message with their neighbour nodes and this control massage contains their new role. Thus, the nodes in each layer can identify their CH. If no CH exists in a given layer, the sensor node with the largest weight is selected as a cluster head in the layer.

Afterwards, clusters are constructed from optimal cluster heads and their cluster members. The cluster members sense data from the environment and send them to their assigned

Algorithm 1: Select Candidate of CH in EWCP

1: Input all WSN nodes
2: Calculate node's weight using (7)
3: **For** each $j \in \{1,2,\dots,layer\}$ **do**
4: **For** each $i \in \{1,2,\dots,node\}$ in j **do**
6: Receive energy, node number and weight of neighbour
7: **If** $i != CH$ **then**
8: **If** number of CHs $<=$ $\frac{\text{number of live node in layer}}{3}$ **then**
9: **If** node weight > average of neighbour node's weigth **then**
10: $i = CH$
11: **If** distance among CHs < node's radious **then**
12: Counter_CHs=Counter_CHs+1
13: **end if**
13: **Else**
14: max nodes weight in layer = CH
15: Counter_CHs=Counter_CHs+1
16: **end if**
17: **end if**
18: **end if**
19: **end for**
20: **end for**
21: Select CHs Candidate

Algorithm 1: Select Candidate of CH in EWCP.

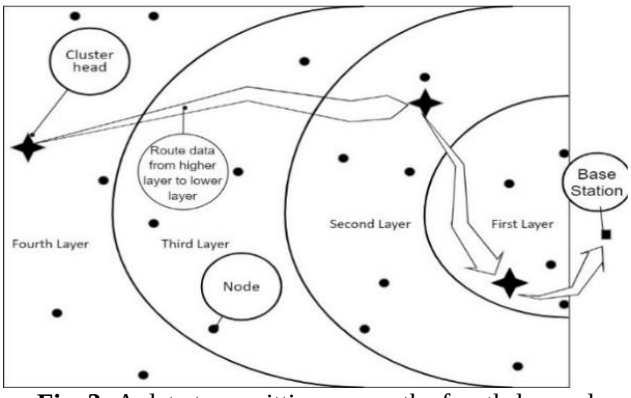

Fig. 3: A data transmitting across the fourth-layered network.

cluster heads. CHs aggregate data and transmit them further to the BS using multi-hop communication. Transmitting data from CH to BS is done in such a way that each CH sends data to the CH in a lower layer until data packages reach the base station. Fig. 3 depicts data transmitting across the fourth-layered network.

As shown in Fig.3, when there is no CH in the third layer, the CH in the fourth layer transmits data to BS via the CH in the second layer and hop over the third layer. When all nodes are dead, the situation is mainly valid in the final iteration. In this situation, data packages are transferred to the lower available layers, which encompass live CH.

Once the data package is transferred to BS, the assigned weight of CH is reduced, based on (14).

$$weight_r = weight_{r-1} - \frac{cluster\_count}{rmax} \quad (14)$$

where $cluster\_count$ is the number of times the node has been a CH. $rmax$ is the maximum number of rounds, and $weight_{r-1}$ is the weight of the node in the previous round. The reduced weight of each node is directly proportional to the number of times it has taken the CH role. The reduction of node's weight decreases the possibility of nodes being selected as CH in the next round. It gives a chance to the other nodes to be selected as CH, and conseq¨ently, the load is evenly divided among nodes.

3.3. Model of Total Dissipated Energy in a Layered Network

Total energy consumption in the network includes four elements as follows:

- Energy consumption for intra-cluster data transmission
- Energy consumption for inter-cluster data transmission
- Energy consumption for intra-cluster and inter-cluster transmitting the control packages
- Total energy consumption for receiving data and control packages.

The total energy consumption is presented by (15).

$$E_{total} = \sum_{i=1}^{M} E_{TXinner}(k_i, d_i, N_i) + E_{TXutter}(k_i, D_i, N_i) + E_{TXcontrol}(k_i, d_i, dis_i, N_i) + E_{RX}(k_i, N_i) \quad (15)$$

where intra-cluster communication is single-hop and inter-cluster communication is multi-hop. In inter-cluster communication, CHs route data destination for the BS through intermediate CHs. Thus, intermediate CHs can act as routers for other CHs' data. Energy consumption is reduced by using multi-hop communication among CHs. Therefore, this protocol helps CHs to save their energy and enhances their lifetime. Moreover, we should add the energy consumption of transmitting/receiving control packages.

If we assume the quantity of transmitted bit data for all nodes identically, the total energy consumption of intra-cluster data transmitting is illustrated by (16).

$$E_{TXinner}(k_i, d_i, N_i) = k \sum_{i=1}^{M} [(N_i - 1)(E_{elect} + e_{fs} d_i^2)] \quad (16)$$

where,

M Represent the number of clusters

d_i Represent the distance of nodes in ith cluster and their assigned CH

D_i Represent the distance of ith CH from (i-1) CH or BS

N_i Represent the number of nodes in ith cluster

k_i Represent the length of transmitted bit data

dis_i Represent distance between ith CH and BS

Considering the assumptions of (16), in (15), the inter-cluster transmitting energy consumption can be presented using (17).

$$E_{TXutter}(k_i, D_i, N_i) = k \sum_{i=1}^{M} [(N_i)(E_{elect} + e_{mp} D_i^2)] \quad (17)$$

The energy for transmitting control packets is illustrated by (18).

$$E_{TXcontrol}(k_i, d_i, dis_i, N_i) = k \sum_{i=1}^{M} [(N_i)(E_{elect} + e_{mp} dis_i^2)] \quad (18)$$

$$+k\sum_{i=1}^{M}[(N_i-1)(E_{elect}+e_{fs}d_i^2)]$$

Finally, total energy consumption for total receiving packets in the layered network is expressed in (19)

$$E_{RX}(k_i,N_i)=kE_{elect}\sum_{i=1}^{M}[(N_i-1)+\sum_{j=i+1}^{M}N_j] \qquad (19)$$

4. Result and Analysis

This section investigates the impact of EWCP on the reduction of energy consumption of WSNs. The results of EWCP is compared with other clustering protocols concerning energy consumption, lifetime and coverage of the network. Two examples are introduced to perform the comparison. These examples are determined according to the network model, networks' parameters, and node number. The network model and layers are configured around BS, as shown in Fig. 3.

4.1. First Example

In the first example, network with a 200-nodes which distributed randomly across a 200m × 200m network. The initial energy of 0.5 *J* is assumed. Implementation of clustering is iterated until all sensor nodes are dead (network's lifetime). The nodes communicate to their CHs using single-hop in all rounds of simulation. Also, CH communicates with the BS by multi-hop communication through network layers. The BS location is (100,250). The node's radius ($R_{sensing}$) and communication radius ($R_{communicatio}$) equals 25 m and 50 m, respectively. The parameters of the applied energy consumption model are shown in Table 1. In addition, Table 2 reports the PSO tuned parameters.

The selected benchmark clustering protocols for comparison in the first example are GCA [29], SCP [30] and UCIFA [31]. Besides these clustering protocols, the research conducted in Mirsadeghi *et al.* [32] (Mir) is selected as an additional benchmark since a similar example is analysed in this research work.

4.1.1 Energy consumption comparison

Network coverage is an effective factor in network energy consumption. So, the rate of network coverage for various clustering protocols are compared in Fig. 4.

As shown in Fig. 4, EWCP has relatively high coverage among other protocols. However, GCA has a higher coverage rate, but the other factors must be considered in comparing protocols.

Another factor that impacts the network lifetime is the number of *orphan nodes.* Orphan nodes cannot communicate with any CH or BS. Therefore, they waste their energy due to aggregate information cannot send to BS. If the network coverage is efficient, the number of *orphan nodes* will be reduced significantly. If the number of orphan nodes is declined, the network can save energy consumption. The number of orphan nodes for different clustering protocols is compared in Table 3. On the other hand, the average number of CHs is another vital factor in evaluating the energy consumption of WSNs. The high number of CHs indicate high energy consumption. Furthermore, this factor is shown in Table 3 as well.

Table 1: Parameters of the network

Parameters	Value
E_{elec}	$50nJ/bit$
E_{DA}	$5nJ/bit/signal$
ε_{emp}	$0.0013pJ/bit/m^4$
ε_{fs}	$10pJ/bit/m^2$
d_0	$87m$
l	$2000bits$

Table 2: PSO Parameters

Parameters	Tuned value
Particles	40
Iterations	200
Inertia weight (W)	0.7298
Learning factor 1 (C1)	1.4962
Learning factor 2 (C2)	1.4962

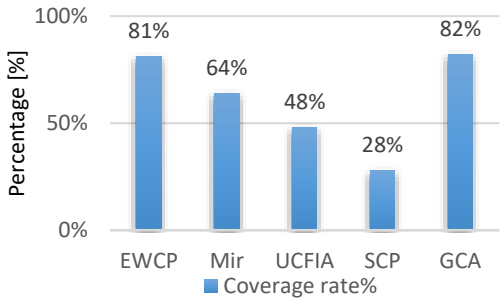

Fig. 4: Coverage rate of different clustering protocols.

Table 3: Orphan node rate

Method	Orphan node rate	Average number of CHs
EWCP	0.9	18
Mir	0.00038	37
UCFIA	9.1	8
SCP	8	15
GCA	1.5	83

Table 3 depicts EWCP has an approximately lower orphan node rate than the other protocols. Mir protocol has a moderately lower orphan node rate than EWCP; however, EWCP has a higher coverage rate than Mir protocol. Moreover, GCA has a higher orphan node rate than EWCP.

According to Table 3, it noted that GCA has the highest coverage rate with a high number of CHs at each round. Thus, the energy consumption of GCA is increased and cannot be considered an effective energy efficient protocol. Also, EWCP improves the energy consumption and provides a proper number of CHs considering its coverage rate and orphan node rate of the network.

The graph of Fig. 5 presents the comparison of the energy consumption of various clustering protocols in 100 iterations. EWCP has the lowest energy consumption in comparison with the other clustering protocols, which is due to its superiority of practical aspects in energy consumption, i.e., parameters considered in node weight presented in (7).

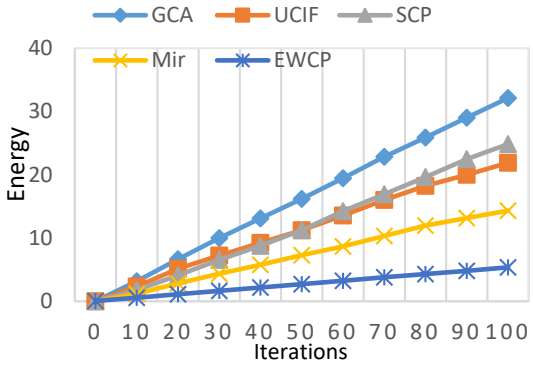

Fig. 5: Energy consumed in 100 iteration

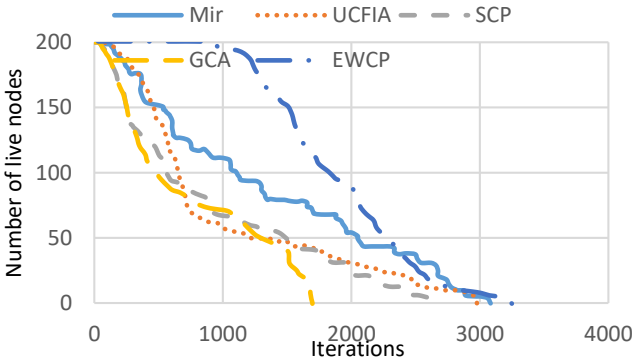

Fig 6: Lifetime of network.

Decreasing energy consumption impact WSN lifetime. Hence, it is expected that the network lifetime is extended by decreasing the energy consumption of the proposed method. The lifetime of different protocols compare based on three criteria which are explained as follows:

- First Node Dies (FND): shows the number of iterations before the first sensor node dies
- Half Nodes Die (HND): indicates the number of iterations when half of the sensor nodes dies.
- Last Node Dies (LND): shows the number of iterations when the last sensor node dies.

4.1.2 Lifetime comparison

In Table 4, all lifetime criteria, i.e., FND, HND, and LND values, compare with various protocols. This table shows that EWCP exhibits a better choice in term of energy-efficient than the other considered protocols. It is obvious in FND and HND criteria.

Fig. 6 present the number of live nodes in each iteration. Based on this figure, EWCP has high live nodes in various iterations in comparison with the other clustering protocols, and it advocates the prior results. It is noted that Mir protocol has more live nodes around iteration 2500; but, EWCP has a longer lifetime than Mir protocol. Thus, it obvious that EWCP has efficient energy consumption over the other protocols.

4.2. Second Example

In this example, we use another method-CWCA [17], for comparing the proposed method. Based on [17], the coefficients of weight in CWCA are assumed to be as (20):

$$\alpha_1 = 0.2\,, \alpha_2 = 0.2\,, \alpha_3 = 0.3, \alpha_4 = 0.1 \qquad (20)$$

In this example, we consider the network with 100m × 100m, where 100 nodes randomly distributed over the network with 0.5 J initial energy. The other parameters of the network are explained in Table 5. The nodes send collected data to CHs using single-hop, and CHs send aggregated data further between layers to BS using multi-hop.

The other parameters of the network, such as energy parameters and the tuned parameters of the PSO algorithm, are the same as the previous example, i.e., Tables 1 and 2.

Table 4: Lifetime criteria of WSN

Method	FND	HND	LND
EWCP	933	1811	3242
Mir	122	1118	3077
UCFIA	70	661	2980
SCP	51	554	2609
GCA	61	496	1919

Table 5: Parameters of the network in the second example

Parameters	Value
Range of sensing	15 m
Base station location	150 × 50
Range of sending	20 m
lengh of packet	500 bits

4.1.3 Comparison of lifetime

This subsection compares the lifetime of the proposed method (EWCP) with CWCA method [17] to equating. In this respect, the parameters of the lifetimes such as FND, HND and LND are shown in Table 6. Moreover, the average number of CHs and the number of packets received to BS are included in the Table 6.

As seen in Table 6, the parameters of FND and HND are higher in EWCP than CWCA. However, LND parameters are lower than CWCA, and this is related to the fact that the number of packets that received to BS is higher in EWCP than CWCA, but CHs are approximately similar in two methods, so the impact of this parameter cannot be pronounced indifference of lifetime parameters. The number of live nodes in each iteration is shown in Fig. 7 in both methods. As shown, in most of the iterations, the number of live nodes is dominated in EWCP over CWCA. However, since the sending packets to BS are more in EWCP, the lifetime of this method is lower, and nodes die earlier, but the difference is not very significant.

5. CONCLUSION

The energy capacity of WSNs is limited, so designing an effective and scalable routing protocol is necessary to improve the network performance and lifetime. Clustering protocols are considered an effective technique to reduce energy consumption and improve the lifetime of WSNs.

This paper has proposed EWCP as a new energy-

Table 6: Lifetime criteria of WSN in the second example

Method	FND	HND	LND	Packets to BS	Average number of CHs
EWCP	1237	4384	5766	68147	11
CWCA	641	3927	6028	63547	10

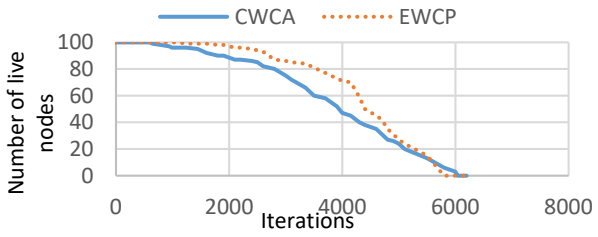

Fig. 7: Lifetime of the network in the second example

efficient clustering protocol. EWCP find the optimal CHs by PSO and find the cluster members of each CH. According to their residual energy level, a proper candidate for CHs is passing into the PSO algorithm, distance to BS, and network density. PSO aims to minimise energy consumption, minimise the number of orphan nodes and maximise coverage. Therefore, this method achieves 81% coverage rate and a under 1% orphan node rate. Moreover, the lifetime of the network is enhanced by 5% approximately.

The EWCP compared with state-of-the-art clustering protocols based performance. EWCP have better performance than the other protocols in orphan nodes, network lifetime, and energy efficiency. The simulation results advocate these claims. It is concluded that selecting CHs and cluster members by considering the energy-efficient parameters has a vital enhancement in increasing the performance of the proposed protocol.

CRediT Authorship Contribution Statement

Ebrahim Farahmand: Conceptualization, Data curation, Formal analysis, Methodology, Software, Visulization, Roles/Writing - original draft. **Ali Mahani:** Conceptualization, Data curation, Formal analysis, Methodology, Supervision, Validation, Writing - review & editing.

Declaration of Competing Interest

The authors declare that they have no known competing financial interests or personal relationships that could have appeared to influence the work reported in this paper. The ethical issues; including plagiarism, informed consent, misconduct, data fabrication and/or falsification, double publication and/or submission, redundancy has been completely observed by the authors.

References

[1] I. F. Akyildiz, W. Su, Y. Sankarasubramaniam, and E. Cayirci, "Wireless sensor networks: a survey," *Computer networks*, vol. 38, no. 4, pp. 393-422, 2002.

[2] G. Anastasi, M. Conti, M. Di Francesco, and A. Passarella, "Energy conservation in wireless sensor networks: A survey," *Ad hoc networks*, vol. 7, no.3, pp. 537-568, 2009.

[3] J. N. Al-Karaki, and A. E. Kamal, "Routing techniques in wireless sensor networks: a survey," *IEEE wireless communications*, vol. 11, no. 6, pp. 6-28, 2004.

[4] S. P. Singh, and S. Sharma, "A survey on cluster based routing protocols in wireless sensor networks," *Procedia computer science*, vol. 45, pp. 687-695, 2015.

[5] V. Kumar, S. Jain, and S. Tiwari, "Energy efficient clustering algorithms in wireless sensor networks: A survey," *International Journal of Computer Science Issues*, vol. 8, no. 5, pp. 259-268, 2011.

[6] M. A. Mahmood, W. K. Seah, and I. Welch, "Reliability in wireless sensor networks: A survey and challenges ahead," *Computer Networks*, vol. 79, pp. 166-187, 2015.

[7] E. Lattanzi, E. Regini, A. Acquaviva, and A. Bogliolo, "Energetic sustainability of routing algorithms for energy-harvesting wireless sensor networks," *Computer Communications*, vol. 30, no. 14-15, pp. 2976-2986, 2007.

[8] G. Venkataraman, S. Emmanuel, and S. Thambipillai, "DASCA: a degree and size based clustering approach for wireless sensor networks," in *2005 2nd International Symposium on Wireless Communication Systems*, 2005, pp. 508-512.

[9] A. A. Aziz, Y. A. Sekercioglu, P. Fitzpatrick, and M. Ivanovich, "A survey on distributed topology control techniques for extending the lifetime of battery powered wireless sensor networks," *IEEE communications surveys & tutorials*, vol. 15, no. 1, pp. 121-144, 2013.

[10] W. R. Heinzelman, A. Chandrakasan, and H. Balakrishnan, "Energy-efficient communication protocol for wireless microsensor networks," in *System sciences, proceedings of the 33rd annual Hawaii international conference on system sciences*, 2000, pp. 10.

[11] O. Younis, and S. Fahmy, "HEED: a hybrid, energy-efficient, distributed clustering approach for ad hoc sensor networks," *IEEE Transactions on Mobile Computing*, vol. 3, no.4, pp. 366-379, 2004.

[12] A. Manjeshwar, and D. P. Agrawal, "TEEN: a routing protocol for enhanced efficiency in wireless sensor networks," in *Proceedings of 15th International Parallel and Distributed Processing Symposium*, 2001, pp. 2009-2015.

[13] S. Lindsey and C. S. Raghavendra, "PEGASIS: Power-efficient gathering in sensor information systems," in 2002 *Aerospace conference proceedings*, 2002, pp. 3-1125-3-1130.

[14] P. Ding, J. Holliday, and A. Celik, "Distributed energy-efficient hierarchical clustering for wireless sensor networks," in *2005 International Conference on Distributed Computing in Sensor Systems*, 2005, pp. 322-339.

[15] M. Sabet, and H. R. Naji, "A decentralised energy efficient hierarchical cluster-based routing algorithm for wireless sensor networks," *AEU-International Journal of Electronics and Communications*, vol. 69, no. 5, pp. 790-799, 2015.

[16] J. Yu, Y. Qi, G. Wang, and X. Gu, "A cluster-based routing protocol for wireless sensor networks with non-uniform node distribution," AEU-International Journal of Electronics and Communications, vol. 66, no. 1, pp. 54-61, 2012.

[17] C. Tang, S. K. Shokla, G. Modhawar, and Q. Wang, "An effective collaborative mobile weighted clustering schemes for energy balancing in wireless sensor networks," *Sensors*, vol. 16, no. 2, p. 261, 2016.

[18] P. K. Agarwal, and C. M. Procopiuc, "Exact and approximation algorithms for clustering", *Algorithmica*, vol. 33, no. 2, pp. 201-226, 2002.

[19] S. K. Verma, N. K. Sood, and A. K. Sharma, "Genetic algorithm-based optimised cluster head selection for single and multiple data sinks in heterogeneous wireless sensor network," *Applied Soft Computing*, vol. 85, 105788, 2019.

[20] E. Farahmand, S. Sheikhpour, A. Mahani, and N. Taheri, "Load balanced energy-aware genetic algorithm clustering in wireless sensor networks," in *Proc. 2016 1st Swarm Intelligence and Evolutionary Computation Conference*, 2016, pp. 119-124.

[21] Q. Huamei, L. Chubin, G. Yijiahe, X. Wangping, J. Ying, "An energy-efficientnon-uniform clustering routing protocol based onimproved shuffled frog leaping algorithm for wirelesssensor networks," *IET Communications*, 2021, 374-383.

[22] V. K. Arora, V. Sharma, and M. Sachdeva, "ACO optimised self-organised tree-based energy balance algorithm for wireless sensor network," *Journal of Ambient Intelligence and Humanized Computing*, vol. 10, no. 12, 4963–4975, 2019.

[23] N. Sawyer, M. Naderi Soorki, W. Saad, D. B. Smith and N. Ding, "Evolutionary games for correlation-aware clustering in massive machine-to-machine networks," *IEEE Transactions on Communications*, vol. 67, no. 9, pp. 6527-6543, 2019.

[24] H. Ali, U. U. Tariq, M. Hussain, L. Lu, J. Panneerselvam, and X. Zhai, "Arsh-fati a novel metaheuristic for cluster head selection in wireless sensor networks," *IEEE Systems Journal*, vol. 15, no. 2, pp. 2386-2397, 2021

[25] N. A. Latiff, C. C. Tsimenidis, and B. S. Sharif, "Energy-aware clustering for wireless sensor networks using particle swarm optimisation," in *2007 IEEE 18th International Symposium on Personal, Indoor and Mobile Radio Communications*, 2007, pp. 1-5.

[26] P. S. Rao, P. K. Jana, and H. Banka, "A particle swarm optimisation based energy efficient cluster head selection algorithm for wireless sensor networks," *Wireless Networks*, vol. 23, no. 7, pp. 2005-2020, 2017.

[27] W. B. Heinzelman, A. P. Chandrakasan, and H. Balakrishnan, "An application-specific protocol architecture for wireless microsensor networks," *IEEE Transactions on Wireless Communications*, vol. 1, no. 4, pp. 660-670, 2002.

[28] X. Shen, J. Chen, and Y. Sun, "Grid scan: A simple and effective approach for coverage issue in wireless sensor networks," in *2006 IEEE International Conference on Communications*, 2006, pp. 3480-3484.

[29] S. H. Lee, S. Lee, H. Song, and H. S. Lee, "Gradual cluster head election for high network connectivity in large-scale sensor networks," in 13th International Conference on Advanced Communication Technology (ICACT), 2011, pp. 168-172.

[30] A. K. Tripathy, and S. Chinara, "Staggered clustering protocol: SCP an efficient clustering approach for wireless sensor network," in 2012 *World Congress on Information and Communication Technologies*, 2012, pp. 937-941.

[31] M. Song, and C.-l. ZHAO, "Unequal clustering algorithm for WSN based on fuzzy logic and improved ACO," *The Journal of China Universities of Posts and Telecommunications*, vol. 18, no. 6, pp. 89-97, 2011.

[32] M. Mirsadeghi, A. Mahani, and M. Shojaee, "A Novel distributed Clustering Protocol using fuzzy logic," *Procedia Technology*, vol. 17, pp. 742-748, 2014.

BIOGRAPHY

Ebrahim Farahmand received the B.Sc. degree in Electrical engineering- communication systems in 2012, and M.Sc. degree in electrical engineering Electronics in 2016 both from Shahid Bahonar University of Kerman (SBUK). He is currently a PhD student in electronic engineering SBUK, Iran. His research interests include brain-inspired computing, approximate computing, machine learning accelerator, Fault-tolerant design and Networked System.

Ali Mahani received the B.Sc. degree in electronic engineering from Shahid Bahonar University of Kerman, Iran, in 2001, The M.Sc. and Ph.D. degrees both in Electronic Engineering from Iran University of Science and Technology (IUST), Tehran, Iran, in 2003 and 2009 respectively. Since then he has been with the electrical engineering department of Shahid Bahonar University of Kerman, where he is currently an associate professor. His research interests focus on Fault-tolerant design, FPGA-based accelerators, approximate digital circuits, stochastic computing and Networked System.

Copyrights
© 2021 Licensee Shahid Chamran University of Ahvaz, Ahvaz, Iran. This article is an open-access article distributed under the terms and conditions of the Creative Commons Attribution –NonCommercial 4.0 International (CC BY-NC 4.0) License (http://creativecommons.org/licenses/by-nc/4.0/).

Shahid Chamran University of Ahvaz

Iranian Association of Electrical and Electronics Engineers

Journal of Applied Research in Electrical Engineering

E-ISSN: 2783-2864
P-ISSN: 2717-414X
Homepage: https://jaree.scu.ac.ir/

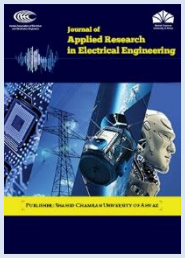

Research Article

A Novel Method of Modeling for Dynamic Behavior of Hydro-Electric Turbines During Load Rejection

Saman Ghahghahzadeh[1,*], and Mohammad Reza Afsharnia[2]

[1] *Department of Electrical* Engineering, *Masjed-Soleiman Branch, Islamic Azad University, Masjed-Soleiman, Iran*

[2] *Sama Technical and Vocational* Training *College, Islamic Azad University, Masjed-Soleiman Branch, Masjed-Soleiman, Iran*

[*] *Corresponding* Author*: samanghahghahzadeh@yahoo.com*

Abstract: This work proposes a new model for dynamic behavior of hydro-electric turbines on the basis of inlet mechanical power with different loads together with reactions of wicket gates and governor during load rejection. Then, practical experiments are investigated, and their results are compared with simulated results developed in SIMULINK. The results show that proposed modeling satisfies practical behavior of real systems.

Keywords: Modeling, hydroelectric turbine, load rejection, regression.

Article history
Received 26 May 2020; Revised 23 May 2021; Accepted 02 June 2021; Published online 29 June 2021.
© 2021 Published by Shahid Chamran University of Ahvaz & Iranian Association of Electrical and Electronics Engineers (IAEEE)
How to cite this article
S. Ghahghahzadeh, and M. R. Afsharnia, "A novel method of modeling for dynamic behavior of hydro-electric turbines during load rejection," *J. Appl. Res. Electr. Eng.*, vol. 1, no. 1, pp. 79-85, 2022. DOI: 10.22055/jaree.2021.33523.1009

Check for updates

1. INTRODUCTION

Hydroelectric plants demonstrate particular behaviors during power generation due to their physical construction. Sudden changes in the load are an example of situations that may influence plant parameters. Hence, the load rejection test is prevalent to investigate the reaction of turbine-generator combination reaction, which examines the robustness of plant units. However, the results may differ based on the percent of nominal power delivered by the hydroelectric unit before the load rejection test. Turbine speed, wicket gate position, pressure head in the spiral case, and so on are generally investigated during the load rejection process. Regarding these quantities, the governor design and parameters are to be attended. In [1], the results of the simulation indicate that the higher the power level, the greater the disturbance caused by the load rejection. The nuclear power plant operating with full load is necessary to be equipped with the protection system for load rejection. In practice, load rejection may occur in special cases, such as short circuits in network. In [2], an experimental study has been conducted to estimate synchronous generator parameters through a sudden short circuit in the laboratory.

In [3], a complete analysis is investigated with a focus on the electrical aspects of load rejection and the variations of generator voltages and currents. Also, transient processes of load rejection caused by different accident conditions and elaborating the characteristics of different types of load rejection are studied in [4] in which a numerical simulation method of different types of load rejection is then established.

Amazing models for load rejection of thermal power plants, which helped and guided us through this work, are applied in [5]. Paper [6] presents a nonlinear mathematical model of the Francis turbine in a hydropower plant evaluated by full-scale field tests involving steady and transient operations that use a conventional turbine model developed by IEEE [7]. Besides several field tests have globally been performed although most of them may not be released to the public, such as [8] and [9].

Regarding these strong researches and other works such as [10-14], our study numerically evaluates turbine behavior in which mechanical aspects are considered with a newly developed model processed in SIMULINK®.

Section 2 reviews the theory of modeling according to [15], which is a famous reference. In Section 3, the experimental results of mechanical parameters related to the Masjed-Soleiman hydropower plant are presented. The new model is developed and the results are presented in Section 4.

In Section 5, the results are applied to regression and formulation. Finally, some conclusions are made in Section 6.

2. MODELING

When there is an unbalance between the torques acting on a rotor, the net torque causing acceleration is

$$T_a = T_m - T_e \tag{1}$$

in which T_e, T_a, and T_m are the electromagnetic torque, accelerating torque, and mechanical torque, respectively. In (1), T_e and T_m are positive for a generator, and the prime mover is accelerated by the unbalance in the applied torques. Hence, the main equation of motion is

$$J\frac{d\omega_m}{dt} = T_a \tag{2}$$

where J is combined moment of inertia of generator and turbine in kg.m2, ω_m is angular velocity of the rotor, in rad/s, and t is time in sec.

Equation (2) can be normalized in terms of per unit inertia constant H, defined as the kinetic energy in watt-seconds at rated speed divided by the VA base. Using ω_{0m} to denote the rated angular velocity in mechanical radians per second, the inertia constant is

$$H = \frac{J\omega_m^2}{2VA_{base}} \tag{3}$$

Then, the moment of inertia J will be as below:

$$J = \frac{2H}{\omega_{0m}^2}VA_{base} \tag{4}$$

Substituting the above relation in (2) gives

$$\frac{2H}{\omega_{0m}^2}VA_{base}\frac{d\omega_m}{dt} = T_m - T_e \tag{5}$$

Rearranging yields

$$2H\frac{d}{dt}\left[\frac{\omega_m}{\omega_{0m}}\right] = \frac{T_m - T_e}{VA_{base}/\omega_{0m}} \tag{6}$$

Regarding the relation $T_{\text{base}} = VA_{base}/\omega_{0m}$, the equation of motion in form of per unit is

$$2H\frac{d\overline{\omega_r}}{dt} = \overline{T}_m - \overline{T}_e \tag{7}$$

In (7), we have

$$\overline{\omega_r} = \frac{\omega_r}{\omega_0} \tag{8}$$

in which ω_0 is its rated value of rotor velocity and ω_{r} is the angular velocity of the rotor in electrical rad/s.

On the other hand, supposing δ is the angular position of the rotor in electrical radians with respect to a synchronously rotating reference and δ_0 is its initial value,

$$\delta = \omega_r t - \omega_r t + \delta_0 \tag{9}$$

Taking the time derivative, we have

$$\frac{d\delta}{dt} = \Delta\omega_r \tag{10}$$

$$\frac{d^2\delta}{dt^2} = \omega_0\frac{d(\Delta\overline{\omega_r})}{dt} \tag{11}$$

Substituting for $\frac{d(\Delta\overline{\omega_r})}{dt}$ given by the above equation in (7), we get

$$\frac{2H}{\omega_0}\frac{d^2\delta}{dt^2} = \overline{T_m} - \overline{T_a} \tag{12}$$

It is often desirable to include a component of damping torque, not accounted for in the calculation of T_e, separately. This is accomplished by adding a proportional to speed deviation in the above equation as follows.

$$\frac{2H}{\omega_0}\frac{d^2\delta}{dt^2} = \overline{T_m} - \overline{T_a} - K_D\Delta\overline{\omega_r} \tag{13}$$

The swing equation, expressed as two first-order differential equations, will become

$$\frac{d\Delta\overline{\omega_r}}{dt} = \frac{\overline{T_m} - \overline{T_a} - K_D\Delta\overline{\omega_r}}{2H} \tag{14}$$

$$\frac{d\delta}{dt} = \omega_0\Delta\overline{\omega_r} \tag{15}$$

in which time is in seconds, δ is in electrical radians, and ω_0 is equal to $2\pi f$. The block diagram form of the above two equations is shown in Fig. 1.

3. EXPERIMENTAL TESTS

In this work, we have examined several load rejection tests individually and together on units 5 and 6 of the Masjed-Soleiman hydroelectric plant. The tests were conducted at different states when the units were generating 25%, 50%, 75%, and 100% of their rated power. Figs. 2 to 5 depict the result curves of the above tests. The variations are in terms of time.

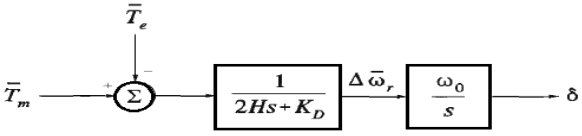

Fig. 1: Block diagram of above equations.

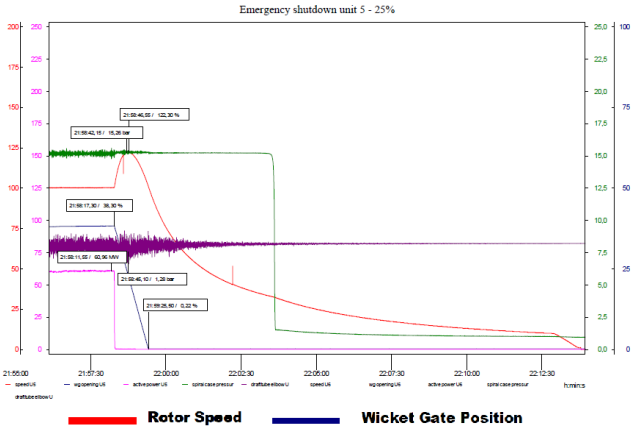

Fig. 2: The results of load rejection on unit 5 of the Masjed-Soleiman plant while delivering 25% of rated power.

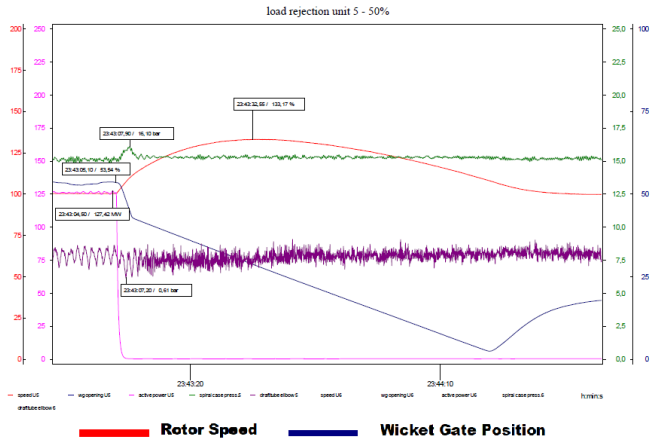

Fig. 3: The results of load rejection on unit 5 of the Masjed-Soleiman plant while delivering 50% of rated power.

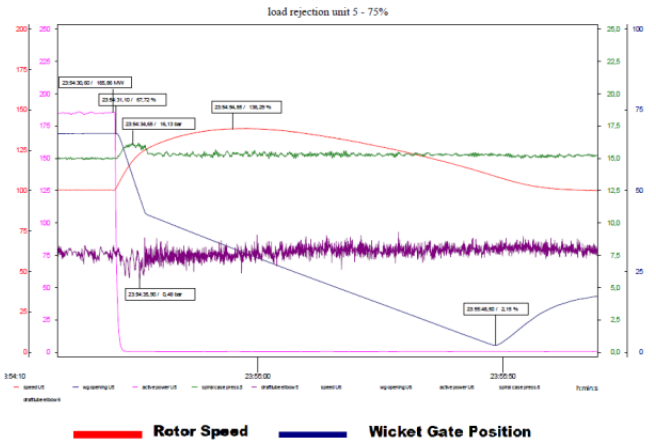

Fig. 4: The results of the load rejection on unit 5 of the Masjed-Soleiman plant while delivering 75% of rated power.

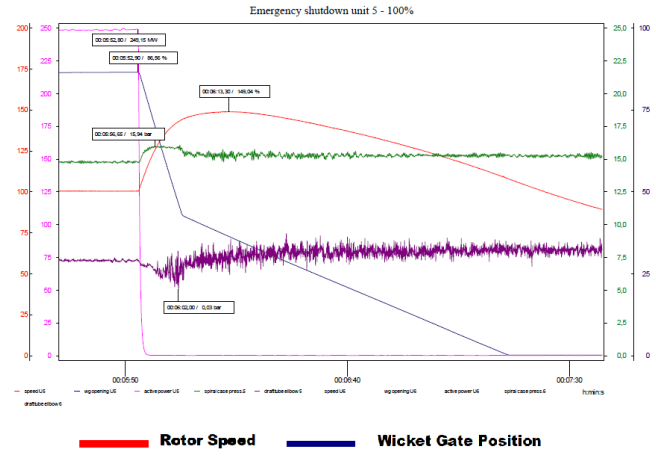

Fig. 5: The results of the load rejection on unit 5 of the Masjed-Soleiman plant while delivering 100% of rated power.

4. Simulation and Results

According to the equations mentioned in Section 2, the mechanical behavior of turbine-generator combination can generally be stated by

$$T_m - T_e - K\,\omega = J\frac{d\omega}{dt} \tag{16}$$

Multiplying both sides of (16) with ω, we have

$$P_m - P_e - K\omega^2 = J\omega\frac{d\omega}{dt} \tag{17}$$

Fig. 6 shows a new block diagram of turbine- generator combination operation, which should be attended to during the load rejection process.

This new block diagram can be implemented in the SIMULINK® environment. Hence, the mechanical braking system is operating after load rejection. Phrase $K_B\omega^2$ will be added to the diagram shown in Fig. 6, which will cause speed reduction together with the governing system.

Consequently, the rotor will get started to reduce speed reaching zero. Fig. 7 shows the implemented diagram in the SIMULINK® environment.

The simulation was executed when the system served different loads before load rejection. In this simulating work, the power delivered by the studied system was 50%, 75%, 80%, and 100% of the rated power. Figs. 8 to 11 depict the behavior of the system by presenting rotor speed variations and wicket gate position during the process in terms of time in Table 1, significant parameters are being collected which will affect design considerations.

5. Formulating and Regression

According to Table 1, two significant functions are to be attended by variations of the percent of rated power delivered before load rejection: percentage of maximum over speed (F1) and time to reach maximum over speed (F2). Functions F1 and F2 are fitted by regression with two following polynomials.

Fig. 12 shows the points on the basis of Table 1 and its related fitness function F1, and Table 2 presents coefficients of function F2 as it is derived from Fig. 13.

$$f_1(l) = -0.0004l^3 - 0.09\,l^2 - 5.74l - 115 \tag{18}$$

$$f_2(l) = 1.9 * 10^{-5}l^3 - 0.0057\,l^2 + 0.5633l - 13 \tag{19}$$

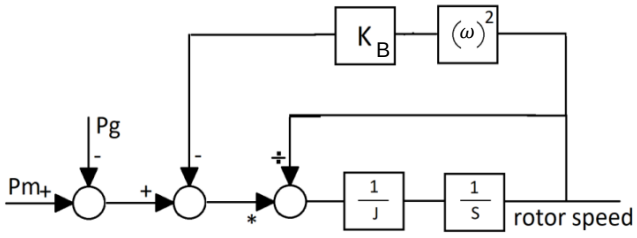

Fig. 6: The block diagram of turbine-generator during load rejection.

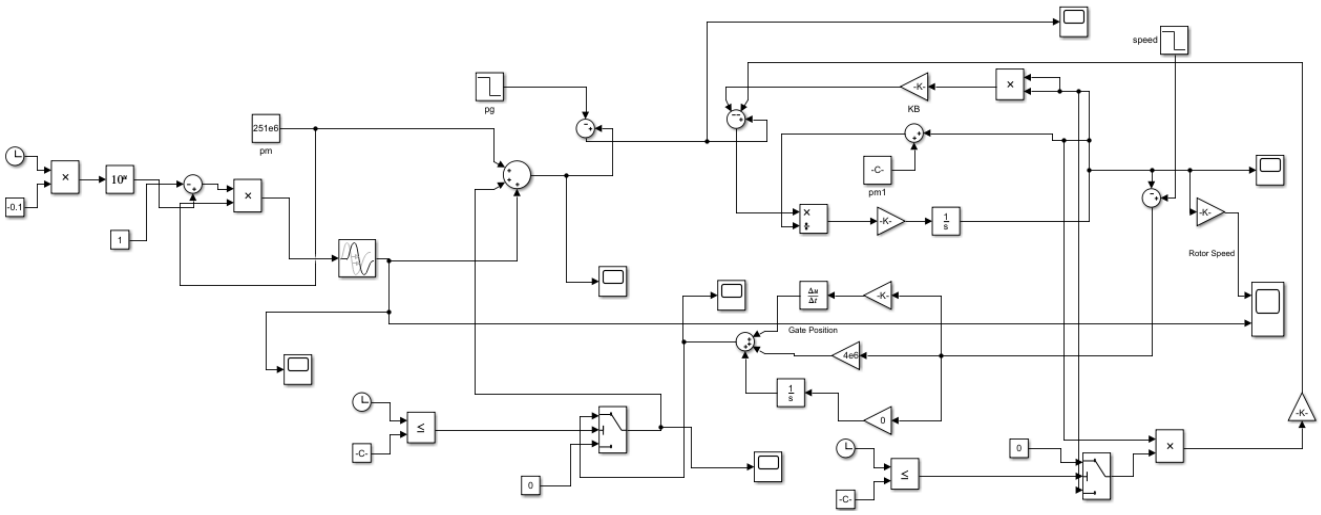

Fig. 7: Implemented diagram in SIMULINK environment.

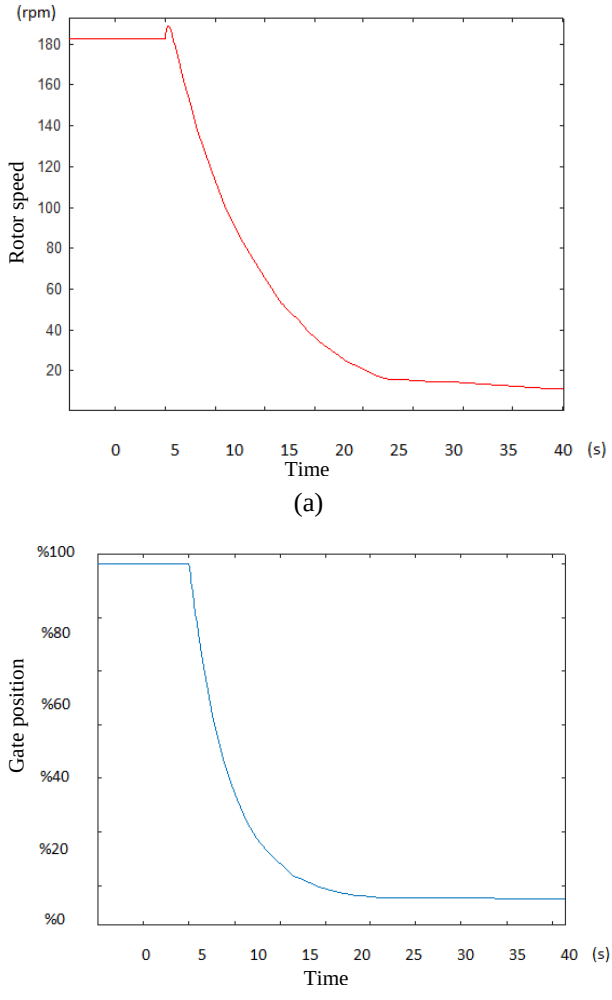

Fig. 8: Variations of (a) rotor speed, and (b) wicket gate position when delivering 50% of the rated power before load rejection.

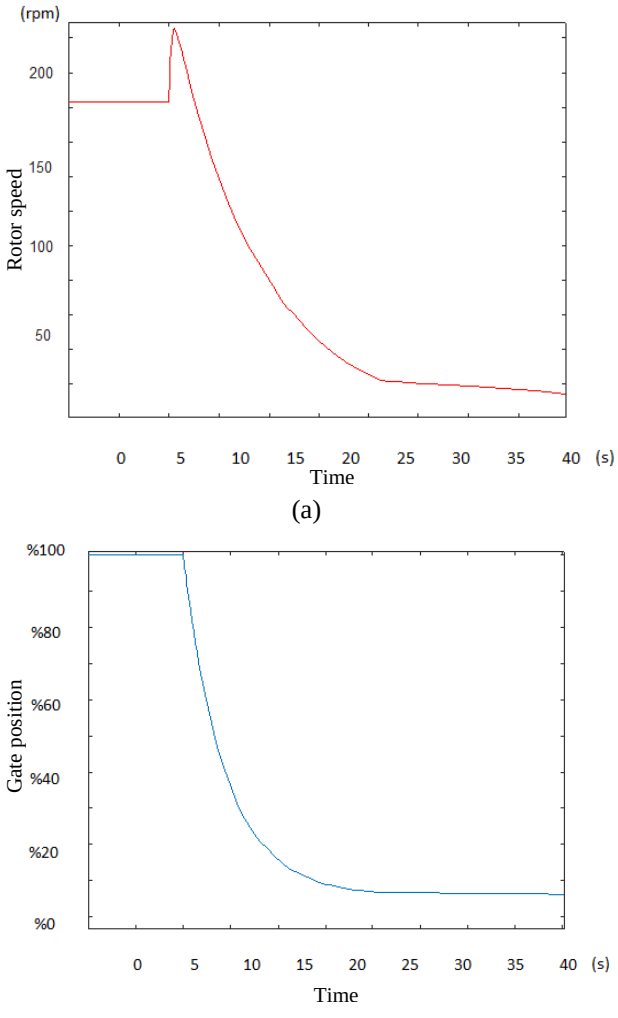

Fig. 9: Variations of (a) rotor speed, and (b) wicket gate position when delivering 75% of the rated power before load rejection.

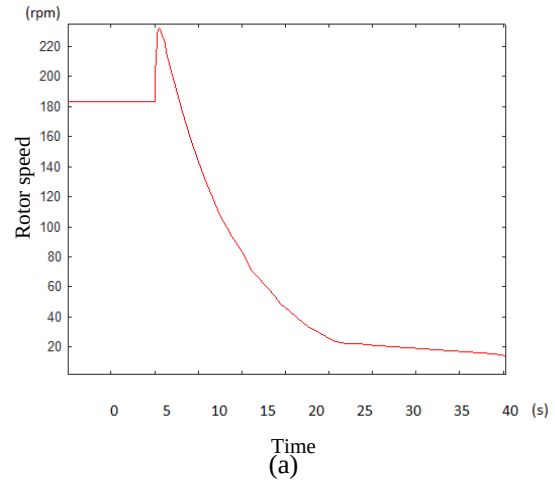

(a)

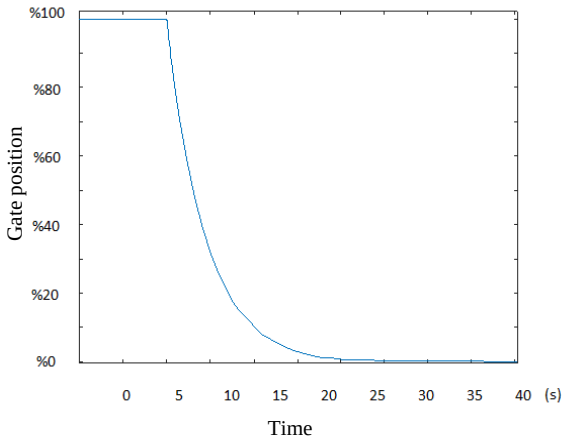

(b)

Fig. 10: Variations of (a) rotor speed, and (b) wicket gate position when delivering 80% of the rated power before load rejection.

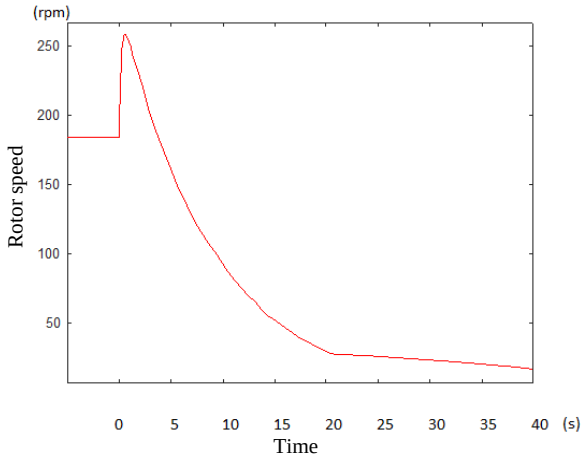

(a)

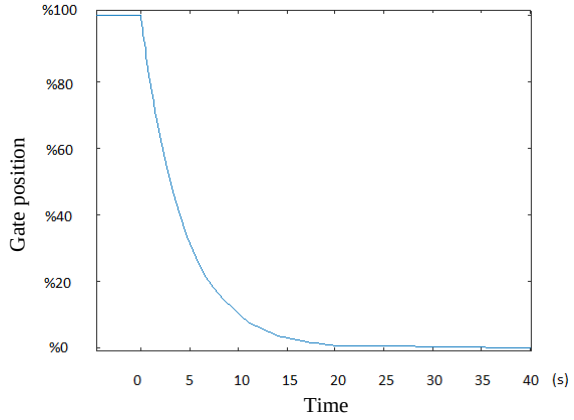

(b)

Fig. 11: Variations of (a) rotor speed, and (b) wicket gate position when delivering 100% of rated power before load rejection.

Table 1: The results of the load rejection at different cases.

Power delivered before load rejection (MW)	Rotor speed before load rejection (RPM)	Maximum speed after load rejection	Percentage of over speed	Time to reach over speed (s)
250 (%100)	184	259	%41	5.58
200 (%80)	183	232	%27	5.48
187 (%75)	184	225	%22	5.35
125 (%50)	183	189	%3	3.36

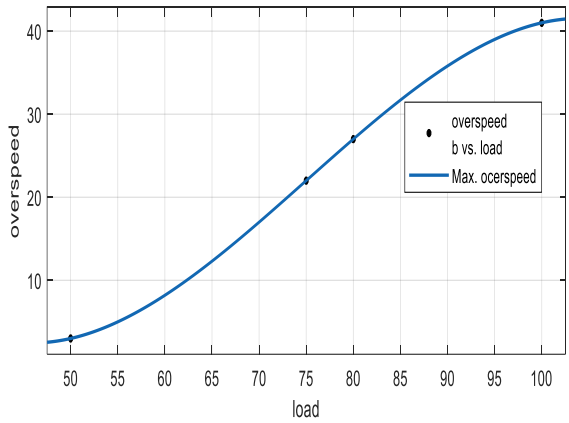

Fig. 12: Fitted function F1 as over speed vs. load percent.

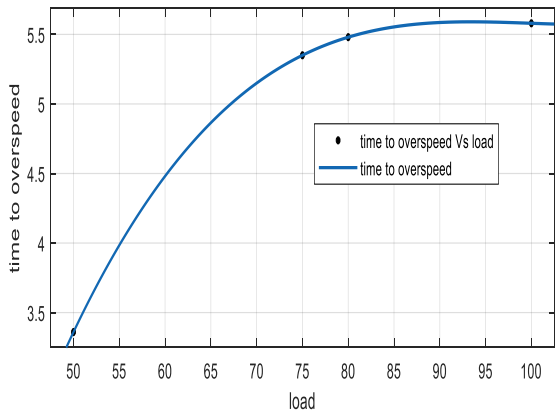

Fig. 13: Fitted function F2 as time to reach over speed vs. load percent.

Table 2: Regression parameters of fitted function F1.

Linear model polynomial f(x) = p1*x^2 + p2*x + p3	
p1 =	-0.0004
p2 =	0.09
p3 =	-5.74
p4 =	115
Goodness of fit SSE: 9.37e-26	

6. Conclusion

After executing the above works and attaining the related results, the following conclusions can be made:

1- Experimental results show that modeling is qualified and can be trusted.

2- Maximum over speed will be increased if the power delivered before load rejection increases.

3- If the power delivered increases, the time of reaching maximum over speed after load rejection will decrease.

Acknowledgement

The first writer would like to thank Sama Technical and Vocational Training College at Islamic Azad University, Masjed-Soleiman branch for their financial support through the contract of "Modeling of Dynamic Behavior of Hydro-Electric Turbines During Load Rejection", contract of 96-25-6196. Also, the writers appreciate Khouzestan Water and Power Authority (KWPA), especially Mr. Pishva, Mr. Jelodar, and Mr. Gholipour for their cooperation in this project.

CRediT Authorship Contribution Statement

Saman Ghahghahzadeh: Conceptualization, Formal analysis, Funding acquisition, Investigation, Methodology, Resources, Software, Roles/Writing - original draft, Writing - review & editing. **Mohammad Reza Afsharnia:** Data curation, Project administration, supervision.

Declaration of Competing Interest

The authors declare that they have no known competing financial interests or personal relationships that could have appeared to influence the work reported in this paper. The ethical issues; including plagiarism, informed consent, misconduct, data fabrication and/or falsification, double publication and/or submission, redundancy has been completely observed by the authors.

References

[1] D. Tiomo, E. Y. Kenfack, and R. Wamkeue, "Dynamic study and analysis of synchronous generator under sudden short circuit and load rejection tests", *2019 IEEE/IAS 55th Industrial and Commercial Power Systems Technical Conference (I&CPS)*, pp. 1-5, 2019.

[2] W. Sheng, and Z. Xu, "Research on load rejection protection of PWR power plants at different power levels", in *2019 IEEE Innovative Smart Grid Technologies - Asia (ISGT Asia)*, pp. 525-530, 2019.

[3] R. Wamkeue, I. Kamwa, F. Baetscher, and J. El Hayek, "A new and efficient approach for analysis of a saturated synchronous generator under the load rejection test", *Electric Power Components and Systems*, vol. 34, no. 5, pp. 539-563, 2006.

[4] T. B. Ng, G. J. Walker, and J. E. Sargison, "Modeling of transient behavior in a francis turbine power plant ", in *15th Australasian Fluid Mechanics Conference*, Sydney, Australia, 2004.

[5] T. Kol sek, J. Duhovnik, and A. Bergant, "Simulation of unsteady flow and runner rotation during shut-down of an axial water turbine", *Journal of Hydraulic Research*, vol. 44, no. 1, pp. 129–137, 2006.

[6] M. H. Afshar, M. Rohani, and R. Taheri, "Simulation of transient flow in pipeline systems due to load rejection and load acceptance by hydroelectric power plants", *International Journal of Mechanical Sciences*, vol. 52, no. 1, pp. 103-115, 2010.

[7] W. C. Guo, J. D. Yang, J. P. Chen, Z. Y. Peng, Y.Zhang, C. C. Chen, "Simulation of the transient processes of load rejection under different accident conditions in a hydroelectric generating Set", *28th IAHR symposium on Hydraulic Machinery and Systems*, vol. 49, no. 5, 2016.

[8] Working Group on Prime Mover and Energy Supply Models for System Dynamic Performance Studies, Hydraulic Turbine and Turbine Control Models for System Dynamic Performance Studies, *IEEE Transactions on Power Systems*, vol. 7, no. 1, pp. 167-179, 1992.

[9] K. Zeng, J. Wen, L. Ma, S. Cheng, E. Lu, N. Wang, "Fast cut back thermal power plant load rejection and black start field test analysis", *Energies*, vol. 7, no. 5, pp. 2740-2760, 2014.

[10] Riasi, A. Nourbakhsh, and M. Raisee, "Numerical modeling for hydraulic resonance in hydropower systems using impulse response" , *Journal of Hydraulic Engineering*, vol. 136, no. 11, pp. 929–934, 2010.

[11] P. Rayner, and S. Ho, "Devil's gate power station–dynamic modeling and tasmanian electricity code compliance assessment", Hydro Electric Corp., Tasmania, Australia, Tech. Rep. GEN-112475-Report-1, 2003.

[12] P. Rayner, and P. Rai. "Machine test guidelines (Rev. 2)," hydro electric corp., Tasmania, Australia. Tech. Rep. GEN-0201-TR-0002. 1999.

[13] G. J. Walker *et al*., "Turbine and waterway modeling: investigation and development of improved models stage II report", School of Engineering, University of Tasmania, Tech. Rep. 2003.

[14] G. J. Walker *et al*., "Turbine and waterway modeling: investigation and development of improved models stage I report", School of Engineering, University of Tasmania, Tech. Rep. 2002.

[15] P. Kundur, *Power System Stability and Control*. McGraw-Hill, 1994.

BIOGRAPHY

Saman Ghahghahzadeh has been with Islamic Azad University as academic staff since 2010. For more than 24 years, he has worked in different sections of power industry as researcher, technical advisor, and project manager. He has executed more than 20 research projects for several clients where he is also distinguished as a senior technical trainer. His main research interests are high-voltage engineering and tests, power transformers, generators, insulation, and power system components. Over the past years, Dr. Ghahghahzadeh has authored and coauthored more than 15 conference and journal scientific papers.

Mohammad Reza Afsharnia received his M.Sc. in electrical engineering from Islamic Azad University, Zanjan Branch of Sciences and Research. He has worked in a Masjed-Soleiman hydropower plant as an electrical engineer since 2010 besides his several experiences in technical design and advisory to the power industry.

Copyrights
© 2021 Licensee Shahid Chamran University of Ahvaz, Ahvaz, Iran. This article is an open-access article distributed under the terms and conditions of the Creative Commons Attribution –NonCommercial 4.0 International (CC BY-NC 4.0) License (http://creativecommons.org/licenses/by-nc/4.0/).

Shahid Chamran University of Ahvaz

Iranian Association of Electrical and Electronics Engineers

Journal of Applied Research in Electrical Engineering

E-ISSN: 2783-2864
P-ISSN: 2717-414X
Homepage: https://jaree.scu.ac.ir/

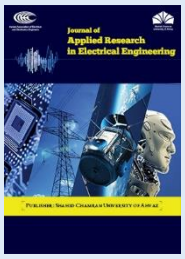

Research Article

A Fault-Resistant Architecture for AES S-box Architecture

Mahdi Taheri[1], Saeideh Sheikhpour[2], Mohammad Saeed Ansari[3], and Ali Mahani[2,*]

[1] *Department of Computer Systems, Tallinn University of Technology, Tallinn 19086, Estonia*

[2] *Department of Electrical Engineering, Shahid Bahonar University of Kerman, Kerman 7616913439, Iran*

[3] *Eideticom Computational Storage, Calgary, AB, Canada*

* *Corresponding Author: amahani@uk.ac.ir*

Abstract: This paper introduces a high-speed fault-resistant hardware implementation for the S-box of AES cryptographic algorithm, called HFS-box. A deep pipelining for S-box at the gate level is proposed. In addition, a new Dual Modular Redundancy-based (DMR-based) countermeasure is exploited in HFS-box for fault correction. The newly introduced countermeasure is a fault correction scheme based on the DMR technique (FC-DMR) combined with a version of the time redundancy technique. In the proposed architecture, when a transient random or malicious fault(s) is detected in each pipeline stage, the error signal corresponding to that stage increases. The control unit holds the previous correct value in the output of the proposed DMR voter in the other pipeline stages as soon as it observes the value '1' on the error signal. The previous correct outputs will be kept until the fault effect disappears. The presented low-cost HFS-box provides a high capability of fault resistance against transient faults with any duration by imposing low area overhead compared with similar fault correction strategies, i.e., 137%, and low throughput degradation, i.e., 11.3%, on the original S-box implementation.

Keywords: Fault-resistant, advanced encryption standard (AES), S-box, high-speed.

Article history
Received 30 December 2020; Revised 28 April 2021; Accepted 11 June 2021; Published online 30 June 2021.
© 2021 Published by Shahid Chamran University of Ahvaz & Iranian Association of Electrical and Electronics Engineers (IAEEE).
How to cite this article
M. Taheri, S. Sheikhpour, M. S. Ansari, and A. Mahani, "A fault-resistant architecture for AES S-box architecture," *J. Appl. Res. Electr. Eng.*, vol. 1, no. 1, pp. 86-92, 2022. DOI: 10.22055/jaree.2021.36230.1020

Check for updates

1. INTRODUCTION

Dependable applications, like secure information systems, remote security services, online banking, etc., play an important role in our daily lives. Secure storage and communication are critical requirements of these applications. Nowadays, cryptography is extensively used in dependable applications to meet these critical requirements, thereby preventing unauthorized access to secure information. Another important requirement of a dependable application is reliability. Therefore, in many cases, a fault resilient approach is incorporated with original hardware implementation [1].

The Advanced Encryption Standard (AES) [2] was standardized by the National Institute of Standards and Technology (NIST) in 1997. Since then, AES has been one of the most common symmetric cryptographic algorithms. Many hardware implementations of AES have so far been proposed with different characteristics [3-6], each of which is suited for different applications with different constraints. Recently, many faults injection attacks have been proposed on AES [7-9]. In a fault attack, attackers inject malicious faults into the VLSI design of cryptographic primitives to extract secure information (i.e., cryptographic key).

On the other hand, with transistor size downscaling, reducing power supply voltage level, increasing operating frequencies, and reducing noise margins, VLSI hardware designs will be more and more sensitive to random faults occurrence [10]. All random faults that occur in VLSI designs can be grouped into transient and permanent faults.

Various fault resilient hardware implementations of AES were proposed to thwart the random and/or malicious faults effect [11-14]. AES includes four basic operations, i.e., SubByte, ShifRows, MixColumns, and AddRoundKey. The hardware implementation of SubByte operation is realized with 16 S-Boxes that are nonlinear mapping in which each byte of state array is replaced with another byte. It also occupies much of the total AES hardware implementation area [15]. In a fault injection attack, an injected fault changes

specific bits or bytes during a special round of the encryption and produces certain differences [16-19]. The nonlinear operations, namely, S-Boxes of the block ciphers, are commonly the target of DFAs. In those DFAs that faults are injected during the encryption process, the fault propagation patterns denote some relations between the input and output difference of the specific S-boxes. In almost all block ciphers, including AES, the S-box values are known, so an attacker can simply conclude the difference distribution table of the utilized S-box. The inputs of S-boxes are mainly combined with the round Keyes's chunk through some mixing operations. The attacker can reduce the search space of some secret information, i.e., a part of the key, exploiting the difference distribution table and the relations between the difference of input and output. This divide-and-conquer method is used to extract the whole cryptographic key of most block ciphers quite efficiently [20]. So, integrating its hardware implementations with an efficient fault resilient scheme is crucial for making AES robust to random and/or malicious faults. There are many online error detection schemes for SubByte implementation of AES; see, for example, [21-22].

Just a few studies among previous research works have addressed fault correction. In fact, most of the previous studies have only considered the detection task, so extra corrective operations should be employed for their solutions. In [23], a hybrid redundancy is proposed in which hardware redundancy and time redundancy are combined for fault correction in S-box. Their proposed S-box architecture can tolerate single faults. It is worth noting that the fault-tolerant S-box in [23] provides a high level of reliability against the natural faults due to the essence of electronic devices, not the malicious faults in the fault attacks.

The present paper is mainly aimed to propose a high-throughput fault-attack resistant hardware implementation of AES S-box. We propose a correction scheme at the hardware level so that the circuit frequency is not significantly affected. In this paper, a high-speed design is considered. In fact, we exploit the features of gate-level implementation of S-box, allowing the pipeline technique to speed up the hardware implementation of SubByte operation of AES. The proposed technique is also practical for any generic cipher block.

We also implement the traditional fault-tolerant configurations, triple time redundancy, and triple module redundancy of the AES S-box and compare the implementation results of the proposed architecture to both of them.

N-tuple modular redundancy (NMR) [24] is a well-known fault-tolerant scheme based on hardware redundancy. Dual modular redundancy (DMR) is the most famous realization of NMR for performing error detection task. Another special case of NMR is triple modular redundancy (TMR) in which three identical units execute the same operation and the output is deduced from the majority voter [25, 26].

Time redundancy is achieved by re-computation of an operation using the same hardware multiple times, saving results, and comparing them for the error correction or detection tasks. N-tuple temporal redundancy is a generic fault-tolerant configuration of time redundancy. The triple time redundancy (TTR) is a special form of N-tuple temporal redundancy. In this scheme, the same input data is processed through the same unit three times. The majority voter generates the output of TTR by the majority vote of these three consecutive processes [26-27].

The main contributions of this paper are as follows:

- We present an implementation of a high-throughput and lightweight S-box in the gate level for high-speed AES encryption.
- We propose a fault-attack resistant technique, i.e., FC-DMR, for real-time applications which cannot tolerate high running time and require a high-speed process. The proposed technique could generally be used in all digital functional units.
- We design a new DMR voter that is composed of standard library components and could be implemented on any digital platform, such as FPGA and ASIC.
- Finally, we implement the AES S-box in TMR and TTR configurations in the same situation as HFS-box for design metrics comparison.

The rest of the paper is organized as follows. Section 2 presents a brief background of the S-box of the AES algorithm and its implementation. Section 3 presents the proposed fault-attack resistant technique (FC-DMR) besides our DMR voter model. It also describes the HFS-box architecture. We evaluate the proposed architecture's architectural characteristics in terms of area, frequency, and throughput in Section 4. Finally, Section 5 concludes the paper.

2. S-BOX IMPLEMENTATION

In this subsection, we describe the S-box operation and its utilized architecture. The proposed S-box architecture using composite-field in [28] is employed in this paper. The S-box operation, which is believed to be most resource-consuming among other AES operations, is a nonlinear mapping on each state array byte. This nonlinear mapping is nothing but finding a multiplicative inverse over $GF(2^8)$, i.e., Galois field, which is arithmetic in a finite field (a field containing a finite number of elements) contrary to arithmetic in a field with an infinite number of elements, like the field of rational numbers. $x^{-1} \epsilon\, GF(2^8)$ is followed by an affine transformation. In other words, if $y = SB(x)$ and $X \epsilon GF(2^8)$ and $Y \epsilon GF(2^8)$, then we have:

$$y = Ax^{-1} + b = \begin{bmatrix} 1 & 1 & 0 & 0 & 0 & 0 & 1 & 0 \\ 0 & 1 & 0 & 0 & 1 & 0 & 1 & 0 \\ 0 & 1 & 1 & 1 & 1 & 0 & 0 & 1 \\ 0 & 1 & 1 & 0 & 0 & 0 & 1 & 1 \\ 0 & 1 & 1 & 1 & 0 & 1 & 0 & 1 \\ 0 & 0 & 1 & 1 & 0 & 1 & 0 & 1 \\ 0 & 1 & 1 & 1 & 1 & 0 & 1 & 1 \\ 0 & 0 & 0 & 0 & 0 & 1 & 0 & 1 \end{bmatrix} x^{-1} + \begin{bmatrix} 0 \\ 0 \\ 0 \\ 0 \\ 1 \\ 0 \\ 1 \\ 1 \end{bmatrix} \quad (1)$$

Since direct multiplicative inversion of S-box computation is costly, multiplicative inversion in composite fields is preferred [29]. This implementation leads to lower complexity and smaller implementation area.

The S-box implementation using composite-field and polynomial basis is illustrated in Fig. 1.

As shown in this figure, the 8-bit input of multiplicative inversion, i.e., $X = \sum_{i=0}^{7} \alpha_i x_i$ in the binary field $GF(2^8)$ using the transformation matrix δ, transforms to composite-field $GF(2^8)/GF(((2^2)^2)^2)$. In turn, the output of the multiplicative inverse from composite-field transforms back to binary field $GF(2^8)$ by the inverse transformation matrix δ^{-1} to obtain X^{-1}. The hierarchical composite-field decomposition, i.e., $GF(((2^2)^2)^2) \rightarrow GF((2^2)^2)$, $GF((2^2)^2) \rightarrow GF(2^2)$, and $GF(2^2) \rightarrow GF(2)$, can be made using the irreducible polynomials of $x^2 + x + \lambda$, $x^2 + x + \varphi$ and $x^2 + x + 1$, respectively. As shown in Fig. 1, the output of the S-box, i.e., Y, is obtained using the affine transformation after inverse transformation (δ^{-1}) [27]. The S-box is composed of the multiplications, squaring, and inversion all of which are over $GF((2^2)^2)$. Besides these arithmetic blocks, the S-box includes modulo-2 addition that is realized by XOR gates (see Fig. 1). Considering this figure, the output of the S-box can be formulated as follows:

$$\sigma_h = ((\xi_h + \xi_l)\xi_l + \xi_h^2\lambda)^{-1}\xi_h \quad (2)$$

$$\sigma_l = ((\xi_h + \xi_l)\xi_l + \xi_h^2\lambda)^{-1}(\xi_h + \xi_l) \quad (3)$$

where ξ and σ are the input and output of the multiplicative inversion, respectively. It is also worth mentioning that we have used the proposed architecture for different parts of the S-box, i.e., adder and multiplier in [28].

3. Proposed Fault Correction Structure (FC-DMR)

3.1. FC-DMR

We propose a correction technique in the DMR implementation of a digital circuit (FC-DMR) depicted in Fig. 2. The proposed FC-DMR protects the operation of both combinational and sequential parts of a digital circuit in each pipeline stage. Fig. 2 depicts an instance pipeline stage *i* in the intended circuit. As depicted in this figure, our FC-DMR consists of the following elements:

- *Pipeline Logic$_i$ (original)*: a part of the system's combinational logic utilized to process data in the original mode in the ith pipeline stage.
- *Pipeline Logic$_i$ (redundant)*: a redundant copy of the original ith pipeline stage utilized to process data in the redundant mode in the *ith* pipeline stage.
- *Register stage$_i$*: the register or sequential part of the *ith* pipeline including DMR register and two DMR voters to preserve the correct state in the presence of a fault.
- *DU*: the fault detection unit, which is actually implemented using a comparator must provide the output error signal *err^i*, which indicates differences in the DMR register in the ith pipeline stage occur.
- *CU*: the control unit producing *Err*, which is a general error signal and indicates fault occurrence in the system (any pipeline stage), i.e., a fault is detected.

The input of each pipeline stage is processed by the pipeline logic and its redundant unit.

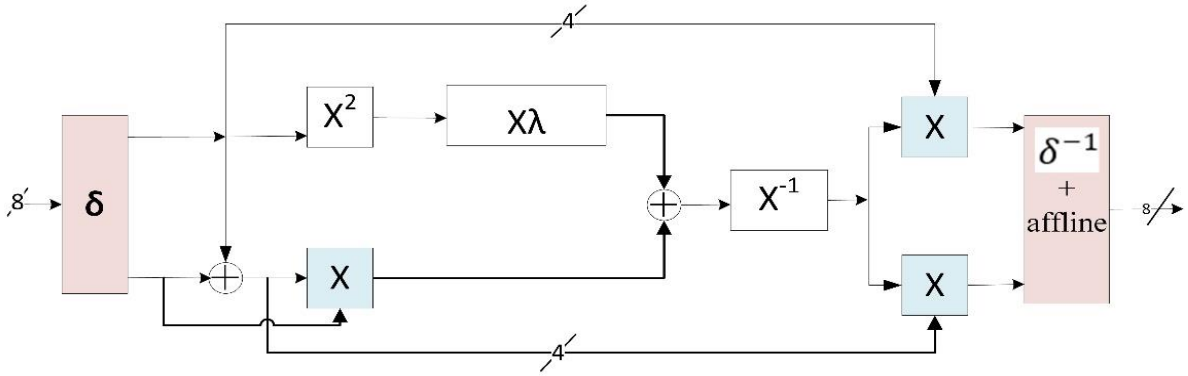

Fig. 1: Composite field-based S-box architecture.

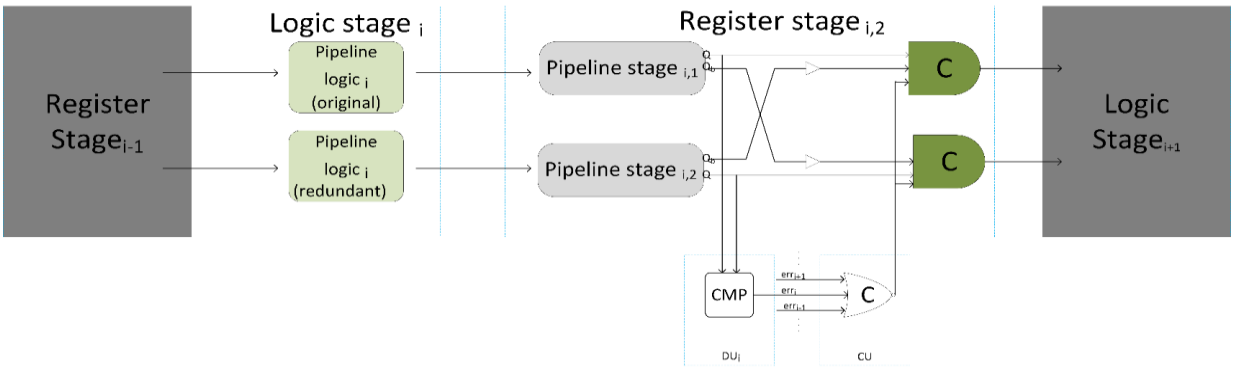

Fig. 2: The proposed fault correction technique in DMR implementation (FC-DMR).

The corresponding output of the original and redundant pipeline logic units are stored in the register stages, i.e., pipeline register$_1$ and pipeline register$_2$, respectively. If the register's contents are identical, no fault is detected. Otherwise, the comparator CMP^i's output in DU^i, i.e., err^i, will be activated. Two DMR voters are employed to protect both combinational and sequential part of the system. The proposed technique can correct any transient fault that occurs in a single S-box. When a fault is detected in any pipeline stage components, either in the logic stages, in the pipeline registers, or in the *DU*, the *CU* will reset its output, i.e., *Err*, and later it will prevent loading the incorrect state on the output of DMR voters.

Hence, the pipeline logics process the previous correct state till the fault effect disappears. When the fault effect disappears, the next correct state is processed without any problem. This solution may put a negligible delay overhead on the critical path due to the comparison and voting.

3.2. Proposed Voter

The employed voter does the two tasks of a majority voter in the DMR technique, i.e., holding the previous state when facing a mismatch and changing the vote signal's value when both modules produce the same output (Fig. 3).

In fact, when the outputs of the two replicas are not the same as each other, which means an error has occurred, the voter holds the previous value until the two replicas' outputs become similar. Besides, our design has a delay module that is useful if the comparator faces a mismatch. This delay makes it possible to affect the enable signals. Enables are provided to control internal wires not to send the faulty signals to voter's output, which means that the pipeline stage is unchanged until the correct value gains and the sequence in our pipeline design remains unaffected.

3.3. HFS-box

The main contribution of this paper is proposing high-throughput fault-attack resistant hardware implementations of S-box.

We propose a full pipeline implementation of S-box in the composite field approach, which leads to the reduction of the circuit critical path. In fact, this solution enables us to enhance the frequency of clock signal in our proposed method and also makes it suitable for meeting the high-speed application requirements.

The proposed pipeline S-box is depicted in Fig. 4. We place pipeline registers into this schema, which are illustrated by the dotted lines. As depicted in this figure, the proposed S-box architecture (shown in Fig. 1) is divided into five stages. These pipeline registers are inserted into S-box architecture so that the critical path is optimally pipelined. This architecture is integrated with the proposed FC-DMR to achieve fault tolerance for any transient fault in both combinational and sequential parts in any pipeline stage of a single S-box, named HFS-box. In HFS-box, each DMR implementation of pipeline logic is lied between two register stages to check against fault occurrence, as depicted in Fig. 2.

4. Implementation Result

To evaluate the proposed HFS-box, we compare it with the TMR and TTR implementation of S-box, as traditional fault-tolerant structures with high fault correction capability. We report the synthesis result by using the TSMC 180 nm CMOS. We employ Verilog as the design entry description language and Synopsys DC as the synthesis tool. It should be noted the 8-bit SubByte operation is considered, so a single S-box is needed in each structure.

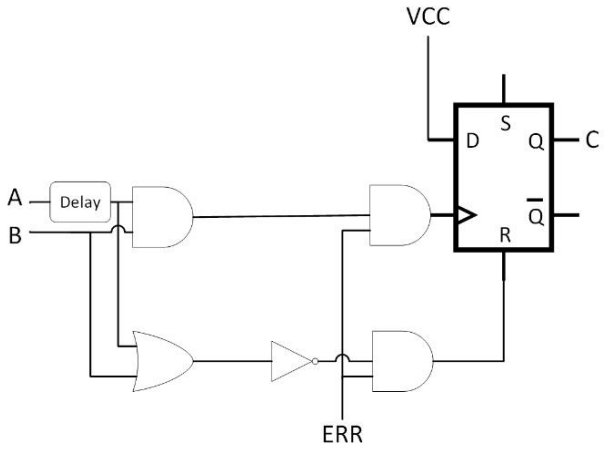

Fig. 3: Proposed voter in gate level.

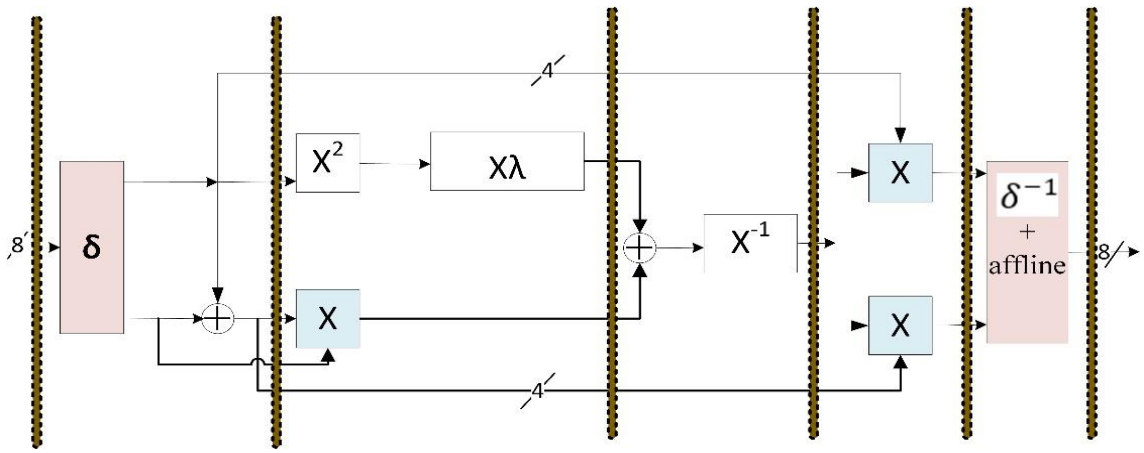

Fig. 4: The architecture of the S-box with the 5-stage pipeline.

Table 1: Throughput, maximum frequency, area result.

Design metric		Original	TMR	TTR	HFS-box
Area	GE	212.42	673.31	279.02	503.46
	% of area overhead	-	216	31.35	137
Freq.	MHz	555	525	519	492
	% of reduction	-	-5.4	-6.4	-11.3
Throuput	Mbps	4440	4200	1384	3936
	% of reduction	-	-5.4	-68.8	-11.3
Fault Tolerance	Transition	×	✓	✓	✓
	Permanent	×	✓	×	×
Security against fault attack		×	✓×	✓××	✓

In this section, the ASIC implementation results of all fault-tolerant S-box implementations are reported and compared. The design features that we consider include area, area overhead, frequency, and frequency overhead. Table 1 presents the implementation results of all fault resilient designs.

In this table, we use (4) to calculate- the-cost overhead.

$$Overhead = \frac{C_{FT} - C_{O}}{C_{O}} \quad (4)$$

where C_{O} is the original implementation cost (area, frequency, throughput, etc.), and C_{FT} is the cost of the fault tolerant implementation. It can be seen that TTR has the lowest area overhead (44.5% and 58.54% reduction compared to HFS-box and TMR, respectively) and, at the same time, lower throughput (64.83% and 67.04% worse than HFS-box and TMR, respectively). HFS-box requires about 503 NAND gate equivalences (GEs). Actually, it puts more area overhead than TTR but still is much better than TMR (25.22% better than TMR). However, TMR achieves the best throughput among all fault resilient architectures, its security and reliability against fault attacks is lower than our HFS-box, and also it puts much more area overhead on the original S-box than HFS-box.

The security of TMR and TTR is overshadowed by the majority voter. In fact, the majority voter is a bottleneck for these traditional fault-tolerant schemes. There are many works focused on introducing fault-tolerant majority voter. But, we do not address them because those research works are out of the scope of this paper. In addition, according to the proposed structure for the voter, it can be seen that the proposed design can detect symmetric transient errors in a very short period. However, TMR and TTR configurations do not have such capability. So, the proposed HFS-box can offer a higher level of reliability and better security against fault attacks, as mentioned in Table 1.

In fact, the proposed low-cost HFS-box can continue its proper task without a considerable negative impact on the system speed or even any traditional recovery scheme. It is a suitable fault-tolerant technique for resource-constrained applications that require a high level of security.

5. Conclusion

In this paper, we proposed a lightweight high-throughput fault-attack resistant architecture for composite field S-box implementation of AES, which consumes the largest space in AES, named HFS-box. The proposed fault-attack resistant technique is based on fault correction in DMR implementation (FC-DMR) combined with a temporal redundancy technique. It can correct transient faults, which may occur in S-box naturally or maliciously. Our solution is valid for any digital circuit implementation (especially block cipher hardware implementation) with different levels of pipelining. HFS-box uses five pipeline stages to meet the real-time application requirements for speed and throughput. Indeed, we inserted pipeline registers in optimal places in the S-box architecture. Furthermore, we introduced a compatible DMR voter with our FC-DMR. The proposed HFS-box and two well-known methods with high fault-tolerant ability, i.e., TMR and TTR, were implemented on ASIC using TSMC 180nm CMOS technology, and their area, frequency, and throughput were derived and reported. The synthesis results pointed out that the HFS-box had a low area overhead (137%) and low throughput degradation (11.3) compared with other fault-tolerant schemes.

CRediT Authorship Contribution Statement

Mahdi Taheri: Conceptualization, Formal analysis, Methodology, Resources, Roles/Writing - original draft, Writing - review & editing. **Saeideh Sheikhpour:** Formal analysis, Writing - review & editing. **Mohammad Saeed Ansari:** Conceptualization**,** Formal analysis. **Ali Mahani:** Project administration, Supervision**,** Writing - review & editing.

Declaration of Competing Interest

The authors declare that they have no known competing financial interests or personal relationships that could have appeared to influence the work reported in this paper. The ethical issues; including plagiarism, informed consent, misconduct, data fabrication and/or falsification, double publication and/or submission, redundancy has been completely observed by the authors.

References

[1] S. Patranabis, and D. Mukhopadhyay, *Fault tolerant architectures for cryptography and hardware security*. Berlin: Springer, 2018.

[2] *Announcing the advanced encryption standard (AES)*, Federal Information Processing Standards Publication 197, no. 1-51, 3-3., Nov. 2001.

[3] D. Bui, D. Puschini, S. Bacles-Min, E. Beigné and X. Tran, "AES datapath optimization strategies for low-

power low-energy multisecurity-level internet-of-things applications", *IEEE Transactions on Very Large Scale Integration (VLSI) Systems*, vol. 25, no. 12, pp. 3281-3290, 2017.

[4] D.-S. Kundi, A. Aziz, N. Ikram, "A high performance ST-Box based unified AES encryption/decryption architecture on FPGA", *Microprocessors and Microsystems*, vol. 41, no. 1, pp. 37-46, 2015.

[5] S. S. Priya,, P. Karthigaikumar, N. M.Siva-Mangai , P. K. Gaurav-Das, "An-efficient hardware architecture for high throughput AES encryptor using MUX based sub pipelined S-box", *Wireless Personal Communications*, vol. 94, no. 4, pp.2259-2273, 2017.

[6] S. Shanthi Rekha and P. Saravanan, "Low-cost AES-128 implementation for edge devices in iot applications", *Journal of Circuits, Systems and Computers*, vol. 28, no.4, pp.1950062, 2019.

[7] E. Biham, A. Shamir, "Differential fault analysis of secret key cryptosystems", in *Advances in Cryptology (CRYPTO '97), FLEXChip Signal Processor (MC68175/D)*, 1997 pp. 513-525.

[8] T. Fuhr, E. Jaulmes, V. Lomné, and A. Thillard, "Fault attacks on AES with faulty ciphertexts only", *2013 Workshop on Fault Diagnosis and Tolerance in Cryptography*, Santa Barbara, CA, 2013, pp. 108-118.

[9] P. Dusart, G. Letourneux, and O. Vivolo, "Differential fault analysis on AES", Cryptology ePrint Archive: Report 2003/010, 2003, [online] Available: http://www.iacr.org.

[10] S. S. Mukherjee, J. Emer, and S. K. Reinhardt, "The soft error problem: an architectural perspective", in *11th International Symposium on High-Performance Computer Architecture*, San Francisco, CA, USA, 2005, pp. 243-247.

[11] X. Guo and R. Karri, "Recomputing with permuted pperands: A concurrent error detection approach", *IEEE Transactions on Computer-Aided Design of Integrated Circuits and Systems*, vol. 32, no. 10, pp. 1595-1608, 2013.

[12] M. Mozaffari-Kermani, A. Reyhani-Masoleh, "Concurrent structure independent fault detection schemes for the advanced encryption standard", *IEEE Transaction on computers*, vol. 59, no. 5, pp. 608-622, 2010.

[13] H. Mestiri, F. Kahri, B. Bouallegue, and M. Machhout, "A high-speed AES design resistant to fault injection attacks", *Microprocessors and Microsystems Journal Elsevier*, vol. 41, pp. 47-55, 2016.

[14] M. Bedoui, H. Mestiri, B. Bouallegue, M. Marzougui, M. Qayyum, and M. Machhout, "An improved and efficient countermeasure against fault attacks for AES", *2017 2nd International Conference on Anti-Cyber Crimes (ICACC)*, Abha, 2017, pp. 209-212.

[15] S. Morioka and A. Satoh, "An optimized s-box circuit architecture for low power aes design", *Cryptographic Hardware and Embedded Systems-CHES*, 2003, pp. 271–295.

[16] N. Liao, X. Cui, T. Wang, K. Liao, D. Yu, and X. Cui, "A high-efficient fault attack on AES S-box", *International Conference on Information Science & Technology*, pp. 210-215, 2016.

[17] Y. Liu, X. Cui, J. Cao, and X. Zhang, "A hybrid fault model for differential fault attack on AES", *2017 IEEE 12th International Conference on ASIC (ASICON)*, 2017, pp. 784-787.

[18] J. Park, S. Moon, D. Choi, Y. Kang, and J. Ha, "Fault attack for the iterative operation of AES S-Box", *5th International Conference on Computer Sciences and Convergence Information Technology*, 2010, pp. 550-555.

[19] C.-N. Chen and S.-M. Yen, "Differential fault analysis on AES key schedule and some countermeasures", *In Information Security and Privacy, LNCS Springer 2003*, volume 2727, pages 118-129, 2003.

[20] S. Ali, X. Guo, R. Karri, and D. Mukhopadhyay, "Fault attacks on AES and their countermeasures", *in Secure System Design and Trustable Computing*, 2015, pp. 163-208.

[21] M. Mozaffari-Kermani and A. Reyhani-Masoleh, "A lightweight high-performance fault detection scheme for the advanced encryption standard using composite fields", *in IEEE Transactions on Very Large Scale Integration (VLSI) Systems*, vol. 19, no. 1, pp. 85-91, Jan. 2011.

[22] I. Koren, S.Y.H. Su, "Reliability analysis of N-modular redundancy systems with intermittent and permanent faults", *in IEEE Transactions on Computers*, vol. C-28, no. 7, pp. 514-520, July 1979.

[23] F. Flammini, N. Mazzocca, V. Vittorini, and S. Marrone, "A new modeling approach to the safety evaluation of n-modular redundant computer systems in presence of imperfect maintenance", Re*liability Eng. Syst. Safety (RESS)*, vol. 94, no. 9, pp. 1422-1432, 2009.

[24] S. Sheikhpour, A. Mahani, and N. Bagheri, "Reliable advanced encryption standard hardware implementation: 32-bit and 64-bit data-paths", Microprocessors and Microsystems, vol. 81, p.103740, 2021.

[25] M. Mozaffari-Kermani, A. Reyhani-Masoleh, "Fault detection structures of the S-boxes and the inverse S-boxes for the advanced encryption standard", Journal of Electronic Testing, vol. 25, no. 4, pp. 225-245, 2009.

[26] T. An, L. A. d. B. Naviner, and P. Matherat, "A low cost reliable architecture for S-boxes in AES processors", *2013 IEEE International Symposium on Defect and Fault Tolerance in VLSI and Nanotechnology Systems (DFTS)*, 2013, pp. 155-160.

[27] M. Taheri, S. Sheikhpour, MS. Ansari, and A. Mahani, "DMR-based technique for fault tolerant AES S-box architecture", arXiv preprint arXiv:2009.05329. 2020.

[28] N. Ahmad, S. M. Rezaul Hasan, "Low-power compact composite field AES S-box/Inv S-box design in 65 nmCMOS using Novel XOR Gate", *Integration*, vol. 46, no. 4, pp. 333-344, 2013.

[29] S. Sheikhpur, M. Taheri, M.S. Ansari, and A. Mahani, "Strengthened 32-bit AES implementation: Architectural error correction configuration with a new voting scheme", *IET Computers & Digital Techniques*, 2021.

BIOGRAPHY

Mahdi Taheri received his B.Sc. degree in electronic engineering from the Khaje Nasir University of Technology (KNTU), Tehran, Iran, in 2017 and his M.Sc. degree in Electronic Engineering from the Shahid Bahonar University of Kerman, Kerman, Iran, in 2020. Since then, he was with the RSS Lab at the Shahid Bahonar University of Kerman for 1 year, and now, he is studying his Ph.D. at the Tallinn University of Technology (TalTech). His research interests focus on hardware assessment and reliability of neural networks, fault-tolerant designs, and FPGA-based accelerators.

Saeideh Sheikhpour received her Ph.D. in Electrical Engineering from the Shahid Bahonar University of Kerman, Kerman, Iran, in 2019. Her current research interests are fault-tolerant designs, reliable and secure cryptographic hardware designs, circuit and system reliability and quality, soft computing, artificial intelligence, and sensor networks.

Mohammad Saeed Ansari received the BSc and MSc degrees in electrical and electronic engineering from the Iran University of Science and Technology, Tehran, Iran, in 2013 and 2015, respectively, and the PhD degree in integrated circuits and systems from the University of Alberta, Edmonton, AB, Canada, in 2019. He is presently a digital design engineer at Eideticom Computational Storage, Calgary, AB, Canada. His research interests include approximate computing and developing hardware accelerator IP cores for data compression/decompression, neural networks, and digital signal processing applications.

Ali Mahani received his B.Sc. degree in Electronic Engineering from the Shahid Bahonar University of Kerman, Iran in 2001, and his M.Sc. and Ph.D. degrees both in Electronic Engineering from the Iran University of Science and Technology (IUST), Tehran, Iran in 2003 and 2009, respectively. Since then, he has been with the Electrical Engineering Department of the Shahid Bahonar University of Kerman, where he is currently an associate professor. His research interests focus on fault-tolerant designs, FPGA-based accelerators, approximate digital circuits, stochastic computing, and networked systems.

Copyrights
© 2021 Licensee Shahid Chamran University of Ahvaz, Ahvaz, Iran. This article is an open-access article distributed under the terms and conditions of the Creative Commons Attribution –NonCommercial 4.0 International (CC BY-NC 4.0) License (http://creativecommons.org/licenses/by-nc/4.0/).

Shahid Chamran University of Ahvaz

Iranian Association of Electrical and Electronics Engineers

Journal of Applied Research in Electrical Engineering

E-ISSN: 2783-2864
P-ISSN: 2717-414X
Homepage: https://jaree.scu.ac.ir/

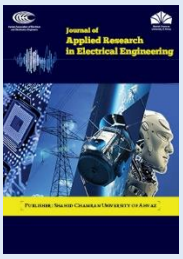

Research Article

Optimal Day-Ahead Scheduling of a CHP and Renewable Resources-Based Energy Hub with the Aim of Improving Resiliency During Input Energy Carriers' Outage

Shabnam Rezaei, and Ahmad Ghasemi *

Department of Electrical and Computer Engineering, Jundi-Shapur University of Technology, Dezful 64615334, Iran

** Corresponding Author: aghasemi@jsu.ac.ir*

Abstract: This paper proposes a novel day-ahead energy hub scheduling framework aimed at improving resiliency. Accordingly, an energy hub including combined heat and power (CHP), boiler, electric-heat pump (EHP), absorption and electric chillers, energy storages and renewable sources is considered. This energy hub is equipped with smart grid (SG) infrastructures, making it possible to implement demand response (DR) programs and optimally operate energy storages. The hub is connected to the electricity and natural gas networks. Outage of input energy carriers causes failure of devices in the energy hub, loss of electrical loads, failure in cooling and heating and thus reduced resiliency. Maintaining the security of the hub consumers' power supply system in the event of such severe disturbances is essential. Therefore, a new strategy based on the use of backup electric energy storages (EES) and DR program is proposed in this paper to improve resiliency. In addition, a numerical index is used to accurately calculate and evaluate resiliency. Numerical studies show that the proposed strategy improves resiliency during the outage of power and gas networks by 12.02% and 14.23% respectively when backup energy storages and DR program are implemented simultaneously.

Keywords: Energy hub, renewable energy sources, energy storage, demand response (DR), resiliency.

Article history
Received 10 February 2021; Revised 11 June 2021; Accepted 12 June 2021; Published online 30 June 2021.
© 2021 Published by Shahid Chamran University of Ahvaz & Iranian Association of Electrical and Electronics Engineers (IAEEE)
How to cite this article
S. Rezaei, and A. Ghasemi, "Optimal day-ahead scheduling of a CHP and renewable resources-based energy hub with the aim of improving resiliency during input energy carriers' outage," *J. Appl. Res. Electr. Eng.*, vol. 1, no. 1, pp. 93-111, 2022. DOI: 10.22055/jaree.2021.36613.1023

Check for updates

NOMENCLATURE

Acronyms

AC	Absorption chiller
CES	Cooling energy storage
CHP	Combined heat and power
DER	Distributed energy resources
DR	Demand Response
EC	Electric chiller
EDS	Electric distribution system
EES	Electric energy storage
EH	Energy hub
EHP	Electric heat pump
HES	Heat energy storage
MINLP	Mixed-Integer Non-Linear Programming
NGDS	Natural gas distribution system
PV	Photo Voltaic
ST	Solar thermal energy
WT	Wind Turbine

Indices

t	Index for time periods
X	Type of storage in terms of energy stored (EES/ HES/ CES)
Y	Original or backup storage (O/B)

Parameters

γ_t^{GE} , γ_t^{NG}	Grid electricity and Natural gas

	prices in time t [$/MWh]
γ^{PV} , γ^{WT} , γ^{ST}	PV, WT and ST operation cost [$/MWh]
γ^{EHP} , γ^{EC} , γ^{AC}	EHP, EC and AC operation cost [$/MWh]
γ^{E}	Electrical DR program cost [$/MWh]
$\gamma^{X,Y}$	Deterioration cost of energy storages [$/MWh]
P_t^D , H_t^D , C_t^D	Electrical, heating and cooling demands at time t [MW]
a , b , c , d , e , f	Coefficients of fuel consumption of CHP unit [1/MWh, -, 1/MWh, -, 1/MWh, MWh]
$(E/H)^{CHP}_{(A/B/C/D)}$	Junction points of feasible operation region of CHP [MW]
M	Large and small enough constants for linearization of feasible operation region of CHP [MW]
η^{Boiler}	Efficiency of boiler [-]
$H^{Boiler}_{\max}$, $H^{Boiler}_{\min}$	Maximum and minimum output heat of boiler [MW]
COP^{EC}_{cool}	Coefficient of performance of electric chiller [-]
C^{EC}_{max} , $C^{EC}_{\min}$	Maximum and minimum output cooling of electric chiller [MW]
COP^{AC}_{cool}	Coefficient of performance of absorption chiller [-]
$C^{AC}_{\max}$, $C^{AC}_{\min}$	Maximum and minimum output cooling of absorption chiller [MW]
COP^{EHP}_{cool}	Coefficients of performance of EHP in cooling mode [-]
$C^{EHP}_{\max}$, $C^{EHP}_{\min}$	Maximum and minimum output cooling of EHP [MW]
$E^{X,Y,ch}_{max}$, $E^{X,Y,dch}_{max}$	Maximum charge and discharge rates of each X and Y [MW]
$E^{X,Y}_{\max}$, $E^{X,Y}_{\min}$, $E^{X,Y}_{0}$	Maximum, minimum and initial charge levels of each X and Y [MW]
$\eta^{X,Y,ch}$, $\eta^{X,Y,dch}$	Efficiencies of charge and discharge of each X and Y [-]
$par^{low,DR}$	Maximum ratio of shifted low electrical load by DR [%]
$par^{high,DR}$	Maximum ratio of shifted high electrical load by DR [%]
$E^{EDS}_{\max}$, $E^{EDS}_{\min}$	Maximum and minimum interacting power with EDS [MW]
F^{NGDS}_{max}	Maximum received power from natural gas distribution system [MW]

Continuous decision variables

E_t^{PV} , E_t^{WT} , H_t^{ST}	Output power of PV, WT and ST in time t [MW]
F_t^{CHP} , E_t^{CHP} , H_t^{CHP}	Fuel consumption, output power and output heat of CHP unit in time t [MW]
H_t^{Boiler} , F_t^{Boiler}	Output heat and fuel consumption of boilers in time t [MW]
C_t^{EC} , E_t^{EC}	Output cooling and input electricity of electric chiller in time t [MW]
C_t^{AC} , H_t^{AC}	Output cooling and input heat of absorption chiller in time t [MW]
C_t^{EHP} , E_t^{EHP}	Output cooling and input electricity of EHP unit in time t [MW]
$E_t^{X,Y,ch}$, $E_t^{X,Y,dch}$, $E_t^{X,Y}$	Electricity/Heating/Cooling charge and discharge rates and the charge level of each X and Y in time t [MWh, MWh, MWh]
E_t^{LNS} , H_t^{LNS} , C_t^{LNS}	Load not supplied at time t [MW]
$P_t^{low,DR}$, $P_t^{high,DR}$	Shifted low and shifted high electrical power by DR at time t [MW]
E_t^{EDS}	Electricity purchased from (+) and sold to (-) EDS in time t [MW]
F_t^{NGDS}	Purchased natural gas from natural gas distribution system in time t [MW]

Binary decision variables

V_t^{CHP}	If CHP unit is on in time t, V_t^{CHP} =1, otherwise 0.
$u_t^{X,Y}$	Binary variable to prevent simultaneous charging and discharging of energy storage
I_t^{low} , I_t^{high}	A binary variable representing shifting high and shifting low condition of electrical load by DR at time t

1. INTRODUCTION

1.1. Aim

Outage of the input electricity or gas of the energy hubs can create disruption in the supply of consumer demand. Therefore, it is necessary to study the behavior of the system subjected to such disturbances and to consider the required preparations in order to maintain resiliency. Resiliency is, in fact, the ability to resist, adapt, and quickly return to normal operation of a system after a severe disturbance [1]. In energy hubs, proper use of energy storage systems with the ability of quick restoration of critical loads can reduce the

damage caused by long-term outages and thus improve network resiliency. Moreover, DR programs seem to be one of the efficient tools for proper load shifting and optimal scheduling of energy hub, leading to increased system resiliency. The objective of this paper is to investigate the effect of the participation of backup energy storages and DR programs on the resiliency improvement during the outage of electrical or natural gas networks using an energy hub day-ahead scheduling framework.

1.2. Literature Review

As a new concept in recent years, energy hub has attracted the attention of many researchers in the field of power system scheduling and management. It is a comprehensive and smart framework that provides the load required by the consumer side by combining, converting and storing various energy carriers. Optimal operation of the energy hub makes it possible to securely supply the required loads. In Ref. [2] the structure of a micro energy grid (MEG) based on energy hub including electrical, heating and cooling sub-hubs with renewable energy sources and energy storages has been presented. Also, a day-ahead dynamic optimal operation model has been formulated by considering DR in order to minimize the daily operation cost [2]. In Ref. [3] a model for scheduling an energy hub including CHP, gas boiler, absorption and electric chillers and electrical, heating and cooling energy storages has been proposed. The on/off switch of controllable equipment has been managed and DR programs have been implemented in this paper [3]. In Ref. [4] a combined energy system (CES) with the concept of energy hub including renewable energy sources such as wind and solar energy, electrical, heating and cooling energy storages, voltage conversion units and pressure and temperature control for storages, in the presence of the DR programs has been proposed. The aim of this system is to maximize the benefits of the energy hub [4]. In Ref. [5], an energy hub with three components of CHP, transformer and boiler, connected to electricity and natural gas networks, has been modeled to study the security of the system during natural gas flow outage.

Natural disasters and destructive actions are among the unpredictable events with low probability that can apply severe damage to the distribution system. Hence, around the world, the need to pay attention to higher network resiliency and energy continuity is felt more than ever due to the various consequences of energy outages at different levels. In general, the concept of resiliency is the capacity of an energy system to tolerate disturbances and continue the process of energy delivery to consumers [1]. In [6], a natural gas replacement scheme with electricity has been provided to improve service resilience at the time of earthquake and the creation of a problem for the gas network. In the project, household gas appliances have been replaced with ordinary and advanced electrical appliances so that consumers provide all their needs through the electricity grid. In this paper, the cost of replacing electrical appliances and also considering that power grid lines are more at risk than gas grid lines, potential problems for the power grid have not been considered [6]. Therefore, in the event of a problem for the power grid during the earthquake, replacing gas appliances with electrical appliances does not help increase service resilience.

The use of DR programs, renewable resources and storages can improve the resiliency of the power system. In [7] a distribution service restoration (DSR) framework using a multi-stage dynamic optimization model has been proposed to achieve a resilient distribution network in the presence of a DR program. In this paper, despite the use of electricity storage in the microgrids, the effect of storage on the improvement of resiliency has not been investigated [7]. In [8], a risk-constrained stochastic framework has been presented for joint energy and reserve scheduling of a resilient microgrid considering demand side management. In this article, the sensitivity of the microgrid profit, reliability indices, and the operator decision making in cases with and without the participation of customers to price-based DR programs have been studied by implementing a security-constrained power flow method in the scheduling process that can guarantee reliable operation of the microgrid under uncertainty, especially in islanding periods. In [9], an energy management strategy for daily networked microgrid scheduling called nested EMS has been proposed to increase system resiliency. In this method, if a microgrid is disconnected from the power grid and enters the island mode, the resiliency of the system through subgroups as well as the battery energy storage system will increase.

In [10], a process of resiliency analysis in networked microgrids in the presence of renewable energy sources along with an EES has been proposed. The EES has been scheduled to control fluctuations in the generation of renewable sources in both rainy and sunny days [10]. Moreover, the EES has been used to support the power distribution system during outage. However, in this paper, the power outage is considered to be a short interval of 3 hours and the solution adopted may not be suitable for long intervals. In [11] a process of resiliency analysis in microgrids along with distributed energy storage (DES) support for load restoration has been presented. In the case of power outage, DESs supply the required electricity by changing to the discharge mode. DESs are charged only through the power grid, which may not be able to restore the load in the event of a power outage and long-term lack of access to the grid, as well as in the event of consecutive outages.

In [12] energy resiliency modeling for a smart home (which is mainly powered by solar energy) with a local EES unit has been presented. Moreover, the effect of different EES operation strategies on resiliency for different generation and consumption patterns have been analyzed in this paper. In this paper, demand response programs are not used to improve resiliency that, better results will be obtained if this issue is considered. Using the idea of different strategies for using smart home batteries to improve the resiliency of the energy hub is useful due to the presence of converters such as CHP, boilers, chillers, etc. Also, the presence of heating and cooling energy carriers, the use of heating and cooling energy storages in addition to electrical energy storage can create more effective results. As mentioned earlier, in the energy hub, despite the smart grid infrastructure, the necessary ground is provided for the use of demand response programs. Therefore, the effect of demand response programs along with the idea of different battery operation strategies on improving resiliency can be examined. Therefore, examining the issue of resiliency and

calculating the degree of resiliency using the metric in the energy hub can be a significant issue that has not been considered based on the knowledge of the authors.

1.3. Contributions

This paper proposes a day-ahead scheduling framework for a CHP-based energy hub and renewables aimed at improving resiliency. The energy hub includes CHP, boiler, absorption chiller, electric chiller, electric heating pump (EHP) and electrical, heating and cooling energy storages. Renewable sources such as wind turbines (WT), photovoltaic panels (PV) and solar-thermal panels (ST) have also been used to meet part of the electricity and heating demand. The hub energy supplies the required energy, gas and part of its required electricity through gas and electricity networks. Any outage or disruption in the electricity or natural gas network will cause heavy damage to the energy hub. Improving hub resiliency can reduce outage damage. Therefore, in this paper, the increase of resiliency and continuity of hub energy during power or gas outages has been addressed. Moreover, in order to improve resiliency, the DR program for electrical load as well as backup battery strategies for all three electrical, heating and cooling loads have been employed. The scope of models in the technical literature and the contribution of this article are summarized in Table 1 (in the appendix). Compared to the existing studies, the main contributions of this article can be summarized as follows.

1. An optimization framework for energy scheduling of a resilient energy hub with DR programs and backup storage has been provided. In the proposed model, the operation has been performed in two modes: normal mode (connected to the grid) and outage mode of energy carriers.

2. The sensitivity of operating costs, load shedding of different loads during outages of input energy carriers and energy hub resiliency in cases with and without the participation of customers to price-based DR programs and the impact of energy backup storage have been studied in the scheduling process that can guarantee resilient operation of the energy hub, especially in outages of input energy carriers periods.

3. The most important devices in the energy hub (CHP and Boiler), which provide the highest amount of energy, consume gas fuel. Also, in areas which their thermal demands depend on natural gas, during the gas lines contingency face with thermal load shedding disaster. Therefore, the study of energy hub resilience during gas network outage is one of the important issues studied in this paper. Also, resiliency has been calculated for all consumer demands (electricity, heating and cooling) using a practical and accurate index.

1.4. Paper Organization

The rest of this paper has been organized as follows: in section 2, the architecture of the energy hub is delineated. In section 3, problem formulation is proposed. Case studies and numerical results are illustrated in section 4. Finally, some related conclusions are derived in section 5.

2. Architecture of the Proposed Energy Hub

The energy hub is a new evolutionary trend for the traditional distribution network, which integrates natural gas, electricity, heating, cooling, etc. Fig. 1 shows the proposed energy hub architecture, in which electricity and gas are considered as input energy carriers. On the other hand, WTs, PVs and STs as renewable energy sources are the sources of electricity and heating, supplying a part of the demands of the energy hub at different hours. Electricity, heating and cooling are also identified as energy hub outputs. CHP, boiler, absorption chiller, electric chiller, EHP as energy converters along with electrical, heating and cooling energy storages form the desired energy hub architecture.

One of the essential aspects of energy management is to ensure system security and increase network resiliency during disturbances [5]. Therefore, the resiliency of the system during power or gas outages is studied in this paper. Accordingly, in order to manage storages in the multi-carrier space of the energy hub, as well as to improve energy efficiency and minimize operating costs and calculate resiliency a new scheduling framework has been presented in this paper as shown in Fig. 2 (in the appendix). The energy hub is equipped with an energy management system (EMS) to schedule its local resources and to trade energy with the main grid. In this scheme, the customers are equipped with house energy management controllers and are able to respond to the electricity prices by adjusting their demand to reduce their consumption costs.

The operation of the energy hub is decomposed into normal and resilient operations. At the normal operation, energy hub is connected to the main grid, thus the EMS schedules the local DERs. However, when a severe disturbance event occurs in the main grid, energy hub can switch into resilient operation (i.e., outage mode). In this mode, EMS schedules available local resources to supply local loads with the lowest mandatory load shedding. Due to the presence of several different energy carriers in the hub, the priority of load supply during outage is considered based on the type of output energy carriers. The first priority is related to electricity load supply. The reason for this is that a summer day is studied in this article and in summer the demand for cooling is high and most of the cooling energy is supplied by the electric chiller and EHP, with electricity consumption. Although cooling energy supply is very

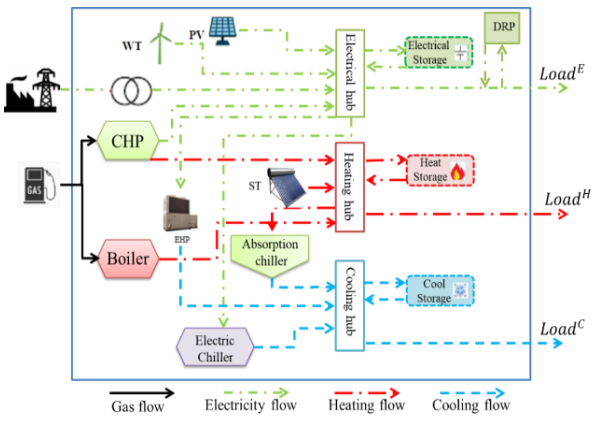

Fig. 1: The energy hub architecture.

important in summer, but the second priority is to provide heating load, which is due to the supply of some cooling energy by the absorption chiller with heating consumption. The electrical, heating and cooling energy storages in the energy hub can reduce the damage caused by long-term outages, and thus improve resiliency by restoring critical loads. Moreover, three more backup batteries have been provided in this paper to reduce the load shedding during the outage hours of energy carriers. In addition to storage devices, the DR program has been designed and implemented to change the pattern of electricity consumption with the aim of further adapting demand with generation hence, reducing load shedding and increasing resiliency at the outage hours of input energy carriers.

It should be noted that the cost of purchasing electricity from the electricity network, during the outage of the gas network, is considered higher than normal. The reason for this is more purchases from the electricity network during the gas network outage. This cost is defined as a step based on the comparison of the purchase of electricity from the electricity network in the normal state and the definite state of the gas network. Also in this model, demand response programs operate during the power network outage, based on the price set by the system operator. The price set by the operator is based on the percentage rate of load in the outage state compared to the normal state.

3. Mathematical Formulation

The general formula for the energy hub has been considered with respect to the effect of DR implementation and backup storage on system resiliency by creating different scenarios. This section includes objective function formulas, energy converters, and problem constraints. The formulation of energy converters has been presented to determine the relationship between the devices used in the energy hub.

3.1. The Objective Function

The objective function (1a) is to minimize the total cost of the energy hub across the scheduling horizon, i.e., overnight. The cost of an energy hub consists of two terms. The first term, defined in (1b), Refers to the cost of the energy hub in the conditions connected to the network. The second term, defined in (1c), Refers to the cost of the energy hub during the outage of the input energy carriers (electricity or gas networks). and include several costs that are defined separately. Term, defined in (1d), refers to the cost of fuel (natural gas) CHP and boiler. Term, defined in (1e), refers to the cost of buying/selling electricity from/to the grid. Term, defined in (1f), refers to the cost of photovoltaic panels and wind turbines. Term, defined in (1g), refers to the costs of generating cooling and heating energy by EHP, electric and absorption chillers, and solar-thermal panels. Term, defined in (1h), Refers to the cost of energy storage by the original storage in the energy hub. Term, defined in (1i), Refers to the cost of energy storage by the backup storage in the energy hub. Term, defined in (1j), refers to the cost of DR.

$$Min\ TotalCost = \mathrm{Cos}tNormal + \mathrm{Cos}tOutage \tag{1a}$$

$$\mathrm{Cos}tNormal = CostNG + CostGE + CostE + CostC\ \&\ H + \mathrm{Cos}tOStorage + CostDR \tag{1b}$$

$$\mathrm{Cos}tOutage = \begin{cases} \mathrm{Cos}tNG + \mathrm{Cos}tE + \mathrm{Cos}tC\ \&\ H + \mathrm{Cos}tOStorage + \\ \mathrm{Cos}tBStorage + \mathrm{Cos}tDR \qquad \text{Outage=Network Power} \\ \\ \mathrm{Cos}tGE + \mathrm{Cos}tE + \mathrm{Cos}tC\ \&\ H + \mathrm{Cos}tOStorage + \\ \mathrm{Cos}tBStorage + \mathrm{Cos}tDR \qquad \text{Outage=Network Gas} \end{cases} \tag{1c}$$

$$CostNG = F_t^{CHP} + \left(F_t^{Boiler} \times \gamma_t^{NGDS}\right) \tag{1d}$$

$$\mathrm{Cos}tGE = \sum_t \gamma_t^{GE} \times E_t^{EDS} \tag{1e}$$

$$CostE = \sum_t \gamma^{PV} \times E_t^{PV} + \sum_t \gamma^{WT} \times E_t^{WT} \tag{1f}$$

$$CostC\ \&\ H = \sum_t \gamma^{EHP} \times C_t^{EHP} + \sum_t \gamma^{EC} \times C_t^{EC} + \sum_t \gamma^{AC} \times C_t^{AC} + \sum_t \gamma^{ST} \times H_t^{ST} \tag{1g}$$

$$\mathrm{Cos}tOStorage = \sum_{t,X} \gamma^{X,O} \times \left(E_t^{X,O,ch} + E_t^{X,O,dch}\right) \tag{1h}$$

$$\mathrm{Cos}tBStorage = \sum_{t,X} \gamma^{X,B} \times \left(E_t^{X,B,ch} + E_t^{X,B,dch}\right) \tag{1i}$$

$$CostDR = \sum_t \gamma^{E} \times \left(P_t^{low,DR} + P_t^{high,DR}\right) \tag{1j}$$

3.2. CHP Modeling

CHP units receive gas as input energy and generate electricity and heating simultaneously. Therefore, CHP plays a key role in the energy hub by connecting the three energy carriers. It should be noted that the electricity and heating generation of CHP units are interdependent and cannot be controlled separately [13]. In other words, the electricity and heating are generated by each CHP unit overlap. This means that the electricity generated by the CHP limits its heating output and vice versa [3]. Each CHP unit has a practical operation area, which shows the interdependence of electricity and heating generation. The operating cost of CHP units is a function of electricity and

heating generated defined as (2a):

$$F_t^{CHP} = a \times E_t^{CHP} + b \times \left(E_t^{CHP}\right)^2 + c + d \times H_t^{CHP} + e \times \left(H_t^{CHP}\right)^2 + f \times H_t^{CHP} E_t^{CHP} \quad (2a)$$

$$E_t^{CHP} - E_A^{CHP} - \frac{E_A^{CHP} - E_B^{CHP}}{H_A^{CHP} - H_B^{CHP}} \times \left(H_t^{CHP} - H_A^{CHP}\right) \le 0 \quad \forall t \quad (2b)$$

$$E_t^{CHP} - E_B^{CHP} - \frac{E_B^{CHP} - E_C^{CHP}}{H_B^{CHP} - H_C^{CHP}} \times \left(H_t^{CHP} - H_B^{CHP}\right) \ge -\left(1 - V_t^{CHP}\right) \times M \quad \forall t \quad (2c)$$

$$E_t^{CHP} - E_C^{CHP} - \frac{E_C^{CHP} - E_D^{CHP}}{H_C^{CHP} - H_D^{CHP}} \times \left(H_t^{CHP} - H_C^{CHP}\right) \ge -\left(1 - V_t^{CHP}\right) \times M \quad \forall t \quad (2d)$$

$$E_C^{CHP} \le E_t^{CHP} \le E_A^{CHP} \times V_t^{CHP} \quad \forall t \quad (2e)$$

$$0 \le H_t^{CHP} \le H_B^{CHP} \times V_t^{CHP} \quad \forall t \quad (2f)$$

The feasible operation region for the CHP units studied in this paper has been shown in Fig. 3. This region is modelled by (2b) - (2d). Equation (2b) models the area below the line AB and (2c) models the area above the BC line. Also, the area above the CD line has been modeled using (2d). In these equations, M represents a very large number, and indices A, B, C and D represent the four margin points of the feasible operation region for CHP. And E_A^{CHP}, E_B^{CHP}, E_C^{CHP} and E_D^{CHP} are the electrical power and H_A^{CHP}, H_B^{CHP}, H_C^{CHP} and H_D^{CHP} are the thermal power points of the CHP areas. In (2c) and (2d), if the binary variable V_t^{CHP} is zero, the CHP output power and heating will be zero. Equations (2e) and (2f) express the power and heating generation constraints of CHP units.

3.3. Boiler Modeling

The boilers receive natural gas, F_t^{Boiler}, as their input energy source and convert the consumed gas to heat, H_t^{Boiler}, with the conversion efficiency of η^{Boiler} in (3a). The heating energy generated by the boilers is limited using (3b).

$$F_t^{Boiler} = \eta^{Boiler} \times H_t^{Boiler} \quad \forall t \quad (3a)$$

$$H_{min}^{Boiler} \le H_t^{Boiler} \le H_{max}^{Boiler} \quad \forall t \quad (3b)$$

3.4. Electric Chiller Modelling

The electric chiller uses electricity E_t^{EC} to generate cooling energy C_t^{EC}, where the amount of electricity consumed and the cooling generated are related by the chiller's coefficient of performance, COP_{cool}^{AC}; this relationship has been defined in (4a). Also, the cooling energy generated by the chiller is limited in (4b).

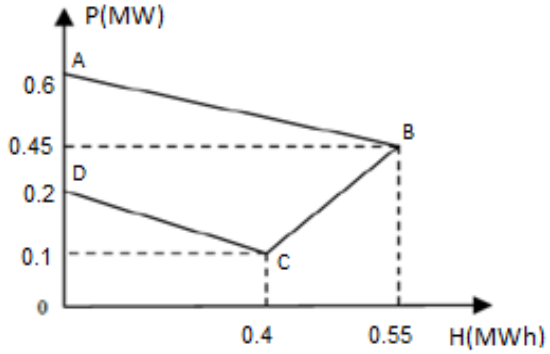

Fig. 3: Heat-power feasible operation region for the CHP.

$$C_t^{EC} = E_t^{EC} \times COP_{cool}^{EC} \quad \forall t \quad (4a)$$

$$C_{min}^{EC} \le C_t^{EC} \le C_{max}^{EC} \quad \forall t \quad (4b)$$

3.5. Absorption Chiller Modeling

The main difference between an absorption chiller and an electric chiller is that the input energy of the absorption chiller is heat, while the input energy of the electric chiller is electricity. The relationship between consumed heating, H_t^{AC}, and generated cooling of the absorption chiller, C_t^{AC}, as well as the constraint related to the generated cooling of the absorption chiller have been defined in (5a) and (5b), respectively.

$$C_t^{AC} = H_t^{AC} \times COP_{cool}^{AC} \quad \forall t \quad (5a)$$

$$C_{min}^{AC} \le C_t^{AC} \le C_{max}^{AC} \quad \forall t \quad (5b)$$

3.6. EHP Modeling

EHPs are of the most widely used equipment in the design of energy hubs, which work with electrical energy. These systems use heating stored in air, water and land to generate heating or cooling [14-16]. The electricity consumed in these systems is used to extract the stored heating and not to generate it. In these systems, several units of heating are usually extracted from the environment for the consumption of one unit of electrical energy [17]. EHPs are employed only for heating generation in winter and cooling generation in summer [3]. Given that this paper examines a summer day, EHP is used only to generate cooling. As demonstrated in (6a), power consumption, E_t^{EHP}, and generated cooling, C_t^{EHP}, are interconnected by the EHP coefficient of performance, COP_{cool}^{EHP}. Also, the cooling energy generated by EHP is limited by on (6b).

$$C_t^{EHP} = E_t^{EHP} \times COP_{cool}^{EHP} \quad \forall t \quad (6a)$$

$$C_{min}^{EHP} \le C_t^{EHP} \le C_{max}^{EHP} \quad \forall t \quad (6b)$$

3.7. Storage's Modeling

Energy storage devices are essential components for energy hubs, which have the ability to transfer energy in time dimensions. Storage devices store excessive energy or low-cost energy, and use it in times of energy shortages or high-priced hours [18]. The process of charging and discharging energy is similar for all the electrical, heating and cooling energy storages, which depends on the charge/discharge constraints, storage capacity and technical constraints [19]. The amount of energy stored is expressed in (7a) for scheduling horizon periods, and the constraints on the amount of energy stored are defined in (7b). The constraints on the amount of charge and discharge of energy have been defined in (7c) and (7d), respectively. Notably, the storage cannot charge and discharge energy simultaneously and, the binary variable $u_t^{X,Y}$ has been used to prevent simultaneous charging and discharging. Equation (7e) ensures that the initial charge level of the storage is equal to the end of the scheduling horizon.

$$E_t^{X,Y} = E_{t-1}^{X,Y} + \eta^{X,Y,ch} \times E_t^{X,Y,ch} - E_t^{X,Y,dch} \quad \forall X, \forall Y, \forall t \tag{7a}$$

$$E_{min}^{X,Y} \le E_t^{X,Y} \le E_{max}^{X,Y} \quad \forall X, \forall Y, \forall t \tag{7b}$$

$$0 \le E_t^{X,Y,ch} \le u_t^{X,Y} \times E_{max}^{X,Y,ch} \quad \forall X, \forall Y, \forall t \tag{7c}$$

$$0 \le E_t^{X,Y,dch} \le \left(1 - u_t^{X,Y}\right) \times E_{max}^{X,Y,dch} \quad \forall X, \forall Y, \forall t \tag{7d}$$

$$E_{24}^{X,Y} = E_0^{X,Y} \quad \forall X, \forall Y \tag{7e}$$

Superscript X indicates the type of storage in terms of energy stored in it, which is electrical energy storage (EES), heating energy storage (HES) and cooling energy storage (CES), whereas the superscript Y indicates the type of storage, i.e., original (O) or backup (B). $E_t^{X,Y}$ is the energy stored after charging/discharging energy, while $E_{t-1}^{X,Y}$ is the energy stored before charging/discharging energy at time t. $E_t^{X,Y,ch}$ is the charge rate and $E_t^{X,Y,dch}$ is the discharge rate at time t.

3.8. DR Program Modeling

DR program is an efficient tool for transferring load from peak to off-peak hours in order to optimally manage the energy hub [20], reduce electricity and natural gas consumption, as well as energy hub costs [21]. In this paper, in addition to the aforementioned applications, the DR program has been used as a tool to reduce the load shedding during the outage of energy carriers and increase resiliency. The following equations show the formulation of DR program constraints.

Equation (8a) show the balance between shifted high and low of electrical load. Or, in other words, the load shifting from high price time, $P_t^{high,DR}$, had to be done equally at a lower price time, $P_t^{low,DR}$. Equation (8b) express the limits allowed for the shifted high load at the low-price time with respect to the percentage of participation in the DR. The allowable limits for the shifted low load at the high price time and with respect to the percentage of participation in DR is expressed by (8c). Equation (8d) also states a constraint to prevent simultaneous load changes during high price hours and low-price hours, for which the binary values I_t^{low} and I_t^{high} have been used.

$$\sum_{t=1}^{24} P_t^{high,DR} = \sum_{t=1}^{24} P_t^{low,DR} \quad \forall t \tag{8a}$$

$$0 \le P_t^{high,DR} \le par^{high,DR} P_t^D I_t^{high} \quad \forall t \tag{8b}$$

$$0 \le P_t^{low,DR} \le par^{low,DR} P_t^D I_t^{low} \quad \forall t \tag{8c}$$

$$0 \le I_t^{high} + I_t^{low} \le 1 \quad \forall t \tag{8d}$$

3.9. Constraints of Connection Lines

The amount of electricity exchanged with the power grid, E_t^{EDS}, and the gas exchanged with the gas network, F_t^{NGDS}, should not exceed the maximum connection line between the energy hub and the electricity and natural gas network, where the constraints have been defined in (9a) and (9b).

$$E_{min}^{EDS} \le E_t^{EDS} \le E_{max}^{EDS} \quad \forall t \tag{9a}$$

$$0 \le F_t^{NGDS} \le F_{max}^{NGDS} \quad \forall t \tag{9b}$$

3.10. Energy Balance

- Balance in the electrical sector

$$E_t^{EDS} + E_t^{EES,Y,dch} \times \eta^{EES,Y,dch} + E_t^{CHP} + E_t^{WT} + E_t^{PV} + P_t^{high,DR} = P_t^D + E_t^{EES,Y,ch} + E_t^{EC} + E_t^{EHP} + P_t^{low,DR} \quad \forall t \tag{10a}$$

- Balance in the heating sector

$$H_t^{CHP} + H_t^{Boiler} + E_t^{HES,Y,dch} \times \eta^{HES,Y,dch} + H_t^{ST} + H_t^{EHP} = H_t^D + E_t^{HES,Y,ch} + H_t^{AC} \quad \forall t \tag{10b}$$

- Balance in the cooling section

$$C_t^{EC} + C_t^{AC} + E_t^{CES,Y,dch} \times \eta^{CES,Y,dch} = C_t^D + E_t^{CES,Y,ch} \quad \forall t \tag{10c}$$

3.11. Resiliency Modeling

Resiliency is the ability of a system to tolerate the events with a low probability of occurrence and high destructive effects by minimizing outages and returning to normal operation of the power system [22]. In power systems, load shedding is widely known as a disturbance which directly affects the system restoration process [23]. In the proposed model, the gas or electricity networks outage has been considered for the energy hub, and the effect of the participation of the power DR program and the backup storage on the load shedding and resiliency of the system is investigated. From the point of view of the system resiliency

index presented in Ref. [23], system performance is defined as the load supply at any time *t* as shown in Fig. 4. It should be noted that the lower the load shedding and the more resilient the system, the smaller the hatched area [23].

Then, the resiliency of the system can be determined as follows:

$$Resilience = \int_{t_0}^{t_1} \left[Q_0(t) - Q_1(t) \right] dt \quad (11)$$

This index is used to assess the overall resiliency of the system under a particular disturbance. $Q_0(t)$ represents the load supply in normal state. $Q_1(t)$ denotes the load shedding after a gas or power outage in the time interval $[t_0, t_1]$.

4. Numerical Studies

4.1. Data and Assumptions

As mentioned earlier, the sample energy hub has been connected to the electricity and natural gas networks, and supplies its natural gas and part of the electricity demand through the electricity and natural gas networks. The maximum amount of electricity and gas received from electricity and natural gas networks are 0.78 and 0.6 MW/h, respectively. This paper has studied the resiliency of an energy hub during a power or gas network outage for 9 consecutive hours during a day (a typical summer day). Electrical, heating and cooling demands on this summer day have been shown in Fig. 5. In the desired energy hub, wind and solar energy has been used to meet a part of consumer demand. The output power of wind turbine, photovoltaic panel and solar-thermal panel has been shown in Fig. 6. Also, the cost of electricity and natural gas has been presented in Fig. 7, and information about the parameters of the energy hub components is summarized in Table 2 (in the appendix). Changes in the cost of purchasing electricity from the electricity network during the gas network outage are shown in Table 3. Also, the price set by the operator for the utilization of load response programs during the power outage, based on the cost of the power grid in normal mode is shown in Table 4. It is noteworthy that the proposed design has been formulated as an MINLP problem and is solved by GAMS [24] software and SBB solver. The SBB solver is used in GAMS software to solve MINLP models. The problem-solving method by this solver is usually based on a combination of standard branch and bound methods [25]. The average computation time on a core i5 PC, 2.6 MHz with 8 GB of RAM is less than a minute.

4.2. Case Studies

With the aim of analyzing the optimal operation of the energy hub and investigating the effect of DR program and backup storages on reducing load shedding and increasing system resiliency during the hours of gas or electricity networks outage, six different scenarios are examined (Table 5). In scenarios 1, 2 and 3, the energy hub resiliency is studied during the natural gas network outage. In scenario 1, no measures have been considered to increase the resiliency. In Scenario 2, backup storages, and in Scenario 3, backup

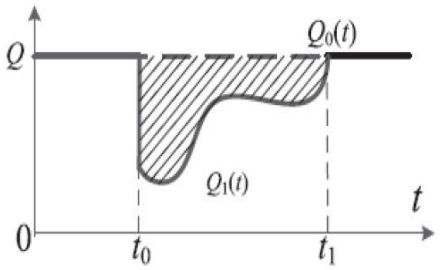

Fig. 4: Resiliency triangle.

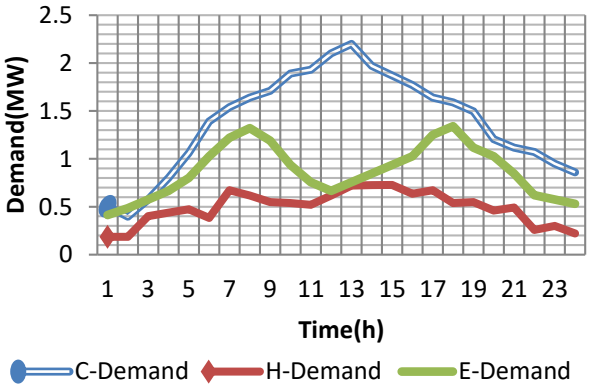

Fig. 5: The electrical, heating and cooling demand of the energy hub.

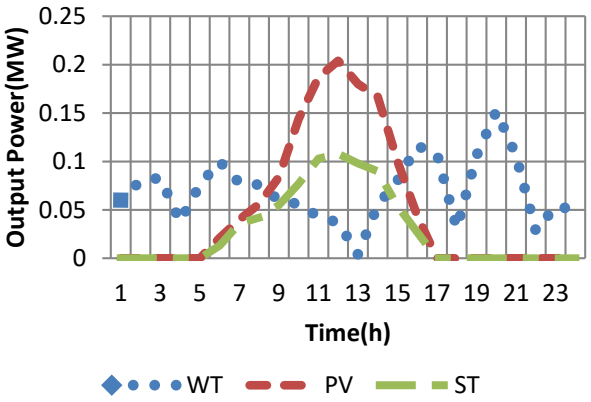

Fig. 6: Output power of WT, PV and ST.

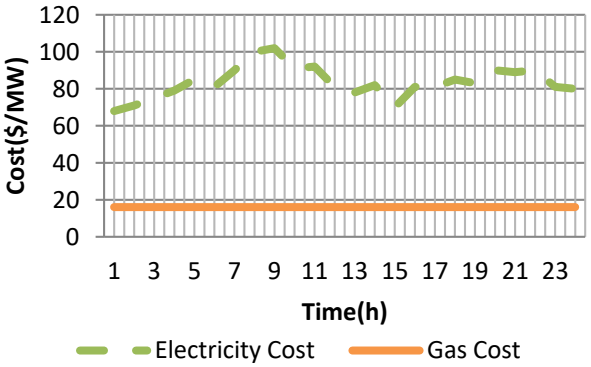

Fig. 7: The cost of electricity and gas.

Table 3: Changes in the cost of purchasing electricity from the grid during the outage network gas

The difference between buying electricity from the network in the normal state and the outage state of the gas network (MW)	Price($)
0	γ_t^{GE}
0.001-0.2	$1.05\gamma_t^{GE}$
0.201-0.4	$1.1\gamma_t^{GE}$
0.401-0.6	$1.15\gamma_t^{GE}$
0.601-0.8	$1.2\gamma_t^{GE}$

Table 4: The price set by the operator for the use of demand response programs during power network outage

The percentage of load in the outage state compared to the normal state	Price($)
0 – 20%	$1.2\gamma_t^{GE}$
21% - 40%	$1.15\gamma_t^{GE}$
41% - 60%	$1.1\gamma_t^{GE}$
61% - 80%	$1.05\gamma_t^{GE}$
81% - 100%	γ_t^{GE}

storages and DR program have been used simultaneously with the aim of enhancing resiliency in the energy hub. In Scenarios 4, 5 and 6, resiliency has been studied during the power outage. In Scenario 4, as in Scenario 1, no backup is provided to make the system resilient. In Scenario 5, only backup storages and in Scenario 6, in addition to backup storages, the DR program has been used to increase resiliency.

4.3. Simulation Results

4.3.1. Energy balance in scenarios related to gas network outages

- Electrical balance

The electrical balance for the first three scenarios, which are related to the gas network outage, has been shown in Fig. 8. In this figure, the upper bar charts show generation and the lower bar charts show consumption. CHP is one of the devices used to reduce energy purchases from the power grid, and consequently decrease operating costs in energy hubs. The CHP is switched off with gas network outage between 9- and 17-hours local time due to the gas fuel it uses. The CHP generates almost as much power as possible during all the hours it is in the circuit. This value shows the power generation corresponding to above point B in the operational area applicable to CHP in Fig. 3. According to Fig. 8, in all the first three scenarios, the purchase of electricity is less than EDS during the connection hours of the CHP. This is because the generation by CHP is cheaper than buying from EDS. However, during CHP outage, the amount of electricity purchased from the grid is at its maximum value of 0.78 MWh. Another efficient tool used in this energy hub to meet part of the electricity demand is renewable energy sources such as WT and PV. The maximum electricity generated by WT is 0.152 MW/h and the maximum generated electricity by PV is 0.204 MW/h, which reduces operating costs by generation. The original EES charge/discharge pattern is influenced by electricity tariffs.

Table 5: Scenarios

Scenario	Outage of		Backup storage	DR program
	Gas network	Electricity network		
1	❄	-	-	-
2	❄	-	❄	-
3	❄	-	❄	❄
4	-	❄	-	-
5	-	❄	❄	-
6	-	❄	❄	❄

In the first three scenarios, the original EES starts loading at low price hours and in case of excess electricity, the original of electricity stored in the original EES decreases at high price hours and if needed during CHP outage hours. As observed in Fig. 8, in the early hours of the day (1-3) and also sometimes in the middle hours of the day (11-14) when electricity costs are low, the original EES is charging. Also, in the hours 7-10 and 15-19 that the cost of electricity is high or there is a shortage of electricity, it is discharging energy. Therefore, the original EES system causes less energy to be purchased from the grid at high price hours and the cost of operating the energy hub is reduced. In scenarios 2 and 3, backup EES has also been used in addition to the original EES system. According to Fig. 8, in Scenario 1, which does not use backup EES and DR, the load shedding during the CHP outage hours is significant. But in Scenario 2, some of the load related to CHP outage hours is supplied by backup EES, and the load shedding is less than that in Scenario 1. In Scenario 3, a DR program has been also used in addition to the backup EES. With the participation of the DR program, some of the load related to the CHP outage hours has been transferred to the off-peak hours when the CHP is connected, and the load shedding has been reduced compared to scenarios 1 and 2.

- Cooling balance

The cooling balance for the first three scenarios has been shown in Fig. 10. In this figure, the upper bar charts show generation and the lower bar charts show consumption. Due to the fact that we have a summer day to study, the demand for cooling is high. Therefore, electric chiller, absorption chiller, EHP and CES have been used to

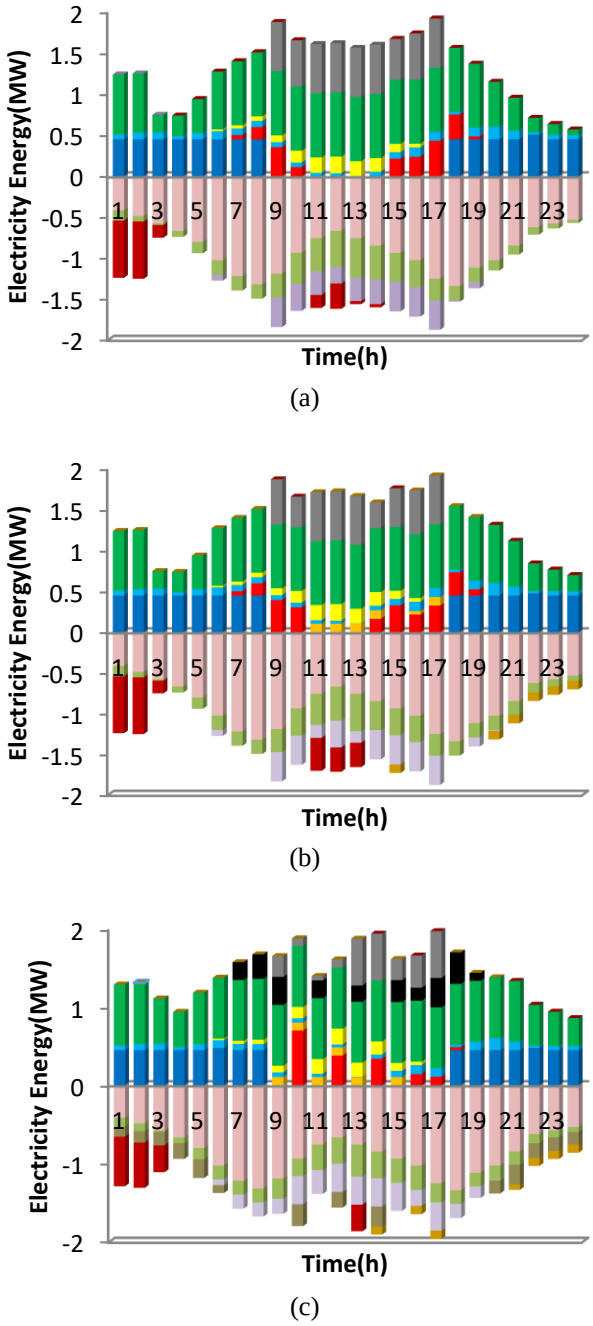

Fig. 8: Electrical balance in three scenarios related to gas network outages, (a) Scenario 1, (b) Scenario 2, and (c) Scenario 3.

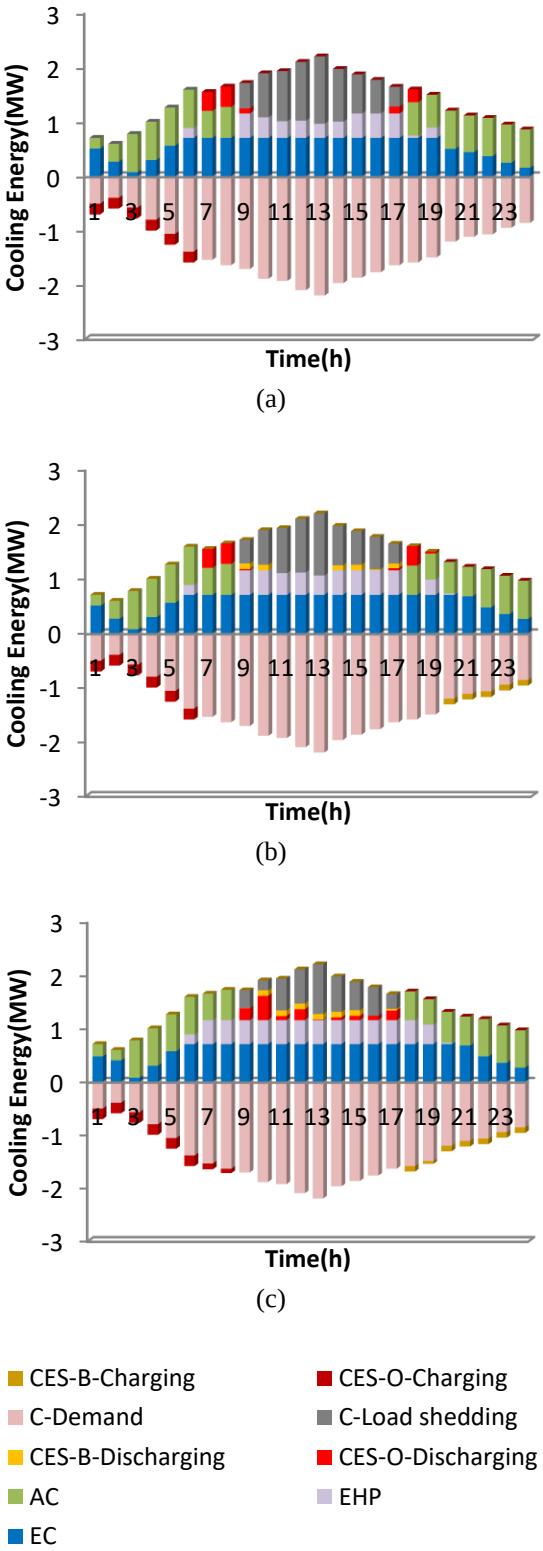

Fig. 9: Cooling balance in three scenarios related to gas network outage, (a) Scenario 1, (b) Scenario 2, and (c) Scenario 3.

supply the cooling demand. In the early and last hours of the day, which are off-peak heating hours, most of the cooling demand is met by the absorption chiller. The reason for this is the use of heating energy by absorption chiller to generate cooling. After the absorption chiller, the electric chiller is more economical than EHP to generate cooling energy due to its higher coefficient of performance, as it uses less electricity to generate cooling energy. Absorption chiller generates cooling energy only at off-peak heating hours and electric chiller at almost all hours. EHP also helps generate

cooling energy during peak cooling hours. Like the HES, the original CES stores excess cooling generation in the early hours of the day, which are off-peak cooling hours, and the original CES in the discharge mode during the outage hours of the gas network when there is a cooling load shedding and a lack of this energy. According to Fig. 9, the cooling load shedding is too high in Scenario 1 where there is no backup CES and DR program. But in Scenario 2, due to the use of backup CES and its help to supply a part of the cooling demand, the load shedding is less than that in Scenario 1. In Scenario 3, using backup CES and DR, the cooling load shedding compared to Scenario 2 has changed at different hours.

- Heating balance

The heating balance for the first three scenarios has been shown in Fig. 10. In this figure, the upper bar charts show generation and the lower bar charts show consumption. CHP also generates heating at the same time as generating electricity. The generated heat, like the electricity in all hours of the CHP ON state, is almost at the maximum possible value corresponding to point B in the CHP operating range. Therefore, for all hours, the CHP operating point changes with the AB line, where the electricity varies between 0.45 to 0.6 MWh, and the heating generated varies up to a maximum of 0.55 MWh. In addition to CHP, a boiler has been also used to generate heating energy in this energy hub. Boiler, like CHP, reduces the cost of operating an energy hub due to the use of natural gas as fuel. The boiler is also disconnected during the outage hours of the gas network. During all the hours that the boiler is in circuit, the heating output is very close to the maximum possible value. Due to the fact that there is no device for generating heating in the energy hub other than the boiler and CHP, the heating load shedding is significantly high. Since heating energy, in addition to meeting the demand for cooling generation is used to a large extent, the load shedding is also slightly reduced by using the backup HES. Moreover, since electricity load is not used in heating generation, DR has little effect on heating load shedding. According to Fig. 10, a small portion of the heating energy is supplied by ST, with a maximum output of 0.108 MWh. The original HES system helps to manage the hub energy to reduce operating costs. This system supplies the hub's energy demand by charging and discharging when needed. According to Fig. 9, the original HES is in the charging mode in the early hours of the day (1-6) when the boiler and CHP are in circuit and the heating energy is excess and, it helps to meet the demand by draining the heating in the outage hours of the gas network when there is a shortage of heating energy.

4.3.2. Energy balance in power outage scenarios

- Electrical balance

The electrical balance for the second three scenarios, which are related to the electrical network outage, has been shown in Fig. 11. In this figure, the upper diagrams show the electricity generation and the lower bar diagrams show the electricity consumption. Energy hubs supply a part of the electricity they need to supply the power for their through the electrical network. Disconnecting the energy hub from

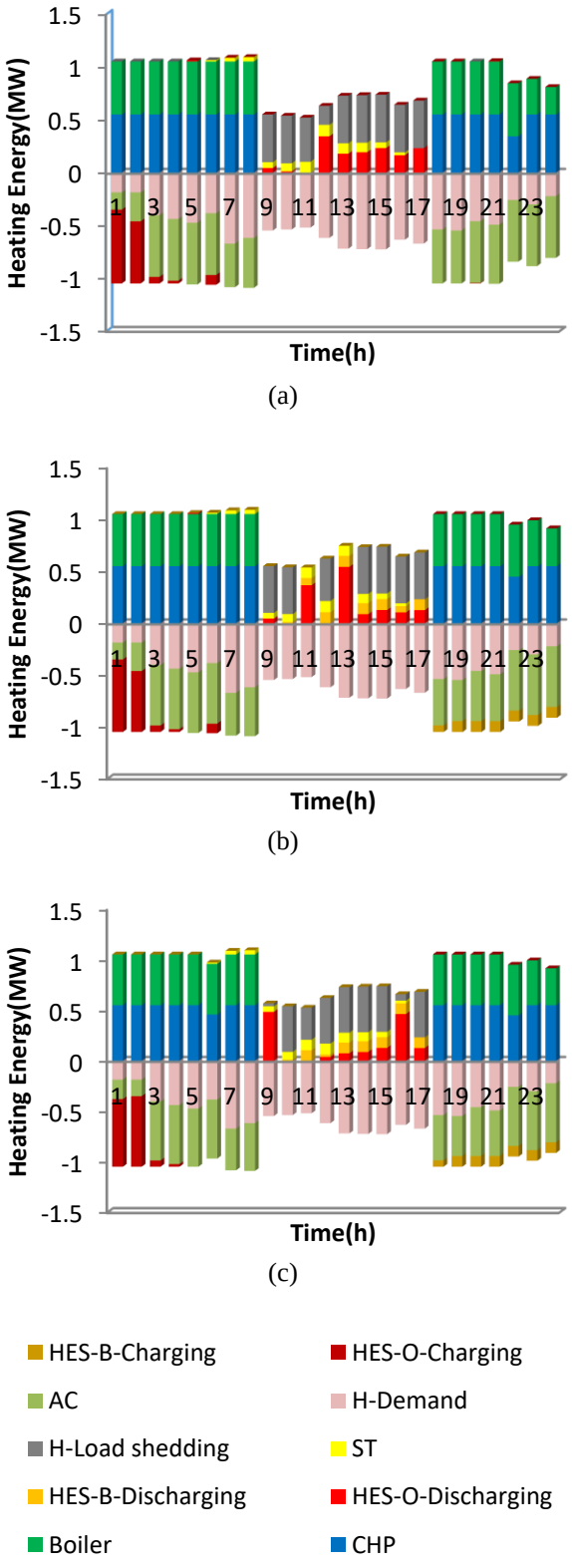

Fig. 10: Heating balance in three scenarios related to gas network outages, (a) Scenario 1, (b) Scenario 2, and (c) Scenario 3.

the electrical network for a few hours will cause much damage to the energy hub. According to Fig. 11, the connection of the electrical network with the energy hub has been terminated during 9-17 hours local time. During these

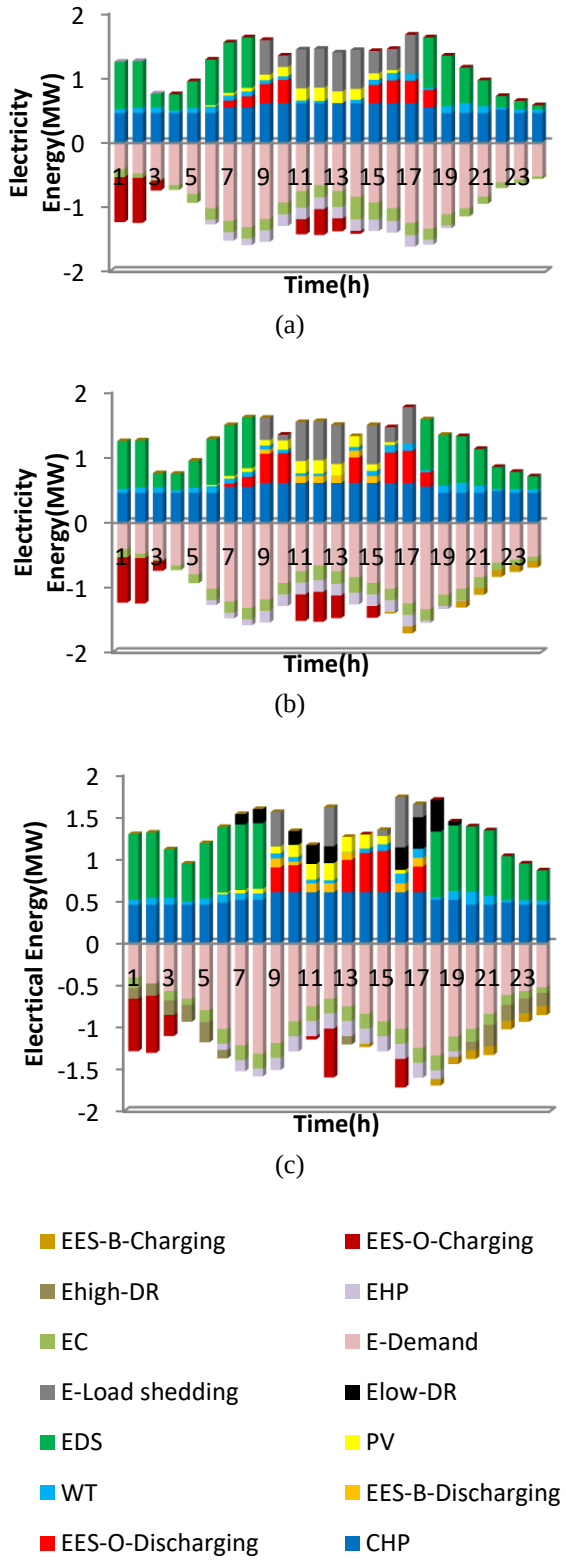

Fig. 11: Electrical balance in three scenarios related to electrical network outage, (a) Scenario 4, (b) Scenario 5, and (c) Scenario 6.

hours, the CHP generates maximum electricity to compensate for the outage of electrical network. In the second three scenarios, as in the first three scenarios, renewable sources such as PV and WT have been used to meet a part of the electricity demand. According to Fig. 11, in the second three scenarios, the charging/discharging pattern of the original EES is affected by electricity prices defined by the operator and begins to store energy in the early hours of the day due to low electricity prices. In addition, it is in discharging mode in high price hours and hours when there is a shortage of electricity. According to Table 2 (in the appendix), in Scenarios 5 and 6, backup EES is also used in addition to the original EES. In Scenario 4, which does not use backup EES and DR, the electrical load shedding is significantly high. In Scenario 5, which uses backup EES during a power outage, the load shedding is less than that in Scenario 4. Using DR along with the backup EES in Scenario 6, the electrical load shedding is significantly reduced compared to Scenarios 4 and 5.

- Heating balance

The heating balance for the second three scenarios has been shown in Fig. 12. In this figure, the upper bar graphs show heating generation and the lower bar graphs show heating consumption. According to Fig. 12, with the outage of electrical network, the heating load shedding does not occur and the CHP and the boiler meet all the heating demands being in the circuit. According to Fig. 12, the CHP and the boiler have their maximum generation at almost all hours in the second three scenarios. This is due to the replacement of heating energy for electricity for cooling generation, during the hours of the electricity network outage. In these three scenarios, a small part of the heating energy is provided by ST. In the second three scenarios, as in the first three scenarios, the original HES is in the charging mode during the hours when there is excess heating energy and during the hours of electrical network outage, when more heating is used to generate cooling. During the hours of lack of heat, the original HES is discharged to help meet heating demand.

- Cooling balance

The cooling balance has been demonstrated in Fig. 13 for the second three scenarios. In this figure, the upper bar diagrams show the cooling generation and the lower bar diagrams illustrate the cooling consumption. As can be seen in Fig. 13, the electrical network outage cause cooling load shedding, and since the boiler and CHP generate heating at all hours, most of the cooling demand is supplied by the absorption chiller. Like the first three scenarios after the absorption chiller, the electric chiller has the highest contribution in cooling energy generation. The EHP also helps meet demands for cooling during peak cooling hours, which is equivalent to off-peak electricity hours, due to the use of electricity to generate cooling. The original CES is also in charge mode during off-peak hours and in discharge mode during peak hours. According to Fig. 13, the cooling load shedding is too high in Scenario 1 where there is no backup CES and DR program. But in Scenario 2, due to the use of backup CES and its help to supply a part of the cooling demand, the load shedding is less than that in Scenario 1. In Scenario 3, using backup CES and DR, the cooling load shedding is reduced to zero.

4.3.3. Scheduling the operation of backup storages and implementation of the DR program

As shown in Table 5, backup storages have been used in

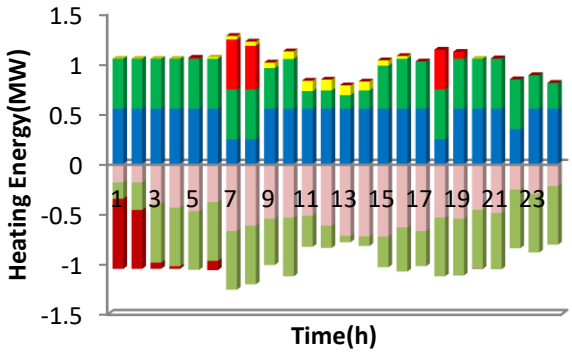

(a)

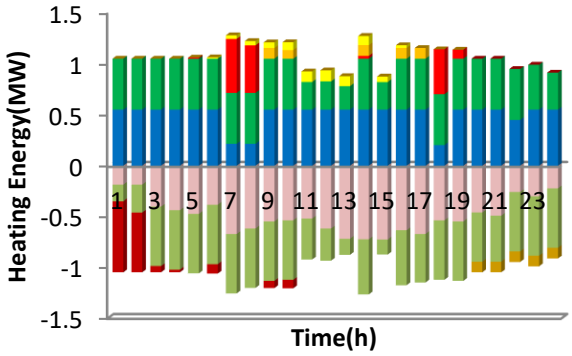

(b)

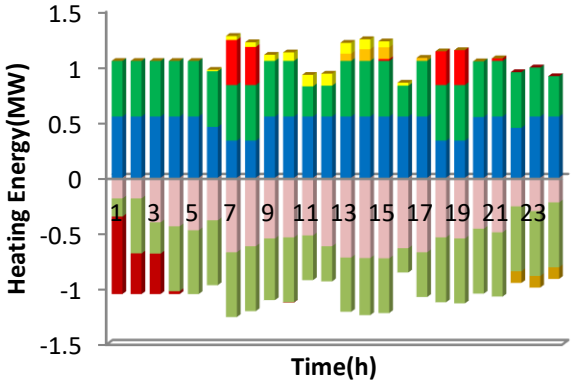

(c)

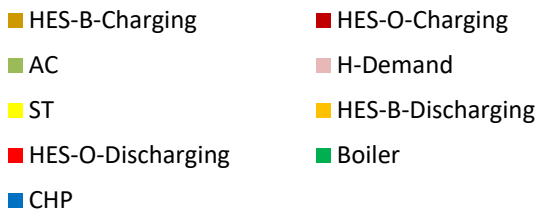

Fig. 12: Heating balance in three scenarios related to electrical network outage, (a) Scenario 4, (b) Scenario 5, and (c) Scenario 6.

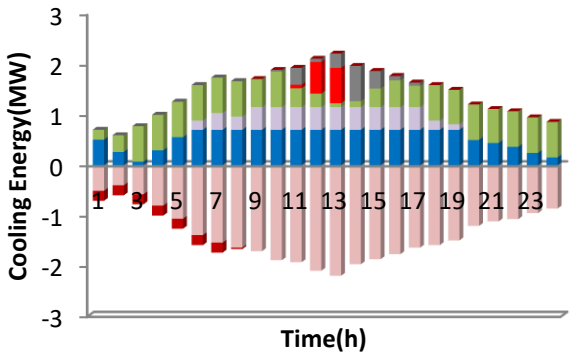

(a)

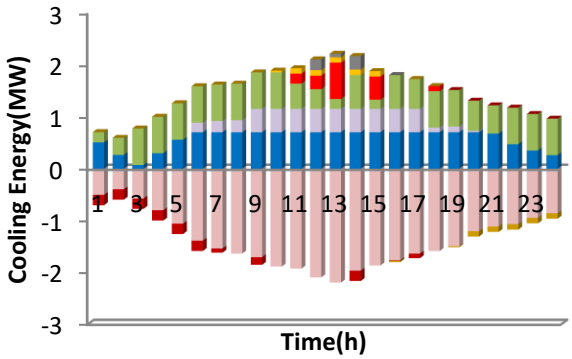

(b)

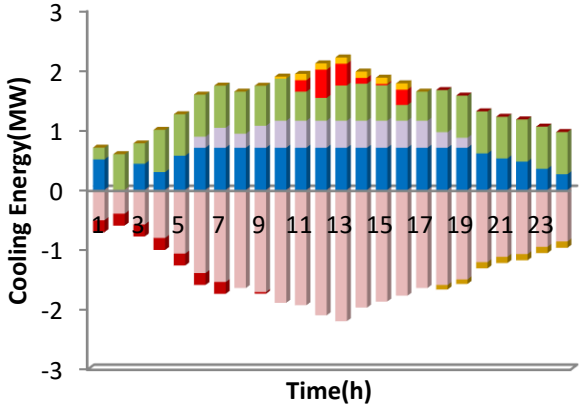

(c)

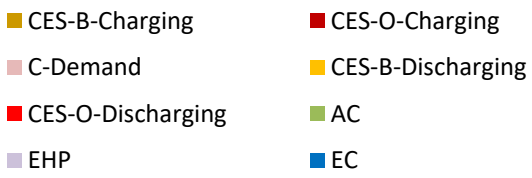

Fig. 13: Cooling balance in three scenarios related to electrical network outage, (a) Scenario 4, (b) Scenario 5, and (c) Scenario 6.

Scenarios 2, 3, 5, and 6. Fig. 14 shows the operation schedule of backup storages in 4 scenarios. In this figure, the upper bar diagrams show the battery discharge mode and the lower bar diagrams demonstrate the battery charge mode. Backup storages are in discharge mode in 4 scenarios during 9-17 hours local time, which are the outage hours of input energy carriers. And due to successive discharges, the level of energy stored in the backup storage devices decreases. Therefore, they are in charging mode in the last hours of the

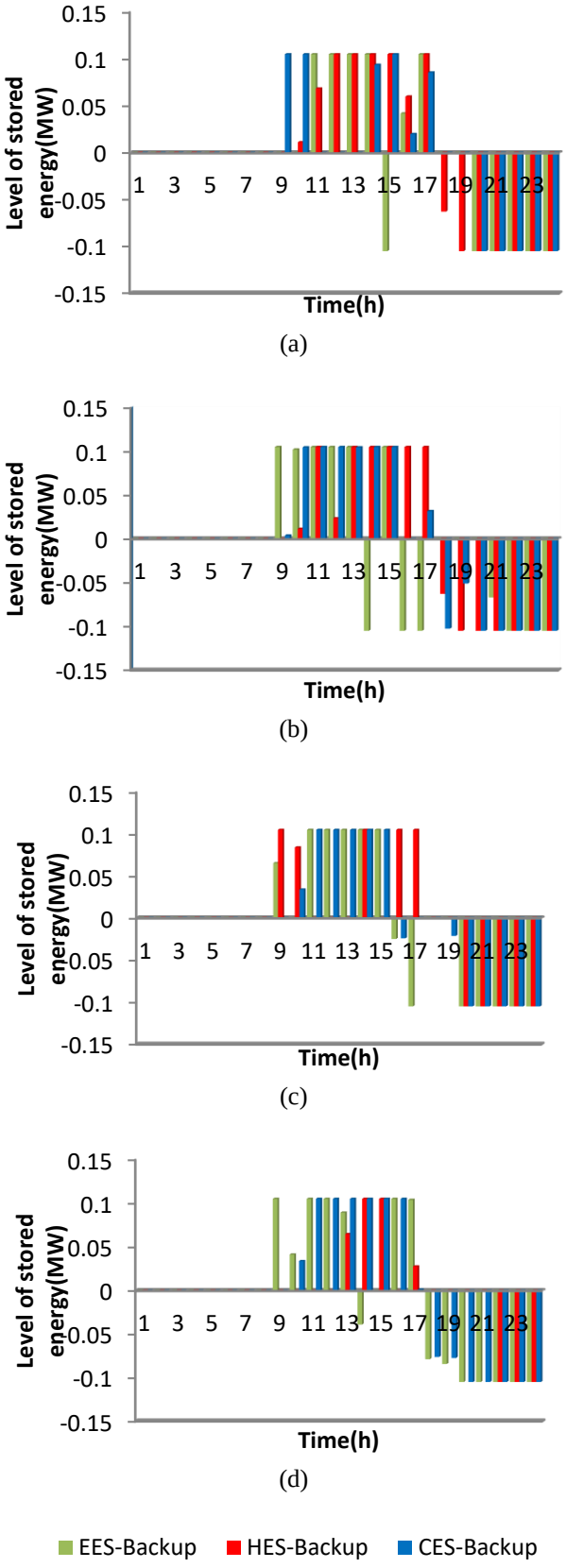

Fig. 14: Scheduling of backup storages operations, (a) Scenario 2, (b) Scenario 3, (c) Scenario 5, and (d) Scenario 6.

day to maximize their reserve amount to be ready to support any outages the day ahead. According to Fig. 14, in Scenario

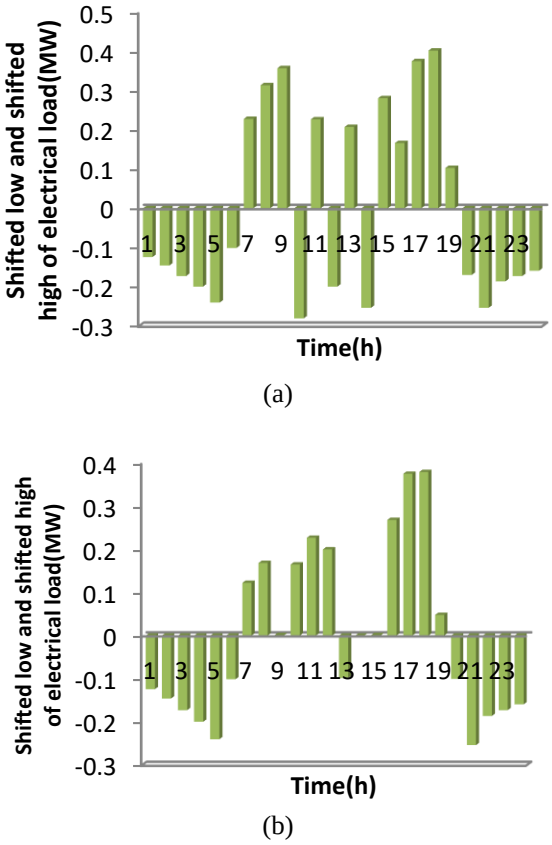

Fig. 15: Scheduling of DR program implementation, (a) Scenario 3, and (b) Scenario 6.

2, the battery works longer than in Scenario 3 in discharge mode, because of the effect of the DR program used in Scenario 3 on the displacement of the electrical load over time. Scenarios 5 and 6 are related to electrical network outages. As shown in the section on energy balance, the only results of electrical network outage is electrical and cooling loads shedding. However, diagrams in Scenarios 5 and 6 show that the backup heating battery are also charging/discharging. Moreover, since electricity is used to generate cooling and heating, the activity of heating and cooling backup batteries reduces the need for electricity, hence reducing electrical load shedding.

According to Table 5, the DR program has been used in two Scenarios 3 and 6 in order to flatten the demand curve. Fig. 15 shows the scheduling of load changes by executing a DR program for the two scenarios. According to Fig. 15, the electricity load has shifted from the hours of high electricity prices, to off-peak hours and low prices. Consequently, it has a great effect on reducing load shedding and improving resiliency in the outage hours of input energy carriers.

4.3.4. Resiliency and economic analysis of energy hub

According to Fig. 16 and the results obtained above, the effect of proper use of backup storages and participation of DR program in the optimal operation of the energy hub can be observed. In this paper, the resiliency of the energy hub has been calculated according to the total electrical, heating and cooling load shedding in the outage hours of natural gas or electricity network for the six scenarios, since there is a

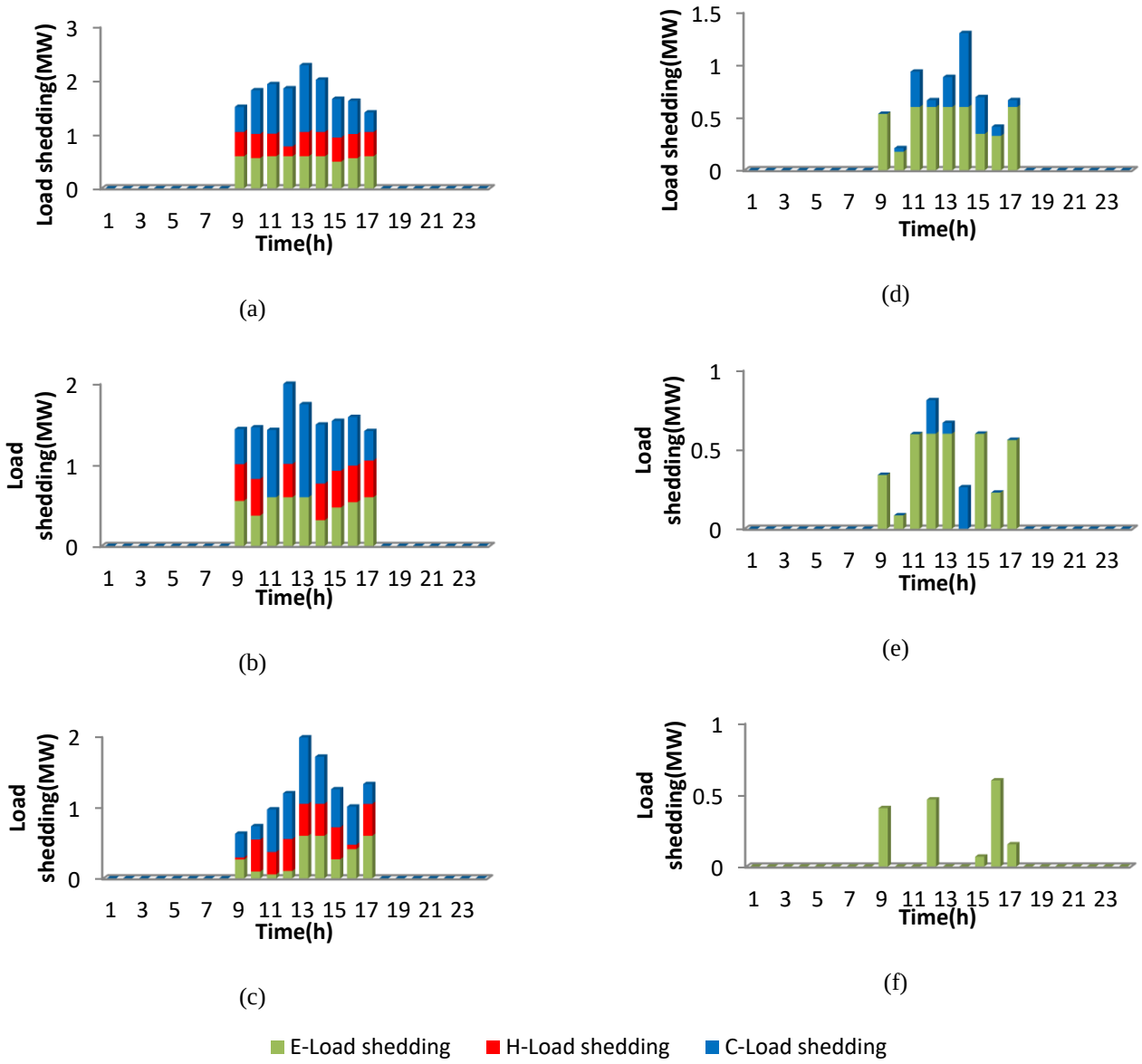

Fig. 16: Load shedding in six scenarios, a) Scenario 1, b) Scenario 2, c) Scenario 3, d) Scenario 4, e) Scenario 5, and f) Scenario 6.

relationship between electricity, heating and cooling loads. Also, the cost of load penalties is not provided and the total cost for all six scenarios have been presented in Table 6 (in the appendix). The first three scenarios in Table 6 are associated with gas network outages. According to Table 6, the total cost in Scenario 1, where the backup storage and DR program is not used, is 5600.134$. Nonetheless, the total cost for Scenario 2 where only backup storage is used and for scenario 3, where the DR program has been used in addition to backup storage, has decreased to 5310.221$ and 4815.829$, respectively.

According to Table 6, the resilience of the whole system and the amount of load shedding at the hours of the natural gas network outage in the first three scenarios are equal to 21.764 – 23.182 - 27.335MWh and 16.148 - 15.024 - 10.826MWh, respectively. Also, the Percentage of resiliency of the whole system at the hours of the natural gas network outage in the first three scenarios is equal to 57.40%, 60.67% and 71.63%, respectively. These values indicate an increase in the resiliency of the energy hub through backup storage and DR during outage hours of the gas network. The second three scenarios in Table 3 are associated with power outages. According to Table 6, the total cost in Scenario 4, which lacks backup storage and DR, is 3448.813$, and the total cost for Scenario 5, where only backup storage has been used, and Scenario 6, where both backup storage and DR have been used, has decreased to 3085.937$ and 2808.270$, respectively. According to Table 6, the resilience of the whole system and the amount of load shedding at the hours of the power network outage in the second three scenarios are equal to 32.261 – 36.256 – 37.738MWh and 6.295 - 4.154 - 1.697MWh, respectively. Additionally, the resiliency of the system in the second three scenarios is 83.67%, 89.72% and 95.69%, respectively, which indicates an increase in resiliency in Scenarios 5 and 6 compared to Scenario 4.

5. CONCLUSION

In this study, we investigated the optimal energy hub scheduling based on CHP and renewable resources with the aim of minimizing costs and improving resiliency. Backup storages and DR program have been used in order to improve resiliency and reduce load shedding during power outages or natural gas. The proposed strategy has been evaluated by conducting extensive numerical studies in the form of multiple scenarios, and a numerical metric has been employed to accurately calculate resiliency. The results show that, in the event of a gas network outage, the use of backup storage alone will improve resiliency and reduce operating costs by 3.27% and 289.913$, respectively. Also, if DR programs are practiced alongside backup storage, the reduction in the resiliency improvements and operating costs will be 14.23% and 784.305$, respectively. In addition, during electrical network outage, the use of backup storage alone will improve resiliency and reduce operating costs by 6.05% and 362.876$, respectively. Also, in the case of the application of DR programs alongside backup storage, the resiliency improvements and operating costs decrease will be 12.02% and 640.543$, respectively. Therefore, the proposed strategy in the condition of the outage of input energy carriers can significantly improve the resiliency and reduce the operating cost of the hub.

CREDIT AUTHORSHIP CONTRIBUTION STATEMENT

Shabnam Rezaei: Data curation, Formal analysis, Investigation, Software, Validation, Roles/Writing - original draft, Writing - review & editing. **Ahmad Ghasemi:** Conceptualization, Methodology, Project administration, Writing - review & editing.

DECLARATION OF COMPETING INTEREST

The authors declare that they have no known competing financial interests or personal relationships that could have appeared to influence the work reported in this paper. The ethical issues; including plagiarism, informed consent, misconduct, data fabrication and/or falsification, double publication and/or submission, redundancy has been completely observed by the authors.

APPENDIX

Table1: Summary of literature review and scope and contribution of this article

References		[2]	[3]	[4]	[5]	[6]	[7]	[8]	[9]	[10]	[11]	[12]	This study
Operation mode	Grid-Connected	√	√	√	√	-	-	√	√	-	√	-	√
	Network outage	-	-	-	√	√	√	√	√	√	√	√	√
Power network outage		-	-	-	-	-	√	√	√	√	√	√	√
Gas network outage		-	-	-	√	√	-	-	-	-	-	-	√
Improves power load shedding during outages		-	-	-	-	-	√	√	√	√	√	√	√
Improves heating and cooling load shedding during outages		-	-	-	√	√	-	-	-	-	-	-	√
Calculate rates of resiliency by the index		-	-	-	-	√	-	-	-	-	-	-	√
CHP		√	√	√	√	-	-	√	-	-	-	-	√
Boiler		√	√	√	√	-	-	-	-	-	-	-	√
Chiller		√	√	√	-	-	-	-	-	-	-	-	√
EHP		-	√	-	-	√	-	-	-	-	-	-	√
Renewable energy		√	-	√	√	-	√	√	-	√	-	√	√
Energy storage		√	√	√	√	-	√	-	√	√	√	√	√
Study the impact of storage on resiliency		-	-	-	-	-	-	-	√	√	√	√	√
DR		√	√	√	-	-	√	√	-	-	-	-	√
Study the impact of DR on resiliency		-	-	-	-	-	√	√	-	-	-	-	√

Table2: Parameters of energy hub components

Renewable resource parameters				
$\gamma^{PV} = 151$	$\gamma^{WT} = 28$	$\gamma^{ST} = 126$		
CHP parameters				
$a = 0.1035$	$34.5\,b =$	$c = 26.5$	$d = 0.025$	$e = 2.203$	$f = 0.051$
$H_A^{CHP} = 0$	$H_B^{CHP} = 0.55$	$H_C^{CHP} = 0.4$	$H_D^{CHP} = 0$	
$E_A^{CHP} = 0.6$	$E_B^{CHP} = 0.45$	$E_C^{CHP} = 0.1$	$E_D^{CHP} = 0.2$	
Boiler parameters				
$H_{\min}^{Boiler} = 0$	$H_{\max}^{Boiler} = 0.5$	$\eta^{Boiler} = 0.95$		
Electric chiller parameters				
$C_{min}^{EC} = 0$	$C_{max}^{EC} = 0.7034$	$COP_{cool}^{EC} = 4$	$\gamma^{EC} = 2$	
Absorption chiller parameters				
$C_{min}^{AC} = 0$	$C_{max}^{AC} = 0.7034$	$COP_{cool}^{AC} = 1.2$	$\gamma^{AC} = 2$	
EHP parameters				
$C_{min}^{EHP} = 0$	$C_{max}^{EHP} = 0.45$	$COP_{cool}^{EHP} = 2.5$	$\gamma^{EHP} = 1$	
Original electrical energy storage parameters				
$E_{min}^{EES,O} = 0.4$	$E_{max}^{EES,O} = 1.8$	$E_{max}^{EES,o,ch} = 0.7$	$E_{max}^{EES,o,dch} = 0.7$	$\eta^{EES,o,ch} = 0.9$
$\eta^{EES,o,dch} = 0.9$	$E_0^{EES,O} = 0.4$	$\gamma^{EES,O} = 1$		
Power backup storage parameters				
$E_{min}^{EES,B} = 0.035$	$E_{max}^{EES,B} = 0.7$	$E_{max}^{EES,B,ch} = 0.105$	$E_{max}^{EES,B,dch} = 0.105$	$\eta^{EES,B,ch} = 0.9$
$\eta^{EES,B,dch} = 0.9$	$E_0^{EES,B} = 0.7$	$\gamma^{EES,B} = 1$		
Original heating energy storage parameters				
$E_{min}^{HES,O} = 0$	$E_{max}^{HES,O} = 1.8$	$E_{max}^{HES,o,ch} = 0.7$	$E_{max}^{HES,o,dch} = 0.7$	$\eta^{HES,o,ch} = 0.96$
$\eta^{HES,o,dch} = 0.96$	$E_0^{HES,O} = 0.4$	$\gamma^{HES,O} = 1$		
Heating backup storage parameters				
$E_{min}^{HES,B} = 0.035$	$E_{max}^{HES,B} = 0.7$	$E_{max}^{HES,B,ch} = 0.105$	$E_{max}^{HES,B,dch} = 0.105$	$\eta^{HES,B,ch} = 0.96$
$\eta^{HES,B,dch} = 0.9$	$E_0^{HES,B} = 0.7$	$\gamma^{HES,B} = 1$		
Original cooling energy storage parameters				
$E_{min}^{CES,O} = 0$	$E_{max}^{CES,O} = 1.8$	$E_{max}^{CES,o,ch} = 0.2$	$E_{max}^{CES,o,dch} = 0.7$	$\eta^{CES,o,ch} = 0.98$
$\eta^{CES,o,dch} = 0.98$	$E_0^{CES,O} = 0.4$	$\gamma^{CES,O} = 1$		
Cooling backup storage parameters				
$E_{min}^{CES,B} = 0.035$	$E_{max}^{CES,B} = 0.7$	$E_{max}^{CES,B,ch} = 0.105$	$E_{max}^{CES,B,dch} = 0.105$	$\eta^{CES,B,ch} = 0.98$
$\eta^{CES,B,dch} = 0.98$	$E_0^{CES,B} = 0.7$	$\gamma^{CES,B} = 1$		
Electricity DR parameters				
$par^{high,DR} = 30\%$	$par^{low,DR} = 30\,\%$	$\gamma^{E} = 1$		

Table 6: Results in various case studies

Scenario	Total cost($)	Load shedding (MWh)	Resiliency (MWh)	Resiliency(%)
1	5600.134	16.148	21.764	57.40%
2	5310.221	15.024	23.182	60.67%
3	4815.829	10.826	27.335	71.63%
4	3448.813	6.295	32.261	83.67%
5	3085.937	4.154	36.256	89.72%
6	2808.270	1.697	37.738	95.69%

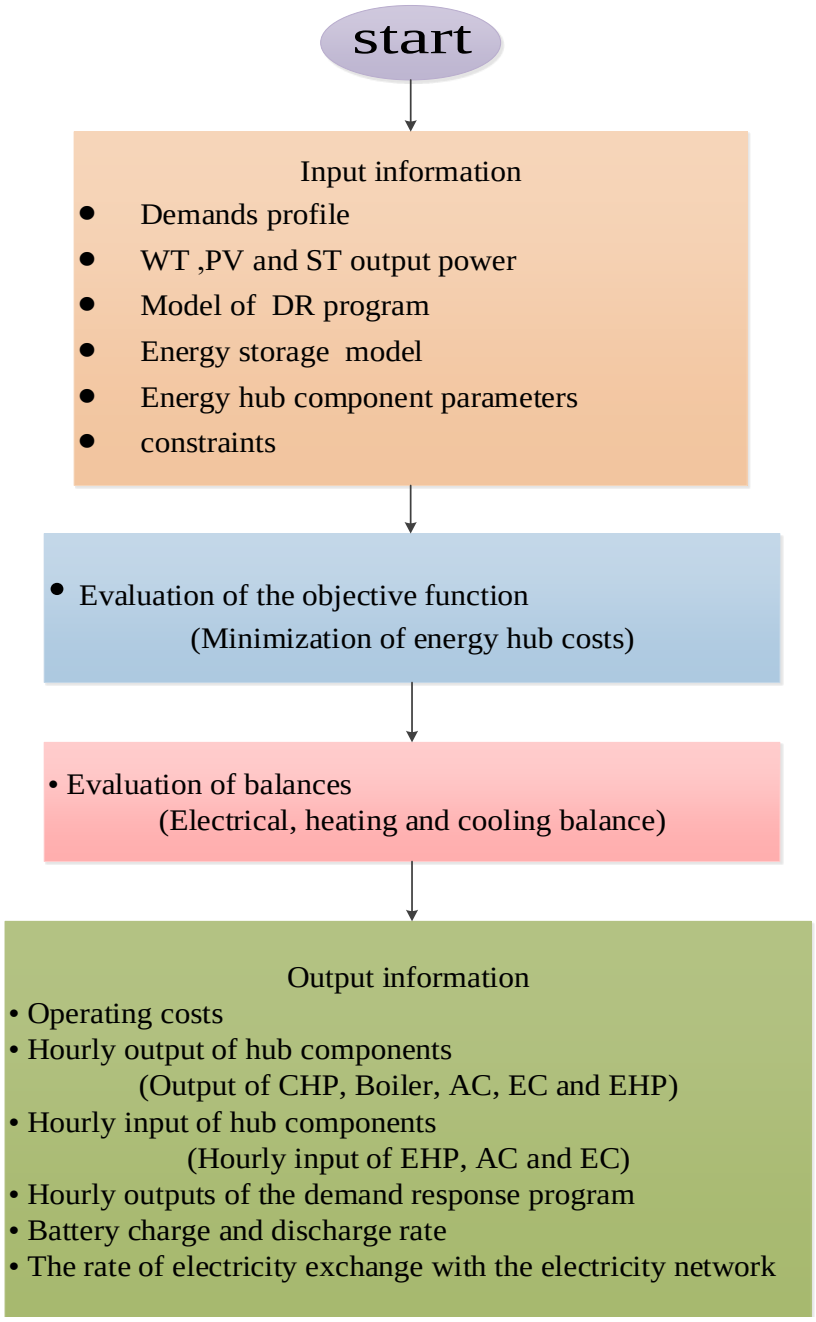

Fig. 2: The proposed scheduling framework.

REFERENCES

[1] M. Panteli, and P. Mancarella, "Modeling and evaluating the resilience of critical electrical power infrastructure to extreme weather events,"*IEEE Systems Journal*, vol. 11, no. 3, pp. 1733-1742, 2015.

[2] M. Tengfei, W. Junyong, and H. Liangliang, "Energy flow modeling and optimal operation analysis of the micro energy grid based on energy hub", *Energy Conversion and Management*, vol. 133, pp. 292–306, 2017.

[3] M. Salehimaleh, A. Akbarimajd, Kh. Valipour, and A. Dejamkhooy, "Generalized modeling and optimal management of energy hub based electricity, heat and cooling demands", *Energy*, vol. 159, pp. 669-685, 2018.

[4] D. Rakipour, and H. Barati, "Probabilistic optimization in operation of energy hub with participation of renewable energy resources and DR", *Energy*, vol. 173, pp. 384-399, 2019.

[5] N. Gholizadeh, M.J. Vahid-Pakdel, and B. Mohammadi-ivatloo, "Enhancement of demand supply's security using power to gas technology in networked energy hubs", *Interational Journal of Electrical Power and Energy Systems*, vol. 109, pp. 83–94, 2019.

[6] M. Salimi, D. Faramarzi, S. H. Hosseinian, and G. B. Gharehpetian, "Replacement of natural gas with electricity to improve seismic service resilience: An application to domestic energy utilities in Iran", *Energy*, vol. 200, 117509, 2020.

[7] F. Hafiz, B. Chen, Ch. Chen, and A. Rodrigo de Queiroz, I. Husain, "Utilizing DR for distribution service restoration to achieve grid resiliency against natural disasters", *IET Generation, Transmission & Distribution*, vol. 13, pp. 2942-2950, 2019.

[8] M. Vahedipour-Dahraie, H. Rashidizadeh-Kermani, and A. Anvari-Moghaddam, "Risk-based stochastic scheduling of resilient microgrids considering demand Response programs", *IEEE Systems Journal*, vol. 15, pp. 971 – 980, 2021.

[9] Hussain, V. H. Bui, and H. M. Kim, "A resilient and privacy-preserving energy management strategy for networked Microgrids" *IEEE Transactions on Smart Grid*, vol. 9, pp. 2127 – 2139, 2018.

[10] E. Galvan, P. Mandal, and Y. Sang," Networked microgrids with roof-top solar PV and battery energy storage to improve distribution grids resilience to natural disasters", *Interational Journal of Electrical Power and Energy Systems*, vol. 123, pp. 106-239, 2020.

[11] C.P. Nguyen, and A.J. Flueck, "Agent based restoration with distributed energy storage support in smart grids", *IEEE Transactions on Smart Grid*, vol. 3, pp. 1029-1038, 2012.

[12] H. Ghasemieh, B.R Haverkort, M.R. Jongerden, and A. Remke, "Energy resilience modelling for smart houses". in *45th Annual IEEE/IFIP International Conference on Dependable Systems and Networks*, 2015, pp. 275-286.

[13] M. Alipour, B. Mohammadi-ivatloo, and K. Zare, "Stochastic Scheduling of Renewable and CHP based Microgrids", *IEEE Transactions on Industrial Informatics*, vol. 11, pp. 1049-1058, 2015.

[14] Vranjes, D. Milenic, and P. Vasiljevic, "Criteria for use of groundwater as renewable energy source in geothermal heat pump systems for building heating/cooling purposes," *Energy and Buildings*, vol. 02, pp. 209–257, 2010.

[15] Vanden Borre, "Definition of heat pumps and their use of renewable energy sources," *REHVA Journal*, vol. 48, pp. 38-39, 2011.

[16] F. Madonna, and F. Bazzocchi, "Annual performances of reversible air-to-water heat-pumps in small residential buildings," *Energy and Buildings*, vol. 25, pp. 299–309, 2013.

[17] N. Zhu, P. Hu, L. Xu, and Zh. Jiang, "Recent research and applications of ground source heat pump integrated with thermal energy storage systems: A review," *Applied Thermal Engineering*, vol. 71, pp. 102-151, 2010.

[18] Faeze, H. Masoud, and J. Shahram, "Optimal electrical and thermal energy management of a residential energy hub, integrating DR and energy storage system", *Energy Build*, vol. 90, pp. 65-75, 2015.

[19] Li, L. Wenjian, C. Jiejin, H. Bowen, and W. Chengshan, "A two-stage optimal planning and design method for combined cooling, heat and power microgrid system", *Energy Convers Manage*, vol. 74, pp. 433–445, 2013.

[20] Sheikhi, S. Bahrami, and A. Ranjbar, "An autonomous DR program for electricity and natural gas networks in smart energy hubs", *Energy*, vol. 89, pp. 490-499, 2015.

[21] M. Shams, M. Shahabi, and M. Khodayar, "Stochastic day-ahead scheduling of multiple energy Carrier microgrids with DR", *Energy*, vol. 155, pp. 326-338 2018.

[22] J.M. Arroyo, "Bilevel programming applied to power system vulnerability analysis under multiple contingencies." *IET Generation, Transmission & Distribution*, vol. 4, pp. 178-190, 2010.

[23] L. Xiaonan, H. Kai, J. Hongjie, and Zh. Junbo, M. Lamine, M. Yunfei, R. Jusong, L. Yunkai," A resilience assessment approach for power system from perspectives of system and component levels", *Interational Journal of Electrical Power and Energy Systems*, vol. 118, 105837, 2020.

[24] GAMS Webpage, (accessed 2021), [Online]. Available: http://www.gams.com;.

[25] Branch & Bound, (accessed 2021) [Online]. Available: https://www.mutah.edu.jo/userhomepages/CS252/branchandbound.html, 2008.

BIOGRAPHY

Shabnam Rezaei received the B.Sc. from Lorestan University, Khorram-abad, Iran in 2017 and the M. Sc. degree from Jundi-Shapur University of Technology, Dezful, Iran, in 2020. Her research interests include power system operation, resiliency and energy manag-ement of energy hubs.

Ahmad Ghasemi received the B.Sc. from Amirkabir University of Technol-ogy, Tehran, Iran in 2004 and the M. Sc. And Ph. D. degrees from Shahid Chamran University, Ahvaz, Iran, in 2008 and 2015, respectively. Since 2015, he has been an Assistant Prof-essor with the Department of Electrical and Computer Engineering, Jundi-Shapur University of Technology, Dezful, Iran. His research interests are oriented to different aspects of Micro-Grid energy management and demand side management.

Copyrights
© 2021 Licensee Shahid Chamran University of Ahvaz, Ahvaz, Iran. This article is an open-access article distributed under the terms and conditions of the Creative Commons Attribution –Non-Commercial 4.0 International (CC BY-NC 4.0) License (http://creativecommons.org/licenses/by-nc/4.0/).

Journal of Applied Research in Electrical Engineering

Vol. 1, No. 1, Winter and Spring 2022

jaree.scu.ac.ir

Iranian Association of Electrical and Electronics Engineers

Shahid Chamran University of Ahvaz